A Contribution to the Experimental Validation in Lorentz Force Eddy Current Testing

Dissertation

zur Erlangung des akademischen Grades

Doktoringenieur

(Dr.-Ing.)

vorgelegt der
Fakultät für Maschinenbau der
Technischen Universität Ilmenau

von Herrn
M.Sc. Matthias Carlstedt
(geb. Wiegand)
geboren am 12.02.1984 in Nordhausen

Datum der Einreichung: 05.12.2016
Datum der wissenschaftlichen Aussprache: 05.04.2017

Gutachter:

Univ.-Prof. Dr.-Ing. habil. Klaus Zimmermann, *Technische Universität Ilmenau*
Univ.-Prof. Dr.-Ing. habil. Hannes Töpfer, *Technische Universität Ilmenau*
Univ.-Prof. Dr.-Ing. habil. Hendrik Rothe, *Helmut-Schmidt-Universität Hamburg*

A bend in the road

"[To] mechanical progress there is apparently no end: for, as in the past so in the future, each step in any direction will remove limits and carry us past barriers which have till then blocked the way in other directions; and so what for the time may appear to be a visible end or practical limit will turn out but a bend in the road."

<div align="right">

Osborne Reynolds
Opening address to the Mechanical Science Section in Nature (15 Sep 1887) [110]

</div>

ABSTRACT

Nondestructive testing (NDT) of electrically conductive components and assemblies is an integral part of the product life cycle of almost every technical product in our daily life. Particularly in the automotive and aerospace industry, the use of modern light-weight materials allows the development of ever more powerful and efficient mechanical structures. These heavy duty components must be tested for their structural integrity in the production phase as well as in the subsequent operating phase in order to ensure safe and reliable operation. *Lorentz force eddy current testing* (LET), which is investigated in this work, is one of the testing methods that are capable to meet the growing requirements of these industries.

The thesis begins with a brief introduction into the state-of-the-art in NDT and a presentation of the involved industrial markets. Subsequently, the related work in the field of *motion-induced eddy current testing* methods is described. A particular focus is on the experimental investigations carried out in previous feasibility studies.

The consideration of the physical phenomena relevant to the measuring principle, by means of the *dimensional analysis*, allows a deepening insight into the interactions of the electromagnetic and geometric parameters. A comprehensive numerical study accompanies this study and leads to the elaboration of practical *scaling laws*.

The most comprehensive part of the thesis is the classification and the systematic description of the measurement procedure of LET and a representative overview of the measurement performance of the developed experimental setup. In this study, a novel *multi-component sensor system* is used, which allows simultaneous recording of the occurring measuring forces as well as their accelerating effect on the measurement setup. The idealized (deterministic) measurement process is extended to a real measurement process by considering the involved physical quantities as random variables. It is analyzed that the statistical properties of the measurement result, e.g. mean and variance of a physical quantity, are not independent of time. Thus, a measurement signal of a single measurement can not provide a complete measurement result for the non-stationary measurement process. Therefore, the assembling of an *artificial signal ensemble* of sequential measurements is suggested, which for the first time enables the calculation of complete measurement results in LET.

The mechanical modeling of the dynamics of the experimental setup is another novelty in the theoretical description of LET measurement process. For this purpose, the process of *system identification* is presented exemplary for two practically relevant examples. This allows a straight modeling of the mechanical system by an appropriate signal preprocessing and a model-specific parameter estimation.

Based on these mechanical models, the design process of digital filters is shown in order to compensate the frequency-dependent sensitivity of the applied force sensor.

ZUSAMMENFASSUNG

Die zerstörungsfreie Materialprüfung elektrisch leitfähiger Komponenten und Baugruppen ist ein integraler Bestandteil im Produktlebenszyklus heutiger technischer Produkte. Insbesondere im Automobilbau sowie der Luft- und Raumfahrttechnik ist durch den Einsatz moderner Leichtbaumaterialien die Entwicklung immer leistungsfähigere mechanischer Komponenten möglich. Diese hochbeanspruchbaren Bauteile müssen sowohl in der Fertigungsphase als auch in der späteren Betriebsphase auf ihre strukturelle Integrität geprüft werden, um einen sicheren und zuverlässigen Betrieb gewährleisten zu können. Die in dieser Arbeit untersuchte *Lorentzkraft-Wirbelstromprüfung* ist eines der Prüfverfahren, welche in diesem Zusammenhang erforscht und weiterentwickelt werden.

Nach einer kurzen Einführung in den Stand der Technik der zerstörungsfreien Materialprüfung und einer Vorstellung der relevanten Märkte, werden die vorangegangen Arbeiten auf dem Gebiet der *bewegungsinduzierten Wirbelstromprüfverfahren* beleuchtet. Ein beonderes Augenmerk liegt dabei auf den experimentellen Untersuchungen, welche in vorangegangenen Machbarkeitsstudien erfolgreich durchgeführt wurden.

Die Betrachtung der für das Messprinzip relevanten physikalischen Phänomene ermöglicht mittels der durchgeführten *Dimensionsanalyse* einen vertiefenden Einblick in die Wechselwirkungen der elektromagnetischen und geometrischen Größen. Umfassende numerische Studien begleiten diese Untersuchung und führen zur Formulierung von praktischen *Skalierungsregeln*.

Den umfassendsten Teil der Arbeit bilden die Klassifizierung und die systematische Beschreibung des untersuchten Messverfahrens, sowie die repräsentative Darstellung experimenteller Studien. Hierbei kommt ein *mehrkomponentiges Sensorsystem* zum Einsatz, welches die zeitgleiche Erfassung der auftretenden Messkräfte sowie deren Beschleungungswirkung auf den Messaufbau ermöglicht. Das idealisierte Messverfahren wird durch die Betrachtung der beteiligten physikalischen Größen als Zufallsvariablen zu einem realen Messprozess erweitert. Dabei zeigt sich, dass die statistischen Eigenschaften des Messprozesses nicht zeitunabhängig sind und somit ein Messsignal einer einzelnen Messung kein vollständiges Messergebnis, im Sinne einer experimentellen Standardabweichung, liefern kann. Aus dieser Einsicht heraus werden Ansätze für die Bildung von *künstlichen Signalscharen* beschrieben und in unterschiedlichen experimentellen Studien erpobt. Diese Signalensemle, welche aus Einzelsignalen bestehen, ermöglichen dabei erstmals eine statistische Auswertung der Messergebnisse.

Einen Neuheitswert stellt ebenfalls die in der Arbeit vorgestellte Erweiterung des Messmodells zu einem nicht rückwirkungsfreien Messverfahren dar, welches die mechanische Wechselwirkung der Lorentzkraft und des mechanischen Messaufbaus beschreibt. Hierfür werden für zwei praktisch relevante Beispiele geeignete Verfahren zur *Systemidentifikation* vorgestellt, welche sowohl in der Signalvorverarbeitung als auch der modellspezifischen Parameterschätzung eine einfache Modellbildung des mechanischen Systems ermöglichen.

Aus den so gewonnenen mechanischen Modellen wird anschließend beispielhaft der *Entwurf digitaler Filter* zur Kompensation des frequenzabhängigen Übertragungsverhaltens dargestellt.

NOMENCLATURE

Acronyms

ACFM	alternating current field measurements
ADC	analog-to-digital converter
AE	acoustic emission testing
BNA	Barkhausen noise analysis
DAQ	data acquisition
DFT	discrete Fourier transform
DiLET	differential Lorentz force eddy current testing
DOE	design of experiment
DOF	degree of freedom
DRS	defect response signal
DSP	digital signal processing
EC	eddy currents
ECT	eddy current testing
eSDM	experimental standard deviation of the mean
ET	electromagnetic testing
FEM	finite element method
FIR	finite impulse response
FML	fibre-metal laminate
GLARE	glass laminate aluminum reinforced epoxy
GMR	giant magnetoresistance
GPR	ground penetrating radar
GW	guided wave testing
IR	thermal/infrared testing
ISO	International Organization for Standardization
LET	Lorentz force eddy current testing
LFV	Lorentz force velocimetry
LM	laser testing methods
LT	leak testing
LTI	linear time-invariant

MCS	measurement control system
MECT	motion-induced eddy current testing
MEMS	micro-electro-mechanical system
MFL	magnetic flux leakage
MIMO	multi-input/multi-output
MSE	mean squared error
MT	magnetic particle testing
NDE	nondestructive evaluation
NdFeB	neodymium iron boron
NDT	nondestructive testing
NI	National Instruments
NR	neutron radiographic testing
NRMSE	normalized root mean squared error
ODE	ordinary differential equation
PM	permanent magnet
PSD	power spectral density
PT	liquid penetrant testing
PXI	PCI eXtensions for Instrumentation
QSA	quasi-stationary approach
R&D	research and development
RFT	remote field testing
ROI	region of interest
RT	radiographic testing
SDM	standard deviation of the mean
SDOF	single degree of freedom
SDR	signal to distortion ratio
SI	International System of Units
SISO	single-input/single-output
SME	small and medium-sized enterprises
UT	ultrasonic testing
UUT	unit under test
VA	vibration analysis
VIM	international vocabulary of metrology
VT	visual testing

Symbol	Meaning	Unit
$\mathbf{A}$	acceleration of the measurement frame	$\mathrm{m\ s^{-2}}$
$\mathbf{B}^{(p)}$	primary magnetic field	T

$\mathbf{B}^{(\mathrm{s})}$	secondary magnetic field	T
B_{r}	remanent magnetization of magnetic material	T
c_i	the damping coefficient (viscous damper)	$\mathrm{kg\ s^{-1}}$
$\mathbf{D}$	dimensional matrix	
D	diameter of a cylindrical magnet	m
d	defect depth	m
$\mathbf{F}(t)$	Lorentz force	$\mathrm{kg\ m\ s^{-2}}$
$\tilde{F}$	dimensionless force	1
f_{c}	cut-off frequency of digital filter	Hz
f_{s}	sampling frequency	Hz
f_0	(undamped) eigenfrequency of the oscillator	Hz
$\left[\mathbf{G}\right]$	consistent system of units	
g_{DF}	gain	
$\mathbf{H}$	magnetic field strength	$\mathrm{A\ m^{-1}}$
$H(s)$	transfer function in Laplace space	
H	height of a cylindrical magnet	m
h	distance between the PM and plate/UUT	m
$\mathbf{J}$	eddy currents density	$\mathrm{A\ m^{-2}}$
$\mathbf{J}_{\mathrm{s}}$	surface current density	$\mathrm{A\ m^{-1}}$
$\mathrm{J}_1(\cdot)$	first order Bessel function of the first kind	
k_i	stiffness of the system	$\mathrm{kg\ s^{-2}}$
k_x	transform variable in x-direction	
k_y	transform variable in y-direction	
$\mathbf{M}$	magnetization	$\mathrm{A\ m^{-1}}$
m	mass	kg
N_z	number of turns of the coil	
$\left[\mathbf{R}\right]$	rotation matrix	
R_{m}	magnetic Reynolds number	1
$\mathbf{S}$	solution matrix	
S	coordinate system of the plate/UUT	
S'	coordinate system of the PM	
s	sensor sensitivity	
$s(\cdot)$	experimental standard deviation	
s_{l}	linear scaling factor	1
T_{s}	sampling period	s
t	plate thickness	m
t	time	s
$\tilde{t}$	dimensionless time	1

Symbol	Meaning	Unit
t_{c}	characteristic time	s
$u(\cdot)$	expanded uncertainty (cf. $s(\cdot)$)	
V_z	induced voltage	V
$\mathbf{v}$	relative motion of PM and UUT	$\mathrm{m\,s^{-1}}$
$\mathbf{x}$	list of the physical parameters x_i	
$[x_i]$	dimension of physical parameter x_i	
x, y, z	coordinates of Cartesian coordinate system	m

Symbol	Meaning	Unit
α, β, γ	yaw, roll, and pitch angle	1
δ	dimensionless diameter of cylindrical magnet	1
κ_A	correlation factor of acceleration components	1
μ	magnetic permeability	$\mathrm{V\,s\,A^{-1}\,m^{-1}}$
μ_r	relative permeability	1
Π	dimensional parameter	1
$\Phi_z(t)$	magnetic flux	$\mathrm{kg\,m^2\,A^{-1}\,s^{-2}}$
σ	electrical conductivity	$\mathrm{S\,m^{-1}}$
σ_F	experimental standard deviation of the force	$\mathrm{kg\,m\,s^{-2}}$
τ	dimensionless plate thickness	1
τ_i	time-lag of the i–th observation	1
ω_{0i}	undamped angular frequency	$\mathrm{s^{-1}}$
ξ	aspect ratio of PM	1
ζ_i	dimensionless damping ratio	1

TABLE OF CONTENTS

LIST OF TABLES

LIST OF FIGURES

INTRODUCTION

1.1 Motivation

Nondestructive testing (NDT) is an integral part of the product life cycle of almost every technical product in our daily life. Whether in the production of disc brakes of a motorcycle or the maintenance of a nuclear power plant, NDT methods help to meet highest quality requirements and to ensure the technical reliability of critical infrastructural systems.

Modern lightweight construction materials have always been a standard in aviation, but nowadays they are becoming increasingly popular also in the automotive and railway industry, as well as in competitive sports and prosthetics. Despite of the ever increasing use of plastics, the majority of materials being used are electrically conductive. Whether carbon-fiber-reinforced structural components or fiber-metal laminates, like in modern aircrafts, many of these materials are investigated using electromagnetic testing methods. In many applications manufacturing errors and material aging occur at the surface of components which are important for operation. Therefore, the use of surface testing methods, such as classical eddy current testing, is an indispensable tool for the evaluation of structural integrity. However, in many cases the volumetric examination is indispensable to identify material failure, often derived from an existing defects, at an early stage.

The novel NDT-method of *Lorentz force eddy current testing* (LET) was invented to complement established methods by overcoming the well known detection limitations for subsurface defects.

1.2 Thesis Aims and Objectives

The aim of this thesis is to provide a scientific contribution to the understanding of this novel NDT-method for the purpose of utilizing it for industrial use. The primary focus is on the experimental application of LET in a controlled environment and under repeatable conditions.

One important goal is to provide qualitative insights into the measurement principle of LET and to answer the question whether there are operating areas that can be described by simple dependencies of the physical quantities involved. Furthermore, the goal is to develop scaling laws in order to accelerate the future development of new prototypes for LET applications.

Since the method of LET can still be regarded as novel, a classification into already established NDT-procedures has to be carried out. As will be apparent in the survey of the state-of-the-art, the preparatory work is to be classified as a proof-of-concept, which has several deficiencies with respect to repeatability and industrial relevance. Therefore, further experimental investigations are carried out for the purpose of statistical evaluation and to provide complete measurement results. On the one hand, the focus is on applications for the validation of numerical models, also for ferromagnetic materials. On the other hand, components made of lightweight construction materials are tested which allows the assessment of detection capabilities of LET in modern engineering applications.

Another important aim of this work is to analyze the sources of disturbances for LET measurements. For this purpose, filtering measures used in the related preparatory work are discarded and the measurement procedure is redeveloped in order to be able to separate systematically recurring disturbances from random errors. Therefore, the existing force sensor is to be extended to an enhanced sensor system, which should improve the observability of the experiment. Based on the expected insights, the measurement model, which is limited to the electromagnetic field problem, shall be expanded by the interaction of the unit under test (UUT) and the experimental setup.

1.3 Thesis Layout

In Chapter 2 the thesis deals with the introduction into the state-of-the-art of NDT with special focus on the description of LET. The most frequently used NDT methods are presented and the preparatory work related to LET is described. In Chapter 3 an electromagnetic problem directly related to the measurement principle of LET is discussed. The focus here is on the dimensional analysis of the electromagnetic problem and the development of scaling laws. Chapter 4 is focused on the experimental contribution of this thesis and is divided into three major sections. At first, the measurement procedure of LET is described in terms of measurement principle and measurement method. The second section of this chapter gives a detailed description of the experimental setup used for laboratory experiments in this thesis. Afterwards, the developed digital signal processing (DSP) for LET is explained. In the next section, a representative overview of the measurement performance of the experimental setup is given, including defect

free UUTs made from aluminum and stainless steel, as well as a specially prepared specimen made of a fiber-metal laminate common in aerospace industry. Chapter 5 deals with the mechanical modeling of systematic harmonic distortion observed during the experimental investigations. The process of system identification for experimental setups in LET is presented for two typical operation points and an optimized compensation filter is designed which results in an significantly improved prediction of the Lorentz force. The thesis concludes in Chapter 6 with a section on summary and discussion and an outlook for future work.

In this chapter an introduction is given into the state-of-the-art in NDT with special focus on the description of Lorentz force eddy current testing (LET). First, the most frequently NDT methods used in industry are described and particular applications are given. Second, the LET method is introduced and the related preparatory work is described.

2.1 Nondestructive Testing

NDT is the process of inspecting materials, single components, or complete assemblies for detecting unwanted property variations and anomalies without permanently altering the objects properties or reducing its serviceability. It is one of the key technologies in modern engineering applications and is considered as a basic need in industries such as aerospace and power generation. The terms nondestructive examination, inspection, and evaluation are not clearly separated from each other and are often used interchangeably. In the framework of this thesis the term NDT is used for the process of acquiring and processing measurement data in order to *detect* material flaws and other anomalies. The term nondestructive evaluation (NDE) is used for the characterization process for determining the anomalies properties from these data. This process can involve a physical model of the measurement process and an algorithm to solve the inverse problem. The decision process, if the unit under test (UUT) fulfills the requirements to pass the test or not, is based on a threshold criteria depending on the particular application and is out of focus of this thesis.

In contrast to NDT, *destructive testing methods* are often applied to specially prepared samples in order to determine the mechanical, thermal, or chemical properties of the material under test, e.g. tensile strength, ductility, flammability, or fatigue strength. Besides these methods for *material testing*, *structural testing* is used to test components and entire products

for critical properties like ultimate load, impact resistance, and crash behavior.

2.1.1 NDT Methods

NDT includes various methods, each based on a particular physical or chemical principle. The naming of these different methods is non-consistent and refers to different aspects such as the used equipment, the involved process media, or the physical nature of the emitted energy (e.g. acoustic or electromagnetic) for testing in combination with its characteristic range of wavelengths (e.g. ultra sonic, infrared, or X-ray).

The six most frequently used NDT methods in industry are magnetic particle testing (MT), liquid penetrant testing (PT), radiographic testing (RT), ultrasonic testing (UT), electromagnetic testing (ET), and visual testing (VT) [58, 77]. Other methods used are acoustic emission testing (AE), guided wave testing (GW), ground penetrating radar (GPR), laser testing methods (LM), leak testing (LT), magnetic flux leakage (MFL), microwave testing, neutron radiographic testing (NR), thermal/infrared testing (IR), and vibration analysis (VA) [7, 71]. In the following the six most frequently used NDT methods are presented briefly.

2.1.1.1 Magnetic Particle Testing

Magnetic particle testing is used to find near-surface defects in ferromagnetic materials and offers one of the highest sensitivities for surface cracks. The method uses different magnetization techniques to introduce an magnetic field into the UUT. When the magnetic field is disturbed by a discontinuity of the magnetic properties of the material transverse to the direction of the magnetic field (e.g. cracks), a magnetic flux leakage field is produced (Fig. 2.1a). This magnetic
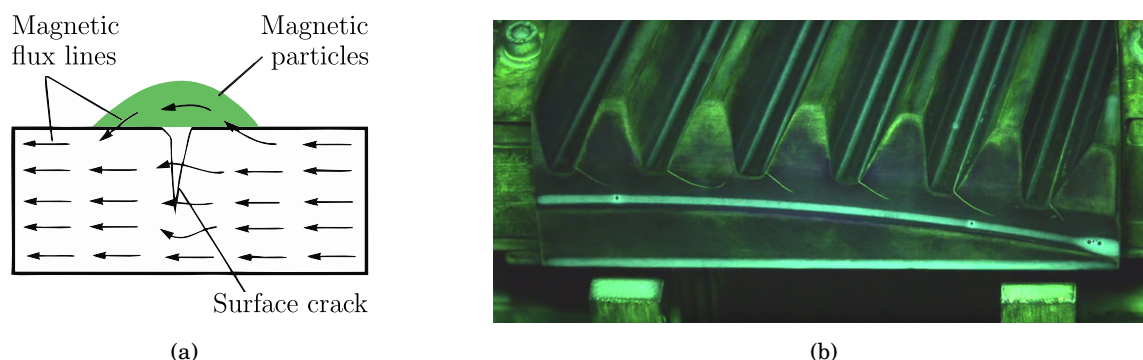
Figure 2.1: Basic principle of MT: (a) schematic of magnetic flux disturbance and particle distribution by surface cracks; (b) photo of surface cracks at the tooth base of a gear wheel (direct induction at a wet bath machine) [111].

flux leakage field can be made visible with colored or fluorescent magnetizable particles (dry powder or suspended in a liquid solution) applied to the UUT. Because the magnetic resistance of air is much larger than that of the magnetic particles, the particles are drawn into the leakage field and reduce the air gap which produces a visible indication (Fig. 2.1b).

The different magnetization techniques are classified as direct and indirect induction techniques. In the *direct induction* an electric current is introduced into the UUT generating a circular magnetic field around two electrodes. The magnetic field induced is perpendicularly oriented to an imagined straight line drawn between the two electrodes. Thus, the magnetic field can only be disturbed significantly by defects parallel to this line. The electrodes are available in various shapes and are typically called prods for hand-held use and heads when used in wet bath machines.

The *indirect induction* uses an electric coil to generate a magnetic field which is introduced into the UUT. In most field inspections the magnetic field is introduced via an articulated AC/DC yoke. Because the magnetic flux lines in this case run from one leg to the other, this technique is also known as longitudinal magnetization. Thus, the magnetic field is only disturbed by defects perpendicular to the imagined straight line drawn between the two articulated legs of the yoke.

The biggest advantage of MT compared to other NDT methods is that it can be used for more complicated geometries with only marginal need for surface preparation. It is a low-cost method and easily portable. Disadvantageous is the need for pre and post cleaning as well as the requirement of demagnetization of the UUT for many applications.

2.1.1.2 Liquid Penetrant Testing

Liquid penetrant inspection [55, 56] is a low-cost inspection method used for the detection of surface-breaking defects in nearly all non-porous materials, e.g. metals, plastics, and ceramics [70]. The basic principle is to apply a low-viscosity liquid which penetrates open material

1) Penetrant   2) Developer   3) Indication

(a)   (b)
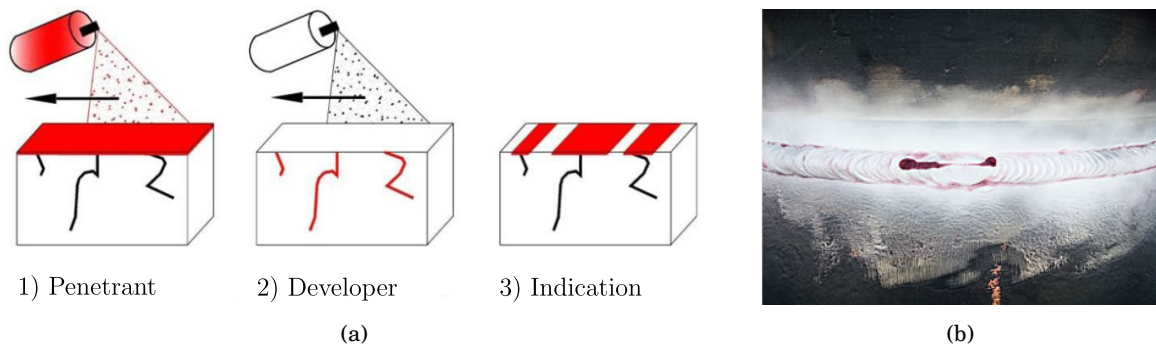
Figure 2.2: Basic principle of PT: (a) schematic of necessary steps for liquid penetrant testing; (b) photo of a surface crack at a weld seam [106].

separations like fissures and voids open to the surface. This liquid can be colored or fluorescent and will remain after an intermediate cleaning of the surface where it serves as an indicator (Fig. 2.2a).

In order to improve the penetration process, the surface of the UUT must be carefully cleaned and free of any unwanted materials or liquids which might otherwise block the penetrant from entering. After the intermediate cleaning step, some penetrants require an additional light

coating of developer for a visible indication (Fig. 2.2b). These fine-grained powders significantly improve the visibility of the indications, but extend the whole process by the required developer dwell time.

Liquid penetrant inspection shares the advantages of low cost equipment and high portability with MT. It is based on only a few steps allowing fast training of the testing operator. PT also share the disadvantage of pre and post cleaning and the strict restriction to open surface defects.

2.1.1.3 Radiographic Testing

Radiographic testing is a volumetric testing method which allows to detect surface defects and internal discontinuities, e.g. inclusions, porosity, corrosion, and density changes, in nearly all technical materials. It is capable of detecting misaligned parts in assemblies and to measure geometry variations, making RT one of the most-used NDT methods in industry [58, 77].

The basic principle is based on the ability of short wavelength electromagnetic radiation (higher energy photons) to penetrate an object depending on its thickness and density. Therefore, the UUT is exposed to radiation given off by an X-ray tube or decaying radioactive materials (gamma radiation). The intensity of radiation emerging from the opposite side of the UUT is measured and used to determine thickness or composition of the inspected material (Fig. 2.3).

The used RT techniques are film radiography, computed radiography, digital radiography, and computed tomography. Film radiography uses a film made up of a thin transparent foil of plastic which is coated with a layer of radiation-sensitive silver halide crystals (e.g. silver bromide). When exposed to radiation, these crystals undergo a chemical reaction resulting in a
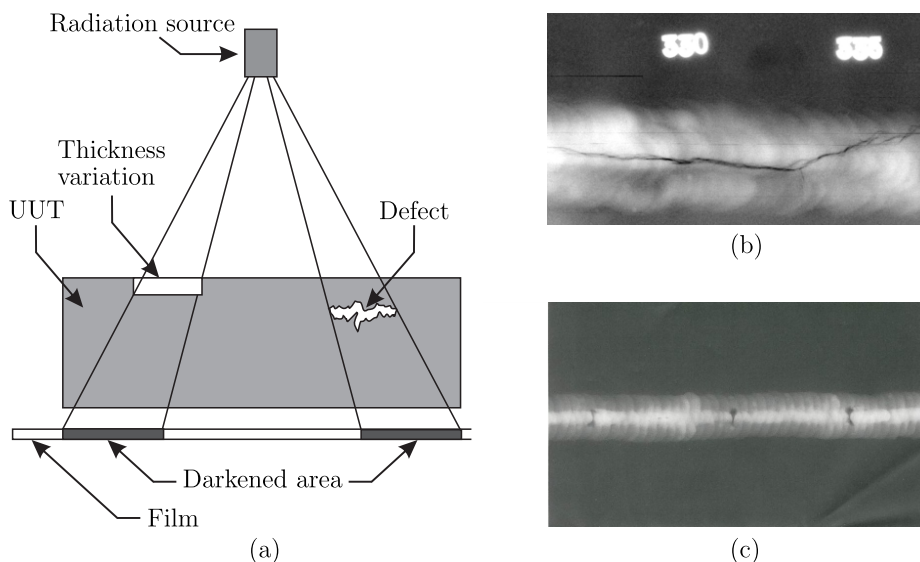
Figure 2.3: Basic principle of RT: (a) schematic of film radiography of the UUT exposed to radiation; (b) and (c) finished radiographic films of flawed weld seams [12, 67].

8

latent image. This image is made visible in the subsequent developing process resulting in a finished radiographic film.

In computed radiography the film is replaced by a reusable, photo-stimulated phosphor plate. It is exposed in the same way as in the case of film radiography, but the plate is digitized afterwards with an optical scanner. This allows to store and transfer the image after the testing, making it also easier available for interpretation.

Digital radiography is the most time efficient radiographic testing technique by completely bypassing the chemical processing from the procedure. Instead of a radiographic film, a detector is used which transforms the radiation going through the UUT into visible light or electric impulses.

Computed tomography uses computer algorithms of images from multiple directions to construct an image of a cross sectional plane of the UUT. This technique allows to precisely determine the position of discontinuities inside the UUT which is making it possible to create a three-dimensional representation of the scanned object.

A common aspect of all radiographic testing techniques is the importance of knowledge about the biological effects of radiation, making radiation safety crucial factor for all RT applications. Besides all the advantages of RT mentioned at the beginning, RT equipment is the most expensive of all NDT methods and it requires well trained operators. Another import fact is that RT requires simultaneous access to at least two sides of the UUT.

2.1.1.4 Ultrasonic Testing

Ultrasonic testing is another volumetric testing method which allows to detect internal discontinuities in most technical materials. It is based on the interaction of an ultrasonic impulse, emitted into the UUT, with a boundary surface or a material with different acoustic properties. The ultrasonic impulses emitted are longitudinal waves (pressure waves) or transverse waves (shear waves) which are reflected, shadowed, refracted or attenuated.

To generate an acoustic pulse, a piezoelectric transducer converts an electrical pulse into a mechanical vibration (sound waves) (Fig. 2.4a). The coupling medium replaces the unwanted air gap and couples the mechanical vibration into the UUT. The received sound waves, e.g. reflection from a defect or the back-wall, are converted back into electric impulses that can be processed and displayed on screen for interpretation (Fig. 2.4b).

Different UT techniques are used in industry depending on the specific testing task. Straight beam inspection uses pressure waves traveling through the UUT which are reflected and attenuated. When the back-wall reflection is identified, all waves reflected before, are received earlier at the transducer and allow to determine the distance of the reflecting surface.

Another widely used UT technique is the angle beam inspection, where the transducer is mounted on a wedge of known angle in order to transmit the pressure wave in the desired angle and direction. This can greatly improve the accessibility of welds leading to an increased detection capability.
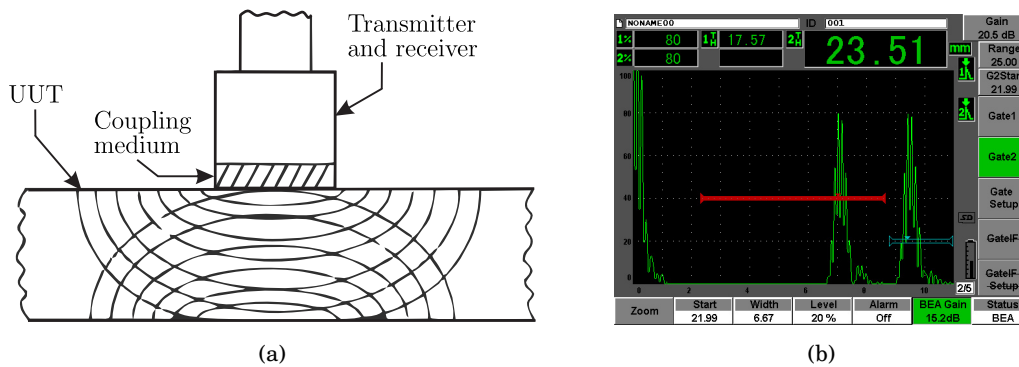
Figure 2.4: Basic principle of UT: (a) schematic of pulse-echo technique of UT [79]; (b) response of flaw echo examination with backwall echo attenuation [97].

A modern alternative to the use of wedges to steer the pressure wave are phased array transducers. Instead of transmitting the wave under on fixed angle, a probe with multiple elements that can be individually activated is used to emit multiple waves. With the correct timing, the direction of the resulting wave can be controlled so that the wave front is very similar to this of an angle beam inspection. Furthermore, the received signals can be combined to construct an image of a cross sectional slice of the UUT.

The advantages of the UT method are its high penetration capabilities and its high sensitivity to even small cracks. However, the operator needs to be especially trained to be able to benefit from the complex propagation of sound waves. Another challenge is to test UUTs of complex geometry, bad surface conditions, or simply small UUTs.

2.1.1.5 Electromagnetic Testing

Electromagnetic testing describes a group of testing methods which use the induction of electric currents into an electrically conducting UUT while measuring the resulting magnetic field or its gradient. This definition does also include magnetic particle testing, but in industry MT is considered as a stand alone method. The methods included in ET are eddy current testing (ECT), alternating current field measurements (ACFM), and remote field testing (RFT). Some textbooks also consider magnetic flux leakage and magneto-elastic techniques like Barkhausen noise analysis (BNA) [88], but again, no consistent classification exists.

In eddy current testing an alternating current carrying coil is placed near the examination area of the electrically conductive UUT (Fig. 2.5a). The associated alternating magnetic field $\mathbf{B}^{(p)}$ (primary magnetic field) induces closed electric currents $\mathbf{J}$ inside the UUT, i.e. eddy currents. These small currents also create a magnetic field $\mathbf{B}^{(s)}$ (secondary magnetic field) which is superimposed with the primary magnetic field. Any geometric or electromagnetic parameter that affects the electrical conductivity of the examined area influences the induction process and changes the total magnetic field. A change in the total magnetic field can be observed by the current-carrying coil or a sensitive pickup coil nearby (Fig. 2.5b). For the examination of
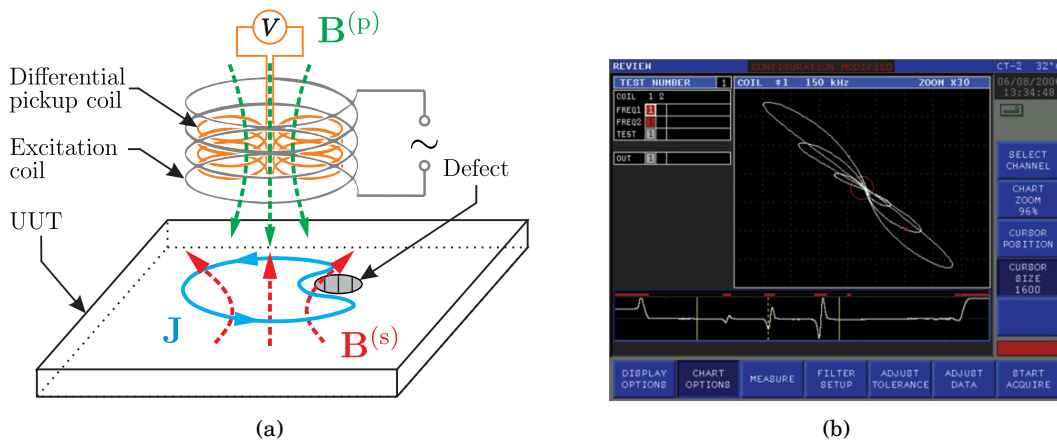
Figure 2.5: Basic principle of ECT: (a) schematic of eddy current induction by an excitation coil and observation of the variation of the total magnetic field by a differential pickup coil; (b) response signal of different surface breaking defects [150].

semi-finished products, e.g. wires, bars, tubes and profiles, encircling coils are used.

Alternating current field measurements are very similar to the direct induction technique in MT with the difference that the magnetic field is not visualized by magnetic particles, but measured with an additional probe. If a discontinuity is present near the surface, the induced magnetic field is perturbed and can be detected by the magnetic field probe.

Remote field testing is commonly applied in the examination of ferromagnetic pipes in petrochemical industries. A typical RFT probe consists of one exciter coil and one or more receiving coils, rigidly fixed at a constant axial distance. The exciter coil carries an alternating electric current of low frequency which produces an associated primary magnetic field. The induced eddy currents extend along the pipe axis and dominate the total magnetic field at a distance of about two times the pipe diameter from the exciter coil [83]. The receiving coils are placed at this distance so that the induced voltage can be observed for changes in the pipe walls, e.g. corrosion or cracks.

One of the biggest advantages of the described electromagnetic methods are the high examination speed and the very low effort for surface preparation. Except for alternating current field measurements, no probe contact is necessary at all. Compared to RT and UT the cost for equipment are generally lower and it takes less time for training.

However, the methods are restricted in examination depth by the skin effect of alternating electric currents. For the majority of applications the combination of excitation frequency (usually in the range of multiple kHz) and conductivity of the tested material results in a significant penetration depth of only a few millimeters. Advanced techniques like multi-frequency, swept frequency, or pulsed eddy current testing are intended to overcome this limitation, but they often require significantly more expensive equipment and increase the required testing time.

11

2.1.1.6 Visual Testing

Visual testing is a surface testing method which is the most commonly used test method in industry. The basic principle of VT is to illuminate the UUT and to examine the surface for corrosion, surface defects, misalignment of parts or structural damage.

In its basic form, unaided eye inspection, it is inherent in almost all other testing methods which are performed manually. However, the detection capabilities of VT are clearly increased when employing special equipment like bevel gauges (Fig. 2.6a), magnifying glasses and mirrors (Fig. 2.6b), microscopes, endoscopes, or (fibre optic) video borescope cameras (Fig. 2.6c).

(a) bevel gauge   (b) inspection mirror   (c) television camera

Figure 2.6: Examples of VT: (a) shape tolerance testing of welded component [4]; (b) and (c) visual quality inspection of an inside thread [69].

Realizing that the VT method is simply the improvement of visual perception by illumination, magnification, and improvement of accessibility, then magnetic particle testing and liquid penetrant testing could be reassigned to the group of visual testing techniques. However, in practice these contrast improving methods are clearly distinguished from each other.

An advantage of the VT method is the simple and inexpensive use for practitioners and the ability to examine otherwise inaccessible areas. The biggest downside of the method is that its reliability heavily depends on the operator's experience.

2.1.2 Applications

NDT plays an important role in almost all phases of the products life cycle, but the main fields of application are production and maintenance. The main goal for the application of NDT methods is to prevent breakage or malfunction of a product during use in order to prevent serious accidents which could cause injury to people or result in environmental contamination. Thus, NDT is a key factor for ensuring product reliability.

Depending on the physical nature of the examined product properties, different NDT methods are applied. During the *production phase* different NDT methods are used to validate that the product fulfills the technical requirements which were defined in the design phase. Furthermore, NDT is used for establishing new manufacturing processes and reducing manufacturing costs. During the *use phase* of a product NDT methods are used to detect degradations, like

cracking and wall thinning, or to track material deformation and damage development which may result in malfunction of the product. Most NDT applications take place in the use phase.

The global NDT equipment markets for NDT are depicted in Fig. 2.7 based on recent market examinations [58, 76, 77].
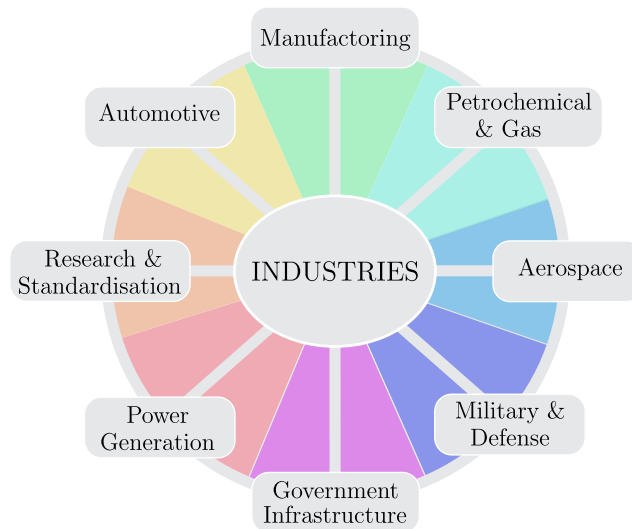
Figure 2.7: NDT markets by industries most relevant for.

The NDT markets by verticals can by divided into eight major industries. The *manufacturing industry* is one of the most diverse markets for NDT applications and covers mining industry, iron foundry, pipe and tube manufacturing, shipbuilding industry and metal industry. It is based on the fabrication, processing, or preparation of products from raw materials and commodities and also includes foods, chemicals, textiles, machines, and equipment as well as refined metals and minerals from extracted ores and wood and paper products. The *petrochemical and gas industry* uses various NDT methods for inspection of refining facilities, transmission and subsea pipelines, storage tanks, and liquefaction for liquefied natural gas. In the *aerospace industry* the main applications are aircraft engine part production and aircraft maintenance. These traditional key applications are assumed to be supplemented by increasing modern composite airframe manufacturing [40]. The *military and defense* sector is composed of the global defense industry and the nation's military. The defense industry shares the major aspects with the aerospace industry and applies NDT methods in the whole product life cycle. Within the armed forces the major NDT applications are maintenance, repair and overhaul of infrastructure, vehicles and equipment. Another diverse market is the *government infrastructure* and *public safety* section including airport security, railway industry [152], bridges and tunnels, border crossing as well as nuclear waste storage and decommissioning. The *power generation industry* is mainly driven by nuclear power but covers also fossil fuel power and the renewable energy sector with wind and solar power. A commonly unrecognized sector in the specification of NDT markets is the area of *research and development* (R&D), *technology transfer* and international

and industrial *standardization*. New NDT technologies are generally developed by academic R&D and small and medium-sized enterprises (SME), but are not adopted by major users without being validated and supported by international standards [80].

2.2 Lorentz Force Eddy Current Testing

It has been shown that a large variety of testing methods are applied to test electrically conducting objects. Especially electromagnetic testing methods (Sec. 2.1.1.5) like ECT are widely applied due to their easy-to-use equipment, low preparation efforts, low requirements on the measurement environment, and the comparatively low equipment costs [47, 62, 63]. One of the major limitations in ECT is the low penetration depth of the induced eddy currents which restricts the method to near-surface examination. The physical effect behind is the well known *skin effect* which describes the frequency dependent tendency for an alternating current to flow mainly near the outer surface of an electrical conductor. A method to overcome this limitation LET was introduced in 2008 by Brauer and Ziolkowski [17].

2.2.1 Basic principle

LET is an electromagnetic testing method which allows the contactless examination of electrically conducting objects. It belongs to the group of motion-induced eddy current testing (MECT) methods which is a subgroup of ET. In contrast to classical eddy current testing, MECT is characterized in that a constant magnetic field source like a permanent magnet (PM) is put in relative motion to the UUT in order to induce eddy currents inside the UUT. The eddy currents have a different distribution compared to eddy currents induced in ECT and they depend highly on the type of motion. The basic principle of LET is illustrated in Fig. 2.8. A PM made
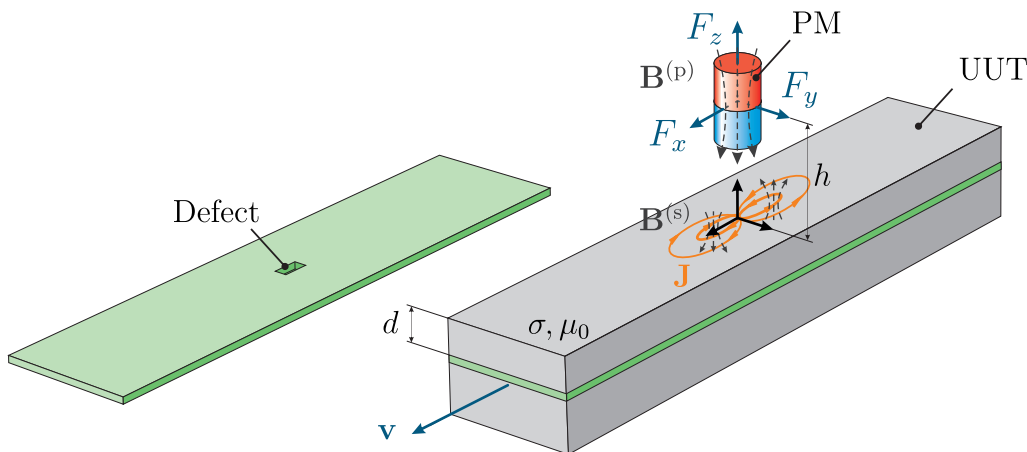
Figure 2.8: Basic principle of Lorentz force eddy current testing. Defect depth d is defined by smallest distance from defect volume to investigated surface. Defect level is highlighted green.

from alloys of rare earth elements, i.e. rare-earth magnet, provides a primary magnetic field

$\mathbf{B}^{(p)}$ which is in relative motion to the electrically conducting UUT. The motion-induced eddy currents $\mathbf{J}$ inside the UUT generate a Lorentz force acting on the UUT. Due to Newton's 3rd law an equivalent force acts on the PM in the opposite direction. In LET this force is measured in order to observe variations in the induced eddy current distribution indicating a change in conductivity for a known motion.

2.2.2   Non-NDT Application of Motion-Induced Eddy Currents

The phenomenon of producing Lorentz force for the purpose of electromagnetic levitation or as a braking force is described well by the Lorentz force law. As reviewed by the author [22], corresponding technical developments have been made in this area for over 100 years and it is a standard element in higher education. However, the application in the field of non-destructive testing has gained international attention only in the last few years.

At present, the phenomenon had numerous different applications, including magnetic bearing [10, 14, 137], coupling [20], precision actuation [61, 151], magnetic suspension [33, 36, 66, 132, 133], and energy harvesters [158, 159]. However, the best known technical applications are magnetically levitated trains, which use electromagnets, PMs, or superconducting magnets for levitation and guidance. Magnetically levitated trains were first proposed by Bachelet in 1912 [8], but high speed transportation systems became popular in the early 1970s and they have evolved into a recognized form of modern transportation in the 21st century. There has been great success in the development of sufficient expressions of the underlying field problem [15, 29, 42, 73, 87, 115, 116, 120]. During the 1990s, great efforts were made [51, 60, 96, 104, 105, 127], which laid the foundations for the current world speed record of the Japan's seven-car maglev train (L0-Series) in a test run of 603 km/h [82].

In educational applications, the slowing down of a magnet falling in a non-ferromagnetic, electrically conducting pipe is employed as a popular demonstration to introduce engineering and physical science students to the basics of electromagnetic induction phenomena. This problem has been studied extensively by focusing on experimental, analytical, or numerical solutions [30, 31, 44, 53, 54, 74, 75, 101, 142]. Notable contributions to the falling magnet problem using dimensional analysis were made by [13, 102, 125], where these studies briefly demonstrated the possibility of estimating the terminal velocity of the magnet based on dimensional analysis supported by laboratory experiments.

2.2.3   NDT Application of Motion-Induced Eddy Currents

More recently, the phenomenon of motion-induced eddy currents has been investigated in the context of non-destructive testing and in the evaluation of electrically conductive materials using constant magnetic field sources. Two different approaches are employed for material characterization to utilize the secondary magnetic field obtained from the motion-induced eddy currents: measuring the secondary field using magnetic field probes or measuring the Lorentz force acting on the magnetic field source, i.e. the PM.

Measuring the secondary magnetic field

The first approach was investigated by Ramos *et al.* [112, 113] using a moving DC coil as magnetic field source to induce eddy currents in a stationary electrically conductive plate. The perturbation of the secondary magnetic field due to the presence of surface breaking defects was observed using a single giant magnetoresistance (GMR) sensor. In the course of further investigations [114, 121] the research group compared their findings on the usability of GMRs to more common pickup coil configurations. Furthermore, the DC coil was replaced by a single PM to enable a significant increase in magnetic field strength for higher defect responses. One of their major findings was that accurate sensor placement is crucial for GMRs in order to avoid unwanted sensor saturation. The biggest advantage identified for using pickup coils was that the sensor principle is sensitive only to changes of the magnetic field. Thus, saturation effects are no limitation.

In a subsequent study, the usability of Hall effect magnetometers was investigated [122] and included in an overall comparison of the three mentioned measurement principles [123]. The applied measurement principle is depicted in Fig. 2.9. The in *x*-direction moving probe
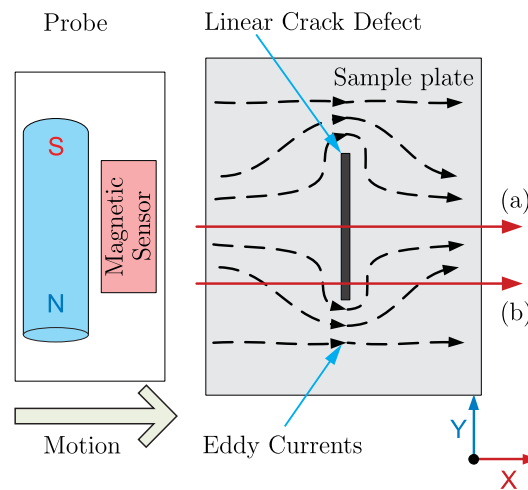
Figure 2.9: Measurement principle of comparative study by Ramos *et al.* [123].

consists of an axially magnetized PM oriented along the *y*-axis and a magnetic field sensor (differential coil, GMR, or Hall effect sensor). Motion-induced eddy currents (dashed lines) are perturbed by a surface-breaking slit defect and the resulting secondary magnetic field is observed. However, the applied sensor orientations are not suitable for comparison of the sensor principles because each single-axis sensor measures a different component of the magnetic field or its temporal variation. The main result of this study was that the compared sensor principles differed regarding the realized sensitivity for the investigated surface breaking defects. The depicted sensor paths (a) and (b) show the identified paths for highest sensor sensitivity for perturbations of the *x*- and *y*-component of the eddy currents, respectively. A comprehensive study which examines the discussed sensor principles for all three field components has not

been carried out.

Measuring the Lorentz force

The second approach employed for material characterization is based on *Lorentz force velocimetry* (LFV), a non-contact technique for velocity measurement in electrically conducting fluids published in 2006 by Thess *et al.* [139, 140]. The flowmeter here presented has been shown to be independent of the shape of the velocity profile if the magnetic field is homogeneous and the flow is unidirectional and axisymmetric [131]. While this assumption might not be fulfilled in most practical cases[1], the method has been applied to measure the flow rate of weakly conducting fluids like liquid metal flows, molten glass and salt melts in a straight rectangular duct [45, 108].

Parallel to these investigations, Brauer and Ziolkowski extended the idea of contactless flow rate measurements to a novel nondestructive testing method called Lorentz force eddy current testing (first abbreviated *LF-ECT*) [17]. Published in 2008, this first proof of concept of LET demonstrated that the Lorentz force acting on a system of PMs can be used to detect defects. The presented experimental investigation was supported by 2D numerical field simulations which showed the dependence of the measured force on the used velocity as well as on the depth of the defect.

Figure 2.10 shows the experimental setup (a) and the measured force profile (b) for an aluminum bar with multiple surface and subsurface defects at 150 mm/s. This was the first

(a)	(b)
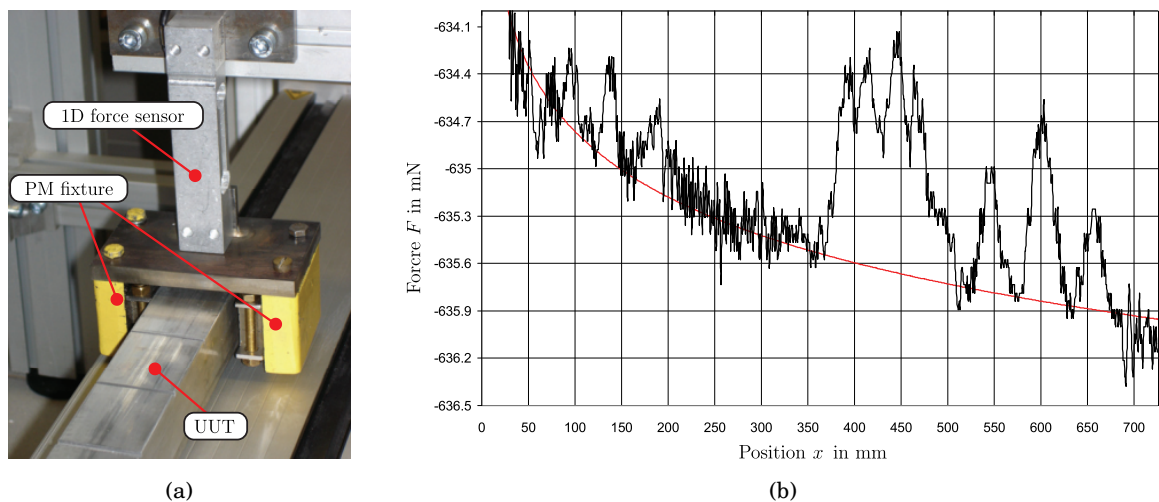
Figure 2.10: First experimental investigation for LET [17]: (a) experimental setup including 1D force sensor and PM system; (b) measurement result of the drag force along the inspected UUT.

published experimental investigation for LET. The PM fixture was used to ensure the correct position of the PMs and, in addition, as iron yoke to concentrate the magnetic flux. The

---

[1] In order to obtain a reliable result of the average flow rate, dry calibration from a solid conductor moving at a constant velocity are required as well as accurate knowledge about the velocity distribution of the flow [136].

superimposed drift of the measured drag force (red line) is very likely caused by the unwanted deflection of the unilaterally clamped UUT resulting in a changing covered cross-section.

In 2011, Uhlig *et al.* [143] published a redesigned experimental setup with multiple changes to the former setup (Fig. 2.11(a)). The study was primarily intended to validate analytical and

(a)   (b)
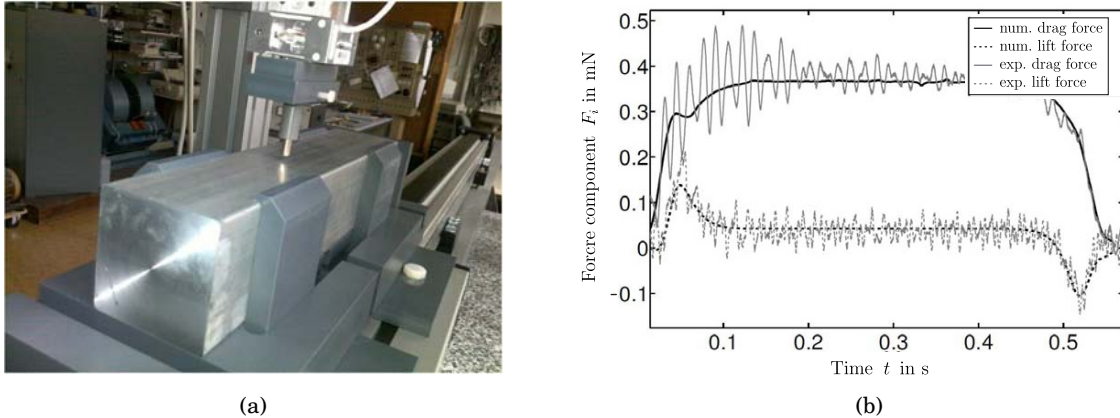
Figure 2.11: Second experimental investigation for LET [143]: (a) experimental setup including 3D force sensor and single PM; (b) comparison of numerical results and measurement results for the drag force and the lift force along the defect-free UUT.

numerical models, which is why the investigated UUT contained no defects. Instead of a system of PMs, a single PM is used in order to reduce the complexity on the created magnetic field. This PM is mounted on a multi-component force sensor in order to measure all three components of the Lorentz force. Furthermore, the PM is positioned near the top surface of the UUT which is of significantly reduced length compared to the specimen investigated in the first proof of concept. The redesigned setup also has a faster linear drive and an improved guidance of the moving UUT. The force components shown (Fig. 2.11(b)) suggest a good overall agreement of the numerical results with the experiments. However, the measured force components show significant distortions with strong oscillations and a continuously high noise level. The authors apply Fourier and wavelet transformation to the measured signals and suggest to attenuate specific frequencies using band-stop filters of different stop-bands and the use of a discrete approximation of the Meyer wavelet filter [1, 27]. The filtered signals are not shown, so there is no assessment of the effectiveness of the suggested measures.

In 2013, Uhlig describes in his thesis [141] an improved experimental setup with multiple modifications to encounter mechanical vibrations. Figure 2.12(a) gives an overview of the mechanical components of the system and Fig. 2.12(b) a detailed view on the PM attached to the force sensor. Besides minor redesigns of the measurement frame, the most important modifications in his thesis are anti-vibration pads between the linear guidance and the optical bench and additional clamping tools for stiffening the structure. The modified fixture allows the mounting of UUTs build from stacked aluminum sheets which enables the investigation of artificial, subsurface defects at different depths.

(a)

(b)

Figure 2.12: Improved version of the second experimental setup for LET [141]: (a) overview of the mechanical components; (b) detailed view on the multi-component force sensor and the attached cylindrical PM.

Figure 2.13 gives a representation of the achieved measurement capability of the improved setup and the developed signal processing. A defect sheet, including the investigated artificial defect, is shown in Fig. 2.13(a). Figures 2.13(b)-(d) show the post-processed measurement result of the force $\mathbf{F}(t)$ linearly mapped to the relative position x of the PM for different y-positions. The UUT is built of stacked aluminum sheets including a $12\,\mathrm{mm} \times 2\,\mathrm{mm} \times 2\,\mathrm{mm}$ defect at depth $d = 2\,\mathrm{mm}$. The defect response allows to localize the defect for all three components. However, the plotted results (aspect ratio of about $\Delta x : \Delta y \approx 10 : 1$) show significant diagonal patterns and distortions at the edges for all three components. It is not clarified, whether the source of these distortions lies in the raw data itself or in the filtering and subsequent alignment. A interim solution of this problem is given by Uhlig, suggesting to use the ratio of the lift and the drag component (not shown) which shows a reduced relative distortion.

(a)

(b)

(c)

(d)
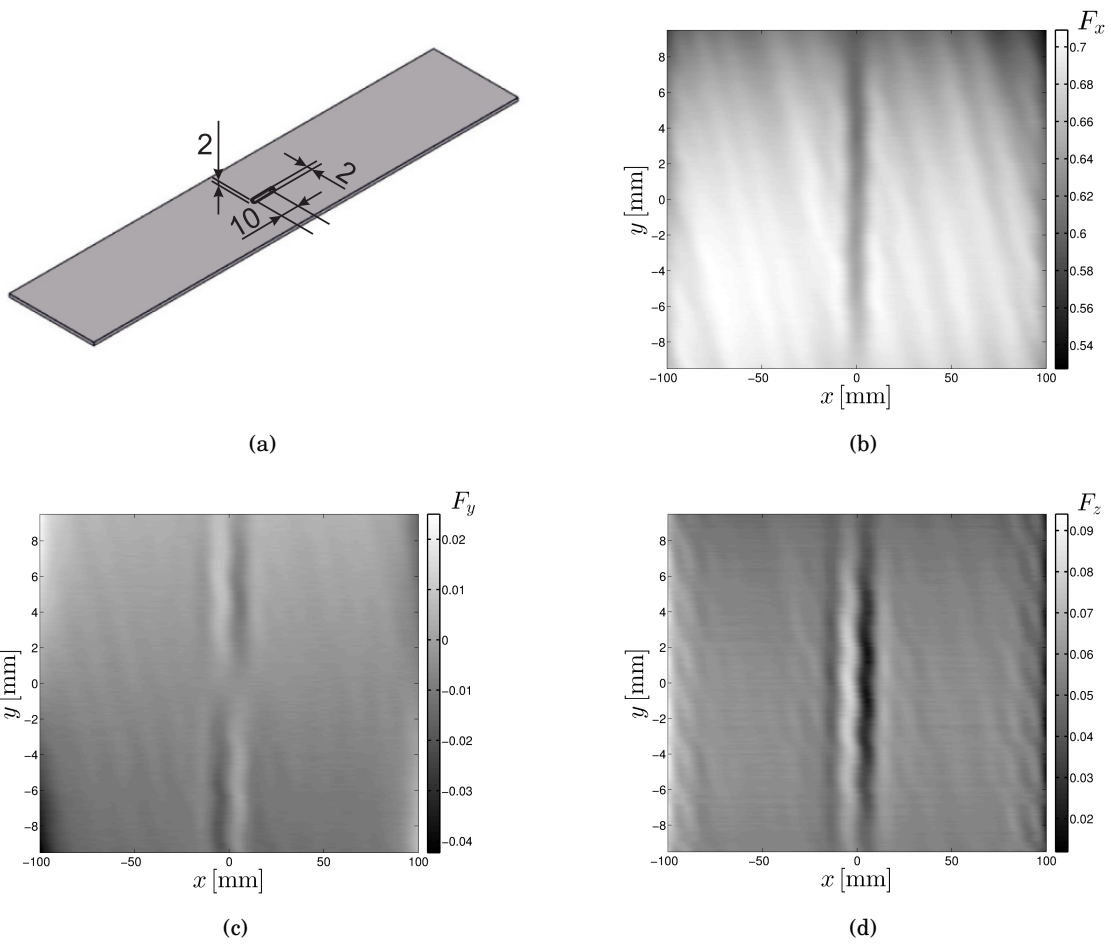
Figure 2.13: Representative result for accessing the measurement capability of improved experimental setup: (a) sketch of the artificial defect; (b)-(d) post-processed measurement result of the force $\mathbf{F}(t)$ linearly mapped to the relative position x of the PM for different y-positions.

Dimensional Analysis and Scaling Laws

I n this chapter, an electromagnetic levitation and braking problem is discussed to gain insight into the measurement principle of LET. The main focus is on the dimensionless representation of the problem and the illustration of the dependencies in order to develop appropriate scaling laws. First, the governing equations of the problem are provided and the relevant physical parameters are identified. Afterwards, the step-by-step procedure of dimensional analysis is described in detail for the given problem. A dimensionless model with a reduced number of parameters is obtained, which highlights the dominant dependencies and is invariant to the dimensional system employed. Using the dimensionless model, an exhaustive study of the dependencies of the Lorentz force on the dimensionless parameters is provided and a generalized representation of the problem is developed. Finally, appropriate scaling laws are derived and illustrated based on practical examples.

3.1   Problem Definition

In the problem considered in this study, a PM and an infinite plate made of non-ferromagnetic, electrically conducting material are in constant rectilinear relative motion with respect to each other (Fig. 3.1). Two coordinate systems (frames of reference) are defined as S' and S for the plate and the PM, respectively. The relative motion of both parts is described by the velocity $\mathbf{v} = v\mathbf{e}_x$ of the moving frame S' in the fixed frame S. In the analyzed problem, the PM has a cylindrical shape with diameter D and height H. It is assumed that the PM material is homogeneous and magnetized in the axial direction with the magnetization $\mathbf{M} = M\mathbf{e}_z$ and $M = B_\mathrm{r}/\mu_0$, where B_r is the remanent magnetization of the magnetic material. The base of the cylinder ($z = h$) is parallel to the surface of the plate. The plate of thickness t is made of non-magnetic material with a homogeneous electrical conductivity σ. The PM shown in Fig. 3.1
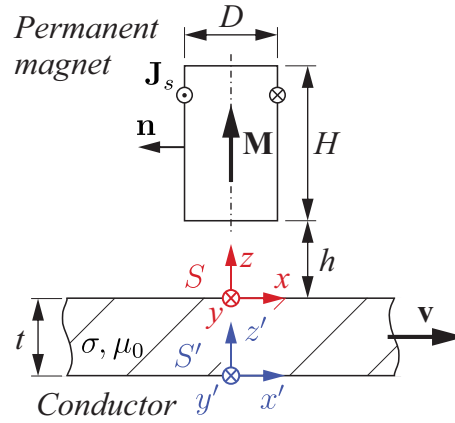
Figure 3.1: Geometry and parameters of the problem under investigation. A vast, non-magnetic, electrically conducting plate moves rectilinear with a constant velocity under the axially magnetized cylindrical PM at rest.

is described by means of the surface current model with $\mathbf{J}_s = \mathbf{M} \times \mathbf{n}$ [39]. In order to determine the force acting on the PM, first the problem of finding the magnetic field $\mathbf{H}$ of an infinitely thin loop with current $J_s \mathrm{d}z$, located in the vicinity of the moving plate, is formulated and later on extended to the case of the PM of finite height. It is assumed that displacement currents can be neglected because only the cases are of interest where the plate is traveling at velocities much lower than the speed of light ($v \ll c$).

In the quasi-static case ($v = \text{const}$), the governing equations derived from Maxwell's equations take the following form in the frame S:

$$\nabla^2 \mathbf{H} - \sigma \mu_0 (\mathbf{v} \cdot \nabla) \mathbf{H} = \mathbf{0}, \qquad \text{in the conductor,} \tag{3.1}$$

$$\nabla^2 \mathbf{H} = \mathbf{0}, \qquad \text{outside the conductor,} \tag{3.2}$$

$$\nabla \cdot \mathbf{H} = 0, \qquad \text{everywhere.} \tag{3.3}$$

The equations with the appropriate boundary conditions can be solved analytically using the 2D Fourier transform approach [116], [73], [157].

The Lorentz force exerted on the PM is calculated using Parseval's theorem [16] as

$$\mathbf{F} = \frac{\mu_0}{4\pi^2} \mathfrak{Re} \left\{ \int\limits_{h}^{h+H} \int\limits_{-\infty}^{\infty} \int\limits_{-\infty}^{\infty} \widehat{\mathbf{J}}_{\mathrm{s}}^* \times \widehat{\mathbf{H}}^{(\mathrm{e})} \mathrm{d}k_x \mathrm{d}k_y \mathrm{d}z \right\}, \tag{3.4}$$

where k_x and k_y are the transform variables, and $\widehat{\mathbf{H}}^{(\mathrm{e})}$ is the Fourier transform of the magnetic field associated with the eddy currents induced in the conductor. The 2D Fourier transform $\widehat{\mathbf{J}}_{\mathrm{s}}$ of the source current density is given by

$$\widehat{\mathbf{J}}_{\mathrm{s}} = [\widehat{J}_{\mathrm{s}x}, \widehat{J}_{\mathrm{s}y}]^{\mathrm{T}} = \mathrm{j}\pi J_{\mathrm{s}0} D \mathrm{J}_1(k\tfrac{D}{2}) [\tfrac{k_y}{k}, -\tfrac{k_x}{k}]^{\mathrm{T}}, \tag{3.5}$$

where $k^2 = k_x^2 + k_y^2$, $J_{\mathrm{s}0} = B_{\mathrm{r}}/\mu_0$ is the magnitude of the surface current density, and $\mathrm{J}_1(\cdot)$ denotes the first order Bessel function of the first kind. The components of the force $\mathbf{F}$ are given by the

following formulas:

$$F_x = \frac{\mu_0}{2\pi^2} \int\limits_0^\infty \int\limits_0^\infty \Im[T(k,\beta)] \left(k_x |\widehat{J}_{sy}|^2 - k_y \widehat{J}_{sy}^* \widehat{J}_{sx}\right) \times$$

$$\times \frac{\left(1 - e^{-kH}\right)^2}{k^3} e^{-2kh} \, dk_x dk_y, \tag{3.6}$$

$$F_y = 0, \tag{3.7}$$

$$F_z = \frac{\mu_0}{2\pi^2} \int\limits_0^\infty \int\limits_0^\infty \Re[T(k,\beta)] \left(|\widehat{J}_{sx}|^2 + |\widehat{J}_{sy}|^2\right) \times$$

$$\times \frac{\left(1 - e^{-kH}\right)^2}{k^2} e^{-2kh} \, dk_x dk_y, \tag{3.8}$$

with $T(k,\beta)$ obtained as:

$$T(k,\beta) = \frac{(\beta^2 - 1)\tanh\beta k t}{2\beta + (1 + \beta^2)\tanh\beta k t}, \tag{3.9}$$

where $\beta = \alpha/k$, and $\alpha^2 = j\mu_0\sigma v k_x + k^2$.

The set of equations (3.6)-(3.8) builds the *mathematical model* for the problem under investigation. It describes the relation between the dependent parameter of interest **F** and eight relevant physical parameters $v, \mu_0, \sigma, B_r, D, H, h$, and t. The model is validated by comparison with finite element computations in [157]. For the subsequent study, all shown results are solutions of (3.6) and (3.8) solved using MATLAB™ [81].

3.2 Dimensional Analysis

In this section, the procedure of dimensional analysis is applied to obtain a dimensionless representation of the analyzed problem. It is assumed that any complete physical relation must be dimensionally consistent, which is also known as the statement of dimensional homogeneity [9, 18, 50]. Furthermore, it is assumed that any physical relationship that is expressed by a *complete equation* must be invariant to the applied dimensional system [18, 19, 50]. The dimensionless representation of the problem is the basis for later numerical studies.

3.2.1 Definition of the Physical Model

The first step in the dimensional analysis procedure is the preliminary physical analysis of the system and the definition of the problem. In general, this step does not lead to a complete mathematical description, but rather a dedicated view on the phenomena involved.

The next step is to create a list of the physical parameters x_i of $\mathbf{x} = \{x_1, x_2, \dots, x_I\}$, which are expected to be relevant to the features of the phenomena of interest. These parameters should be described using a consistent system of units $[\mathbf{G}] = \{[G_1], [G_2], \dots, [G_K]\}$, which comprises fundamental units $[G_k]$ that are sufficient to define the magnitude of any physical quantity [138]. It should be mentioned that it is customary (as suggested by Maxwell [11]) to

denote the dimension of a quantity ϕ by $[\phi]$. The dimension $[x_i]$ of any physical parameter x_i can be written as the product of the powers of the fundamental units

$$[x_i] = \prod_{k=1}^{K} [G_k]^{d_{ki}} , \tag{3.10}$$

where d_{ki} denotes the power to which the k–th fundamental unit is raised in the i–th physical parameter of $\mathbf{x}$. To improve the clarity of the description, the dimensional analysis employs the International System of Units (SI), but the procedure can be conducted with any appropriate system [43].

The first element in the list of physical parameters is the force $\mathbf{F}$ acting on the PM. Since the dimensional analysis is performed in scalar form, the force as a vector quantity has to be decomposed into orthogonal components. Due to the symmetry of the problem, only F_x and F_z are of interest because $F_y \equiv 0$ (cf. (3.7)). Additional parameters are the magnitude of the relative velocity v, the electrical conductivity of the plate σ, and the PM's remanence B_r, which are assumed to be relevant to the acting force. The next parameter in the list is the magnetic permeability $\mu = \mu_0 \mu_r$, where μ_0 is the vacuum permeability and μ_r is the relative permeability of the plate. The following investigation is restricted to non-ferromagnetic materials ($\mu_r \equiv 1$), so only the vacuum permeability μ_0 is considered in the list of physical parameters. It should be mentioned that the vacuum permeability μ_0 appears in the list because all parameters are described in SI units. Other systems of units would also lead to other constants, such as the electromagnetic velocity c in Gaussian or Heaviside-Lorentz units. Finally, a group of geometrical parameters is employed to describe all of the lengths and distances in the problem, i.e. the cylinder diameter D and height H, the distance between the PM and the plate h (lift-off distance), and the plate thickness t.

In the considered problem, the full list contains 10 ($I = 10$) parameters:

$$\mathbf{x} = \{F_x, F_z, v, \sigma, B_\mathrm{r}, \mu_0, D, H, h, t\}, \tag{3.11}$$

which comprise the *physical model* $\mathbf{x}$ of the problem.

The result of the second step is summarized in Table 3.1, where the dimensions are in fundamental units. Clearly, all of the elements of the physical model $\mathbf{x}$ can be described using a reduced base of $K = 4$ fundamental units expressed in terms of mass $[G_1] = \mathrm{M}$, length $[G_2] = \mathrm{L}$, time $[G_3] = \mathrm{T}$, and electric current $[G_4] = \mathrm{I}$.

Table 3.1: List of the physical parameters and constants

Symbol	Name	Dimensions
F_x	Drag force	M L T^{-2}
F_z	Lift-off force	M L T^{-2}
v	Velocity	L T^{-1}
σ	Electrical conductivity	$\text{M}^{-1}\text{L}^{-3}\text{ T}^3\text{ I}^2$
B_r	Remanence	$\text{M T}^{-2}\text{ I}^{-1}$
μ_0	Vacuum permeability	$\text{M L T}^{-2}\text{ I}^{-2}$
D	Diameter of the PM	L
H	Height of the PM	L
h	Lift-off distance	L
t	Thickness of the plate	L

A comprehensive form to represent all elements of $\mathbf{x}$ and their corresponding dimensions is given by the *dimensional matrix* $\mathbf{D}$, with elements d_{ki} defined by (3.10) such that:

$$
\mathbf{D} =
\begin{array}{c}
\\
\text{M} \\ \text{L} \\ \text{T} \\ \text{I}
\end{array}
\begin{array}{cccccccccc}
F_x & F_z & v & \sigma & B_\mathrm{r} & \mu_0 & D & H & h & t \\
\left[\begin{array}{cccccccccc}
1 & 1 & 0 & -1 & 1 & 1 & 0 & 0 & 0 & 0 \\
1 & 1 & 1 & -3 & 0 & 1 & 1 & 1 & 1 & 1 \\
-2 & -2 & -1 & 3 & -2 & -2 & 0 & 0 & 0 & 0 \\
0 & 0 & 0 & 2 & -1 & -2 & 0 & 0 & 0 & 0
\end{array}\right],
\end{array}
\tag{3.12}
$$

e.g. the dimension of the velocity v is the product of the fundamental unit $[\text{L}]$ raised to the power of 1 and $[\text{T}]$ to the power of -1.

To continue the analysis, it must be asserted that the physical model is complete, i.e. it includes all parameters required to build a correct mathematical model. This model must be dimensionally homogeneous and thus invariant to the dimensional system used. This is evident from the problem definition given in the previous section. However, without any knowledge of the mathematical model the completeness would only be a hypothesis.

3.2.2 Calculation of a Dimensionless Basis Set

Using the complete physical model, a functional relationship can be defined that includes all of the previously identified parameters. Without loss of generality, this relationship can be written as

$$
g(\mathbf{x}) = g(F_x, F_z, v, \sigma, B_\mathrm{r}, \mu_0, D, H, h, t) = 0,
\tag{3.13}
$$

where g is an unknown function.

From Buckingham's *Π-theorem* [19] it is known that a dimensionally homogeneous equation can be reduced to a relation of independent dimensionless parameters Π_j for a basis set

$\Pi = \{\Pi_1, \ldots, \Pi_J\}$ such that

$$G(\mathbf{\Pi}) = G(\Pi_1, \Pi_2, \ldots, \Pi_J) = 0, \tag{3.14}$$

where G still is an unknown function, but $J \leq I$. Each dimensionless parameter Π_j is a product of the powers of the governing parameters x_i with independent dimensions [11]:

$$\Pi_j = \prod_{i=1}^{I} x_i^{s_{ij}}, \ j = 1 \ldots J \tag{3.15}$$

where s_{ij} denotes the power to which the i–th physical parameter is raised in the j–th dimensionless element of $\mathbf{\Pi}$.

To find such a basis set $\mathbf{\Pi}$, the dimensional equations (3.15) have to be evaluated:

$$\left[\Pi_j\right] = \prod_{i=1}^{I} \left[x_i\right]^{s_{ij}}. \tag{3.16}$$

Analogously to (3.10), the dimension of each element Π_j is described as a product of the powers of the fundamental units

$$\left[\Pi_j\right] = \prod_{k=1}^{K} \left[G_k\right]^{c_{kj}} . \tag{3.17}$$

If they are dimensionless, each $\left[\Pi_j\right]$ must be equal to one, so it can be concluded that $c_{kj} \equiv 0, \forall k, j$. Furthermore, the dimensional formula for the right-hand side of (3.16) are written by using (3.10) such that

$$\prod_{i=1}^{I} \left[x_i\right]^{s_{ij}} = \prod_{i=1}^{I} \left(\prod_{k=1}^{K} \left[G_k\right]^{d_{ki}}\right)^{s_{ij}} . \tag{3.18}$$

By combining (3.18) and (3.17), the dimensional equation (3.16) can be written as

$$\prod_{k=1}^{K} \left[G_k\right]^{c_{kj}} = \prod_{i=1}^{I} \left(\prod_{k=1}^{K} \left[G_k\right]^{d_{ki}}\right)^{s_{ij}} . \tag{3.19}$$

For the sake of simplicity, (3.19) is rewritten by taking the logarithm of both sides as

$$\sum_{k=1}^{K} c_{kj} \log\left[G_k\right] = \sum_{i=1}^{I} s_{ij} \sum_{k=1}^{K} d_{ki} \log\left[G_k\right], \ \forall j , \tag{3.20}$$

which holds in the non-trivial case for $\left[G_k\right] \neq 1$ only if

$$c_{kj} = \sum_{i=1}^{I} s_{ij} d_{ki}, \ \forall j, k . \tag{3.21}$$

Using matrix notation, it is evident that the unknown basis set of dimensionless parameters is equal to the non-trivial solutions of the *homogeneous system of linear equations*:

$$\mathbf{c}_j = \mathbf{D}\mathbf{s}_j , \quad \mathbf{c}_j \equiv \mathbf{0}, \ \forall j , \tag{3.22}$$

with the dimensional matrix $\mathbf{D}$ given by (3.12) and the basis set vectors $\mathbf{s}_j$. $\mathbf{D}$ is underdetermined, so infinitely many solutions form a vector space. The vector space dimension is equal to J, the number of dimensionless products in a complete set of parameters. It is called the *nullity* of $\mathbf{D}$ and can be determined from the *rank-nullity theorem* of linear algebra as:

$$J = \mathrm{nul}(\mathbf{D}) = I - \mathrm{rk}(\mathbf{D}), \tag{3.23}$$

where I is the number of columns and rk is the rank of the dimensional matrix $\mathbf{D}$. Consequently, from the physical model (3.11) with $I = 10$ parameters and the dimensional matrix (3.12) of rank $\mathrm{rk}(\mathbf{D}) = 4$, the problem is fully described by a set of $J = 6$ independent dimensionless parameters Π_j.

The solutions set of (3.22) represents the *kernel* (null space) of $\mathbf{D}$. It can be calculated using the Gaussian elimination. Given that $\mathbf{D}$ is built initially using an arbitrary ordering of the physical parameters, then the row echelon form of the underdetermined system depends mainly on the arrangement selected. Therefore, it is possible to reorder the columns of the dimensional matrix in any form desired. In the following, a slightly modified matrix $\mathbf{D}$ is used, where the physical parameter h is moved to the fourth place of $\mathbf{x}$, to obtain a sparse null space basis. This yields a clearly arranged result in which the distance h is set to the *characteristic length* of the problem.

The calculation of a rational null space of the reordered matrix yields six vectors that correspond to dimensionless parameters Π_j, which are combined into the solution matrix $\mathbf{S} = \begin{bmatrix} \mathbf{s}_1; \mathbf{s}_2; \ldots; \mathbf{s}_J \end{bmatrix}$ as follows:

$$\mathbf{S} = \begin{array}{c} \\ F_x \\ F_z \\ v \\ h \\ \sigma \\ B_\mathrm{r} \\ \mu_0 \\ D \\ H \\ t \end{array} \begin{array}{cccccc} \mathbf{s}_1 & \mathbf{s}_2 & \mathbf{s}_3 & \mathbf{s}_4 & \mathbf{s}_5 & \mathbf{s}_6 \\ \left[\begin{array}{cccccc} -1 & -1/2 & 0 & 0 & 0 & 0 \\ 1 & 0 & 0 & 0 & 0 & 0 \\ 0 & 1/2 & 1 & 0 & 0 & 0 \\ 0 & 3/2 & 1 & -1 & -1 & -1 \\ 0 & 1/2 & 1 & 0 & 0 & 0 \\ 0 & 1 & 0 & 0 & 0 & 0 \\ 0 & 0 & 1 & 0 & 0 & 0 \\ 0 & 0 & 0 & 1 & 0 & 0 \\ 0 & 0 & 0 & 0 & 1 & 0 \\ 0 & 0 & 0 & 0 & 0 & 1 \end{array}\right] \end{array} \tag{3.24}$$

The corresponding set of dimensionless parameters Π_j is constructed using (3.15) for each solution vector $\mathbf{s}_j$, where $\mathbf{x}^{\mathbf{s}_j} = \begin{bmatrix} x_1^{s_{j1}}, x_2^{s_{j2}}, \ldots, x_{10}^{s_{j10}} \end{bmatrix}$ is employed as a shorthand notation for this computation, as suggested by [107].

27

The calculated set of independent dimensionless parameters $\mathbf{\Pi}$:

$$\Pi_1^* = \mathbf{x}^{\mathbf{s}_1} = F_z/F_x, \tag{3.25a}$$

$$\Pi_2^* = \mathbf{x}^{\mathbf{s}_2} = \sqrt{\sigma v B_r^2 h^3/F_x}\,, \tag{3.25b}$$

$$\Pi_3^* = \mathbf{x}^{\mathbf{s}_3} = \mu_0 \sigma v h, \tag{3.25c}$$

$$\Pi_4^* = \mathbf{x}^{\mathbf{s}_4} = D/h, \tag{3.25d}$$

$$\Pi_5^* = \mathbf{x}^{\mathbf{s}_5} = H/h, \tag{3.25e}$$

$$\Pi_6^* = \mathbf{x}^{\mathbf{s}_6} = t/h, \tag{3.25f}$$

comprises a *dimensionless model* of the problem and this is the result of the third step of the dimensional analysis.

In contrast to the previously defined physical model $\mathbf{x}$, the new formulation is invariant to the dimensional system used. More importantly, it fully describes the phenomenon of interest using only six parameters instead of the original 10 parameters.

3.2.3 Discussion and Reformulation of the Dimensionless Basis Set

The last step of the dimensional analysis is to evaluate and interpret the derived dimensionless basis set in the light of observations or confirmed mathematical models. To be able to interpret these results it is useful to discuss (3.25) in the given form.

The first dimensionless parameter Π_1^* is the ratio of both force components, F_z and F_x, which can be interpreted intuitively as the direction of the force in the xz-plane. The second parameter Π_2^* illustrates the remarkable features of a dimensional analysis by indicating the dominant dependencies of the parameters. This expression clearly agrees with the statements in [139] about the Lorentz force acting on a magnetic dipole located at a distance L above a semi-infinite electrically conducting fluid. The estimation of the force is given there by the proportionality $F \propto \mu_0^2 \sigma v m^2 L^{-3}$, where m is the magnetic dipole moment $m \propto B_r L^3/\mu_0$. The third dimensionless parameter Π_3^* is called the *magnetic Reynolds number* R_m, which is well known in *magnetohydrodynamics*, where it indicates the ratio of magnetic advection relative to magnetic diffusion [28]. The last three dimensionless parameters indicate shape or geometric similarity [9], and they describe the relative sizes of the bodies involved.

Depending on the calculated basis set, it can be useful to modify the basis set to obtain a form with increased utility for a specific investigation. This particular basis set of dimensionless parameters might be too abstract for a convenient description of the Lorentz force exerted on the PM in the defined problem. Thus, it is useful to find a formulation that clearly distinguishes independent and dependent variables, as well as their parameters. The basis set vectors $\mathbf{s}_j$ are orthogonal and they span a null space, so any linear combination of these vectors is a solution of the homogeneous system (3.22). Thus, it is possible to transform the initial basis set by multiplying the dimensionless parameters with each other to any desired power.

After some simple calculations and reordering, a reformulated basis set is given by:

$$R_{\mathrm{m}} := \Pi_1 = \mu_0 \sigma v h \tag{3.26a}$$

$$\delta := \Pi_2 = D/h \tag{3.26b}$$

$$\xi := \Pi_3 = D/H \tag{3.26c}$$

$$\tau := \Pi_4 = t/h \tag{3.26d}$$

$$\tilde{F}_x := \Pi_5 = \mu_0 F_x/(B_{\mathrm{r}} h)^2 \tag{3.26e}$$

$$\tilde{F}_z := \Pi_6 = \mu_0 F_z/(B_{\mathrm{r}} h)^2 \ , \tag{3.26f}$$

which provides a more suitable representation for the following discussion. In the reformulated basis set, the magnetic Reynolds number R_{m} is defined as the independent variable Π_1. The variables $\tilde{F}_x$ and $\tilde{F}_z$, where tilde indicates a dimensionless force component, are defined as the dependent variables. They are linear combinations of (3.25a) - (3.25c). Furthermore, the dimensionless geometric parameters δ, ξ, and τ are defined by rearranging (3.25d) – (3.25f).

3.3 Numerical Studies

This section present some numerical studies on the defined problem. The advantages of the dimensionless representation over the dimensional representation are demonstrated. The dependencies of the Lorentz force on the magnetic Reynolds number R_{m} and the dimensionless plate thickness τ are discussed. Finally, a generalized dimensionless representation is developed, which is the basis for the formulation of scaling laws for the analyzed problem.

3.3.1 Dimensionless Representation of Complex Data

The procedure of computation of the dimensionless Lorentz force components is shown schematically in Fig. 3.2. As mentioned in section 3.1, all calculated force components are solutions of (3.6) and (3.8) implemented in MATLAB™. This process is depicted as box *LF*. Since the equations are formulated in terms of dimensional parameters, two conversions between dimensional and dimensionless parameters are necessary for the study of the dimensionless model. The conversions are denoted $(\Pi \rightarrow x)$ and $(x \rightarrow \Pi)$.
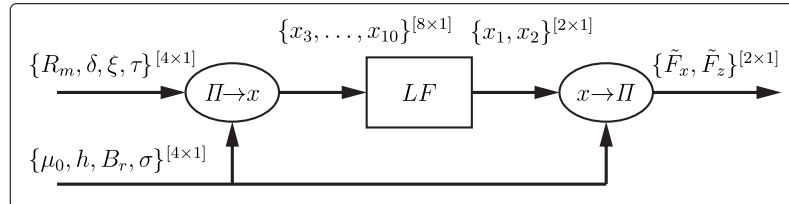
Figure 3.2: Flowchart of dimensionless Lorentz force calculation. Box *LF* relates to the force calculation described by (3.6) and (3.8). Box $\Pi \rightarrow x$ denotes conversion of dimensionless to dimensional parameters, while box $x \rightarrow \Pi$ denotes conversion of $F_{x,z}$ to $\tilde{F}_{x,z}$

At this point the benefit of a dimensionless representation becomes evident. The dimensionless model is fully defined by the four dimensionless parameters $R_\mathrm{m}, \delta, \xi$ and τ. In order to convert these parameters, the dimensional parameters μ_0, h, B_r and σ are chosen arbitrarily. It is even possible to choose these parameters in a way that improves ill-conditioned computations. After the calculation of the two force components $F_{x,z}$, the same dimensional parameters are used for the conversion to dimensionless force components $\tilde{F}_{x,z}$. This effectively reduces the complexity of the problem without any loss of information.

In order to further illustrate the advantages of the dimensionless representation, a concise parametric study is discussed for four different settings as depicted in Table 3.2. PMs of various sizes with typical magnetic remanences for neodymium iron boron (NdFeB) magnetic materials are considered. The electrical conductivity of the plate is in the range of aluminum and copper alloys. All of the settings define systems that are similar in shape to each other, and thus they have identical dimensionless parameters δ, ξ and τ. The geometric similarity is a necessary condition for the complete similarity in the study.

Table 3.2: Example settings S1 − S4

Parameter	Unit	S1	S2	S3	S4
B_r	T	1.4	1.1	1.2	1.3
σ	MS/m	25	45	30	30
h	mm	0.50	0.75	1.00	1.25
D	mm	10.00	15.00	20.00	25.00
H	mm	7.50	11.25	15.00	18.75
t	mm	25.00	37.50	50.00	62.50
$\delta = 20$	$\xi = 1/3$	and	$\tau = 50$		

The results of the parametric study S1 − S4 are shown in Fig. 3.3. The dimensional representations of the calculated force components exerted on the PM are shown in Fig. 3.3(a) versus the velocity up to $v = 35$ m/s. As expected, all four settings differ in terms of the magnitude of the forces generated. In addition, the characteristic points P1 − P4, denoting the intersection of both force components, differ in terms of their velocity and force. Nevertheless, it is clear that all four settings share a common characteristic shape for the resulting forces. This becomes evident for the dimensionless representation shown in Fig. 3.3(b).
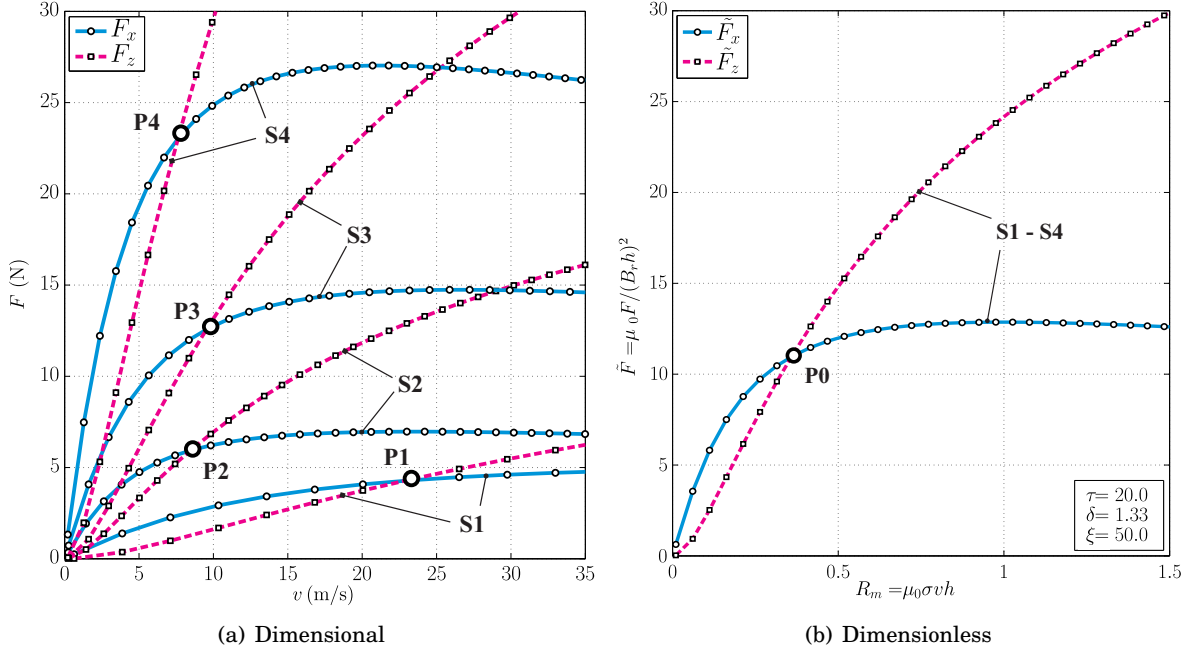
Figure 3.3: Comparison of (a) dimensional and (b) dimensionless representations of the numerical results for the parametric study (Table 3.2).

As predicted, all four configurations yield dimensionless representations with identical results in terms of both their magnitude and shape. The resulting force components F_x and F_z merge in the dimensionless representation into two separate curves, and thus they share one point of intersection P0 at identical magnetic Reynolds numbers. Clearly, identical magnetic Reynolds numbers do not imply that the velocities are the same, but they do indicate electromagnetic similarity. This is why it is not possible to replace the abscissa in Fig. 3.3(b) by a dimensional representation of the velocity without defining the remaining parameters of R_m. Furthermore, it is clear that the remanence B_r does not affect the electromagnetic similarity, and it merely constitutes a scaling factor of the second power for the generated force components.

3.3.2 Dependency on the Magnetic Reynolds Number

In the following study, it is illustrated that the dimensionless representation remains valid without further constraints and it can be used to highlight the dominant dependencies in the problem under consideration. For this reason, the study presented in Fig. 3.3 is extended to a larger range of the magnetic Reynolds number. Furthermore, the hypothesis is examined that the Lorentz force components can be described over a wide range using simple power-law dependencies based on the magnetic Reynolds number. Therefore, the results are plotted in double logarithmic scale, where the underlying power-law dependency is indicated by a straight line. This is also useful for the subsequent estimation of the scaling laws.

31

In the study, it is assumed that the mathematical model used to calculate the Lorentz force components only holds for velocities that are much smaller than the speed of light. Considering the parameters of the study in Table 3.2, the corresponding magnetic Reynolds number would be in the order of $R_{\mathrm{m}} \approx 10^6$. In order to meet the previous assumptions the investigations are restricted to $R_{\mathrm{m}} \leq 10^3$, which is expected to give reliable results.

Figure 3.4 shows the force components calculated for fixed δ, ξ, and τ depending on the magnetic Reynolds number R_{m}. It is clear that for both Lorentz force components two regions exist where the problem is dominantly described by a particular power of R_{m}. It can be clearly distinguished between one region with low and another with high R_{m}. In the region where $R_{\mathrm{m}} \leq 10^{-1}$, the dimensionless force components $\tilde{F}_x$ and $\tilde{F}_z$ are proportional to R_{m} and R_{m}^2, respectively. In the region where $R_{\mathrm{m}} \geq 10^1$, $\tilde{F}_x$ is proportional to $R_{\mathrm{m}}^{-1/2}$ whereas $\tilde{F}_z$ goes to saturation. This observation confirms the hypothesis regarding the dependence on R_{m}.
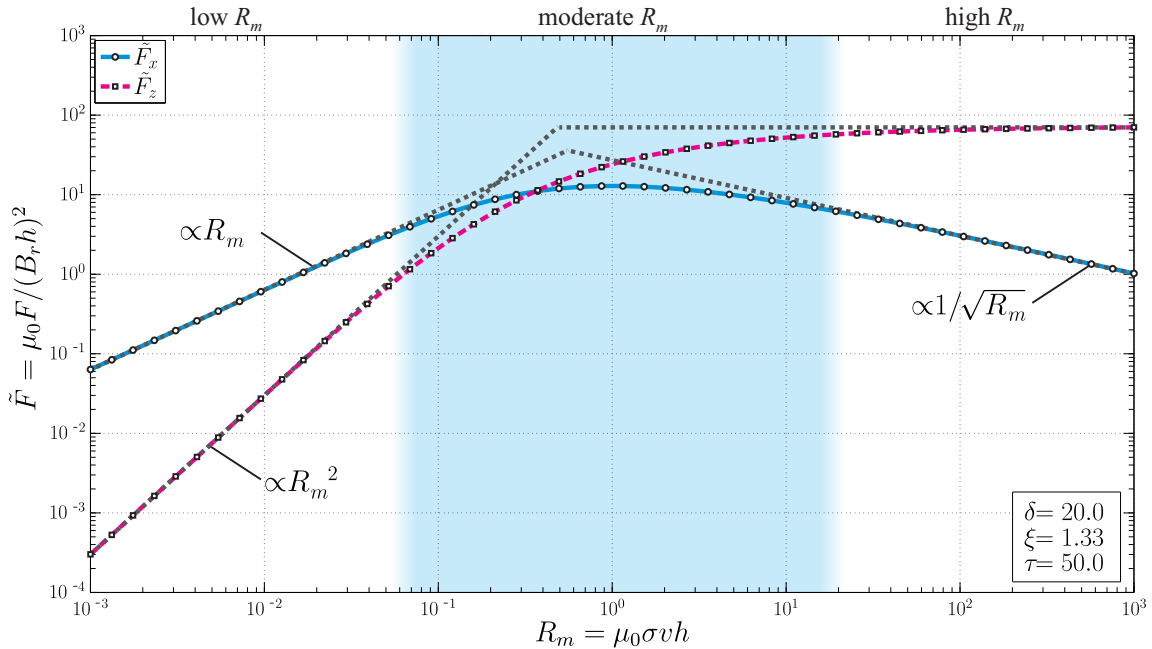
Figure 3.4: Dimensionless Lorentz force components $\tilde{F}_x$ (blue) and $\tilde{F}_z$ (magenta) as functions of the magnetic Reynolds number R_{m} for fixed δ, ξ, and τ. The transition zone for the mixed dominance of advection and diffusion, which separates low and high R_{m}, is highlighted in blue.

It is recalled that the magnetic Reynolds number R_{m} is a measure of the relative strength of advection and diffusion, and thus their respective characteristics can be attributed directly to the corresponding phenomena [28]. Between the regions of low and high R_{m} (moderate R_{m}), both phenomena occur side by side, thereby preventing further characterization using power-law dependencies.

3.3.3 Dependency on the Dimensionless Plate Thickness

Next, it is investigated how the dimensionless Lorentz force components depend on the dimensionless geometric parameter τ. Therefore, the previous study is expanded based on considerations of the influence of the plate thickness τ on the force components. This analysis should have a significant impact because τ determines the available region where the eddy currents are induced. For this purpose, a similar power-law hypothesis is expressed for the dependence on τ.
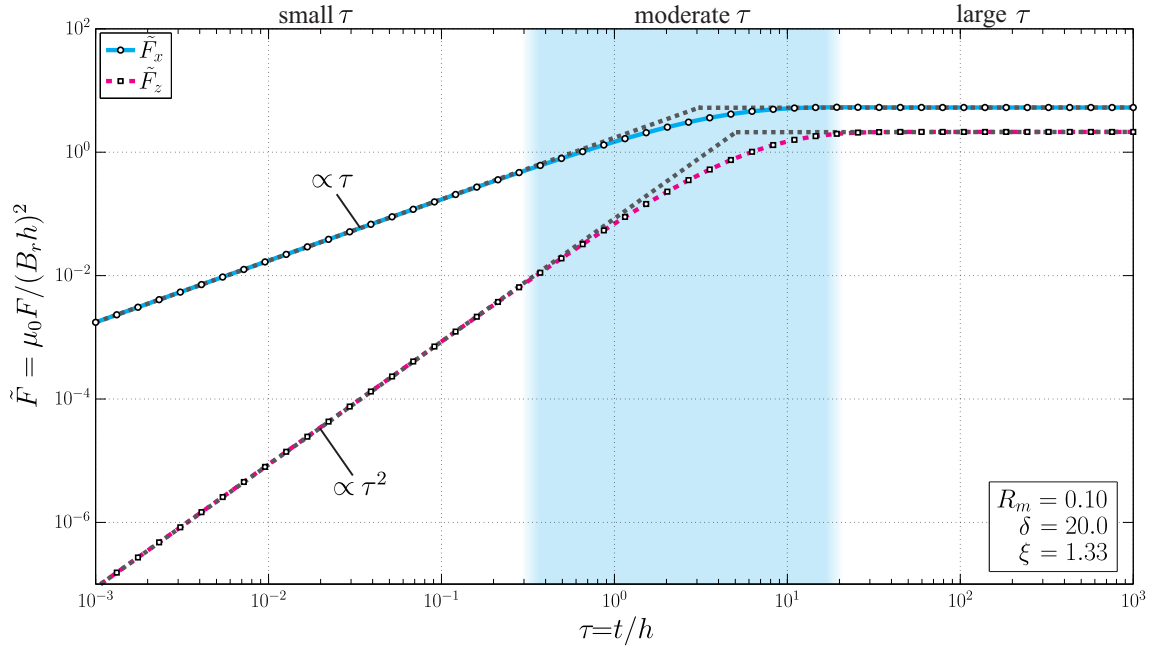
Figure 3.5: Dimensionless Lorentz force components $\tilde{F}_x$ (blue) and $\tilde{F}_z$ (magenta) as functions of the dimensionless plate thickness τ for fixed R_{m}, δ, and ξ. The transition zone that separates small and large τ is highlighted in blue.

Figure 3.5 shows the dependencies of the Lorentz force components on the dimensionless plate thickness τ for fixed R_{m}, δ, and ξ. It is clear that for both force components, two regions exist where the problem is dominantly described by a particular power of τ. It can be clearly distinguished between one region with low and another with high τ. In the region where $\tau \lesssim 10^{-1}$, $\tilde{F}_x \propto \tau$ and $\tilde{F}_z \propto \tau^2$, whereas in the region where $\tau \gtrsim 10^2$, $\tilde{F}_x$ and $\tilde{F}_z$ have no further dependence on τ. This observation also confirms the power-law hypothesis about the dependence on τ.

In the following, the region that has a constant power-law dependence on τ is called *thin plate behavior* and the region without dependence on τ is called *infinite half-space behavior*. Between these two regions, where a moderate τ dominates, no further characterization is useful without additional investigation of the explicit eddy current density distribution.

The next step of the investigation is to analyze how the dependencies of the force components on the dimensionless plate thickness τ change for different values of the magnetic Reynolds

(a) Dimensionless drag force $\tilde{F}_x$

(b) Dimensionless lift force $\tilde{F}_z$

Figure 3.6: Dimensionless force components $\tilde{F}_x$ and $\tilde{F}_z$ as functions of the magnetic Reynolds number R_{m} and the dimensionless plate thickness τ for fixed $\delta = 10$ and $\xi = 1$.

number R_{m}.

Figure 3.6 shows filled contour plots for the common logarithm of the force components as functions of the magnetic Reynolds number R_{m} and the dimensionless plate thickness τ for $\delta = 10$ and $\xi = 1$. The calculated force component is constant along each contour line. Each value is depicted as the power to base 10 in the color bar. The contour interval employed, i.e. the difference in elevation between successive contour lines, is constant in each graph. Thus, the distance between two lines is a measure of the gradient for a force component at a certain point, which is always perpendicular to the contour lines.

At a dimensionless thickness $\tau \geq 10^1$, again two regions are observed, where both force components are proportional to a particular power of R_{m}, similar to that given in Fig. 3.4, but they are invariant to τ. In the region where $\tau \leq 10^{-1}$, $\tilde{F}_x$ is proportional to τ and $\tilde{F}_z$ to τ^2 until a significant Reynolds number, where $\tilde{F}_x$ reaches its maximum for a particular τ. Furthermore, this significant Reynolds number is proportional to τ. The force maximum exceeds that for infinite half-space behavior. After the force maximum is reached, $\tilde{F}_x$ is inversely proportional to R_{m} and τ, whereas $\tilde{F}_z$ again goes to saturation, and thus it has no further dependence on either R_{m} or τ. This observations confirm the hypothesis regarding the power-law dependence on τ.

3.3.4 Generalized Dimensionless Representation of the Problem

At this point it is of interest to generalize the statements of proportionality. It has been shown that it is possible to distinguish between regions that are dominantly described by either magnetic diffusion (low R_{m}) or advection (high R_{m}), and regions with and without dependency on the plate thickness τ. Thus, it is possible to define characteristic values R_{mC} and τ_C that

approximately distinguish between each of these regions. As a result, estimates of the different equilibria are obtained for the phenomenon.

An appropriate way is to define $R_{\mathrm{m}Cx,z}$ as the value of the maximum curvature of $\log(\tilde{F}_{x,z})$ for $\tau = 10^3$ (approximation of infinite half-space) for a particular set of δ and ξ. Analogously, $\tau_{Cx,z}$ can be defined for $R_{\mathrm{m}} = 10^{-3}$ (low R_{m}). However, the definition has two major disadvantages. First, the computation of the curvature is based on multiple partial derivations, which has an increased sensitivity to noise. The second disadvantage comes with the fact that it is not proven that the solution for a maximum curvature is unique and continuous in the considered parameter range.

To avoid these disadvantages, a simple geometric estimate is used. The basic idea is to transform the obtained dimensionless force components into an almost symmetric representation using:

$$\tilde{F}_x^{\mathrm{sym}} = \tilde{F}_x \frac{1}{\tau^{1/2} R_{\mathrm{m}}^{1/4}} \tag{3.27a}$$

$$\tilde{F}_z^{\mathrm{sym}} = \tilde{F}_z \frac{1}{\tau R_{\mathrm{m}}} \tag{3.27b}$$

$$\tilde{F}^{\mathrm{sym}} = \tilde{F} \frac{1}{\tau^{1/2} R_{\mathrm{m}}^{1/2}} \ . \tag{3.27c}$$

The term *symmetric* serves to clarify that the *absolute values* of the exponents of proportionality to R_{m} and τ along $\tau = 10^3$ and $R_{\mathrm{m}} = 10^{-3}$, respectively, are equal to each other after the transformation.

The symmetric representation of the results depicted in Fig. 3.6 are shown in Fig. 3.7. It is evident that a unique maximum exists along $\tau = 10^3$ and $R_{\mathrm{m}} = 10^{-3}$, respectively.

The characteristic values $R_{\mathrm{m}Cx,z}$ and $\tau_{Cx,z}$ are defined as:

$$R_{\mathrm{m}Cx,z}(\delta,\xi) = \underset{\tau_0=10^3,R_{\mathrm{m}}\in\mathbb{R}}{\arg\max}\ \tilde{F}_{x,z}^{\mathrm{sym}}(R_{\mathrm{m}},\tau_0,\delta,\xi), \qquad (3.28\mathrm{a})$$

and

$$\tau_{Cx,z}(\delta,\xi) = \underset{R_{\mathrm{m}0}=10^{-3},\tau\in\mathbb{R}}{\arg\max}\ \tilde{F}_{x,z}^{\mathrm{sym}}(R_{\mathrm{m}0},\tau,\delta,\xi), \qquad (3.28\mathrm{b})$$

whereas $R_{\mathrm{m}Cx,z}$ and $\tau_{Cx,z}$ are only functions of the dimensionless geometric parameters δ and ξ.

Figure 3.8 illustrates the determination of the characteristic values for an arbitrary set of δ and ξ.

Equation (3.28a) and (3.28b) are evaluated numerically using a derivative-free minimization of the negative symmetric representation $-\tilde{F}_{x,z}^{\mathrm{sym}}$ defined by (3.27). The minimization is based on golden section search and parabolic interpolation provided by the MATLAB™ function `fminbnd` [81].

This description of characteristic points is equally valid for the generalization, such as that of the maximum curvature. However, it has particular advantages in the case of real measurements where multiple derivations would lead to incorrect results due to the amplified sensor noise.

When these two characteristic values are determined for a specific set of δ and ξ, it is possible to normalize τ and R_{m}. Furthermore, the dimensionless force components can be normalized against a characteristic value of interest, e.g. the maximum force in a specific parameter range or the force at one of the two characteristic points of the maximum curvature.

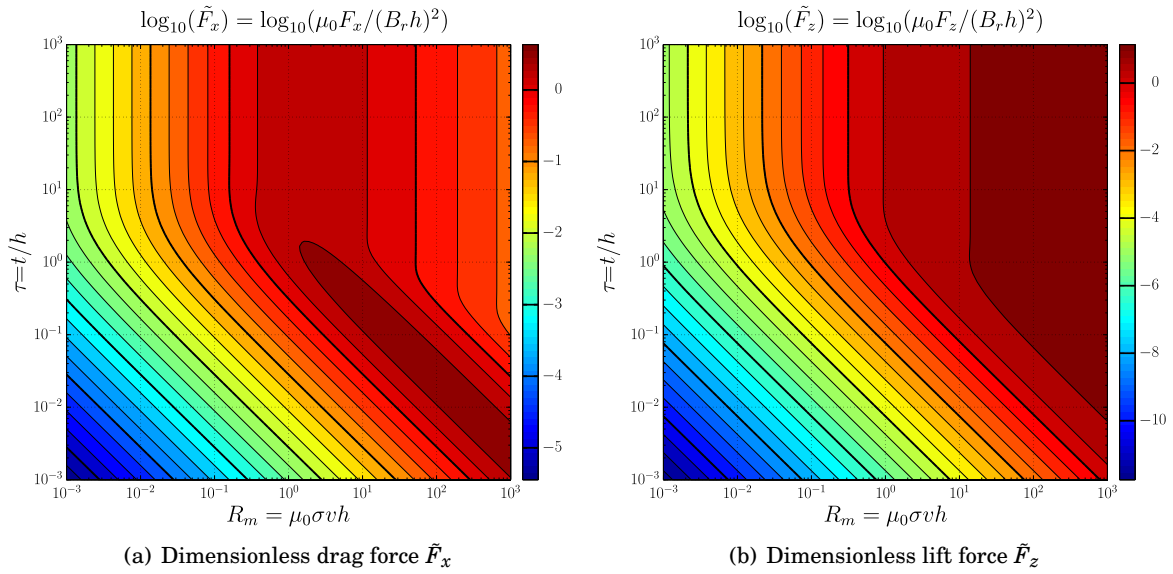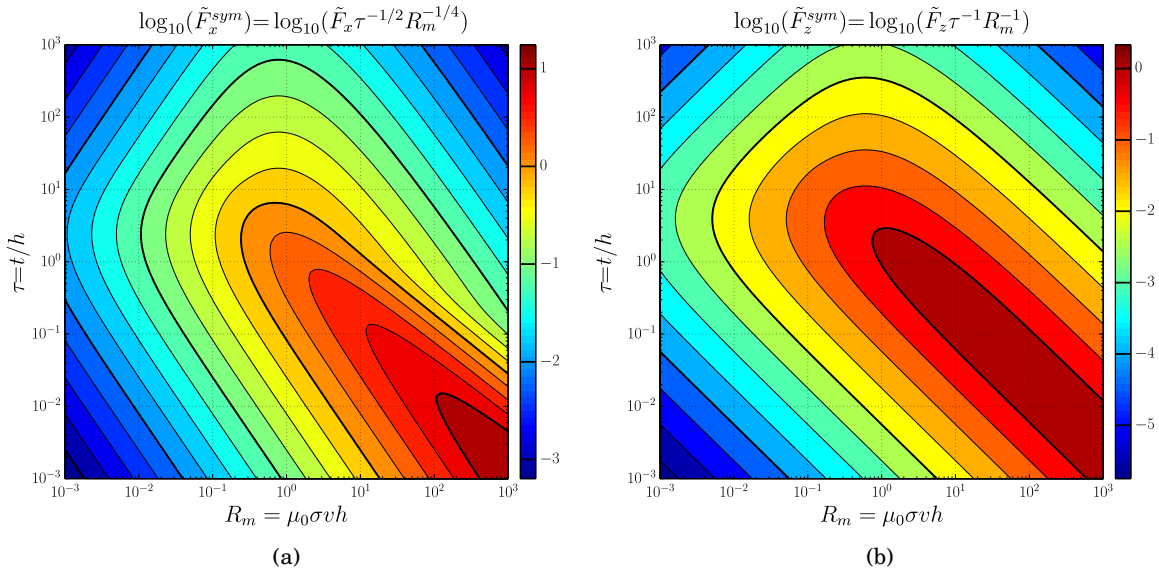Figure 3.7: Symmetric representation $\tilde{F}_{x,z}^{\mathrm{sym}}$ of the dimensionless force components $\tilde{F}_{x,z}$ as functions of the magnetic Reynolds number R_{m} and the dimensionless plate thickness τ for fixed $\delta = 10$ and $\xi = 1$.

(a)

(b)
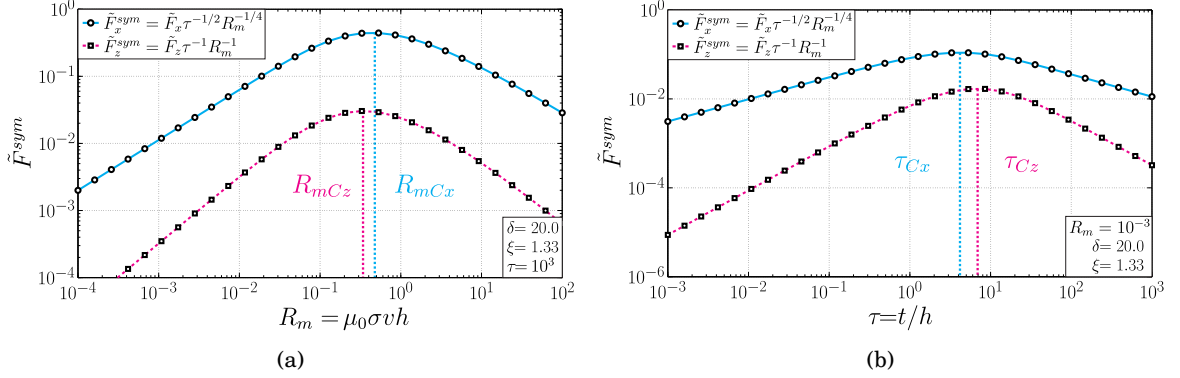
Figure 3.8: Definition of the characteristic values $R_{\mathrm{mC}x,z}$ along $\tau = 10^3$ (a) and $\tau_{\mathrm{C}x,z}$ along $R_{\mathrm{m}} = 10^{-3}$ (b) after the transformation of the dimensionless force components $\tilde{F}_{x,z}$ into a symmetric representation $\tilde{F}_{x,z}^{\mathrm{sym}}$.

Figures 3.9 and 3.10 show filled contour plots for the common logarithm of the force components normalized to their maxima as functions of the generalized magnetic Reynolds number $R_{\mathrm{m}}/R_{\mathrm{mC}x,z}$ and the generalized dimensionless plate thickness $\tau/\tau_{\mathrm{C}x,z}$ for arbitrary δ and ξ. The normalized force component generated is constant along each contour line. Each value is depicted as the power to base 10 in the color bar and the order of magnitude is given relative to the maximum force in the range considered. The contour intervals employed are again constant in each graph.

In Fig. 3.9, the parameter space for the normalized force component $\tilde{F}_x/\tilde{F}_{x,\mathrm{max}}$ is divided into four regions. The red curve separates an infinite half-space and thin-plate behavior. The blue curve distinguishes dominantly diffusive (low R_{m}) and advective (high R_{m}) regions. Each region has specific proportionality to powers of R_{m} and τ. The slope of the red curve for values of $R_{\mathrm{m}}/R_{\mathrm{mC}x} \geq 1$ can be obtained using the proportionalities in the two regions with high R_{m} as

$$\frac{\tau}{\tau_C} = \left(\frac{R_{\mathrm{m}}}{R_{\mathrm{mC}}}\right)^{-1/2}, \quad \frac{R_{\mathrm{m}}}{R_{\mathrm{mC}}} \geq 1. \tag{3.29}$$

The slope of the blue curve for values of $\tau/\tau_C \leq 1$ can be obtained in a similar manner using the two regions with thin-plate behavior as

$$\frac{R_{\mathrm{m}}}{R_{\mathrm{mC}}} = \left(\frac{\tau}{\tau_C}\right)^{-1}, \quad \frac{\tau}{\tau_C} \leq 1. \tag{3.30}$$

Of particular importance are the regions where both advective behavior (high R_{m}) and thin-plate behavior (low τ) dominate. For the dominantly diffusive regions (low R_{m}), the dependencies on R_{m} are retained for both force components. However, in the transition between dominantly diffusive (low R_{m}) and advective (high R_{m}) behavior, the dependencies on τ are inversely proportional.

In a similar manner, it is possible to proceed with the normalized force component $\tilde{F}_z/\tilde{F}_{z,\mathrm{max}}$ (Fig. 3.10). In contrast to Fig. 3.9, the parameter space is divided into only three regions in

37
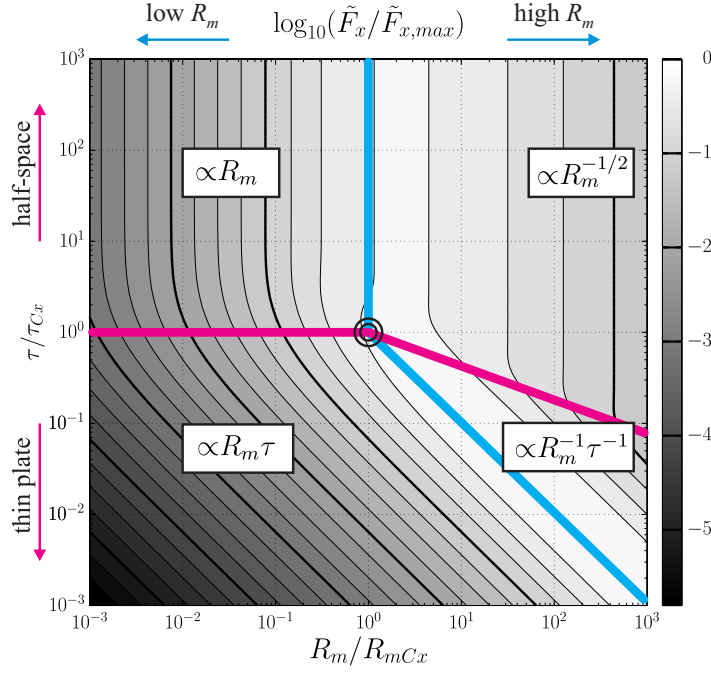
Figure 3.9: Normalized drag force $\tilde{F}_x/\tilde{F}_{x,\mathrm{max}}$ as function of the generalized magnetic Reynolds number $R_\mathrm{m}/R_{\mathrm{mC}x}$ and the generalized dimensionless plate thickness $\tau/\tau_{\mathrm{C}x}$ for arbitrary δ and ξ. Four regions with high or low R_m and thin plate or infinite half-space behavior are distinguished.

this case. The blue curve separates dominantly diffusive and advective behavior with the same estimate as that given by (3.30) but with squared proportionalities compared with the normalized force component $\tilde{F}_x/\tilde{F}_{x,\mathrm{max}}$. The distinction between an infinite half-space and thin-plate behavior is only valid for $R_\mathrm{m}/R_{\mathrm{mC}z} \leq 1$. If for $R_\mathrm{m}/R_{\mathrm{mC}z} \geq 1$, $\tilde{F}_z/\tilde{F}_{z,\mathrm{max}}$ goes to saturation and is almost invariant to changes in R_m and τ (dashed line).

During extensive parametric studies it was observed that the representations, as shown in Fig. 3.9 and 3.10, are completely invariant to changes in the remaining geometrical parameters δ and ξ. Thus, the selected representation includes all of the *similarity solutions* for the defined problem, which are independent of the input parameters selected in **x**.

The characteristic variables $R_{\mathrm{mC}x,z}$ and $\tau_{\mathrm{C}x,z}$, as well as the value $\tilde{F}_{x,z}$ at the specific parameter point must be known to denormalize the standard dimensionless representations. Although, this type of representation is less suitable for calculating the actual values of the force components, but it helps to improve the understanding for phenomenon itself.

Furthermore, during the investigations it was observed that the statement of invariance remained valid for PMs with different base areas, e.g., quadratic or regular octagonal (not explicitly shown here). This observation is rather surprising and it leads to the hypothesis that electromagnetic similarity also exists between PMs with different geometries. However, this does not necessarily mean that different PMs will induce an identical eddy current distribution inside the conductor or that the dimensionless force components will be the same, but it does
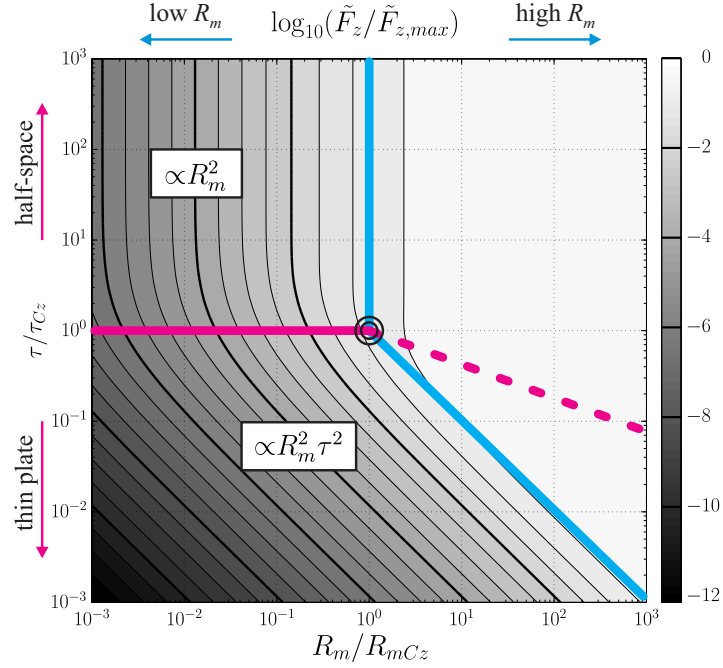
Figure 3.10: Normalized lift force $\tilde{F}_z/\tilde{F}_{z,\text{max}}$ as function of the generalized magnetic Reynolds number $R_\text{m}/R_{\text{mC}z}$ and the generalized dimensionless plate thickness $\tau/\tau_{\text{C}z}$ for arbitrary δ and ξ. Two regions with low R_m and thin plate or infinite half-space behavior are distinguished from a third region with high R_m.

imply the existence of identical normalized representations for PMs with different shapes.

Clearly, the specific values of the characteristic variables $R_{\text{mC}x,z}$ and $\tau_{\text{C}x,z}$ depend on the base area and the geometric parameters of the PM. The dependencies for the cylindrical PM are depicted in Fig. 3.11. It can be observed that the shapes of the curves are similar for $R_{\text{mC}x,z}$ and $\tau_{\text{C}x,z}$ for both force components $\tilde{F}_{x,z}$, as well as for the absolute value of the force $\tilde{F}$ (not shown). In particular, $R_{\text{mC}x,z}$ and $\tau_{\text{C}x,z}$ appear to be inversely proportional to each other over the whole range of δ and ξ. This is confirmed by calculating the product of the factors $R_{\text{mC}x,z}$ and $\tau_{\text{C}x,z}$, and the related standard deviations σ_D (Table 3.3) for the parameter range investigated in Fig. 3.11.

The mean relative standard deviations $\bar{\sigma}_D$ of about 2.5% are probably the results of truncation errors during the numerical integration required for the calculation of the force components. Nevertheless, the constancy of the products can be used to reduce efforts required to determine R_{mC} and τ_C by calculating one from the other. This significantly simplifies their subsequent application to model experiments. Furthermore, it supports the hypothesis that an electromagnetic similarity also exists between PMs with different geometries.
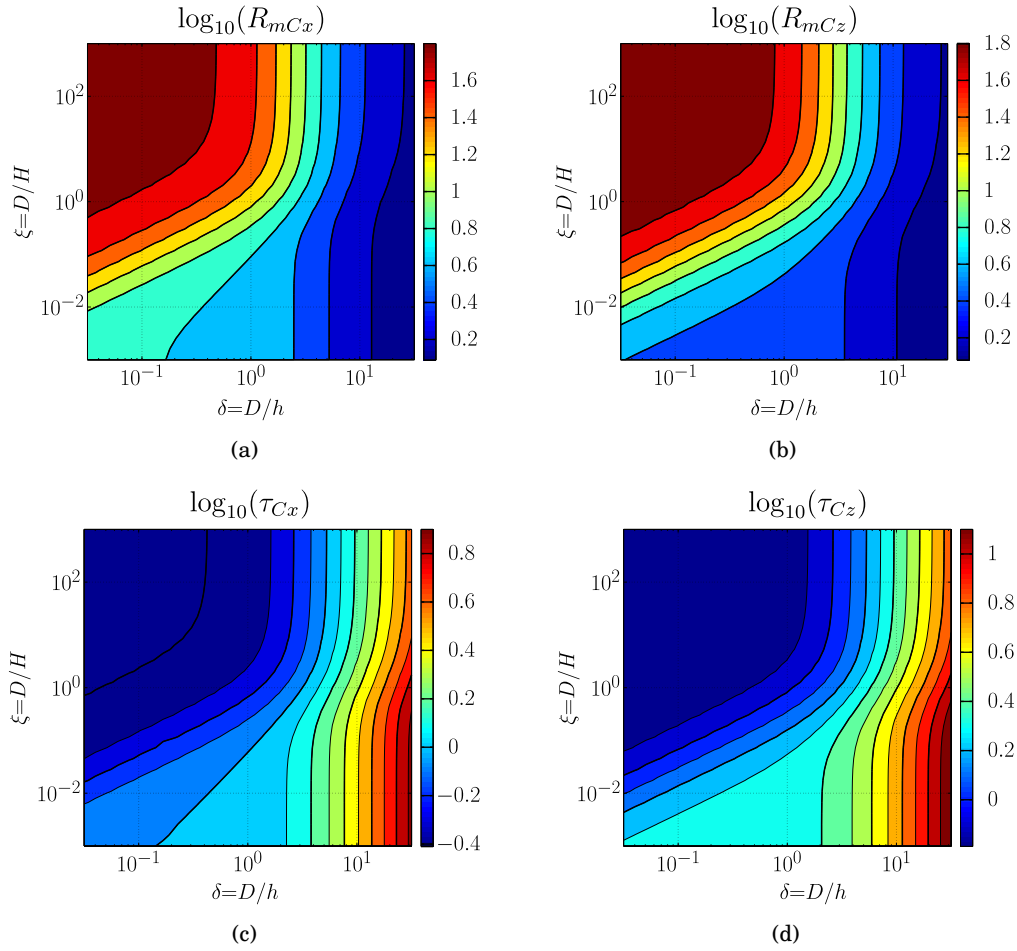
Figure 3.11: Characteristic magnetic Reynolds number $R_{\mathrm{mC}x,z}$ (a+b) and dimensionless plate thickness $\tau_{\mathrm{C}x,z}$ (c+d) along $\tau = 10^3$ and $R_\mathrm{m} = 10^{-3}$, respectively, as functions of δ and ξ.

3.4 Scaling Laws

In section 3.2 the procedure of dimensional analysis is applied to a simple problem that could be solved using exact analytical formulas. However, many engineering problems are so complex that no analytical solution can be obtained. In many of these problems, model experiments are the only way to avoid expensive and time-consuming experiments with wide variation in the governing parameters.

In the current problem, it is of interest to describe the influence of the parameters v, σ, B_r and the geometric parameters D, H, h, and t on the force components F_x and F_z that act on the PM. Based on the dimensional analysis, it is known in which form all of the parameters must appear in the unknown functions that determine the acting force. From the discussion in section 3.3 different regions of dependencies of the force components on R_m and τ can be distinguished. These regions are separated by areas of transition, which include the defined characteristic points R_{mC} and τ_C. These characteristic values are only functions of the dimensionless diameter

40

Table 3.3: Product of the characteristic values R_{mC} and τ_{C} calculated for $\delta = 10^{-1.4} \dots 10^{1.4}$ and $\xi = 10^{-3} \dots 10^{3}$

PM base shape	Component	$R_{\mathrm{mC}}\tau_{\mathrm{C}}$	σ_D
Circle	$\tilde{F}$	3.34	0.04
	$\tilde{F}_x$	1.94	0.07
	$\tilde{F}_z$	2.36	0.03
Rectangle	$\tilde{F}$	3.31	0.10
	$\tilde{F}_x$	1.95	0.07
	$\tilde{F}_z$	2.36	0.05
Regular octagon	$\tilde{F}$	3.35	0.05
	$\tilde{F}_x$	1.96	0.08
	$\tilde{F}_z$	2.37	0.04

δ and the aspect ratio ξ of the PM.

In order to clearly formulate the scaling laws for the problem, in the following it is discriminated between a *prototype*, which is the object of interest, and a *model*, which is employed to perform experiments under controlled conditions. For prototype and model, three different cases of similarity are considered, namely electrodynamic, geometric, and generalized similarity.

3.4.1 Electrodynamic Similarity

In the first case, experiments are performed based on a model with electrodynamic similarity. Electrodynamic similarity includes geometric similarity and it occurs if and only if each dimensionless parameter $(R_{\mathrm{m}}, \delta, \xi, \tau)$ has the same value in the model and the prototype. When the model experiment is designed, then it must be considered that not only all of the geometric parameters need to be scaled linearly. The magnetic Reynolds number R_{m} itself also changes with the geometric scale and it must be adapted by changing the product of σv (cf. Fig. 3.12).

For example, if the same material is used for the plate in an n-times larger model, then the relative velocity between the plate and PM must be decreased by $1/n$ with R_{m} to be constant. The forces obtained from the model experiments should then be rescaled using (3.26e) and (3.26f) to obtain a correct evaluation. Using the n-times larger model, it is known that the measured forces are n^2-times larger than those for the prototype. Furthermore, it is known that if a PM is used with an m-times higher magnetic remanence B_{r}, then the measured forces are also m^2-times larger. Again, it is clear that it is not necessary to use the same grade of PMs material to obtain a similar electrodynamic model. This difference only needs to be considered when the experimental results are evaluated.

All of these statements about scaling in the case of electrodynamic similarity are a direct consequence of the dimensional analysis only.

41
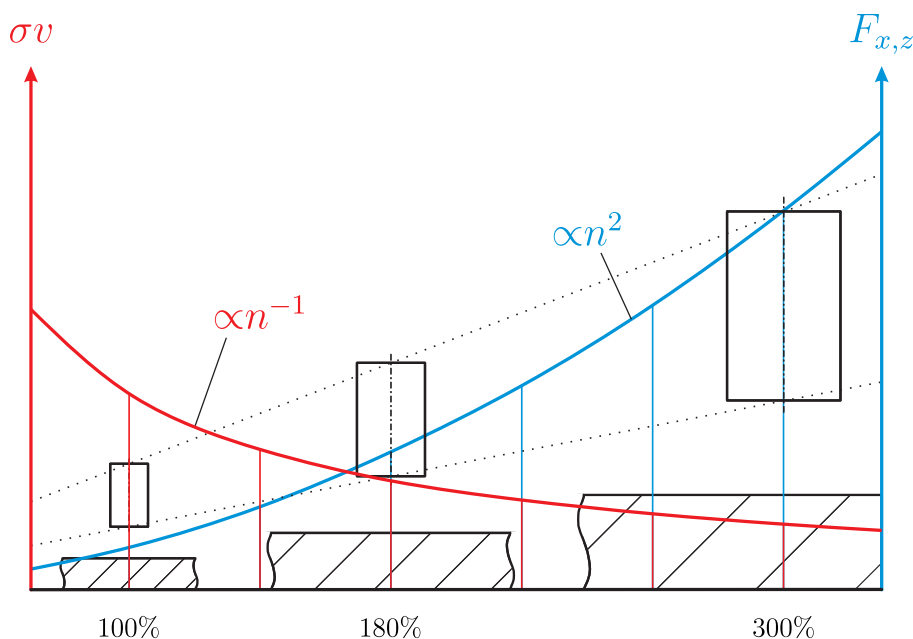
Figure 3.12: Model scaling in case of electrodynamic similarity: product of σv (*red*) for constant magnetic Reynolds number R_m and predicted scaling of force components $F_{x,z}$ (*blue*) in case of identical PM material.

3.4.2 Geometric Similarity

In the second and more general case, experiments are performed on a model where only δ and ξ are equal to those of the prototype (cf. Fig. 3.13). In contrast to the electrodynamic similarity, R_m and τ can differ within a certain range as long as the prototype and the model used in experiments are located in the same characteristic region. This is achieved by estimating the region that contains the prototype and ensuring that the model experiment is designed to belong to the same region. If the model is closer to the transition zones than the prototype, but it is still outside, then they share the same proportionality to R_m and τ and the measured forces in the model can be scaled to these of the prototype. To identify the characteristic region where the model is located, R_m and τ are varied slightly and the changes in the measured force components are observed. If the changes fit to the proportionalities of the assumed characteristic regions, then the results can be scaled for all prototypes which are not closer to the transition zone than the designed model.

To illustrate this kind of similarity, two simple examples are discussed and depicted in Fig. 3.13 by E1 and E2. In the first example, an n-times larger model is built in order to investigate the behavior of the problem with assumed *half space behavior* at *low R_m* (E1). While the geometry of the magnet and the distance to the plate surface are scaled accordingly, the thickness of the plate is kept constant. In consequence, R_m increases at the same velocity and for identical plate material by the factor of n, while τ decreases by $1/n$. To test whether the assumption for the characteristic region for the model holds, t and v are slightly increased.

(a) Dimensionless drag force $\tilde{F}_x$

(b) Dimensionless lift force $\tilde{F}_z$
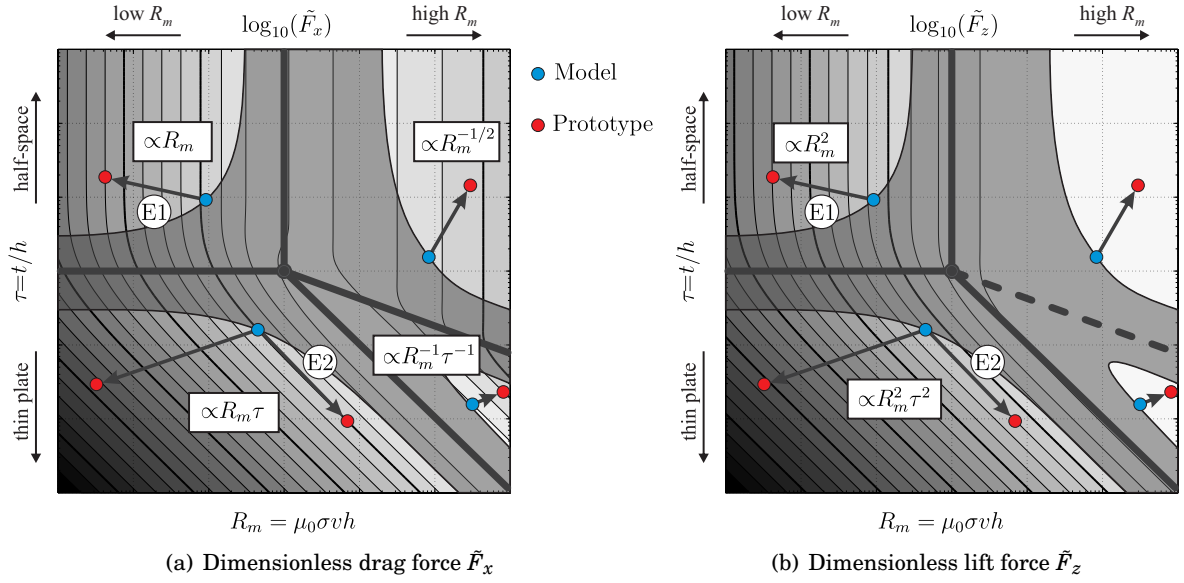
Figure 3.13: Illustration of the geometric similarity.

If the measured forces change as predicted, then the assumption is valid. In consequence, the model design is invariant to an increase of the plate thickness and, in comparison to the prototype, it shows a proportionality of $n\tilde{F}_x$ and $n^2\tilde{F}_x$ in the dimensionless force components. In order to estimate the force components for the prototype, the measured results in the model have to be rescaled by $1/n^3$ and $1/n^4$ for F_x and F_z, respectively.

In the second example, a PM with the corresponding force measurement instrument is used to investigate a problem with assumed *thin plate behavior* at *moderate R_m* (E2). To be able to use the same force measurement instrument, it is expected to be necessary that the ratio as well as the magnitude of the force components are similar in the model and the prototype. Even if for the model experiment only an *n*-times thicker plate of a different material with $1/m$-times lower conductivity is available, then it is still possible to fulfill this requirement.

Because the same magnet size is used, the distance to the plate surface h has to be kept constant in order to fix δ and ξ. Additionally, the velocity in the model experiments has to be scaled by m/n, so that the magnetic Reynolds number R_m does scale with $1/n$. Thus, the products $R_m\tau$ (relevant for $\tilde{F}_x$) and $R_m^2\tau^2$ (relevant for $\tilde{F}_z$) stay the same for model and prototype.

If the assumption for the characteristic region also holds for the model experiment, then in consequence, the model experiments will take place on an *isodyn*, a line of equal dimensionless forces as the prototype. Because h is kept constant, this is also true for the real measured force components and it is possible to use the same force measurement instrument.

3.4.3 Generalized Similarity

In the third case, R_m and τ in the model can differ over the whole range where the phenomenon is still described mainly by the same physical effects. To ensure a correct estimation of the

43

Lorentz force, it is necessary to perform the following four steps.

First, either R_{mC} or τ_{C} has to be found as described in (3.28) by varying the free parameters τ or R_{m}, respectively. It is essential to keep in mind that h is excluded from the variation, as long as the same magnet size is used. Second, the other characteristic value has to be calculated using the corresponding factor from Table 3.3. Third, the axes in Figs. 3.9 or 3.10 have to be denormalized by multiplying the axis scale with the respective characteristic value. Finally, the complete graph is denormalized using the dimensionless force component measured by the model at a single arbitrary point, e.g. the force at the characteristic point from step one. As the result for a specific configuration of δ and ξ, the force components can be estimated for very wide range of settings, but without the need for direct exploration.

As an example of the generalized similarity, a specific set of δ and ξ is taken, i.e. a fixed distance for a specific cylindrical PM. In the first step, the plate thickness t is changed gradually for the velocity that corresponds to a magnetic Reynolds number $R_{\mathrm{m}} = 10^{-3}$. The measured values of the force in the x-direction F_{xn} are multiplied by the associated $\tau_n^{-1/2} R_{\mathrm{m}} n^{-1/4}$ to obtain the symmetric representation given by (3.27). The characteristic value $\tau_{\mathrm{C}x}$ is estimated at the maximum of $\tilde{F}_{xn}^{\mathrm{sym}}$ and stored with the measured force F_x. In the second step, $R_{\mathrm{mC}x}$ is estimated using Table 3.3 for a circular base shape of the PM as $R_{\mathrm{mC}x} = 1.94\tau_{\mathrm{C}x}$. Using these three values, Fig. 3.9 can be denormalized.

3.5   Intermediate Summary

The present study contributes to the procedure of modeling and scaling in Lorentz force applications using dimensional analysis.

For this particular problem a *physical model* was formulated by means of a list of relevant parameters **x** and their individual dimensions [**x**]. Using this list, a dimensional matrix **D** was assembled to calculate a dimensionless basis set **Π** comprising a *dimensionless model* of the problem with a reduced number of parameters independent of the dimensional system used. The basis set **Π** was transformed using linear combinations of the calculated basis set vectors to obtain a representation that is more suitable for the investigation of the problem. This step completed the dimensional analysis. It is a starting point for the numerical studies on the influence of the dimensionless parameters on the dimensionless force components.

A concise parametric study was conducted to illustrate the advantages of the dimensionless representation for displaying complex data in an efficient way. In particular, the influence of the magnetic Reynolds number R_{m} and the dimensionless plate thickness τ on the dimensionless force components $\tilde{F}_{x,z}$ were shown for an arbitrary set of remaining dimensionless geometric parameters. Using a power-law hypothesis for both dependencies, four readily distinguished regions were identified where each can be described by a simple power law.

It was observed, that the location of the transition zones between separated regions depends greatly on the geometric parameters δ and ξ. Therefore, the results were normalized against

the characteristic values R_{mC} and τ_{C}, which are defined as the maxima in the novelly described symmetric representation $\tilde{F}_x^{\mathrm{sym}}$ and $\tilde{F}_z^{\mathrm{sym}}$ of dimensionless force components. This normalization yields a generalized representation of the dimensionless force components, which is completely invariant to changes in the geometric parameters δ and ξ. The apparent inversely proportional relationship between the characteristic parameters R_{mC} and τ_{C} for different PM shapes was a surprising result. It was shown that this introduces an additional simplification which further facilitates the subsequent formulation of scaling laws.

Finally, three different scaling laws are described and illustrated on practically relevant examples.

EXPERIMENTAL STUDIES

This chapter describes experimental investigations, which are the basis for the advancement of the LET method. Furthermore, the experiments provide objective data for the validation of numerical approaches used for theoretical determination of the exerted Lorentz force.

At first, the measurement procedure of LET is described. The underlying measurement principle is analyzed and all operations to perform an LET measurement are explained in the measurement method. Secondly, the final state of the experimental setup that was used for laboratory experiments in this thesis is described. The main components of the setup and their functional relationship are explained and selected elements are described in detail. The digital signal processing (DSP) developed for LET is explained afterwards. DSP is the final step of the description of the measurement method and allows to determine the value of the measurand by means of the arithmetic mean and the experimental standard deviation.

In the next section, a representative overview of the measurement performance of the described experimental setup is given. Four selected applications are presented, including defect free aluminum and stainless steel bars as well as artificial defects in stacked aluminum sheets, and specially prepared specimens of *glass laminate aluminum reinforced epoxy* (GLARE).

Finally, the insights of the experimental studies are condensed in an intermediate summary.

4.1 Measurement Procedure

According to the international vocabulary of metrology (VIM) [64], a *measurement procedure* is defined as a detailed description of a *measurement* according to the *measurement principles* and the given *measurement method*. The measurement method is the description of the logical organization of operations used in a measurement. It is based on a *measurement model* and

includes any calculation to obtain a *measurement result*. The measurement result is a set of quantity values being attributed to a *measurand* and is expressed as a *measured quantity value* and a *measurement uncertainty*.

According to these definitions, the measurement procedure for LET is described in the following sections.

4.1.1 Measurement Principle

The measurand in LET is the Lorentz force $\mathbf{F}(t)$ acting on the PM during an LET experiment. The basic *measurement principle* of LET is based on the electromagnetic interaction of the PM and the UUT. For a better understanding, the interaction can be decomposed into two causally connected physical phenomena: (i) the electromagnetic induction of *eddy currents* (EC) inside the UUT and (ii) the Lorentz force acting on the UUT and the PM.

The decomposition into a causal sequence, in terms of cause and effect, further simplifies the understanding of the LET measurement principle (cf. Fig. 4.1). The initial cause in LET is the relative motion of the PM and the UUT that leads to electromagnetic induction of eddy currents inside the UUT. This effect causes the generation of the Lorentz force due to the interaction of the induced eddy currents with the magnetic field of the PM. The second causal relationship can also be triggered by other current flows, which are independent of a relative motion. In general, no other current flows are present inside the UUT, therefore they are neglected in the following.

Cause – Effect – Relationship I

Initial Cause	Effect
Relative motion of PM and UUT	Electromagnetic induction of EC

Cause – Effect – Relationship II

Cause	Effect
Electromagnetic induction of EC	Lorentz force acting on UUT and PM
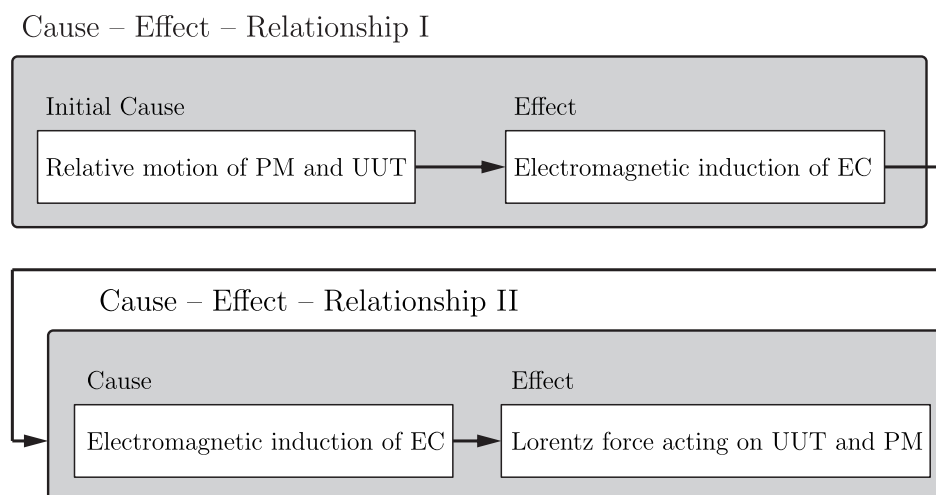
Figure 4.1: Causal sequence of the basic measurement principle in LET.

In order to measure the Lorentz force, one or more measurement principles are necessary to convert the force into an electrical signal. These force measurement principles complete the overall measurement principle of LET. The selected force measurement principles have a significant influence on the result of the measurement, but they do not alter the physical phenomena of interest.

48

4.1.2 Measurement Method

The measurement method describes the logical organization of all operations used to measure the Lorentz force. It involves all information necessary to describe an experiment and to ensure its repeatability. In other words, the description should allow a well-trained person to perform an experiment and to do all calculations necessary to obtain a complete measurement result.

Since the basic measurement principle of LET neither defines the type of relative motion, nor the concrete realization of the force measurement, the following description can only cover a particular realization of the method. The realization discussed next assumes the rectilinear motion of the UUT relative to the stationary PM and describes the attached sensor system. Figure. 4.2 shows the schematic view of the experimental setup. In addition to the UUT (1) and the PM (2) three main devices are necessary: the linear drive (3), the 2D-positioning stage (4), the multicomponent force sensor (5), and the measurement frame (6).

(a) Side view

(b) Front view
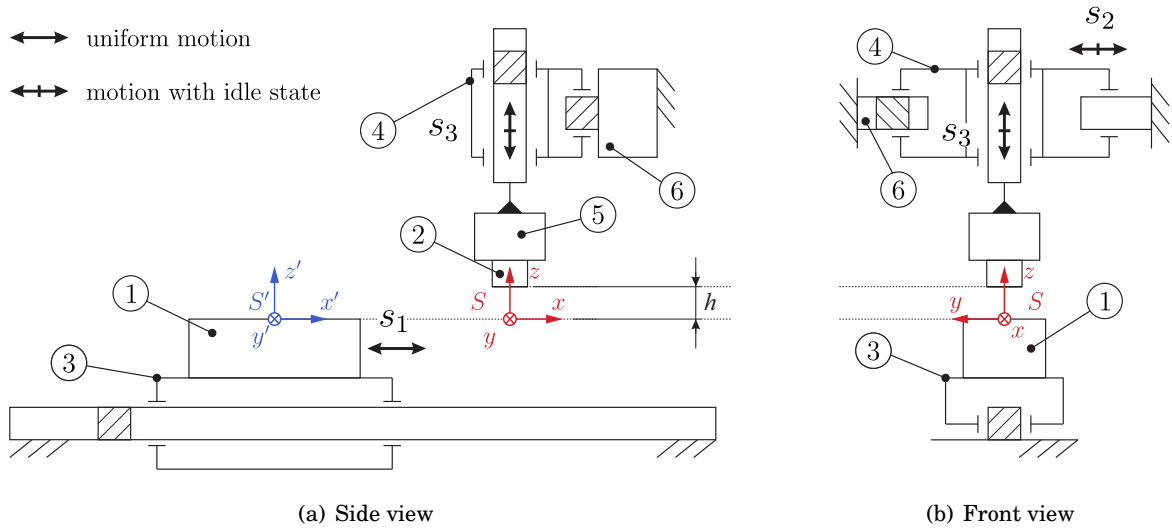
Figure 4.2: Schematic view of experimental setup for LET measurements. The UUT (1) moves along the linear guide of a linear drive (3) relative to a stationary PM (2). The PM is mounted on the multicomponent force sensor (5). The force sensor is attached to the 2D-positioning stage (4), which is mounted on the measurement frame (6). Two frames of reference S' and S are defined analogously to the problem definition in Section 3.1.

The UUT is mounted on the slide of a linear drive that provides the controlled motion and guidance of the UUT. The linear drive is fixed on a heavy load bench, which is assumed to be mechanically insulated from ground vibrations. The PM is indirectly attached to a 2D-positioning stage via a multicomponent force sensor. The 2D-positioning stage provides the positioning of the PM relative to the linear guide of the linear drive. The 2D-positioning stage is fixed on a measurement frame (6), which is assumed to be mechanically insulated from ground vibrations. Due to the placement of the multicomponent force sensor, all forces occurring between the PM and the 2D-positioning stage can be measured in the experiment.

All additional components like power supply, hardware controller, and data acquisition are assumed to be mechanically decoupled from the measurement apparatus so that they do not influence the measurement process.

The logical operations needed to perform an experiment are equal for all experimental studies presented in this thesis. They are explained in the following.

The first step in all experiments is to define the design of experiment (DOE), including the purpose of the investigation. The parameters to be defined in the DOE are the position of the PM during operation (y- and z-position), the desired velocity of the UUT (v), and the number of repetitions of the respective experiment. The DOE also has to include the assignment and ordering of the successive experiments in order to allow further statistical evaluation, e.g. correlation analysis or hypothesis testing.

The next step is the preparation of the UUT according to the DOE and the subsequent fixation on the slide of the linear drive. The positioning of the UUT relative to the slide is part of the definition of the laboratory frame of reference and is crucial for the repeatability of the experimental study. After the fixation of the UUT, the sensor system including PM and the force sensor is mounted on the measurement frame and has to be aligned according to the surface of the UUT and the guide of the linear drive. This step completes the definition of the laboratory frame of reference. In the particular realization of the method, the procedure of alignment can be supported by measuring the contact forces between UUT and PM in order to enhance the repeatability and precision. This method is referred to as force feedback [52].

After the functional check of the sensor system and *data acquisition* (DAQ), the subsequent operations of the measurement process are sequentially motions performed by the linear drive and the 2D-positioning stage. These operations need to be monitored and controlled by separate devices (actuator control) and can therefore be fully automated. Such a process ensures a high level of repeatability and reproducibility.

The *measurement process* is defined as a sequence of single experiments according to the DOE. For each experiment, the UUT moves rectilinearly relative to the PM along the linear guide. During the controlled motion all sensor data are sampled and temporally stored by the DAQ. At the end of the test track the slide stops and the recorded data is stored permanently on the hard disc for later processing. Depending on the intended purpose of the investigation, the next experiment can be started from this position, or the slide is moved back to the desired starting position.

The stored data are referred to as *sensor data*. Each sensor delivers an electrical signal that needs to be multiplied by the specific calibration factor in order to calculate the corresponding physical quantity which is part of the DSP and is discussed in a separate section (cf. Sec. 4.3).

4.2 Experimental Setup

The particular realization of the laboratory setup for LET measurements consists of six main components as shown in Sec. 4.1.2. The UUT and PM are both regarded as problem specific components, thus they will be described in Sec. 4.5 for the respective investigations.

(a) Overview

(b) Positioning unit

(c) Sensor system
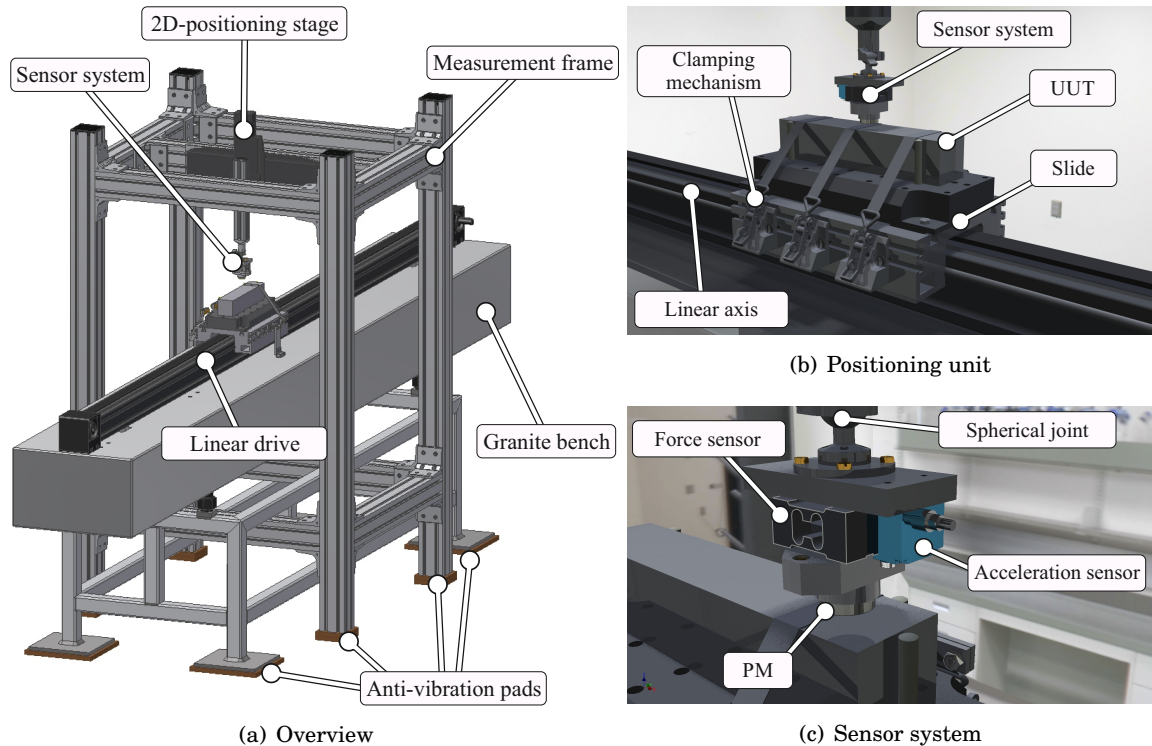
Figure 4.3: Experimental setup for LET measurements: (a) Overview shows the measurement frame and the 2D-positioning stage separated from positioning unit which is mounted on a heavy granite bench; (b) Detail view of the positioning unit for motion of the UUT; (c) View of the sensor system including a PM mounted on the force sensor and separate acceleration sensor.

4.2.1 Linear Drive

The positioning unit consists of a belt driven linear drive designed by *Jenaer Antriebstechnik GmbH* mounted on a linear guide by *Bahr Modultechnik GmbH*. A planetary gear of gear ratio $i = 3$ transmits the torque from the servomotor (type 110B) to the pulley of the belt drive. The belt is directly connected to the slide of the linear guide, which realizes the translational motion of the UUT. In the framework of design improvements the original tooth belt drive was replaced by poly-v belt drive in order to eliminate a source of noise emission, which was introduced by tooth meshing [141]. The maximum velocity of the slide is about $v = 2$ m/s using a third-order motion profile for reduced jerk, with quadratic ramping and de-ramping phases in the velocity. If the jerk is not considered, a maximum velocity of about $v = 3.75$ m/s is possible but leads to increased structural damage (fatigue) of the linear drive.

Figure 4.4: Experimental setup for experimental characterization of the linear guide using a long range multi-beam interferometer by *SIOS Meßtechnik GmbH*. The measurement reflector is placed on the slide for static and dynamic measurements of positioning deviation, pitch and yaw angle [109].

The positioning deviations, as well as pitch and yaw angles of the linear guide are qualified using a long range multi-beam interferometer by *SIOS Meßtechnik GmbH*. As shown in Fig. 4.4, a measurement reflector based on three individual prismatic reflectors is placed on the slide while the multi-beam interferometer is fixed at the end of the linear guide. The experiments are performed for static slide positions as well as for dynamic measurements of up to $v = 0.3$ m/s. It was observed that the positioning deviation along the full travel range of $l_G = 2$ m is about $\Delta x = \pm 0.5$ mm and the lateral displacement of the slide is smaller than $\Delta y = \pm 25$ µm and $\Delta z = \pm 15$ µm [109].

As shown in Fig. 4.2, the velocity deviation of the slide does affect the velocity of the UUT and has a direct impact on the induced eddy current distribution. In the specified velocity range of up to $v = 4$ m/s, the manufacturer guarantees a deviation less than 5% of the predetermined velocity for the predefined control parameters [141]. In the framework of an uncertainty analysis [146], this statement is verified by means of an incremental position encoder TONiC T1000 (*Renishaw plc*) implemented into the experimental setup (cf. Section 4.2.3).

4.2.2 2D-Positioning Stage

The 2D-positioning stage is used for the positioning of the sensor system relative to the linear guide of the linear drive. It is an assembly of two orthogonally oriented precision linear stages of the NLS4 series [93] by *Newmark Systems Inc*. The travel range in y- and z-direction is 300 mm and 100 mm, respectively.

The design of this series of linear stages is improved for high stiffness and repeatability. Pre-stressed linear guide bearings and an internally lubricated plastic drive nut provide zero backlash operation and enable a specified accuracy of 0.6 µm/mm. The used lead screw has a pitch of 1.58 mm/rev (1/16″/rev) and the stepper motor encoder allows 4000 counts/rev, which

results in a resolution of the drive nut position of about 0.4 μm on each axis.

The orientation of the assembly enables a maximum load of the sensor system and fixture devices up to 6.0 kg (max. lifting capacity). The applied static load is given by the weight of the attached cantilever and mounted sensor system. The assembly has an estimated mass of about 1.4 kg and the estimate absolute value of the maximum forces is up to 3 N. Due to these facts, a disturbing influence of the process forces on the specified precision during operation is not expected.

The motion controller used in this setup is an NSC-G3-E series controller [94] with up to 3 individual axes with encoder feedback for stepper motors by *Newmark Systems Inc*. The configured communication between the sensor system and the host computer uses an Ethernet interface.

4.2.3 Sensor System

The sensor system is the set of all transducers used to observe an experiment (Fig. 4.5). It consists of four components: (1) the multi-component force sensor, (2) an additional acceleration sensor, (3) a coil with multiple turns (to measure induced voltage), and (4) an incremental position encoder (not shown). The PM is intentionally excluded from the description since it does not provide additional information during an experiment.

(a) Bottom view   (b) Side view
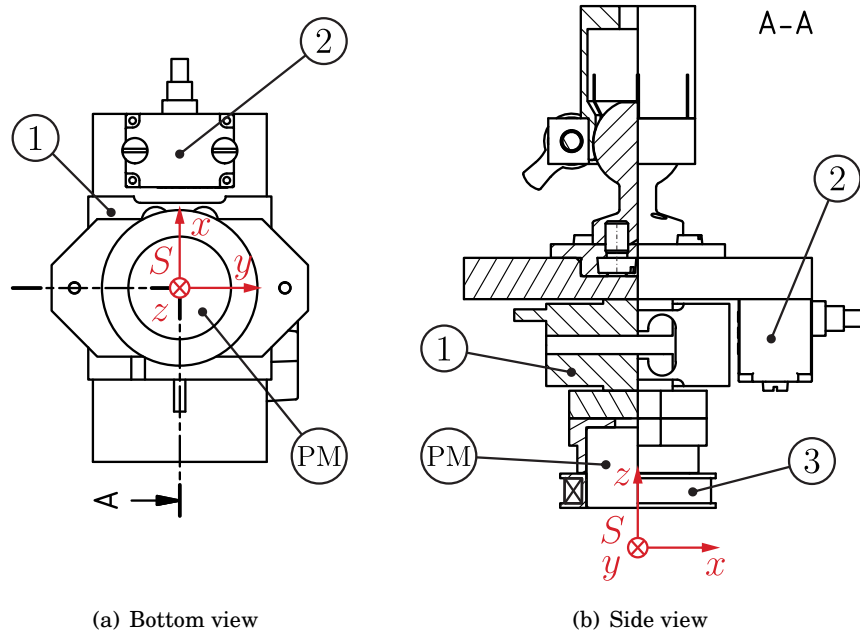
Figure 4.5: Technical drawing of the assembled sensor system of the experimental setup: (1) multi-component force sensor, (2) acceleration sensor, and (3) coil with multiple turns.

As a consequence of the definition of reference frames S' and S, the recorded signals of force $\mathbf{F}(t)$ and acceleration $\mathbf{A}(t)$ are each equal in direction and magnitude for both frames of

reference. However, the relative position of both coordinate systems to each other is measured with different signs in the respective coordinate system. Thus, they have to be distinguished carefully. In fact, the position of the slide of the linear drive measured by the incremental position encoder is recorded in the frame of reference S, whereas the lateral position of the PM y' given by the position of the 2D-positioning stage is only defined in the frames of reference S'. In order to reduce possible confusion with the use of two coordinate systems, in the following the relative position of UUT and PM is always given in frame of reference S' of the UUT, but *without* the primed notation.

4.2.3.1   3-Axes Force Sensor

The essential element of the sensor system is the custom build 3-axes force sensor K3D40 [86] by *ME-Messsysteme GmbH* for nominal loads of $3\,\mathrm{N} \times 3\,\mathrm{N} \times 10\,\mathrm{N}$ in the x-,y-, and z-direction, respectively. According to the data sheet, the sensor accuracy class is $0.5\,\%$ resulting in a nominal measurement error of about $15\,\mathrm{mN} \times 15\,\mathrm{mN} \times 50\,\mathrm{mN}$ for the respective measurement axes.

The measurement principle of the sensor is based on strain measurements on the surface of a compliant mechanical structure which is deflected due to the force of interest. The compliant structure is made of a single aluminum part designed as a series connection of three orthogonal oriented single axes flexure hinges. Each single axes mechanism is equipped with four strain gauges in a balanced Wheatstone bridge. The underlying measurement principle is the piezoresistive effect. Due to the limited bandwidth of the deflection body, this sensor concept is primarily designed for static force measurements.

Since the force sensor has already been used in previous work [141], its reliability was tested multiple times in between experimental studies. Due to the limited dynamic information about the sensor provided by the manufacturer, a comprehensive analysis has also been carried out in order to determine the dynamic sensor characteristics [128].

The sensor is connected to the analogue measurement amplifier is a GSV-1A4 [84] by *ME-Messsysteme GmbH*. According to data sheet, the measurement amplifier provides a bridge supply voltage of $V_\mathrm{S} = 5\,\mathrm{V}$ and an output voltage of $V_\mathrm{A} = \pm 10\,\mathrm{V}$. During operation and an examination of the amplifier's characteristics, both malfunctions and contradictory measurement results were observed. Thus, an overhaul of the device was carried out. The disassembly of the measurement amplifier revealed significant differences of the used hardware components in comparison to the data sheet. Actually, the amplifier consists of four individual strain gage measurement amplifiers of type GSV-1M [85] by *ME-Messsysteme GmbH*. A characterization of the four amplifiers, analogously to [128], showed a gain of $g_\mathrm{F} = 2 \times 10^3$ with fixed input sensitivity of $s_\mathrm{N} = 1.0 \times 10^{-3}\,\mathrm{V/V}$. Multiple contact faults have been rectified and the post-repair tests confirmed a fully functional device.

The sensor and the amplifier are connected via 37-pin Sub-D socket and have been together calibrated by the manufacturer. According to the calibration certificate, nominal output voltages

at nominal loads are $3.1969\,\mathrm{V} \times 4.8835\,\mathrm{V} \times 7.8030\,\mathrm{V}$ in the x-, y-, and z-direction, respectively. Regarding the identified amplifier parameters, this corresponds to nominal sensor sensitivities for the corresponding channels are given by:

$$s_{Fx} = 1.0656 \times 10^{-4}\,\frac{\mathrm{V}}{\mathrm{VN}} \tag{4.1}$$

$$s_{Fy} = 1.6278 \times 10^{-4}\,\frac{\mathrm{V}}{\mathrm{VN}} \tag{4.2}$$

$$s_{Fz} = 7.8030 \times 10^{-5}\,\frac{\mathrm{V}}{\mathrm{VN}}\;. \tag{4.3}$$

4.2.3.2 3-Axes Acceleration Sensor

The second component of the sensor system is the 3-axes accelerometer ASC 5511LN [5] by *Advanced Sensors Calibration – ASC GmbH*. The measurement principle of the accelerometer is based on a capacitive micro-electro-mechanical system (MEMS), which is specially designed for low frequency responses from constant value up to $5\,\mathrm{kHz}$ in a range of $\pm 2\,\mathrm{g}$[1]. The sensitivity of the accelerometer is specified to be invariant to the supply voltage in the range of $V_\mathrm{S} = +8\,\mathrm{V} \cdots +30\,\mathrm{V}$.

The sensor has been calibrated by the manufacturer for all three axes separately. According to the calibration certificate, the nominal accelerometer sensitivities are:

$$s_{Ax} = 98.848 \times 10^{-3}\,\frac{\mathrm{Vs}^2}{\mathrm{m}} \tag{4.4}$$

$$s_{Ay} = 98.535 \times 10^{-3}\,\frac{\mathrm{Vs}^2}{\mathrm{m}} \tag{4.5}$$

$$s_{Az} = 98.955 \times 10^{-3}\,\frac{\mathrm{Vs}^2}{\mathrm{m}}\;, \tag{4.6}$$

at a nominal acceleration of $5\,\mathrm{m/s}^2$ for an excitation frequency of $16\,\mathrm{Hz}$.

In the experimental setup, the 3-axes accelerometer is mounted on the same plate as the 3-axes force sensor (cf. Fig. 4.5). This allows to observe the translational components of the motion of the sensor system during an experiment and to estimate the effects of inertial forces on the PM. In Chapter 5, this additional information is used to develop a low-order mechanical model that describes the dominant dynamic behavior of the experimental setup.

4.2.3.3 1-Axis DiLET Sensor

The third component of the sensor system is a differential Lorentz force eddy current testing (DiLET) sensor. This 1-axis sensor [154], which is a passive pick-up coil with multiple turns winded coaxially on the outer surface of the PM (cf. Fig. 4.5). It is designed as an optional upgrade in order to measure additionally the time variations of the secondary magnetic flux density ($\partial B_z/\partial t$) at the bottom surface of the PM.

---

[1]In the context of accelerometers the term *g-force* refers to the acceleration relative to free-fall. It is described by the standard acceleration due to gravity $\mathrm{g_n}$ which is defined to $9.806\,65\,\mathrm{m/s}^2$ [24].

The concept of this sensor is based on [141] and [153], where a set of passive coils fixed to a PM is proposed to allow the detection of perturbations in the eddy current distribution caused by defect inside the UUT. It is based on the fact that the primary magnetic field $\mathbf{B}^{(p)}$ produced by a permanent magnet is constant in time, while the secondary magnetic field $\mathbf{B}^{(s)}$, connected with the eddy current distribution inside the UUT, is time dependent when a defect is present. Thus, the induced voltage V_i ($i \in \{x, y, z\}$) in a coil fixed to the PM, is only proportional to perturbations of the secondary magnetic field $B_i^{(s)}$ and by that sensitive to disturbances caused by defects.

As shown by [153], the induced voltage V_i is proportional to the first time derivative of the force component parallel to the respective coil axis. Therefore, the proposed technique has been termed differential Lorentz force eddy current testing.

In this thesis, measurement results of the induced voltage $V_z(t)$ are shown using two different 1-axis DiLET sensors mounted on different PMs. It is mentioned that index z denotes the orientation of the coil axis, not a component of a vector. The custom-built DiLET sensors are equal with respect to the number of turns N_z but of different size due to the different outer diameters of the PMs.

Because the different 1-axis DiLET sensors are not calibrated, the respective nominal output voltage V_z and the sensor sensitivity s_{Vz} of the respective sensors are unknown. However, it is possible to provide an estimate of both factors for an *effective* variation of the magnetic flux density $\partial B_{\mathrm{eff},z}(t)/\partial t$ by the following approximations. Assuming that the coil is substituted by a single circle at the bottom of the PM, then the time variation of the magnetic flux density $\partial B_z/\partial t$ can be given by

$$\frac{\partial}{\partial t}\Phi_z(t) = \frac{\partial}{\partial t}\int_S B_z(t)\,\mathrm{d}S \approx \frac{\partial}{\partial t}B_{\mathrm{eff},z}(t)S \;, \tag{4.7}$$

with $\Phi_z(t)$ the magnetic flux through the enclosed surface S of the coil. For a circular coil with diameter D_{eff}, which can be approximated by the mean of inner and outer diameter of the real coil, (4.7) becomes

$$\frac{\partial B_{\mathrm{eff},z}(t)}{\partial t} \approx \frac{4V_z(t)}{\pi D_{\mathrm{eff}}^2 N_z} = \frac{1}{s_{Vz}}V_z(t) \;, \tag{4.8}$$

with the number of turns of the coil N_z and the sensor sensitivity s_{Vz}. For the two used 1-axis DiLET sensors, one with $D_{\mathrm{eff}} = 27\,\mathrm{mm}$ and the other with $D_{\mathrm{eff}} = 30\,\mathrm{mm}$, and both $N_z = 5000$ turns the sensor sensitivities are estimated by:

$$s_{Vz}\big|_{D_{\mathrm{eff}}=27\,\mathrm{mm}} \approx 2.86\,\frac{\mathrm{Vs}}{\mathrm{T}} \tag{4.9}$$

$$s_{Vz}\big|_{D_{\mathrm{eff}}=30\,\mathrm{mm}} \approx 3.53\,\frac{\mathrm{Vs}}{\mathrm{T}} \;. \tag{4.10}$$

The induced voltage $V_z(t)$ is amplified by a self made analogue measurement amplifier. It is based on a precision instrumentation amplifier AD624 [2] by *Analog Devices Inc.* and provides a configurable gain $g_{\mathrm{DF}} = [1, 5, 10, 50, 100, 200, 500, 1000]$ of the DiLET signal. A response test confirmed the measurement amplifier to be fully operational.

The amplified output voltage of the analogue measurement amplifier at a nominal variation of the magnetic flux density $\partial B_{\mathrm{eff},z}(t)/\partial t$ is calculated by

$$V_z(t) = g_{\mathrm{DF}} \; s_{Vz} \; \frac{\partial B_{\mathrm{eff},z}(t)}{\partial t} \; . \tag{4.11}$$

4.2.3.4 Incremental Position Encoder

The incremental position encoder system TONiC by *Renishaw plc.* serves as an external position measurement system of the UUT in the x-direction. It is composed of three components: (i) T1000-50A read head [119], (ii) RGSZ20-S gold plated steel scale [117], and (iii) encoder interface T0100 A40A [118].
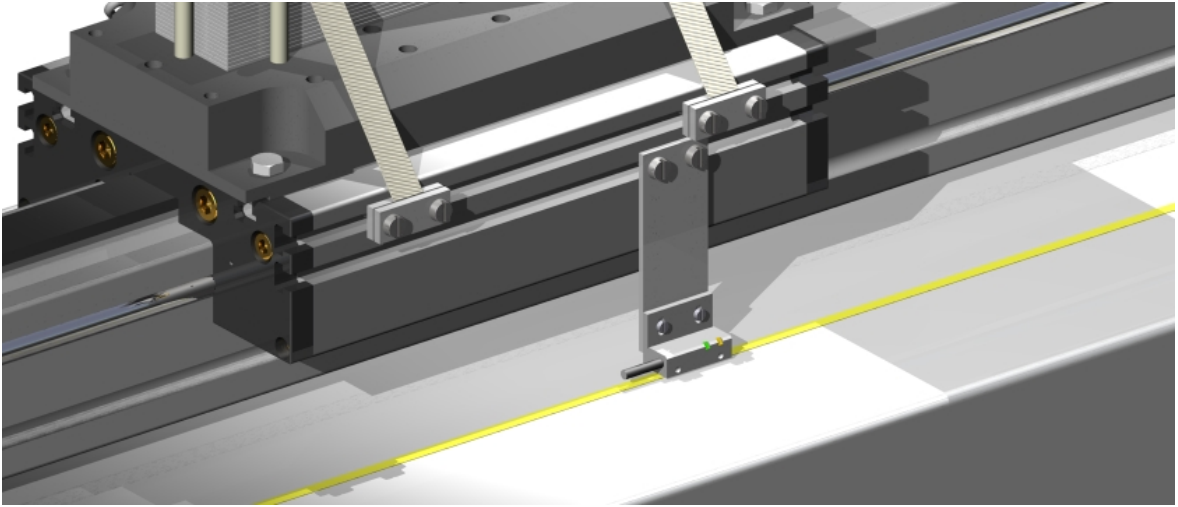
Figure 4.6: Incremental Position Encoder T1000-50A.

This encoder system measures the position of the read head relative to reference marks at both ends of the linear scale. The read head is mounted on the side of the slide of the linear drive. The linear scale, of 1 m length, is fixed on the heavy granite bench below the PM. The combination of optical detector (read head), linear scale (scale pitch 20 µm), and encoder interface results in a specified resolution of 50 nm (interpolated) up to a maximum velocity of 5.4 m/s.

In the framework of the analysis of the linear drive (cf. Section 4.2.1), the incremental position encoder was used to validate the controller estimated slide velocity. The investigation resulted in a correction of the specified pinion diameter and adjusted controller parameters for improved velocity constancy at the velocity operating point of $v = 0.5$ m/s.

4.2.4 Data Acquisition and Measurement Control System

The data acquisition (DAQ) device is used for signal conditioning and digitization of incoming analogue signals from the sensor system. The analog-to-digital converter (ADC) is the main component of the DAQ. In this particular realization of the experimental setup the NI PXI-4472 [91]

by *National Instruments* (NI) is used. It provides 8 simultaneously sampled analogue inputs at a sampling rate of up to 102.4 kHz each. The resolution of the ADC is specified with 24-bit per channel and a dynamic range of 110 dB. The ADC is connected to the Host-PC via the *PCI eXtensions for Instrumentation* (PXI) computer bus. A 6-slot chassis NI PXI-1036 [92] by NI serves as a Host-PC. All results presented in this thesis were sampled at $f_s = 10$ kHz at full input range of $V_{IN} = \pm 10$ V.

The measurement control system (MCS) is used to monitor and to control the experimental setup and its main devices. It provides a graphical user interface that allows the operator to monitor current system states and sensor inputs. Furthermore, the MCS allows to perform single experiments and to control the initialization sequence for the definition of the laboratory frame of reference. The most important task of the MCS is the batch processing of DOE without manual intervention of the operator. This enables comprehensive experimental studies including multiple repetitions without disturbing influences of the operator, while ensuring a high level of repeatability and reproducibility. The MCS has access to an specially established external database for storage of the acquired raw data at the local computing center for improved data security and accessibility. The programming language of the MCS is C++.

4.3 Digital Signal Processing and Basic Statistics

The basic idea of digital signal processing for LET is to provide an estimate of the expected value of the measurand $\mathbf{F}(t)$ and the corresponding experimental standard deviation $\sigma_F(t)$ for a specific experiment. The statistical analysis is necessary because even if the ideal measurement principle of LET (cf. Fig. 4.1) can be considered as deterministic, where no randomness is involved, then at least the realization in a real laboratory setup introduces a vast amount of process noise and measurement errors. Thus, each physical quantity x obtained in the measurement process is considered as a *random variable*.

4.3.1 Concepts of Signal Ensembles

In order to provide statistical information about the measurement process it is necessary to introduce the concepts of the *system ensemble* and *signal ensemble*. In the following, the theoretical concept of the *ideal signal ensemble* is presented as well as the deduced concept of an *artificial signal ensemble*.

4.3.1.1 Ideal Signal Ensemble

A system ensemble describes a set of H equally realizations of the measurement process (cf. Fig. 4.7). Each member of that system ensemble is referred to as system realization or just member of the system ensemble. In theory, each of these H realizations generates simultaneously H individual signals $x_h(t)$ of the measurand $x(t)$. The set of H signals builds the ideal signal ensemble $\{x(t)\}$.
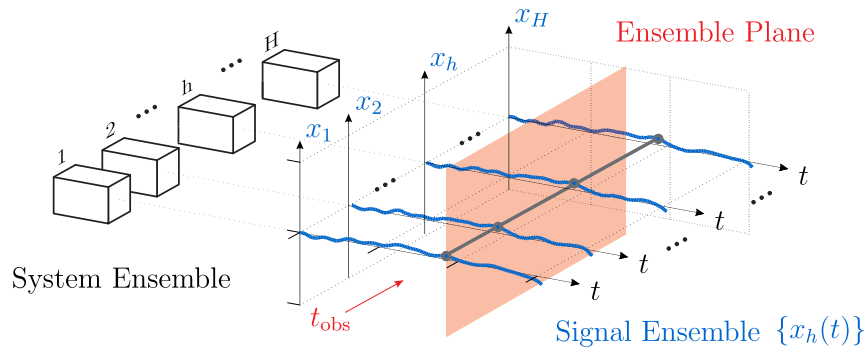
Figure 4.7: Concept of the ideal signal ensemble: A system ensemble of H equally realizations of the measurement process produces H individual signals $x_h(t)$ of the measurand $x(t)$. This set builds the ideal signal ensemble $\{x(t)\}$ that allows to estimate the statistical properties of $x(t)$ in the ensemble plane.

The signal ensemble is evaluated for each time of observation t_{obs} along the ensemble plane (cf. Fig. 4.7). Every continuous signal ensemble $\{x(t)\}$ is represented by an infinite number of random variables $x(t_{\text{obs}})$, which are described by their statistical properties. The presumed sampling process leads to a finite number of observations $x[n]$ at isochronal times $t = nT_{\text{s}}$,

59

with sampling period $T_{\mathrm{s}} = 1/f_{\mathrm{s}}$. The sampling process is assumed to be ideal, i.e. the acquired samples $x[n]$ are equivalent to the instantaneous value $x(nT_{\mathrm{s}})$ of the continuous signal $x(t)$ at the desired point in time $t = nT_{\mathrm{s}}$.

In the special case where all statistical properties of the signal ensemble are independent of time (constant), the signal ensemble is called stationary. For a stationary signal ensemble the result of the statistical evaluation along the ensemble plane is identically to the result of each individual signal. Thus, a single signal $x_h(t)$ can be used to describe the complete signal ensemble.

For experimental studies in LET it has to be assumed that due to the finite size of the UUT or the presence of defects the statistical properties, e.g. mean value of the force, will vary over time. Because of that, it is evident that a single signal $x_h(t)$ of any component of the Lorentz force can not provide a complete measurement result, i.e. expected value of the measurand $\mathbf{F}(t)$ and corresponding experimental standard deviation $\sigma_F(t)$.

4.3.1.2 Artificial Signal Ensemble

In practical applications it is not economically reasonable to build multiple realizations of the same measurement process. Nevertheless, to be able to obtain a good estimate of the statistical properties of the non-stationary signal ensemble, a series of multiple experiments is executed in order to build an artificial signal ensemble.

Figure 4.8 illustrates the concept of building an artificial signal ensemble. In contrast to the
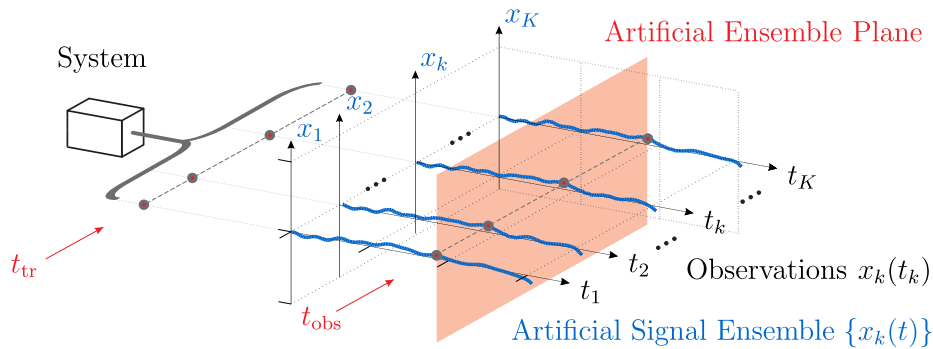
Figure 4.8: Concept of the artificial signal ensemble: A single system realization of the measurement process produces $K \geq H$ serially recorded signals $x_k(t_k)$. The artificial signal ensemble $\{x_k(t)\}$ is created by aligning the individual signals $x_k(t_k)$ according to a trigger time t_{tr}, which allows to estimate the statistical properties of $x(t)$ in the artificial ensemble plane.

ideal signal ensemble $\{x_h(t)\}$, a set of $K \geq H$ experiments is performed on a single realization of the experimental setup. Afterwards, the individual signals $x_k(t_k)$ have to be aligned according to a virtual trigger time t_{tr} which is a representative point in time for the non-stationary signal ensemble $\{x_k(t)\}$. The resulting set of serially recorded signals $x_k(t_k)$ is merged to an artificial signal ensemble $\{x_k(t)\}$ on which all statistical evaluations can be carried out. Additionally to the ideal signal ensemble $\{x_h(t)\}$ one important requirement has to be fulfilled to obtain

representative statistical information from the artificial signal ensemble $\{x_k(t)\}$. The boundary conditions for each signal $x_k(t_k)$ need to be equal, i.e. all influence parameters for the random process need to be *statistically independent*. Especially, it is important that every single experiment is not influenced by any previously performed experiment.

The task of digital signal processing for LET is to create such an artificial signal ensemble and to provide an estimate of statistical properties of non-stationary signals. The requirement of statistically independence can only be a hypothesis.

4.3.2 Basics of Signal Alignment

For the alignment of recorded signals $x_k(t_k)$, a trigger time t_{tr} corresponding to a relative position of UUT and PM has to be defined. The reliability of trigger time determination is crucial for signal alignment since it has direct impact on the expectation value and other statistical properties of the ensemble.

4.3.2.1 Signal Alignment Based on External Trigger Signals

One way to define a trigger time is to detect the presence of the UUT by means of an proximity sensor. This sensor would preferably be based on a measurement principle which is invariant to the investigated electromagnetic properties of the UUT.

In the experimental setup described above, the incremental position encoder could provide this functionality under the following two assumptions. First, the position deviation between UUT and the slide of the linear drive is small, relative to the measurement uncertainty of the incremental position encoder. Second, the relative position of linear drive and measurement frame is fixed, i.e. it does not vary between experiments.

While the first assumption is ensured by the redesigned clamping mechanism (cf. Fig. 4.3), the latter is not fulfilled since the position of the measurement frame can vary between experiments in the case of maintenance and preparation work, e.g. exchange of the PM. Furthermore, the linear scale used is too short and therefore had to be equipped with magnetic triggers as reference marks for the encoder. Reliability tests revealed clear weaknesses in the reproducibility of such a triggering function, resulting in varying absolute position measurements.

An additional external trigger, mounted on the measurement frame has not been implemented. Thus, a signal alignment based on external trigger signals is insufficient for the used experimental setup.

4.3.2.2 Correlation of Time-Continuous Signals

Another possibility to define a trigger time t_{tr}, is to search for repeating patterns in the signals and to align the signals according to the closest match. The most common mathematical tool to find the best match for time-lagged signals is the cross-correlation function $\rho_{XY}(\tau)$.

Let (X_t, Y_t) be two stochastic processes that are jointly wide-sense stationary [32], then

$$\rho_{XY}(\tau) = \frac{\mathrm{E}[(X_t - \mu_X)(Y_{t+\tau} - \mu_Y)]}{\sigma_X \sigma_Y}, \tag{4.12}$$

where E is the expected value operator, $\mu_{X,Y}$ are the mean values, $\sigma^2_{X,Y}$ are the variances of the random processes, and τ is the time-lag between the signals. The value of $\rho_{XY}(\tau)$ lies in the range $[-1, +1]$, with -1 indicating complete anti-correlation and $+1$ indicating complete correlation of analyzed signals. The estimated time delay between signals is determined by

$$\tau_{\mathrm{est}} = \arg\max_{\tau} \rho_{XY}(\tau). \tag{4.13}$$

The necessary condition to apply this method is the presence of significant patterns in these signals. Since the used ADC guarantees a quasi-simultaneous sampling of all recorded signals, a single signal can serve for the time delay estimation. To test signals for repeating patterns, it is useful to have a look on typical signals and their corresponding auto-correlation function $\rho_{XX}(\tau)$. Since all measured signals are real valued $X_t \in \mathbb{R}$, the following discussion is restricted only to the auto-correlation function of real valued signals.

The auto-correlation function $\rho_{XX}(\tau)$ of a wide-sense stationary random process X_t is defined as

$$\rho_{XX}(\tau) = \frac{\mathrm{E}[(X_t - \mu)\,(X_{t+\tau} - \mu)]}{\sigma^2}, \tag{4.14}$$

with μ the mean value, σ^2 the variances of the random process, and τ the time-lag between the signals.

In most practical cases, as well as in the discussed problem, neither μ nor σ^2 of the respective signal ensemble are known. Thus, the above definition is often used without standardization, i.e. without subtracting the mean and dividing by the variance

$$R_{XX}(\tau) = \mathrm{E}[X_t\, X_{t+\tau}], \tag{4.15}$$

which to be more exact is the auto-covariance without mean centering. In the following, the term auto-correlation function refers to definition (4.15) which is most common in physics and engineering. The advantage of this definition is its validity also for non-stationary processes, as in the discussed case. However, it lacks the possibility to compare different physical quantities since the resulting product of the involved units is without any physical meaning.

4.3.2.3 Correlation of Time-Discrete Signals

So far, only time-continuous processes are considered. In order to deal with digitized signals, it is necessary to extend the definition previous definitions to time-discrete signals. The calculation of the time-discrete auto-correlation function is based on the *Wiener-Khinchin theorem* [23]. It describes how the auto-correlation function of a wide-sense-stationary random process has a spectral decomposition given by the *power spectral density* (PSD) of that process.

The auto-correlation of a time-discrete function $x(n)$ of length N is computed in two steps. Firstly, the *discrete Fourier transform* (DFT) of $x(n)$ is computed as

$$X(k) = \sum_{n=1}^{N} x(n) \exp\left(\frac{-\text{j}2\pi(k-1)\,(n-1)}{N}\right),$$

(4.16)

with $1 \le k \le N$. Secondly, by making use of *Parseval's theorem* the inverse DFT of the PSD, i.e. squared absolute value $|X(k)|^2$, is calculated to

$$c(n) = \frac{1}{N} \sum_{k=1}^{N} X(k) \exp\left(\frac{\text{j}2\pi(k-1)\,(n-1)}{N}\right),$$

(4.17)

with $1 \le n \le N$.

$$\tau = \{-1\ldots+1\}\frac{N-1}{f_\text{s}} \qquad \text{and} \qquad R_{ii} = \frac{c_i}{N},$$

(4.18)

The computation via Fourier transform and the inverse transform is implemented by using the MATLAB™ function xcorr [81]. In the representation shown, the time-lag τ is divided by the sampling frequency f_s of the signal to be invariant on this quantity.

4.3.3 Auto-Correlation on Typical Force Signals

In order to test if the measured signal does fulfill the described requirements, a typical result of an experiment is discussed. Figure 4.9 shows representative signals of the three components of the measured force $F_i(t)$ and the corresponding autocorrelation $R_{ii}(\tau)$ with $i \in \{x, y, z\}$. The respective signals are part of the experimental study presented in Section 4.5.1.

Figure 4.9(a) shows three components of the measured force $F_i(t)$ which are normalized to the mean value of the force plateau in the x-component $F_{x0}(t)$ plotted against a dimensionless time

$$\tilde{t} = \frac{t}{t_c} = \frac{t\,\bar{v}}{L_x} \,,$$

(4.19)

with $\bar{v}$ the mean value of the velocity and L_x the length of the UUT in x-direction. The chosen characteristic time t_c for this representation is the time it takes for the UUT to pass the center of the PM. The time count starts when the first edge of the UUT passes the center of the PM.

In this normalized representation, important features of the typical force signals can be observed. The x-component of the measured force $F_x(t)$ is the dominant component and has square-wave-like shape. At $\tilde{t} = 0$ and $\tilde{t} = 1$ the force component has reached approximately 50% of its maximum which could be observed in all experimental studies including a non-ferromagnetic UUT. The y- and z-component of the measured force $F_y(t)$ and $F_z(t)$ show significant peaks near the edges of the UUT and a decreased, nearly constant, plateau in between. When the PM is almost completely covered by the UUT (near the UUT edges), then the absolute value of the peak of $F_y(t)$ and $F_z(t)$ becomes maximal. The force at $\tilde{t} \approx 0.1$ is in the opposite direction in comparison to $\tilde{t} \approx 1 - 0.1$, for both components.

(a)   (b)
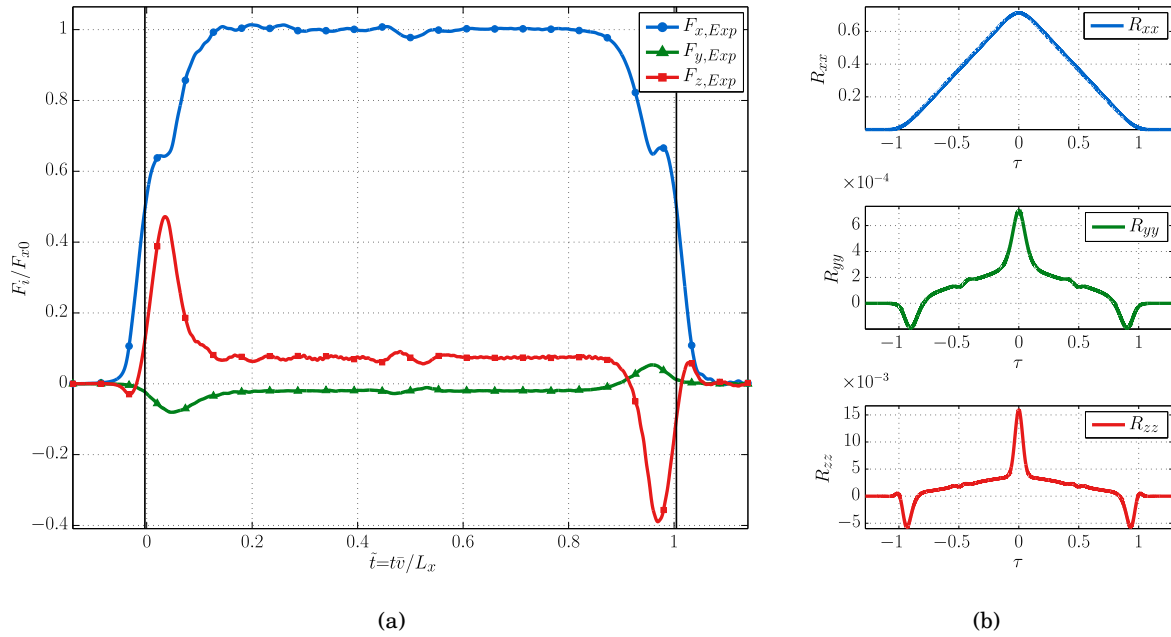
Figure 4.9: Representative signals of the three components of the measured force $F_i(t)$ normalized to $\max\!\big(F_x(t)\big)$: (a) force signals and (b) auto-correlation function $R_{ii}(\tau)$ of each component.

Figure 4.9(b) shows the dimensionless auto-correlation function corresponding to the normalized force components $F_i(t)$ plotted against the dimensionless time-lag τ. As expected from the convolution of a rectangular function, the auto-correlation of the x-component $R_{xx}(\tau)$ is very similar to the triangular function with its maximum at zero lag $\tau = 0$. The auto-correlation function of the y- and z-components, $R_{yy}(\tau)$ and $R_{zz}(\tau)$, are very similar in shape. Due to similar peaks but in opposite directions, the auto-correlation shows negative correlation at $\tau \approx -0.9$ and $\tau \approx +0.9$, and a very sharp peak at $\tau = 0$ for both components.

It is important to mention that due to the performed normalization of the measured signals and the use of a characteristic time scale, the presented auto-correlation plots are representative in shape and magnitude for most studied experiments. All three components of the measured force are real valued, thus the auto-correlation function must be symmetric. According to Parseval's theorem, the auto-correlation function $R_{ii}(0)$ at zero lag $\tau = 0$ corresponds to the total power of the respective signal.

It is shown that all components do fulfill the described requirements and are therefore suitable for estimating the individual time-lags, but not all signals are equally appropriate. $R_{yy}(\tau)$ and $R_{zz}(\tau)$ clearly show a narrow peak at $\tau \approx 0$, but the total signal power of $R_{xx}(\tau)$ is two to three orders of magnitude higher. Under the assumption of a similar noise power for the non-ideal measurement process, it is evident that the force component with the largest signal power provides the most reliable estimate for the time delay τ_{est} between two members of the artificial signal ensemble. In conclusion it becomes clear that the x-component of the force is the most reliable source of information for the assembling of an artificial signal ensemble of similar

experiments from multiple instances. Therefore the cross-correlation of the x-components is used in order to estimate the time-lag between the signals and to allow statistical analysis on the non-ideal measurement process.

4.3.4 Program Flowchart for DSP

In the previous sections the basic concept of DSP in LET is defined and the mathematical methods for the efficient computation are explained. In the following an overview of all computations necessary to obtain a complete measurement result is given. This completes the description of the measurement method (cf. Sec. 4.1.2) and allows to repeat all experimental studies presented in this thesis. Figure 4.10 shows the flowchart of DSP used in LET for the assembling of an artificial signal ensemble of sequential measurements.
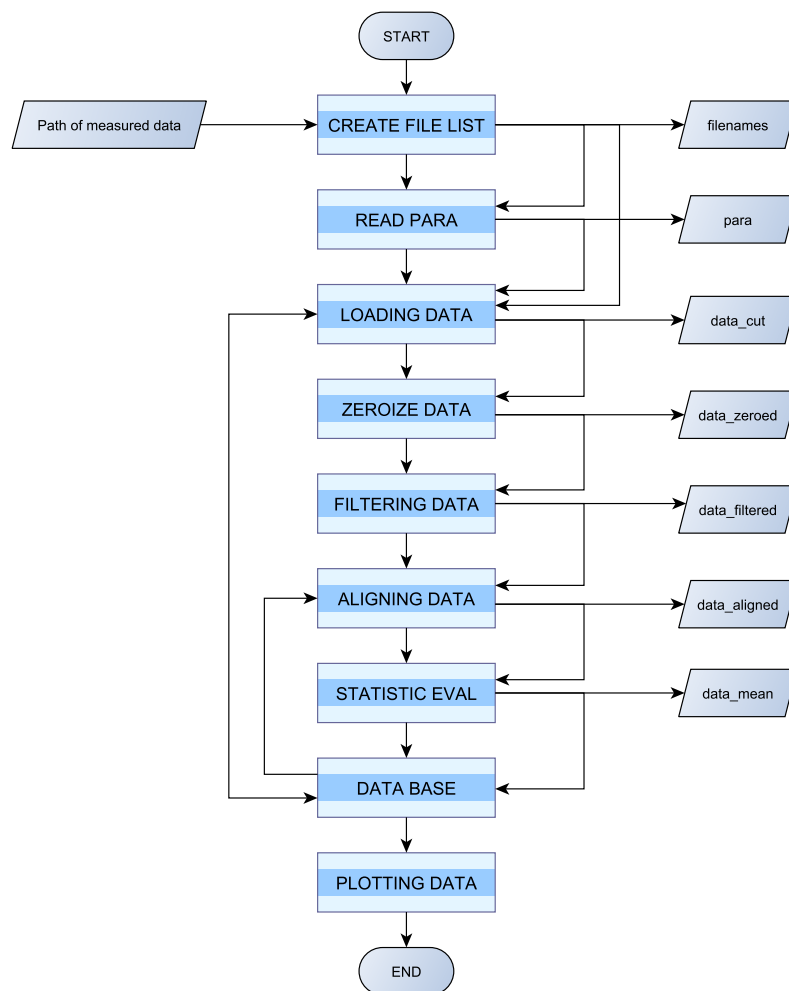
Figure 4.10: Flowchart of DSP applied in LET.

4.3.4.1 Loading data

In the first step, a file list with observations is created that are members of the artificial signal ensemble $\{x_k(t)\}$. Next, the data base is analyzed for experimental parameters (*ensemble parameters*) of each chosen observation, including all known information about geometry, relative position of the PM, and calibration data of the used sensors (cf. Sec. 4.2). Having ensemble parameters, the respective data files are loaded and tested for consistence, e.g. equal number of recorded channels. The observation files contain ASCII-delimited numeric data of the simultaneously sampled sensor output given in Volt, with exception of the data output of the incremental position encoder, which is stored in millimeters.

4.3.4.2 Static offset correction and tailoring

The next step combines (a) static offset correction, (b) sensor output conversion, and (c) tailoring to region of interest (ROI) which results in the *uncorrected result of measurement*.

The *static offset correction* is performed for each signal, except the incremental position encoder signal. It corrects insufficient offset nulling that is performed before an experiment and long-term trends of the used electronic devices as they may arise by temperature drifts.

The *sensor output conversion* is the multiplication of the sensor output signals of force and acceleration sensors by the respective sensor calibration factors. These calibration factors are derived from sensor specific gain and sensitivities (cf. Sec. 4.2.3) and are stored in the ensemble parameters.

The size of a typical observation file with signals of $5\,\mathrm{s}$ duration is about 5.5 MB and includes on average less than 15 % of relevant data where the UUT leads to a significant change in the measured force. In order to reduce computing time, the *signal tailoring* reduces the amount of data to be processed to a region of interest that corresponds to the significant changes. The ROI is a multiple of the UUT's length L_x and is defined relative to the leading and trailing edge of the UUT. Considering findings from Sec. 4.3.3, the edges are estimated by 50 % of the maximum of the absolute value of the measured force. Having identified the edges, the ROI is defined by from N_{ext} samples before the leading edge to N_{ext} after the trailing edge, with $N_{\text{ext}} = f_{\text{s}}k_{\text{ext}}L_x/\bar{v}$, where k_{ext} is the extension factor. The next steps of the DSP are all executed on the uncorrected result of measurement $x_k(t_k)$ (truncated signals) from which the artificial signal ensemble $\{x_k(t)\}$ is built.

4.3.4.3 Filtering data

The observations $x_k(t_k)$ are superimposed with high frequency noise from multiple sources, e.g. analogue measurement amplifier of the force sensor (Sec.4.2.3). In order to improve the estimation of the cross-correlation function, the high frequency noise is reduced by means of a digital low-pass filter. Except for the incremental position encoder, a zero-phase digital filter [99] is applied using the MATLAB™ function `filtfilt`. The designed digital filter is a

Butterworth low-pass filter of 4th order with a cutoff frequency $f_c = 500$ Hz for the 3 dB point below the passband value. The filter is designed to have a maximally flat frequency response in the passband to minimize the distortion of the signals of interest.

4.3.4.4 Aligning data

The next step of DSP in LET is the alignment procedure which uses the x-component of the measured force $F_x(t)$ (Fig. 4.11). Two alignment procedures associated with different assumptions can be applied.
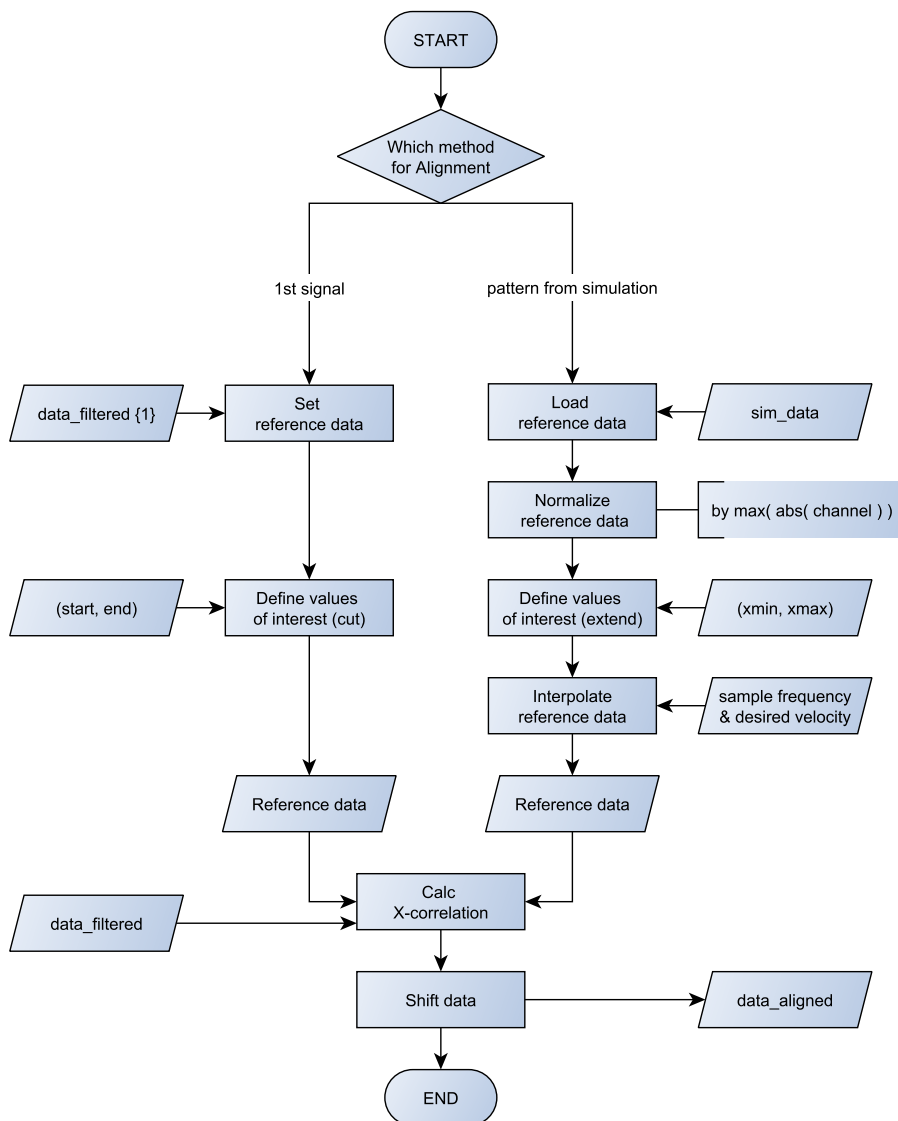
Figure 4.11: Flowchart of the aligning-data-block.

Arbitrary ensemble member as reference signal

The first procedure uses an arbitrary member of the artificial signal ensemble as the reference signal for the estimation of individual time-lags τ_i of remaining ensemble members. The advantage of this procedure is that it can be applied without additional knowledge about the characteristics of the particular signal ensemble $\{x_k(t)\}$. Thus, no information regarding the used PM or the shape and surface of the UUT are necessary. The procedure results in a well aligned artificial signal ensemble $\{x_k(t)\}$ if a significant pattern is included, i.e. the maximum of R_{ii} is an unbiased estimator of the time-lag τ_i. In order to increase the reliability of the alignment, the chosen reference signal can be pre-processed with additional digital filters to reduce impact of random disturbances. The main disadvantage of this approach is the missing possibility to properly define the range of the x-axis for the artificial signal ensemble $\{x_k(t)\}$ due to the insufficient realization for a trigger-based signal alignment (Sec. 4.3.2.1). As a rough approximation, the above-mentioned characteristic 50% threshold in the x-component of the measured force can be used.

QSA simulation as reference signal

The second alignment procedure uses for the estimation of individual time-lags results of numerical simulations as the reference signal that are performed for a similar experiment. For determining the force acting on the PM the finite element method (FEM) [156] with a quasi-stationary approach (QSA) [153] is used. The QSA approach delivers results close to the exact solution if the UUT has constant cross section and the leading and trailing edge are far away from the PM. The software package Comsol Multiphysics v4.4 [25] by *COMSOL, Inc.* is used in this framework. The FEM results used throughout this thesis are based on [145]. The further details on the applied numerical methods can be found in [145, 153, 157].

This alignment procedure has two major advantages. Firstly, the reference signal is free of any kind of noise and distortions, which, most likely, leads to an increased reliability of the alignment. Secondly, it provides a properly defined range of x-axis for the artificial signal ensemble $\{x_k(t)\}$. This x-axis range can be used as a global reference for the entire artificial signal ensemble and thus eliminates the need of using the external position measuring system. It should be mentioned that the evaluation of recorded incremental position encoder signals has shown non-equidistant steps, which results in position variations of individual observations, as well as the corresponding velocity of the UUT. If the x-axis range from the simulation is used, these variations are neglected. Therefore, the measured incremental positions are retained during the whole DSP. As it can be seen later, this information will expose the velocity $v(t)$ as one of the significant sources of distortion and will provide important hints on the validity of the assumption about statistical independence of the successive experiments.

The major disadvantage of this procedure is the necessity of using "suitable results" from numerical simulations, whereas no clear definition of "suitable" can be provided. Besides comparable geometries, it is not evident, what kind of deviations are acceptable for a robust

alignment procedure. It is shown in Chapter 3 that the remanence B_{r} does not affect the electromagnetic similarity, i.e. it can be considered as a scaling factor of the second power for the generated force components. Because τ_{est} in (4.13) is invariant to the magnitude of the correlated signals, it is evident that τ_{est} is invariant to B_{r}. Furthermore, the product σv is expected to have only marginal influence on the characteristic shape of the Lorentz force signal for low R_m, thus τ_{est} of the x-component of the Lorentz force might also be invariant under these conditions. All other parameters, e.g. permeability of the PM or anisotropy of the UUTs conductivity, are expected to have an influence on the characteristic shape of the x-component of the Lorentz force and as they are not known precisely, no prediction on the general robustness of the procedure can be given. However, it can be seen later (Sec. 4.4.2) that the alignment procedure is robust even for UUT of slightly permeable material.

The step of signal alignment results in the artificial signal ensemble $\{x_k(t)\}$, which is reduced to the ROI and is low-pass filtered to be more suitable for interpretation. The sets of signals are stored in the data base and are available for statistic evaluation of the signal ensemble. All measurement results shown in this thesis are aligned by using results of numerical simulations as the reference signal.

4.3.4.5 Statistic evaluation of the signal ensemble

Having defined the artificial signal ensemble $\{x_k(t)\}$, it is possible to calculate an estimate of the statistical properties of the non-stationary signal along the ensemble plane (cf. Fig. 4.8). According to the International Organization for Standardization (ISO) *Guide to the Expression of Uncertainty in Measurements* [59] it is recommended to use classical (frequentist) statistics [37,38] for the evaluation of uncertainty from measurements (*Type A*). The author is aware that this interpretation of the concept of probability contradicts *Bayesian statistics*. However, as shown by [65], in practice the results from classical statistics are almost equal to a consistent Bayesian approach.

The first statistical property of the non-stationary signal is the expected value $\bar{x}(t)$ of the measurand $x(t)$. For a series of K measurements the expected value is calculated as

$$\bar{x}(t) = \frac{1}{K} \sum_{k=1}^{K} x_k(t) \,, \tag{4.20}$$

where $x_k(t)$ denotes the kth observation.

The *experimental standard deviation* $s\big[x(t)\big]$ (sample standard deviation) is the most common quantity for characterizing the dispersion of the measurement result. It is given by

$$s\big[x(t)\big] = \frac{1}{\sqrt{K-1}} \sqrt{\sum_{k=1}^{K} \big[x_k(t) - \bar{x}(t)\big]^2} \,. \tag{4.21}$$

It is worth to mention that using Bessel's correction ($K-1$ instead of K in the denominator) s^2 is the *unbiased* estimator of the population variance while its positive square root s is a *biased*

estimator of the population standard deviation. This bias can be significant for small numbers of observations K and thus has to be considered in the DOE.

In order to estimate the standard deviation of the distribution of $\bar{x}(t)$, the *experimental standard deviation of the mean* (eSDM) is defined as

$$u\left[\bar{x}(t)\right] = s\left[\bar{x}(t)\right] = \frac{s\left[x(t)\right]}{\sqrt{K}} \tag{4.22}$$

also termed *standard uncertainty* [59].

The set of signals and basic statistic properties are stored in the data base, together with the underlying reference signal and a log file including important parameters of the DSP, e.g. parameters of applied filters.

The last function block of the DSP is the plotting procedure, which is a problem specific task adapted for each individual investigation.

4.4 Applications without Defect

In this section, a representative overview of the measurement performance of the described experimental setup is given for applications without defect. Two studies are performed on defect-free monolithic UUTs. The first UUT is made of aluminum and the second is made of stainless steel. The results illustrate the principal features in the signals recorded with the developed sensor system (cf. Sec. 4.2.3). Furthermore, the two studies enable to verify the overall performance of the DSP in LET and its robustness for distinctly different signal shapes. Specifically, the studies demonstrate the sufficiency of the alignment procedure and support the assumptions made for artificial signal ensembles $\{x_k(t)\}$.

4.4.1 Monolithic Aluminum Bar

The first UUT is a monolithic aluminum bar with size $250\,\text{mm} \times 50\,\text{mm} \times 50\,\text{mm}$. It has an isotropic electrical conductivity $\bar{\sigma} \pm 2u(\bar{\sigma}) = (20.0 \pm 0.15)\,\text{MS/m}$ at $20\,°\text{C}$, which is determined using an ECT device Elotest N300 [124] by *Rohmann GmbH*. The used PM is of cylindrical shape with diameter $D = 22.5\,\text{mm}$ and height $H = 17.6\,\text{mm}$. It is axially magnetized and the nominal magnetic remanence provided by the manufacturer is $B_{\text{r,N}} = 1.43\,\text{T}$.

Figure 4.12 shows a technical drawing (a) of the UUT and a picture (b) of the UUT mounted on the slide of the linear drive. The UUT is oriented in the longitudinal direction with respect to the direction of travel.

(a) Drawing of aluminum bar   (b) Fully assembled UUT
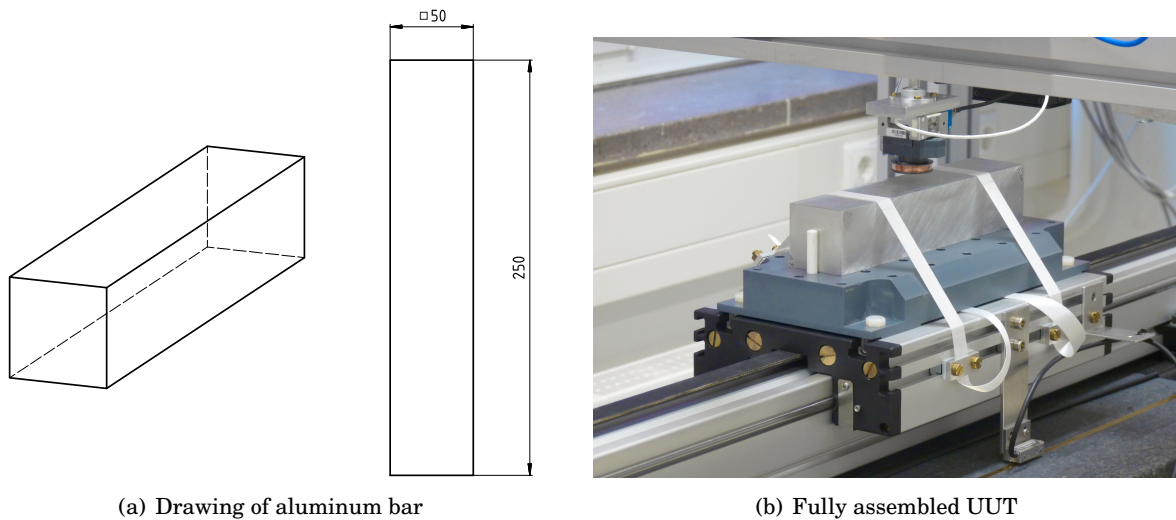
Figure 4.12: Technical drawing (a) and a photograph (b) of the aluminum bar mounted on the slide of the linear drive.

Design of experiment

The experimental study consists of repeated observations at different y-positions of the UUT. This collection of observations forms a *scan* from $y_{\text{min}} = -30.00\,\text{mm}$ to $y_{\text{max}} = 30.00\,\text{mm}$ at steps

Table 4.1: Parameters of the experimental study of a monolithic aluminum bar*.

Parameter		Value	Unit	Description
DOE	K	5		Number of repeated observations
	v	0.50	m/s	Velocity of the UUT
	h	1.00	mm	Lift-off distance
	y_{max}	30.00	mm	Maximum y-position of the PM
	y_{min}	−30.00	mm	Minimum y-position of the PM
	Δy	1.00	mm	Step size of the scan
UUT	σ	20.0	MS/m	Electrical conductivity
	μ_{r}	1		Relative permeability
	l_X	250.0	mm	Length of the UUT
	l_Y	50.0	mm	Width of the UUT
	l_Z	50.0	mm	Height of the UUT
PM	$B_{\text{r,N}}$	1.43	T	Nominal remanence
	D	22.5	mm	Diameter of the PM
	H	17.6	mm	Height of the PM

*Values rounded to significant figures with respect to the standard deviation.

of $\Delta y = 1.00\,\text{mm}$. Each measurement is performed $K = 5$ times with exception of the *centerline* of the UUT ($y = 0.00\,\text{mm}$), where $K_{y=0} = 25$ times. Thus, it is possible to compare the experimental standard deviations of two different ensemble sizes K of the biased estimator. Each of K observations is used to build the artificial signal ensemble $\{x_k(t)\}$ for a particular value of y. All parameters of the experimental study of the monolithic aluminum bar are summarized in Table 4.1.

In addition to the overall purpose of the experimental studies described above, this particular study serves as a reference experiment for the presented realization of the measurement method of LET.

Result of the force measurement $\mathbf{F}(t)$

Figure 4.13 shows the measurement result of the force $\mathbf{F}(t) = \left[F_x(t), F_y(t), F_z(t)\right]^{\text{T}}$ for the monolithic aluminum bar. The three surface-plots show the expected value of the respective force component $\bar{F}_i(t)$, where $i \in \{x, y, z\}$. The black curves in each plot show a complete measurement result as the estimate of the 95%-confidence interval $\left[\bar{F}_i(t) \pm 2u\left(\bar{F}_i(t)\right)\right]$ for selected experiments with $\Delta y = 5\,\text{mm}$. This data is plotted against y, the lateral position of the PM, and the expected value $\bar{x}(t)$ of the centered position of the slide of the linear drive, based on the records delivered by the incremental encoder. The positive x-positions are sampled first in time. For an improved representation of the measurement result, the *plotting data*-block of the DSP (cf. Fig. 3.2) has been extended by a digital Butterworth low-pass filter of order 6 with cutoff frequency $f_c = 70$ Hz. The applied filter reduces the magnitude of significant periodic disturbances in the recorded force and improves the interpretation for the purpose of this study. The variations
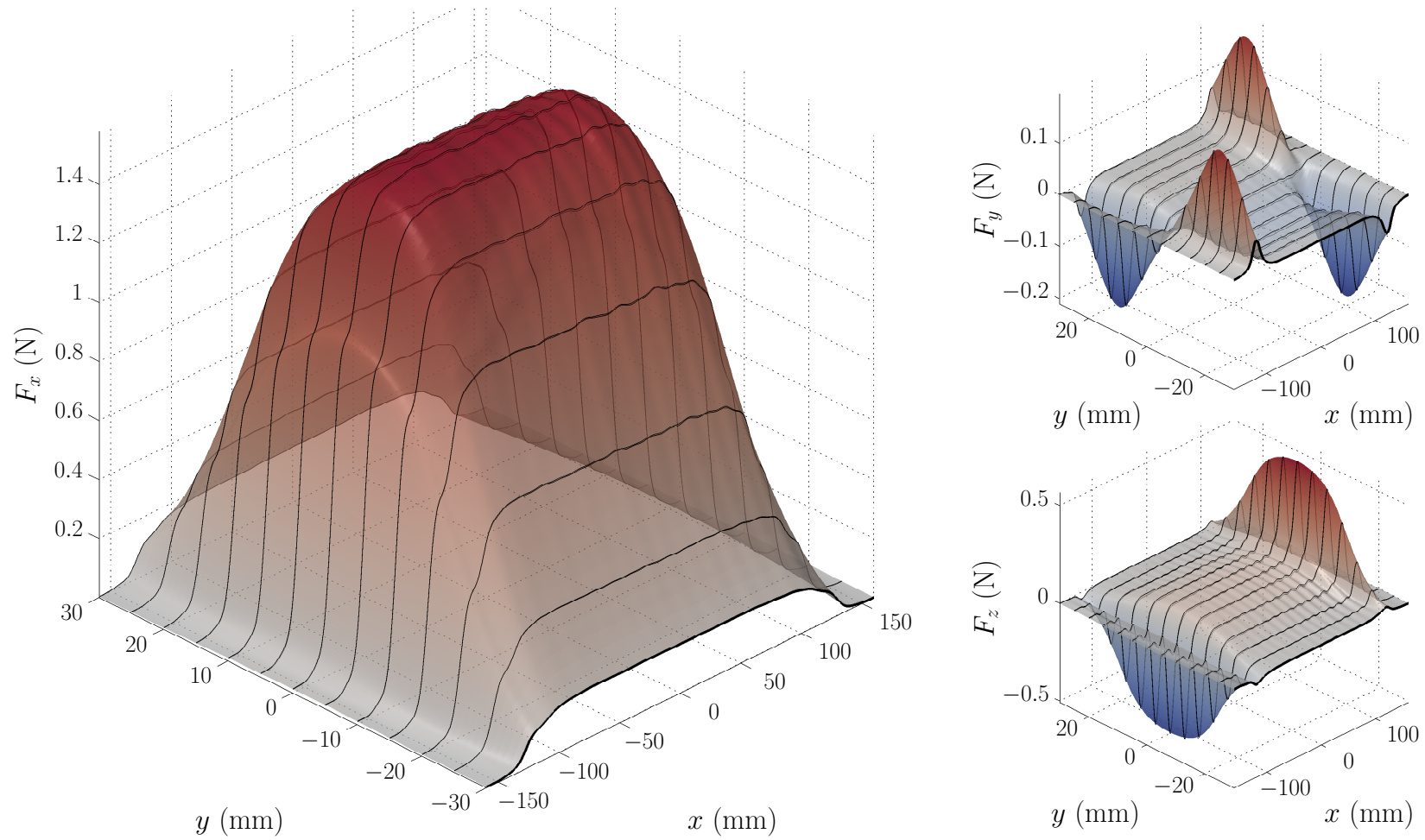
Figure 4.13: Measurement result of the force $\mathbf{F}(t)$ for the monolithic aluminum bar. The surface-plots show the expected value of the measurand $\bar{F}_i(t)$. The black curves show the complete measurement result as the estimate of the 95 %-confidence interval $\left[\bar{F}_i(t) \pm 2u\big(\bar{F}_i(t)\big)\right]$ for selected experiments with $\Delta y = 5\,\text{mm}$.

in the recorded force spectrum are further analyzed in in Chapter 5, where the mechanical modeling of the experimental setup is described.

In order to improve the perception for the sign of the shown force component as well as its magnitude, a bipolar color progression (blue-to-red) with equal intervals is chosen for the surface-plots. Furthermore, the sign of the estimate of partial derivative of the respective component in x-direction is mapped on the colored surface-plots, in order to improve the perception of perturbations and oscillations. This technique, known as 'hill shading' [48], is implemented by calculating the hypothetical illumination of the surface by a hypothetical light source for each surface element in relation to neighboring elements in x-direction. For reasons of consistency, this technique will be applied for all future shown surface-plots. It becomes particularly useful in the analysis of defect response signals (cf. Section 4.5).

The presented results show that the alignment procedure works very well. Every single (artificial) signal ensemble is characterized by a very narrow estimate of the 95%-confidence interval, which is barely visible relative to the expected value of the measurand $\bar{F}_i(t)$. This very low relative experimental standard deviation implies two things. First, the result suggests a negligible influence of random disturbances in the lower frequency domain below $f_c = 70\,\text{Hz}$, which also supports the high repeatability of the automated measurement procedure, as claimed in Section 4.1.2 and 4.2.4. Second, the alignment procedure is able to calculate a reliable estimate of the individual time delays $\tau_{\text{est},k}$, which leads to the robust alignment of successive experiments.

In addition, it is shown that the application of the introduced alignment procedure enables to align experiments at different lateral positions y, even in the case when the reference signal only gives a prediction of the centerline results. The reason for this is the mirror-symmetry of the x-component of the measured force $F_x(t)$ and the invariance of the estimated time delay τ_{est} of the cross-correlation function $R_{xx}(\tau)$ on the magnitude of the correlated functions. It should be noted that a similar result can be obtained for using $F_z(t)$, but it is necessary to modify the alignment procedure when using $F_y(t)$. In the latter case, the maximum absolute value $|R_{yy}(\tau)|$ will provide an adequate estimate of the time delay τ_{est}. However, the x-component of the measured force $F_x(t)$ was observed to be the most reliable source of information for the assembling of (artificial) signal ensemble, as stated in Section 4.3.3.

Result of the acceleration measurement $\mathbf{A}(t)$

Figure 4.14 shows the measurement result of the acceleration $\mathbf{A}(t) = \left[A_x(t), A_y(t), A_z(t)\right]^{\text{T}}$ for the monolithic aluminum bar. As in Fig. 4.13, the expected value of the respective acceleration component is represented by surface-plots of $\bar{A}_i(t)$. The black curves in each plot show a complete measurement result for selected experiments with $\Delta y = 5\,\text{mm}$. The post-processing procedure and the shown range of the x- and y-positions are equal to the previous visualizations used for the force measurement.

It should be mentioned again that in the experimental setup, the 3-axes accelerometer
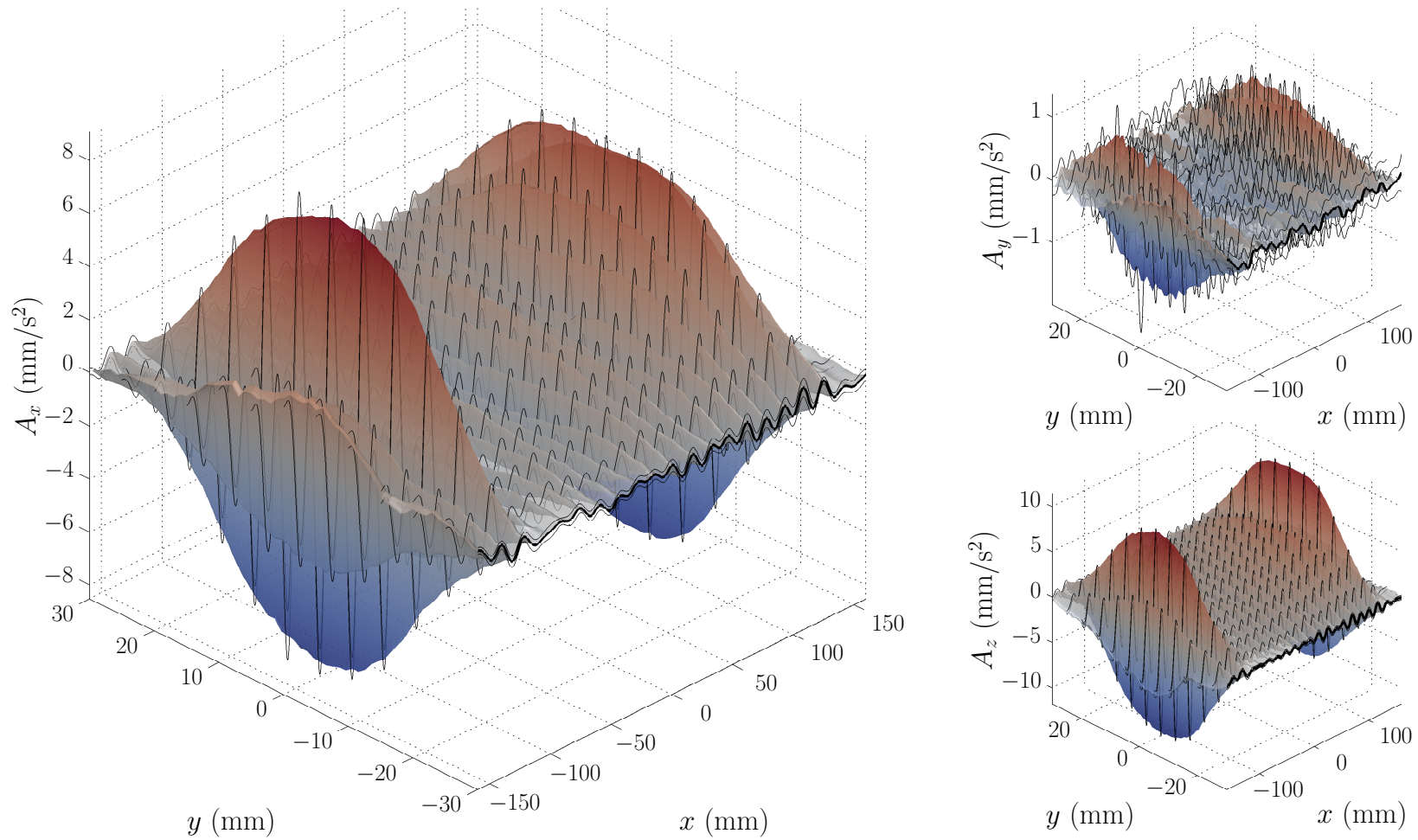
Figure 4.14: Measurement result of the acceleration $\mathbf{A}(t)$ for the monolithic aluminum bar. The surface-plots show the expected value of the measurand $\bar{A}_i(t)$. The black curves show the complete measurement result as the estimate of the 95%-confidence interval $\left[\bar{A}_i(t) \pm 2u\left(\bar{A}_i(t)\right)\right]$ for selected experiments with $\Delta y = 5\,\text{mm}$.

is mounted on the same plate as the 3-axes force sensor (cf. Fig. 4.5). Thus, the effect of the Lorentz force on the experimental setup becomes partially observable and should be interpreted accordingly.

The result of the acceleration $\mathbf{A}(t)$ measurement shows a significant response when the UUT passes the PM. The x- and z-component of the measured acceleration are in the range of $A_{x,z}(t) \approx \pm 10\,\text{mm/s}^2$, while $A_y(t)$ is approximately one order of magnitude smaller.

Taking a look at the confidence intervals, it becomes clear that for this particular setup the y-component of the acceleration is not significant and allows no reliable interpretation. This remains even valid for a significantly higher number of repetitions such as on the centerline.

However, the two main components $A_x(t)$ and $A_z(t)$ are characterized by a very narrow estimate of the 95%-confidence interval. This also confirms the reliability of the applied alignment procedure and gives reason to assume that the influence of random disturbances is negligible in the frequency domain below $f_c = 70$ Hz. A observation worth mentioning is that signals $A_x(t)$ and $A_z(t)$ are remarkably similar to each other and show the same change in magnitude for off-center positions, just as $F_x(t)$ and $F_z(t)$.

A deeper analysis of the interaction of the measured force and acceleration is part of the mechanical modeling in Chapter 5.

Result of the DiLET voltage measurement $V_z(t)$

Figure 4.15 shows the measurement result of the voltage $V_z(t)$ from the 1-axis DiLET sensor and its cumulative sum $\text{cusum}\big(V_z(t)\big)$ for the monolithic aluminum bar using a gain of $g_{\text{DF}} = 10$. The plot is created in the same way as described above. The measurement result of the induced

(a) $V_z(t)$ (b) $\text{cusum}\big(V_z(t)\big)$

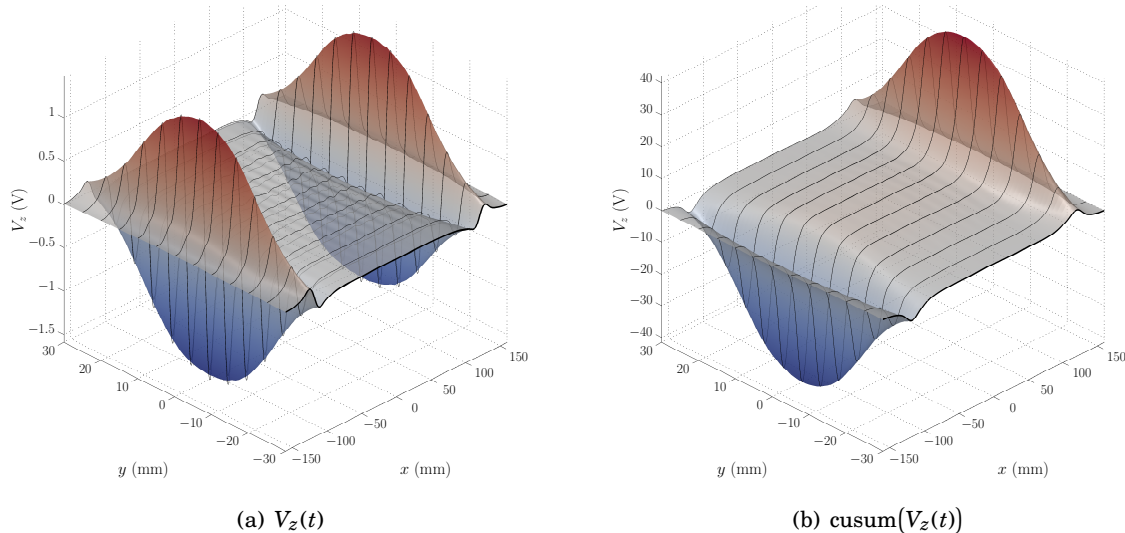Figure 4.15: Measurement result of the voltage $V_z(t)$ (a) and its cumulative sum $\text{cusum}\big(V_z(t)\big)$ (b) for the monolithic aluminum bar. The surface-plot show the expected value of the measurand $\bar{V}_z(t)$ and the corresponding its cumulative sum. The black curves show the complete measurement result as the estimate of the 95%-confidence intervals at $\Delta y = 5\,\text{mm}$.

voltage $V_z(t)$ shows significant changes at the leading and trailing edge of the UUT in the range of $V_z(t) \approx \pm 1\,\mathrm{V}$, which corresponds to an estimated effective variation of the magnetic flux density of $\partial B_{\mathrm{eff},z}(t)/\partial t \approx \pm 0.0349\,\mathrm{T/s}$. The induced voltage $V_z(t)$ in between is approximately equal to zero, with superimposed minor oscillations similar in appearance to the measured accelerations.

The cumulative sum of the induced voltage $V_z(t)$ is shown in order to compare the result with the measured force $F_z(t)$. As stated in [153], both signals are very similar to each other and differ seemingly only by a constant factor. However, a closer look to both signals reveals a systematic difference near the edges of the UUT as well as a slightly lower amplitude of the observed oscillations for $\mathrm{cusum}\big(V_z(t)\big)$.

Concluding remarks

The study of the monolithic aluminum bar shows complete measurement results of the force $\mathbf{F}(t)$, acceleration $\mathbf{A}(t)$, and induced voltage $V_z(t)$ recorded with the developed sensor system. The presented results illustrate the principal features of the obtained signals. The experiment serves as a reference for the presented realization of the measurement method for non-ferromagnetic UUTs with high isotropic electrical conductivity.

The study has been demonstrated that the applied alignment procedure allows to create artificial signal ensembles of the measured force $\mathbf{F}(t)$ for complete scans with very low relative standard deviation. This indicates a low impact of random disturbances in the low frequency domain and a high repeatability of the experiments. However, the observed accelerations revealed a significant response of the experimental setup to the acting Lorentz force which suggests a potentially corrupting effect on the observability of the Lorentz force.

To complete the investigation, some of the key values of the experimental study of a monolithic aluminum bar are summarized in Table 4.2.

Table 4.2: Results of the experimental study of a monolithic aluminum bar*.

Parameter		Value	Unit	y-position	
Force	$\max\big(F_x(t)\big)$	1.578	N	0.00	mm
	$\max\big(F_y(t)\big)$	0.211	N	-16.00	mm
	$\min\big(F_y(t)\big)$	-0.211	N	-16.00	mm
	$\max\big(F_z(t)\big)$	0.563	N	0.00	mm
	$\min\big(F_z(t)\big)$	-0.496	N	0.00	mm
Acceleration	$\max\big(|A_x(t)|\big)$	8.6	mm/s^2	-1.00	mm
	$\max\big(|A_y(t)|\big)$	1.0	mm/s^2	1.00	mm
	$\max\big(|A_z(t)|\big)$	11.4	mm/s^2	-1.00	mm
DiLET	$\max\big(V_z(t)\big)$	1.47	V	-1.00	mm
	$\min\big(V_z(t)\big)$	-1.54	V	0.00	mm

*Values rounded to significant figures with respect to the standard deviation.

4.4.2 Monolithic Stainless Steel Bar

The second UUT without defect is a monolithic stainless steel bar of the same size as the monolithic aluminum bar, i.e. $250\,\text{mm} \times 50\,\text{mm} \times 50\,\text{mm}$. The EN-standard steel name of the material according to the DIN EN 10027-2 is X5CrNi18-10 (1.4301) and is assigned to the group of chromium-nickel austenitic stainless steels. With about 30 % of global stainless steel production in 2015 [135], it is the most common stainless steel, and thus it is suitable as reference material for the evaluation of the LET measurement method for austenitic stainless steels. The relevant material properties are the relative permeability $\mu_{\text{N}r} \leq 1.3$ and the electrical conductivity $\sigma_{\text{N}} = 1.37\,\text{MS/m}$ at 20 °C, which are specified in the regarding EN-standard. The PM used in this study is a custom built cylindrical Halbach structure, which has been designed for detection of small subsurface defects [148]. The specific design of the PM as well as its magnetization is described in detail in [145].

Figure 4.16 shows a technical drawing (a) of the UUT and a picture (b) of the UUT mounted on the slide of the linear drive. The UUT is oriented in the longitudinal direction with respect to the direction of travel.

(a) Drawing of stainless steel bar   (b) Fully assembled UUT
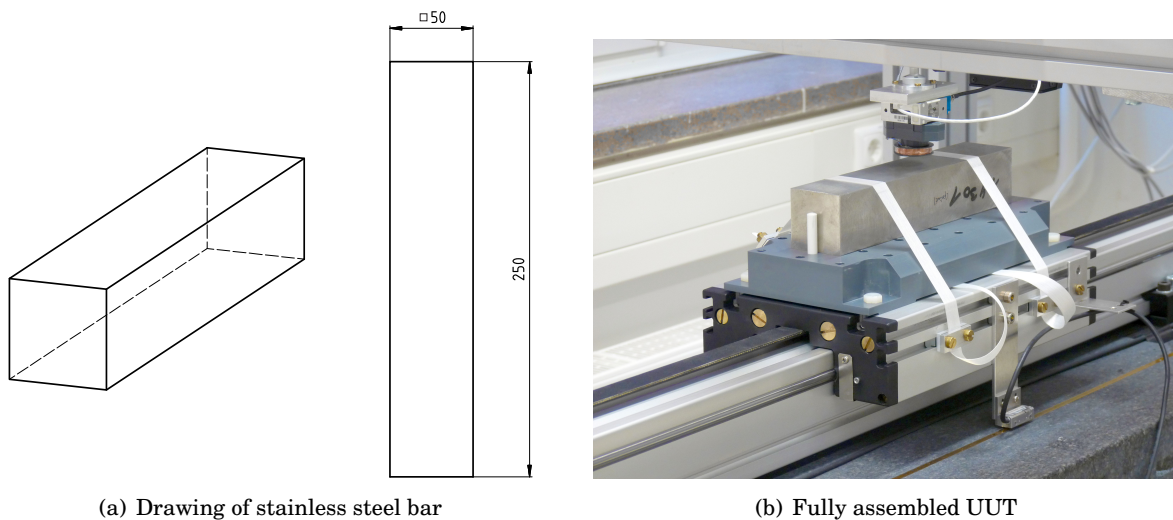
Figure 4.16: Technical drawing (a) and a photograph (b) of the mounted stainless steel bar.

Design of experiment

The experimental study consists of repeated observations at different y-positions of the UUT, very similar to the study of the monolithic aluminum bar. The scan goes from $y_{\text{min}} = -30.00\,\text{mm}$ to $y_{\text{max}} = 30.00\,\text{mm}$ at steps of $\Delta y = 2.00\,\text{mm}$. Each measurement is performed $K = 5$ times with exception to the centerline ($K_{y=0} = 25$) in order to compare the experimental standard deviation for two different ensemble sizes K of the biased estimator. All parameters used in the experimental study of a monolithic stainless steel bar are summarized in Table 4.3. The main purpose of this study is to examine, if the implemented procedures in the DSP are capable

Table 4.3: Parameters of the experimental study of a monolithic stainless steel bar*.

Parameter		Value	Unit	Description
DOE	K	5		Number of repeated observations
	v	0.50	m/s	Velocity of the UUT
	h	2.00	mm	Lift-off distance
	y_{max}	30.00	mm	Maximum y-position of the PM
	y_{min}	−30.00	mm	Minimum y-position of the PM
	Δy	2.00	mm	Step size of the scan
UUT	σ_N	1.37	MS/m	Nominal electrical conductivity
	$\mu_{r,N}$	1.3		Nominal relative permeability
	l_X	250.0	mm	Length of the UUT
	l_Y	50.0	mm	Width of the UUT
	l_Z	50.0	mm	Height of the UUT

*Values rounded to significant figures with respect to the standard deviation.

to achieve good aligned results even with significantly different signals. Therefore, a study is presented where UUT and PM differ significantly in comparison to the first study by means of geometry and electromagnetic properties.

Preliminary studies have shown that a significant attractive force occurs between PM and UUT due to the relative permeability $\mu_r > 1$ of the latter. This attractive force was observed to be above 1N at 1.00mm lift-off distance in the static case (without relative motion). To prevent critical dynamic loads which can overload the 3-axes force sensor, the lift-off distance was increase to $h = 2.00$mm. Furthermore it was observed that the attractive force noticeably differed at the different sides of the UUT, which suggests the magnetic *inhomogeneity* of the UUT. In addition to the main purpose, this study serves as a reference experiment for slightly ferromagnetic UUT with moderate electrical conductivity.

Result of the force measurement F(t)

Figure 4.17 shows the measurement result of the force $\mathbf{F}(t) = \left[F_x(t), F_y(t), F_z(t)\right]^{\mathrm{T}}$ for the monolithic stainless steel bar. As in the previous study (cf. 4.4.1), the expected value of the respective force component is represented by surface-plots of $\bar{F}_i(t)$. The black curves in each plot show a complete measurement result of selected experiments with $\Delta y = 6$mm. The post-processing procedure and the shown range of the x- and y-positions are the same, as in the previous study.

Based on the results shown it is clear that the permeability of the UUT alters the measured force signals significantly in comparison to the non-ferromagnetic aluminum bar.

Depending on the PM position, different distortions caused by the attraction force can be observed for the three components of the measured force. $F_x(t)$ shows a considerable distortion primarily at the edges of the UUT, while $F_y(t)$ and $F_z(t)$ show nearly no similarity with the non-ferromagnetic reference experiment. More specifically, $F_x(t)$ becomes negative when the UUT

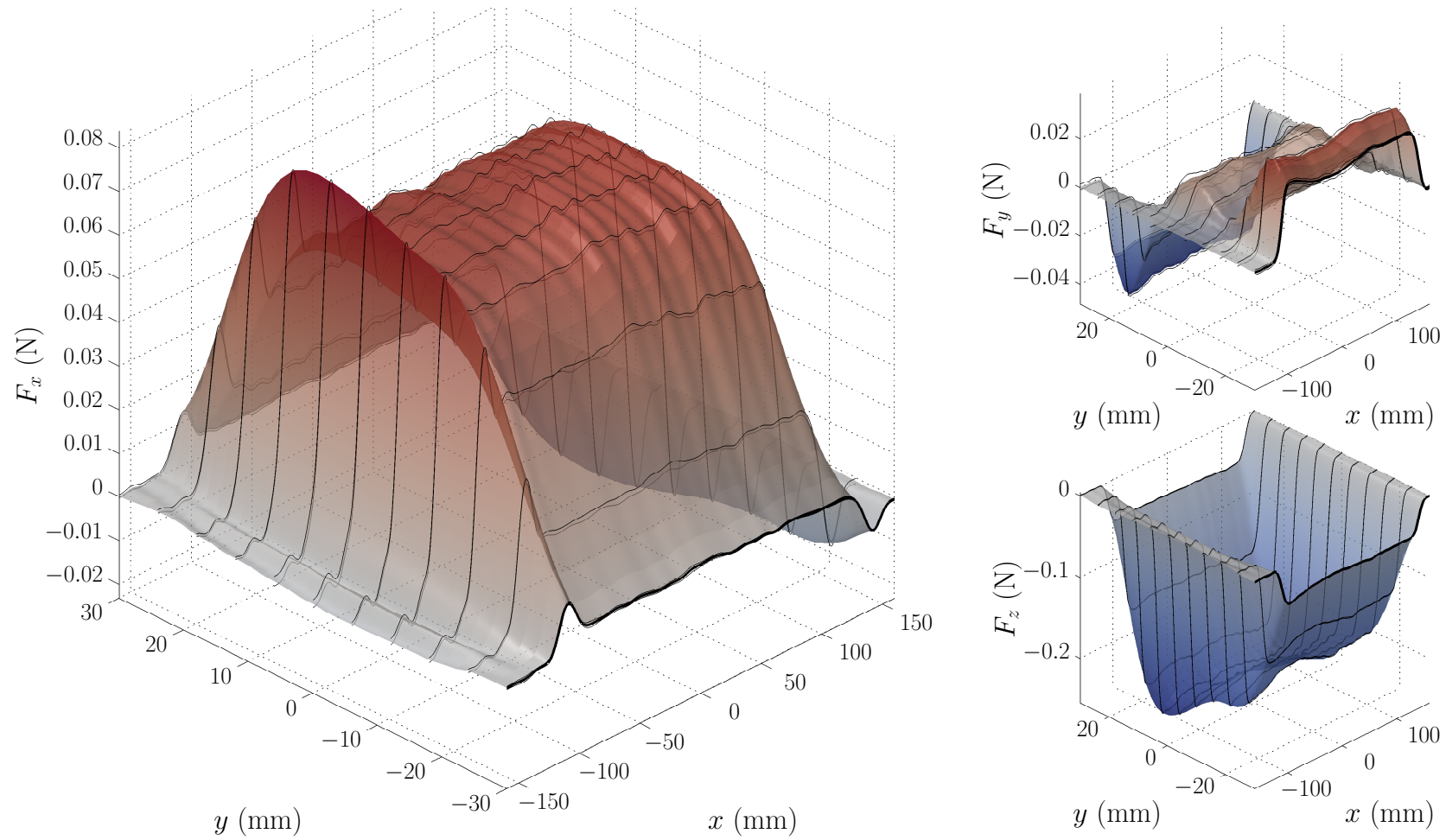Figure 4.17: Measurement result of the force $\mathbf{F}(t)$ for the monolithic stainless steel bar. The surface-plots show the expected value of the measurand $\bar{F}_i(t)$. The black curves show the complete measurement result as the estimate of the 95 %-confidence interval $\left[\bar{F}_i(t) \pm 2u\left(\bar{F}_i(t)\right)\right]$ for selected experiments with $\Delta y = 6\,\text{mm}$, starting from $y = 0\,\text{mm}$.

approaches the PM (attraction in negative x-direction) and positive when the UUT departs from the PM (attraction in positive x-direction). The y- and z-component, however, show a continuous attraction force along the whole UUT. Furthermore, the absolute value of the attraction force increases significantly with increasing y-position, what correlates with the noticed magnetic inhomogeneity of the investigated material.

A surprising fact is that $F_y(t)$ is not only asymmetric with respect to the centerline, but also has a local maximum along the x-direction at $y = 0\,\text{mm}$ which complicates an easy interpretation. In the subsequent additional investigation it was found that at low velocities, e.g. $v = 0.10\,\text{m/s}$, exactly the same force in y- and z-direction is measured as for $v = 0.50\,\text{m/s}$. Only the x-component had a decreasing magnitude between the leading and trailing edge of the UUT. It can be concluded that in this study the measured force $\mathbf{F}(t)$ is not dominantly described by the Lorentz force phenomenon, but on the attractive force between PM and UUT which depends also on the magnetic properties of the UUT.

Result of the DiLET voltage measurement $V_z(t)$

Figure 4.18 shows the measurement result of the 1-axis DiLET sensor $V_z(t)$ together with its cumulative sum $\text{cusum}(V_z(t))$ using a gain of $g_{\text{DF}} = 10$.

As the measured force, the overall result shows nearly no similarity to the non-ferromagnetic reference signals. Instead of a symmetric characteristic with respect to the y-direction at $x = 0\,\text{mm}$, the DiLET signal has a faint resemblance to the z-component of the force in the study of the aluminum bar. However, the cumulative sum $\text{cusum}(V_z(t))$ of the signal is very similar to the absolute value of the simultaneously measured force component $F_z(t)$ (cf. 4.17).
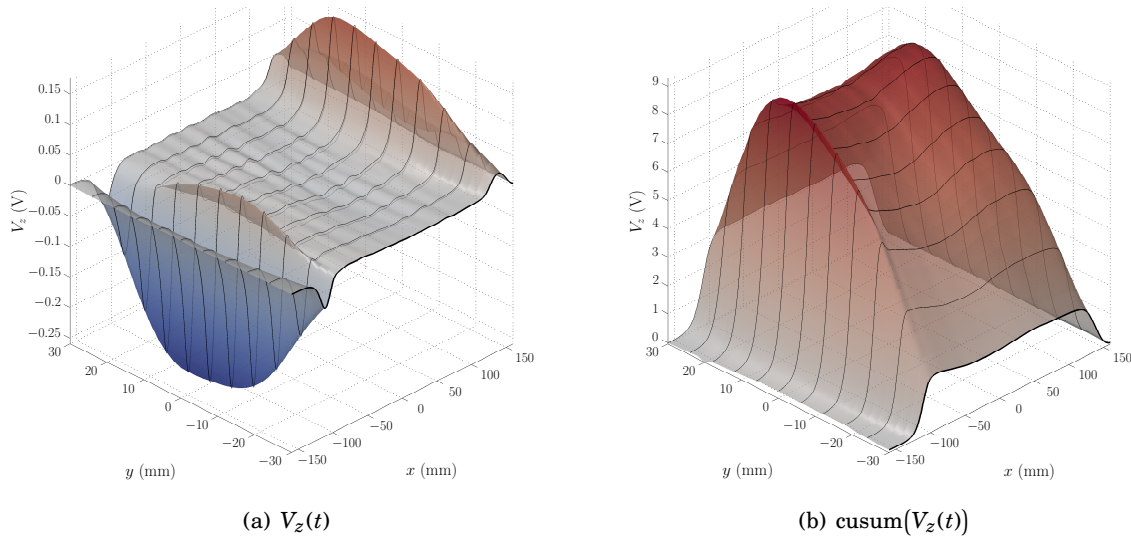
(a) $V_z(t)$ (b) $\mathrm{cusum}\big(V_z(t)\big)$

Figure 4.18: Measurement result of the voltage $V_z(t)$ (a) and its cumulative sum $\mathrm{cusum}\big(V_z(t)\big)$ (b) for the monolithic stainless steel bar. The surface-plot show the expected value of the measurand $\bar{V}_z(t)$ and the corresponding its cumulative sum. The black curves show the complete measurement result as the estimate of the 95 %-confidence intervals at $\Delta y = 6\,\mathrm{mm}$.

Concluding remarks

The study of the monolithic stainless steel bar shows that the measurement method of LET becomes significantly more complex if the UUT is made of ferromagnetic material with moderate electrical conductivity. The measured force $\mathbf{F}(t)$ is dominated by the attractive force between the PM and UUT even in the case of austenitic stainless steel where $\mu_{\mathrm{r,N}} \leq 1.3$. The Lorentz force still has a significant influence on the x-component of the measured force, but is mostly negligible for the y- and z-component. Thus, the information about the Lorentz force is partly obscured which makes the interpretation much harder with regard to conductivity anomalies.

However, it has been demonstrated that the alignment procedure allows to create artificial signal ensembles of the measured force $\mathbf{F}(t)$ for complete scans with very low relative standard deviation. The reason for this good result is that the estimated ROI for data reduction uses the 50 %-threshold of the absolute value of the measured force $|\mathbf{F}(t)|$, which is still of square-wave-like shape due to the dominating attraction force in the z-direction. The subsequent cross-correlation probably calculates a biased estimate of the true location of the UUT relative to the PM (x-axis), but the error is constantly repeated for all observations. Thus, the shown results of the complete scan are reliably aligned but the plotted x-axis might be biased to some extend.

4.5 Applications with Defect

In this section, two studies are presented in order to give a representative overview of the measurement performance of the developed experimental setup for applications including artificial defects. Based on the findings in the previous section, the focus in this studies is on the investigation of defect responses.

The first study is performed on a UUT made of stacked aluminum sheets which allows to include artificial defects at different depths. The investigation illustrates principal characteristics of the defect responses for the measured force $\mathbf{F}(t)$ and the induced voltage $V_z(t)$ from the 1-axis DiLET sensor. The artificial defect used in the study is chosen to be especially large to assure a significant defect response signal (DRS) which can serve as a reference for the characteristics of typical defect responses.

In the second study, a UUT made of *glass laminate aluminum reinforced epoxy* (GLARE) is examined. This lightweight hybrid composite material has become increasingly important in modern aircraft industry, like in the fuselage of the Airbus A380–800, and is used as reference material for the evaluation of LET in recent industrial applications. The UUT is specially prepared with two subsurface defects of different size. The study serves as an illustration of detection capabilities of the developed experimental setup.

4.5.1 Stacked Aluminum Sheets

The first UUT is a stack of 24 aluminum sheets, each with size of $250\,\mathrm{mm} \times 50\,\mathrm{mm} \times 2\,\mathrm{mm}$. Due to size tolerance and shape deviations the complete stack adds up to a height of about $50\,\mathrm{mm}$. The average electrical conductivity measured for each sheet is equal to $\bar{\sigma} \pm 2u(\bar{\sigma}) = (30.48 \pm 0.02)\,\mathrm{MS/m}$ at $20\,°\mathrm{C}$. It is determined at six measurement points for each sheet using an ECT device Elotest N300 [124] by *Rohmann GmbH*. Because all sheets are naturally coated with a thin aluminum oxide layer, they are treated as electrically insulated from each other. In consequence, the UUT is assumed to have an anisotropic electrical conductivity with $\sigma_{zz} = 0\,\mathrm{S/m}$ which is especially important for the discussion of the DRS. The used cylindrical PM is the same as in the study on the monolithic aluminum bar in Section 4.4.1, with $D = 22.5\,\mathrm{mm}$, $H = 17.6\,\mathrm{mm}$, and $B_{\mathrm{r,N}} = 1.43\,\mathrm{T}$.

Figure 4.19(a) shows a technical drawing of a single defect sheet with an artificial defect of $5\,\mathrm{mm} \times 5\,\mathrm{mm} \times 2\,\mathrm{mm}$. Two of these defect sheets are used in the second and third layer from top of the stack, what results in a defect depth of $d = 2\,\mathrm{mm}$. Figure 4.19(b) shows the picture of the UUT mounted on the slide of the linear drive. The UUT is oriented in the longitudinal direction with respect to the direction of travel.

Design of experiment

The experimental study consists of repeated observations at different y-positions of the UUT, similar to the study of the monolithic aluminum bar. The scan goes from $y_{\mathrm{min}} = -30.00\,\mathrm{mm}$ to
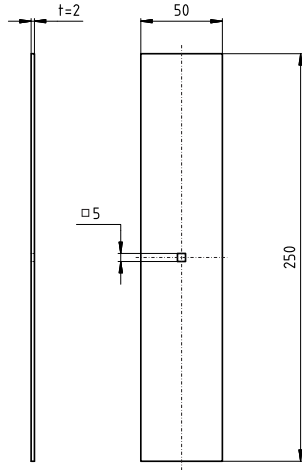
(a) Drawing of defect sheet
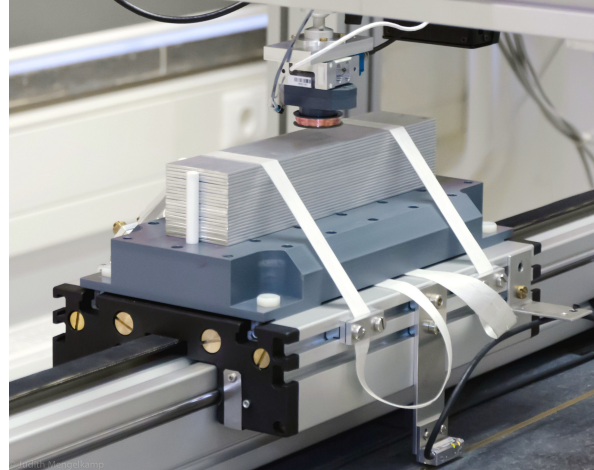
(b) Fully assembled UUT

Figure 4.19: Technical drawing of defect sheet (a) and fully assembled UUT (b). The UUT consists of 22 defect-free aluminum sheets and 2 defect sheets of the same material in the second and third layer from top. The resulting defect is $5\,\mathrm{mm} \times 5\,\mathrm{mm} \times 4\,\mathrm{mm}$ at depth $d = 2\,\mathrm{mm}$.

$y_{\mathrm{max}} = 30.00\,\mathrm{mm}$ at steps of $\Delta y = 1.00\,\mathrm{mm}$. In the region of interest regarding the y-position (ROIy), i.e. from $y_{\mathrm{D,min}} = -5.00\,\mathrm{mm}$ to $y_{\mathrm{D,max}} = 5.00\,\mathrm{mm}$, the scan is refined using a step size of $\Delta y_{\mathrm{D}} = 0.50\,\mathrm{mm}$. The measurements are performed $K = 5$ times outside the ROIy and $K_{\mathrm{D}} = 25$ times inside the ROIy. The distinct increase of repetitions in the close vicinity of the defect is expected to further reduce the experimental standard deviation. All parameters of the experimental study of a stacked aluminum sheets are summarized in Table 4.4.

In addition to the main purpose of illustrating the principal characteristics of the defect responses, this study serves as a reference for DRSs of UUTs with anisotropic electrical conductivity. Besides that, the study unintentionally contests the assumption about statistical independence of the successive experiments.

Result of the force measurement $\mathbf{F}(t)$

Figure 4.20 shows the measurement result of the force $\mathbf{F}(t)$ for the stacked aluminum sheets. As in the previous studies (4.4.1 and 4.4.2), the expected value of the respective force component is represented by surface-plots of $\bar{F}_i(t)$ while black curves show a complete measurement result of selected experiments ($\Delta y = 5\,\mathrm{mm}$). The post-processing procedure and the shown range of the x- and y-positions are likewise, as in the previous study.

The direct comparison with the measurement result of the monolithic aluminum bar (Sec. 4.4.1) reveals two important aspects. First, the ratio of the average forces in the x-direction at $y = 0\,\mathrm{mm}$ ($\bar{F}_{x0}$) is approximately equal to the ratio of conductivities in both studies. Furthermore, the ratio of the average forces in the z-direction at $y = 0\,\mathrm{mm}$ ($\bar{F}_{z0}$) is approximately equal to the ratio of conductivities squared. Both observations confirm the dependencies for low R_{m} determined in Chapter 3, although the assumptions made there are only roughly fulfilled.

Table 4.4: Parameters of the experimental study of a stacked aluminum sheets*.

Parameter		Value	Unit	Description
DOE	K	5		No. of observations
	K_D	25		No. of observations at ROIy
	v	0.50	m/s	Velocity of the UUT
	h	1.00	mm	Lift-off distance
	y_{max}	30.00	mm	Max. y-position of the PM
	y_{min}	−30.00	mm	Min. y-position of the PM
	$y_{D,max}$	5.00	mm	Max. y-position at ROIy
	$y_{D,min}$	−5.00	mm	Min. y-position at ROIy
	Δy	1.00	mm	Step size of the scan
	Δy_D	0.50	mm	Step size of the scan at ROIy
UUT	$\sigma_{xx,yy}$	30.48	MS/m	Electrical conductivity of each sheet
	μ_r	1		Relative permeability
	l_X	250.0	mm	Length of the UUT
	l_Y	50.0	mm	Width of the UUT
	l_Z	50.0	mm	Height of the UUT
PM	$B_{r,N}$	1.43	T	Nominal remanence
	D	22.5	mm	Diameter of the PM
	H	17.6	mm	Height of the PM

*Values rounded to significant figures with respect to the standard deviation.

Figure 4.20: Measurement result of the force $\mathbf{F}(t)$ for the stacked aluminum sheets including a $5\,\text{mm} \times 5\,\text{mm} \times 4\,\text{mm}$ defect at depth $d = 2\,\text{mm}$. The surface-plots show the expected value of the measurand $\bar{F}_i(t)$. The black curves show the complete measurement result as the estimate of the 95%-confidence interval $\left[\bar{F}_i(t) \pm 2u\left(\bar{F}_i(t)\right)\right]$ for selected experiments with $\Delta y = 5\,\text{mm}$.

The second important aspect of the comparison with the result of the monolithic aluminum bar is that the signal perturbations of all three components of the measured force at the edges of the UUT are more pronounced for the stacked aluminum sheets, although the used PM as well as the external dimensions of the UUT are the same. A possible explanation of this observation is the anisotropic electrical conductivity of the stacked aluminum sheets which prevents the generation of eddy currents in the z-direction.

Result of the force DRS $\Delta \mathbf{F}(t)$

Figure 4.21 shows the estimated DRS of the measured force $\Delta \mathbf{F}(t)$ from $x_{\mathrm{D,min}} = -30.00\,\mathrm{mm}$ to $x_{\mathrm{D,max}} = 30.00\,\mathrm{mm}$. The DRS of each force component $\Delta F_i(t)$ is estimated by subtracting the respective average of the force at $x_{\mathrm{D,min}}$ and $x_{\mathrm{D,max}}$, which is an estimate of the force $F_{i0}(t)$ without a defect present.

All three components $\Delta F_i(t)$ show significant responses to the artificial defect. For the x-component of the force DRS $\Delta F_x(t)$ a maximum absolute value of $77\,\mathrm{mN}$ is found. Considering the maximum absolute value of the force in x-direction $\max(F_x(t)) = 2.350\,\mathrm{N}$, a *relative* DRS is given as $\max(|\Delta F_{x,\mathrm{rel}}(t)|) = 3.3\,\%$. The y- and z-component show maximum absolute values of $\max(|\Delta F_y(t)|) = 19\,\mathrm{mN}$ and $\max(|\Delta F_z(t)|) = 52\,\mathrm{mN}$, respectively. In comparison to $\Delta F_x(t)$ the DRSs $\Delta F_y(t)$ and $\Delta F_z(t)$ are less affected by surrounding distortion patterns and thus better recognizable. All three components $\Delta F_i(t)$ are spatially restricted in x-direction to a length of $\approx 40\,\mathrm{mm}$ and $\approx 30\,\mathrm{mm}$ in y-direction. The spatial distribution of the defect response depends more on the size of the PM than on the defect size. This observation corresponds to the *point spread function* of simple PMs which is discussed in [153] and is a typical result in cases where the characteristic length of the defect is smaller than that of the PM.

All three force DRS components are superimposed with significant oscillations, which are similar to the measured accelerations (not shown). The applied hill shading technique increases the perception for this effect, although the amplitudes of these oscillations are much smaller ($< 8\,\mathrm{mN}$) than the respective DRS. The oscillations appear to propagate from the first edge of the UUT ($x = 125\,\mathrm{mm}$) and are sustainably perturbed by the defect response of the respective component (see $\Delta F_z(t)$).

A surprising observation is made when comparing the two regions with $K = 5$ and $K_{\mathrm{D}} = 25$. While for $\Delta F_y(t)$ and $\Delta F_z(t)$ no significant difference in the distortion characteristics can be observed, so it is in $\Delta F_x(t)$. In the range of $y_{\mathrm{D,min}} = -5.00\,\mathrm{mm}$ to $y_{\mathrm{D,max}} = 5.00\,\mathrm{mm}$, a diagonal pattern dominates the signal before and after the defect. This pattern was identified to be proportional to the number of runs in each artificial ensemble as well as to the number of previous observations. The pattern is identified to be an artifact from the calculation of the expected value of the signal ensemble where in each member the underlying distortion is slightly shifted with respect to its respective predecessor. Furthermore, the distortion is proportional to $F_x(t)$ and completely vanishes before and after the UUT passes the PM.

This effect seems to contest the assumption about statistical independence of the successive
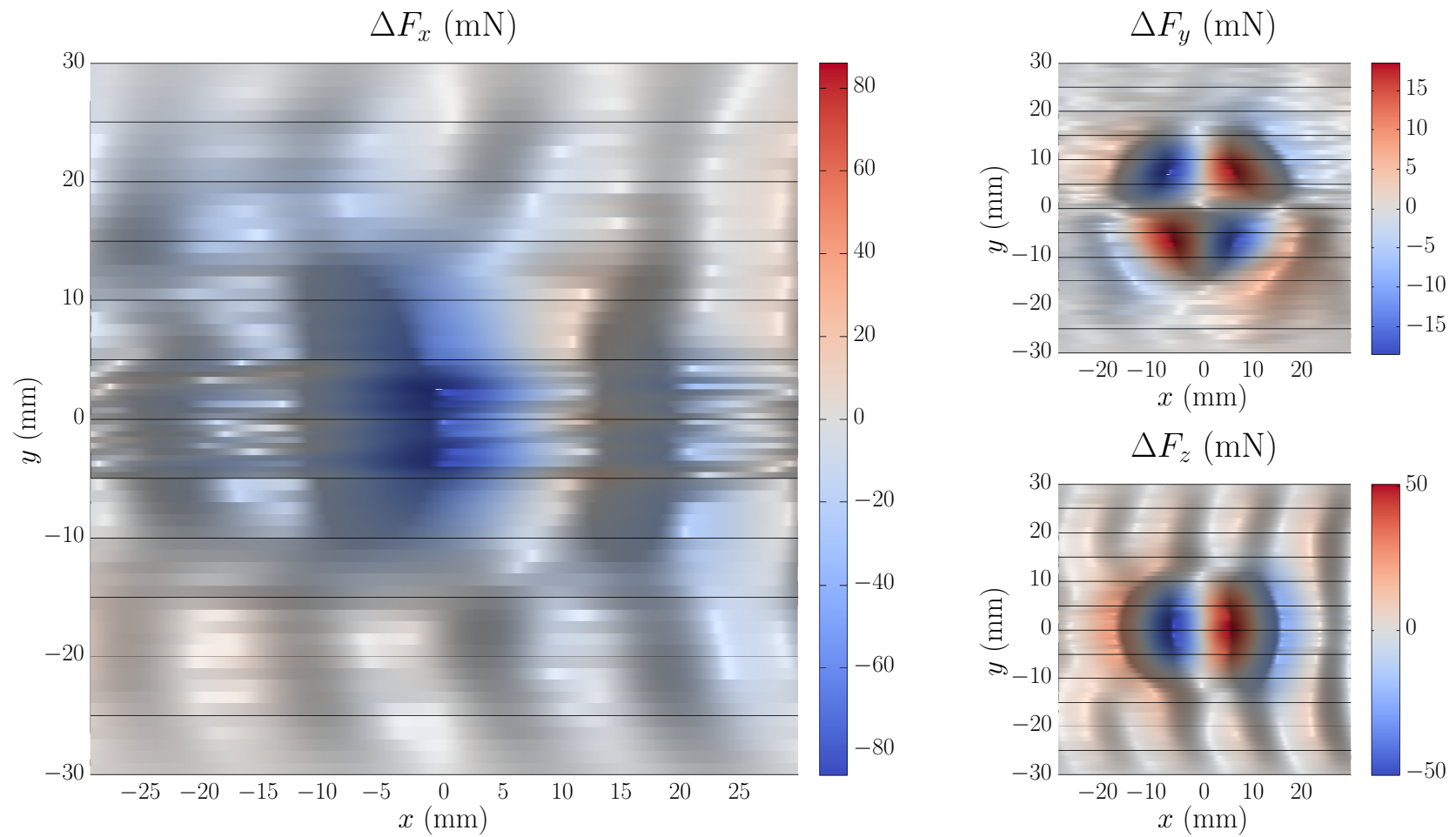
Figure 4.21: Measurement result of the force DRS $\Delta\mathbf{F}(t)$ from $x_{\mathrm{D,min}} = -30.00\,\mathrm{mm}$ to $x_{\mathrm{D,max}} = 30.00\,\mathrm{mm}$ for the stacked aluminum sheets including a $5\,\mathrm{mm} \times 5\,\mathrm{mm} \times 4\,\mathrm{mm}$ defect at depth $d = 2\,\mathrm{mm}$. Significant defect responses in all three force components are observable.

experiments, which is one assumed property for the developed signal alignment procedure. However the distortion pattern shows no significant influence on the very low relative experimental standard deviation because the relative amplitude of the distortion is much smaller than the corresponding x-component of the force.

Result of the DiLET voltage measurement $V_z(t)$

Figure 4.22 shows the measurement result $V_z(t)$ of the 1-axis DiLET sensor (a) and the corresponding DRS $\Delta V_z(t)$ (b) for gain $g_{\text{DF}} = 10$. Since $V_{z0}(t)$ is typically zero mean in the region where the DRS is estimated, $V_z(t)$ and $\Delta V_z(t)$ are equal.

(a) $V_z(t)$

(b) $\Delta V_z(t)$
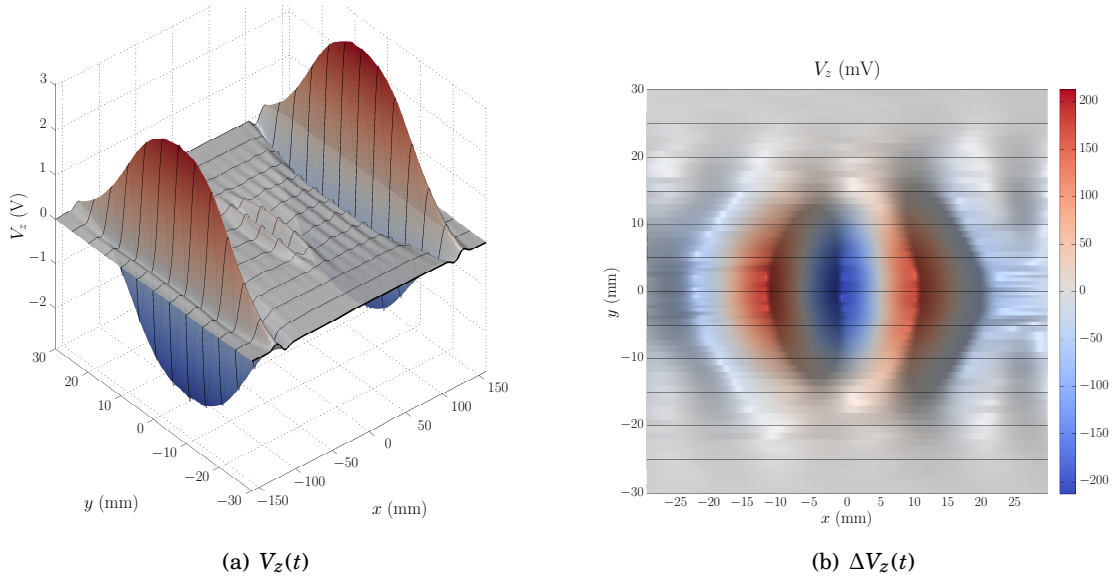
Figure 4.22: Measurement result of the 1-axis DiLET sensor $V_z(t)$ and its DRS $\Delta V_z(t)$ from $x_{\text{D,min}} = -30.00\,\text{mm}$ to $x_{\text{D,max}} = 30.00\,\text{mm}$ for the stacked aluminum sheets including a $5\,\text{mm} \times 5\,\text{mm} \times 4\,\text{mm}$ defect at depth $d = 2\,\text{mm}$.

The measurement result of the induced voltage $V_z(t)$ shows significant responses at the edges of the UUT in the range of $V_z(t) \approx \pm 3\,\text{V}$. This corresponds to an estimated effective variation of the magnetic flux density of $\partial B_{\text{eff},z}(t)/\partial t \approx \pm 0.1049\,\text{T/s}$. The observed effect is approximately three times stronger than for the monolithic aluminum bar, which corresponds to a dependency described by $V_z(t) \propto R_{\text{m}}^{2.71}$. However, based only on these two studies no solid hypothesis can be formulated and further investigations of the effect are necessary.

The estimated DRS $\Delta V_z(t)$ has a maximum absolute value $\max\big(|\Delta V_z(t)|\big)$ of $\approx 0.212\,\text{V}$ and shows a similar spatial disproportion as the force DRS. It can be observed that the signal is also superimposed with oscillations of smaller amplitude than $20\,\text{mV}$ which results in an estimated signal to distortion ratio of about

$$\text{SDR} = 10\log_{10}\left(\frac{0.212}{0.02}\right) \approx 10.3\,\text{dB} \, . \tag{4.23}$$

Concluding remarks

The study of the stacked aluminum sheets with a large artificial subsurface defect has enabled to define the principal characteristics of the DRSs estimated by the measured force $\mathbf{F}(t)$ and the induced voltage $V_z(t)$. The study has built an expectation for the shape and relative magnitude of DRSs of the different sensor components and will serve as a reference experiment for the last experimental study presented in this thesis.

Furthermore, the study revealed a violation of one of the assumptions formulated for the alignment procedure, which will be examined in the last study of this chapter.

In order to complete this investigation, the key values of the experimental study are summarized in Table 4.5. The table includes also the key values of the measured acceleration in order to enable the comparison with previous studies, even if they were not discussed explicitly.

Table 4.5: Results of the experimental study of a stacked aluminum sheets*.

Parameter		Value	Unit	y-position	
Force	$\max(F_x(t))$	2.350	N	0.00	mm
	$\max(F_y(t))$	0.445	N	18.00	mm
	$\min(F_y(t))$	-0.464	N	-16.00	mm
	$\max(F_z(t))$	1.068	N	-1.00	mm
	$\min(F_z(t))$	-0.886	N	0.00	mm
Force DRS	$\max(|\Delta F_x(t)|)$	0.077	N	-0.50	mm
	$\max(|\Delta F_y(t)|)$	0.019	N	-7.00	mm
	$\max(|\Delta F_z(t)|)$	0.052	N	0.50	mm
Acceleration	$\max(|A_x(t)|)$	17.3	mm/s^2	-0.50	mm
	$\max(|A_y(t)|)$	2.3	mm/s^2	13.00	mm
	$\max(|A_z(t)|)$	23.4	mm/s^2	-0.50	mm
DiLET	$\max(V_z(t))$	3.04	V	-0.50	mm
	$\min(V_z(t))$	-2.85	V	0.00	mm
DiLET DRS	$\max(|\Delta V_z(t)|)$	0.212	V	0.50	mm

*Values rounded to significant figures with respect to the standard deviation.

4.5.2 Fibre-Metal Laminate

In the second study, a UUT made of glass laminate aluminum reinforced epoxy (GLARE) is examined. This lightweight fibre-metal laminate (FML) consists of alternating layers of 2024-T3 aluminum and glass fibre reinforced epoxy plies. It provides better damage tolerance characteristics than monolithic aluminum or plain reinforced plastics [78] and has been studied extensively in terms of impact damage resistance and heat resistance [46, 89, 130, 134].

The UUT prepared for this study is made of 5 aluminum sheets and 4 glass fibre reinforced epoxy plies with thickness 0.4 mm and 0.25 mm, respectively. The metal volume fraction is 66.6 %, resulting in a specific mass of $m_S \approx 18 \text{ kg/m}^2$ [46]. The UUT is $350 \text{ mm} \times 150 \text{ mm} \times 3 \text{ mm}$ in size and is especially prepared with two subsurface defects in the third aluminum layer, resulting in a defect depth of $d = 1.3 \text{ mm}$. The electrical conductivity could not be determined using the ECT device Elotest N300 thus is considered to be unknown. The first defect is an $10 \text{ mm} \times 0.8 \text{ mm}$ slot at $y_{D1} = 37.5 \text{ mm}$, oriented in the longitudinal direction with respect to the longest edge of the UUT. The second defect is a drilled through-hole with diameter $\varnothing 2.0 \text{ mm}$ at $y_{D2} = -37.5 \text{ mm}$. Both defects are located approximately at $x_D = 0 \text{ mm}$. The cylindrical PM used in the experimental setup is the same as in previous studies in Section 4.4.1 and 4.5.1, with $D = 22.5 \text{ mm}$, $H = 17.6 \text{ mm}$, and $B_{r,N} = 1.43 \text{ T}$.

Figure 4.23(a) shows the technical drawing of the defect sheet (third aluminum layer) including two artificial subsurface defects and a top view of the prepared UUT in the same scale. Figure 4.23(b) shows the picture of the UUT mounted on the slide of the linear drive. The clamping mechanism is modified to guaranty a homogeneous support of the UUT to avoid unwanted deformation due to the clamping force which can cause significant lift-off distance variations.

(a) Drawing and picture of UUT

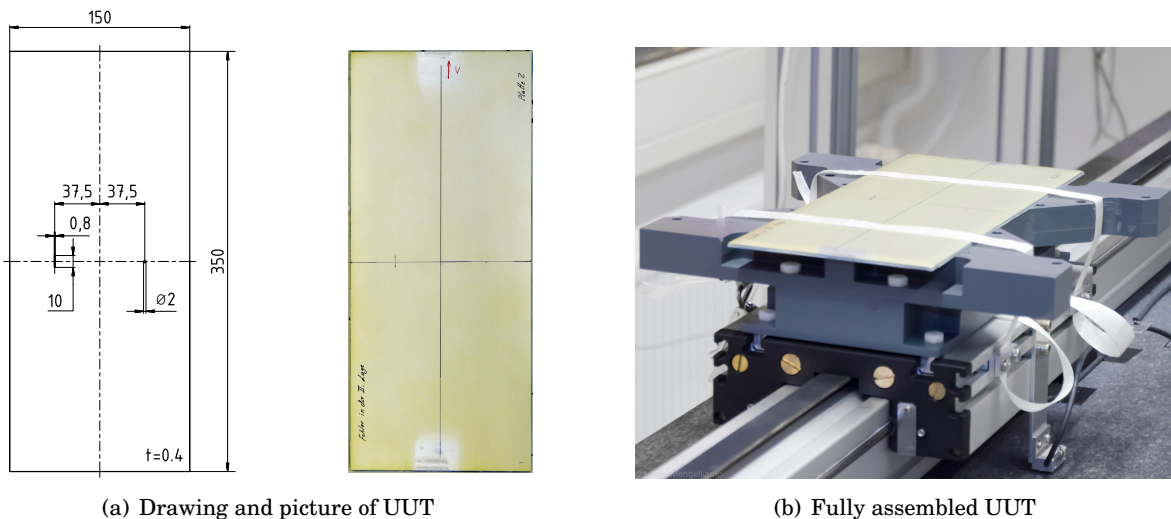(b) Fully assembled UUT

Figure 4.23: Technical drawing of the 3^{ed} aluminum layer and top view of the UUT in same scale (a) and fully assembled UUT (b). The UUT is $350 \text{ mm} \times 150 \text{ mm} \times 3 \text{ mm}$ in size and includes a $10 \text{ mm} \times 0.8 \text{ mm}$ slot and a $\varnothing 2.0 \text{ mm}$ drilled through-hole at a defect depth of $d = 1.3 \text{ mm}$.

Design of experiment

The experimental study consists of repeated observations at different y-positions of the UUT. For the two regions $[y_{D1}]$ and $[y_{D2}]$, where the defects are present, the scanning parameters are adjusted to provide a higher spatial resolution. The goal of such experimental strategy is to prevent the considerable increase of scanning duration for the much larger UUT, and to keep the experimental standard deviation at an acceptable value.

Scans are performed from $y_{min} = -50.00\,\text{mm}$ to $y_{max} = 50.00\,\text{mm}$ using steps of $\Delta y = 0.50\,\text{mm}$. With only $K = 2$ repetitions for each measurement, the degree of freedom v, statistical evaluation, is reduced to $K - 1 = 1$ and thus the factor 2 used for the calculation of the complete measurement result (4.22) encompasses only 70 % of the distribution [103]. In the vicinity of defects the spatial resolution is further increased using steps of $\Delta y_D = 0.20\,\text{mm}$, with the number of repetitions for each measurement equals $K_D = 5$ times. The refined scanning parameters are used from $y_{D1,min} = 35.00\,\text{mm}$ to $y_{D1,max} = 40.00\,\text{mm}$, as well as from $y_{D2,min} = -40.00\,\text{mm}$ to $y_{D2,max} = -36.00\,\text{mm}$.

Since the assumption about statistical independence is contested, the order of experiments becomes very important. First, the overall scan is performed beginning at $y = -50.00\,\text{mm}$ with $\Delta y = 0.50\,\text{mm}$ and $K = 2$ repetitions. Second, the refined scan is performed beginning at $y = -40.00\,\text{mm}$ with $\Delta y = 0.20\,\text{mm}$ and $K = 5$ repetitions, until $y = -36.00\,\text{mm}$. At last, the refined scan is continued from $y = 35.00\,\text{mm}$ to $y = 40.00\,\text{mm}$.

The distinct increase of repetitions at the close vicinity of the defects is expected to reduce the experimental standard deviation of the mean and to repeat the observation of distortion patterns, which are assumed to be proportional to the number of previous observations.

The main purpose of this study is to utilize this lightweight hybrid composite material as reference material for the evaluation of LET in recent industrial applications, in order to illustrate the detection capabilities of the presented experimental setup by means of the minimum defect size of near surface defects. Besides that, the study serves to support the hypothesis on the dependence of the successive experiments, which contest the assumption about statistical independence.

All parameters of this experimental study are summarized in Table 4.6.

Table 4.6: Parameters of the experimental study of the UUT made off GLARE*.

	Parameter	Value	Unit	Description
DOE	K	2		No. of observations
	K_D	5		No. of observations at $[y_{D1}]$ and $[y_{D2}]$
	v	0.50	m/s	Velocity of the UUT
	h	1.00	mm	Lift-off distance
	y_{min}	−50.00	mm	Min. y-position of the PM
	y_{max}	50.00	mm	Max. y-position of the PM
	$y_{D2,min}$	−40.00	mm	Min. y-position for $[y_{D2}]$
	$y_{D2,max}$	−36.00	mm	Max. y-position for $[y_{D2}]$
	$y_{D1,min}$	35.00	mm	Min. y-position for $[y_{D1}]$
	$y_{D1,max}$	40.00	mm	Max. y-position for $[y_{D1}]$
	Δy	0.50	mm	Step size of the scan
	Δy_D	0.20	mm	Step size of the scan at $[y_{D1}]$ and $[y_{D2}]$
UUT	μ_r	1		Relative permeability
	l_X	350.0	mm	Length of the UUT
	l_Y	150.0	mm	Width of the UUT
	l_Z	3.0	mm	Height of the UUT
PM	$B_{r,N}$	1.43	T	Nominal remanence
	D	22.5	mm	Diameter of the PM
	H	17.6	mm	Height of the PM

*Values rounded to significant figures with respect to the standard deviation.

Result of the force measurement $\mathbf{F}(t)$

Figure 4.24 shows the measurement result of the force $\mathbf{F}(t)$ for the UUT made of GLARE. As in the previous studies, the expected value of the respective force component is represented by surface-plots of $\bar{F}_i(t)$. The black curves in each plot show a complete measurement results for selected experiments with $\Delta y = 5\,\text{mm}$. The post-processing procedure similar to the previous studies, but the confidence interval corresponds to approximately 70 % of the distribution.

An important difference compared to previous studies is that no simulated reference signal for this UUT was available for the estimation of the individual time delays. Therefore, the reference signal of the previous study was reused to estimate the simulation result with correct length. In order to compensate for the increased length $\Delta l_x = 100\,\text{mm}$ of the UUT, the QSA result was extended at $x = 0\,\text{mm}$ by Δl_x with $F_{\text{Sim},x}(x = 0\,\text{mm})$, and resampled to fit the number of samples corresponding to $f_s = 10\,\text{kHz}$ and $v = 0.5\,\text{m/s}$.

The measurement result of the force $\mathbf{F}(t)$ shows that the alignment procedure works very well with the extended reference signal. Every single signal ensemble is characterized by a narrow estimate of the confidence interval, although the very low number of repetitions, which further supports the stated high repeatability of the LET measurements. However, the three force components show considerably more distortions between the leading and trailing edge

93
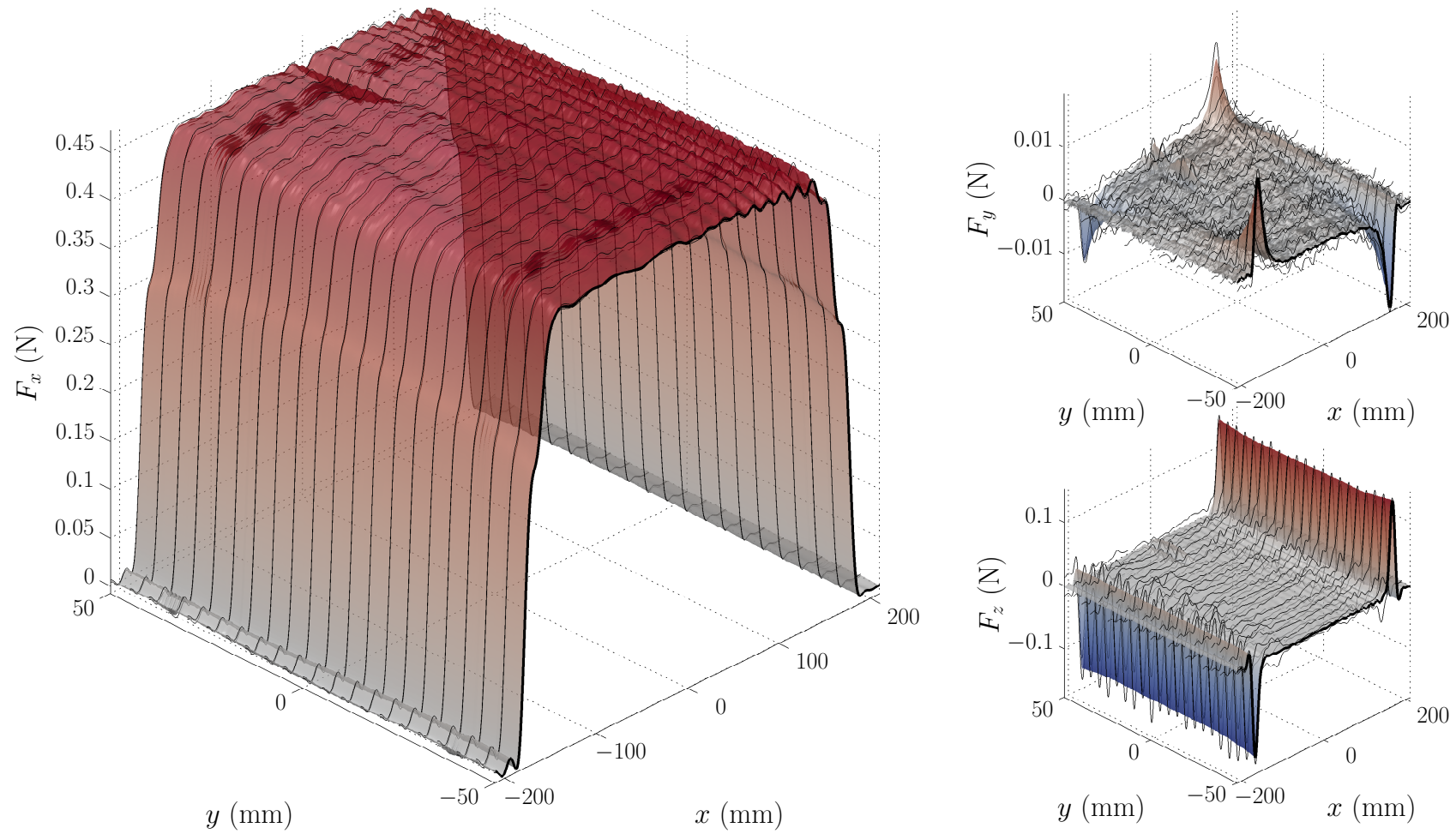
Figure 4.24: Measurement result of the force $\mathbf{F}(t)$ for the UUT made of GLARE including two defects at depth $d = 1.3\,\text{mm}$. The surface-plots show the expected value of the measurand $\bar{F}_i(t)$. The black curves show the complete measurement result as the estimate of the 70 %-confidence interval $\left[\bar{F}_i(t) \pm 2u\left(\bar{F}_i(t)\right)\right]$ for selected experiments with $\Delta y = 5\,\text{mm}$.

of the UUT. The most likely reason for these additional features is the reduced flatness of the UUT surface, recognizable by unaided eye observation.

Furthermore, the measured force components show a significantly smaller maximum force, with maximum values: $\max(F_x(t)) = 472\,\text{mN}$ and $\max(F_z(t)) = 150\,\text{mN}$, while the maximum of $F_y(t)$ is outside the scanning range of $y_{\text{max/min}} = \pm 50\,\text{mm}$.

Another noteworthy feature of the measured force is the different influence of UUT edges. Since the PM does not exceed the UUTs lateral edges, no significant drop of the force in x-direction $F_x(t)$ is observed. However, the overall edge effect is much less pronounced than in the previous studies. The comparison of the relative force for the stacked aluminum bar at $y = \pm 15\,\text{mm}$ with the relative force for the UUT made of GLARE at $y = \pm 50\,\text{mm}$, although both have the same lateral edge distance, shows that the relative force drop in comparison to the centerline is much smaller in the case of GLARE. It can be ruled out that the reason for this difference lies in the much smaller width of the stacked aluminum bar because from $y = \pm 15\,\text{mm}$ until $y = 0\,\text{mm}$ the force further increases significantly, while it does not from $y = \pm 50\,\text{mm}$ until $y = \pm 35\,\text{mm}$ in the case of GLARE. The only reasonable difference between both UUTs, which might explain this effect, is the big difference in the thickness of both, the individual layers, as well as the complete UUT.

Result of the force DRS $\Delta\mathbf{F}(t)$

The estimated force DRS $\Delta\mathbf{F}(t)$ from $x_{\text{D,min}} = -50.00\,\text{mm}$ to $x_{\text{D,max}} = 50.00\,\text{mm}$ is shown in Fig. 4.25. The force DRS of each component $\Delta F_i(t)$ is estimated by subtracting the average of the respective force component at $x_{\text{D,min}}$ and $x_{\text{D,max}}$.

A significant defect response can be observed for the $10\,\text{mm} \times 0.8\,\text{mm}$ slot defect in all three force components, with maximum absolute values

$$\max\left(|\Delta F_x(t)|, |\Delta F_y(t)|, |\Delta F_z(t)|\right) = \left[23\,\text{mN}, 3\,\text{mN}, 11\,\text{mN}\right] .$$

Using the maximum of the force in x-direction, this results in a relative force DRS of about $5\,\%$. The overall characteristics of the DRS are very similar to the DRS observed in the study of the stacked aluminum sheets with respect to the signal shape.

This is not the case for the $\varnothing 2.0\,\text{mm}$ defect located at $y_{\text{D2}} = -37.5\,\text{mm}$. The x- and y-component, of maximum absolute values $\max(|\Delta F_x(t)|) = 6.7\,\text{mN}$ and $\max(|\Delta F_y(t)|) = 0.6\,\text{mN}$, respectively, are superimposed with dominant distortion patterns. The only significant defect response can be observed in the z-component of the DRS with $\max(|\Delta F_z(t)|) = 1.3\,\text{mN}$. However, this results in a relative DRS of $\max(|\Delta F_{z,\text{rel}}(t)|) \approx 7.5\,\%$. Considering the amplitude of oscillations near the defect region with $\leq 0.4\,\text{mN}$, than this results in an estimated signal to distortion ratio of about

$$\text{SDR} \geq 10\log_{10}\left(\frac{1.3}{0.4}\right) \approx 4.1\,\text{dB} . \tag{4.24}$$
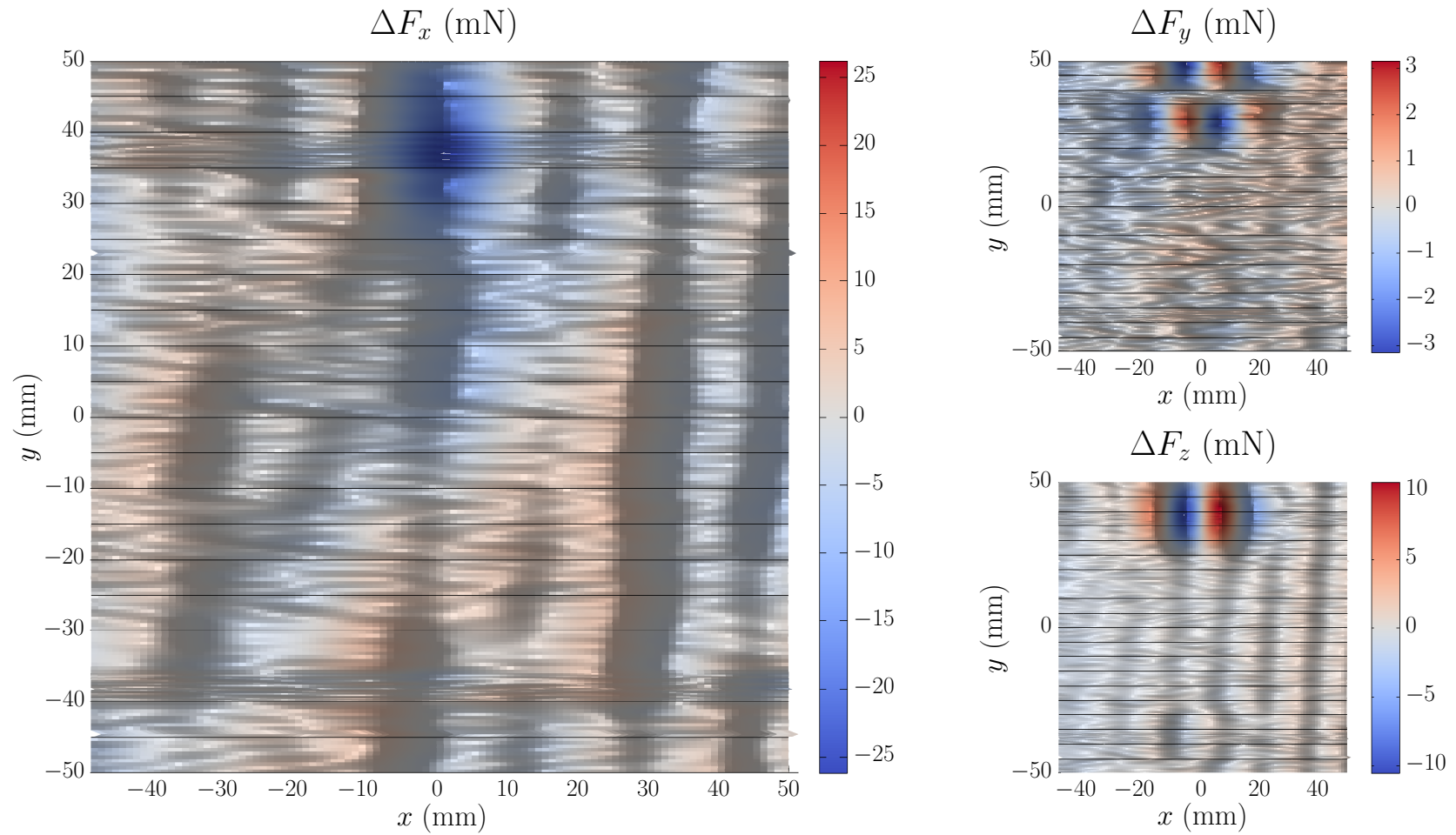
Figure 4.25: Measurement result of the force DRS $\Delta \mathbf{F}(t)$ from $x_{D,min} = -50.00\,\text{mm}$ to $x_{D,max} = 50.00\,\text{mm}$ for the UUT made of GLARE with two defects at depth $d = 1.3\,\text{mm}$. Significant defect responses at the $10\,\text{mm} \times 0.8\,\text{mm}$ slot defect are observable in all three force components. The defect response of the $\varnothing 2.0\,\text{mm}$ defect is obscured by relativly strong distortions. A significant DRS can only be observed for $\Delta F_z(t)$.

Figure 4.26: Measurement result of the acceleration $\mathbf{A}(t)$ for the monolithic aluminum bar. The surface-plots show the expected value of the measurand $\bar{A}_i(t)$. The black curves show the complete measurement result as the estimate of the 95%-confidence interval $\left[\bar{A}_i(t) \pm 2u\left(\bar{A}_i(t)\right)\right]$ for selected experiments with $\Delta y = 5\,\text{mm}$.

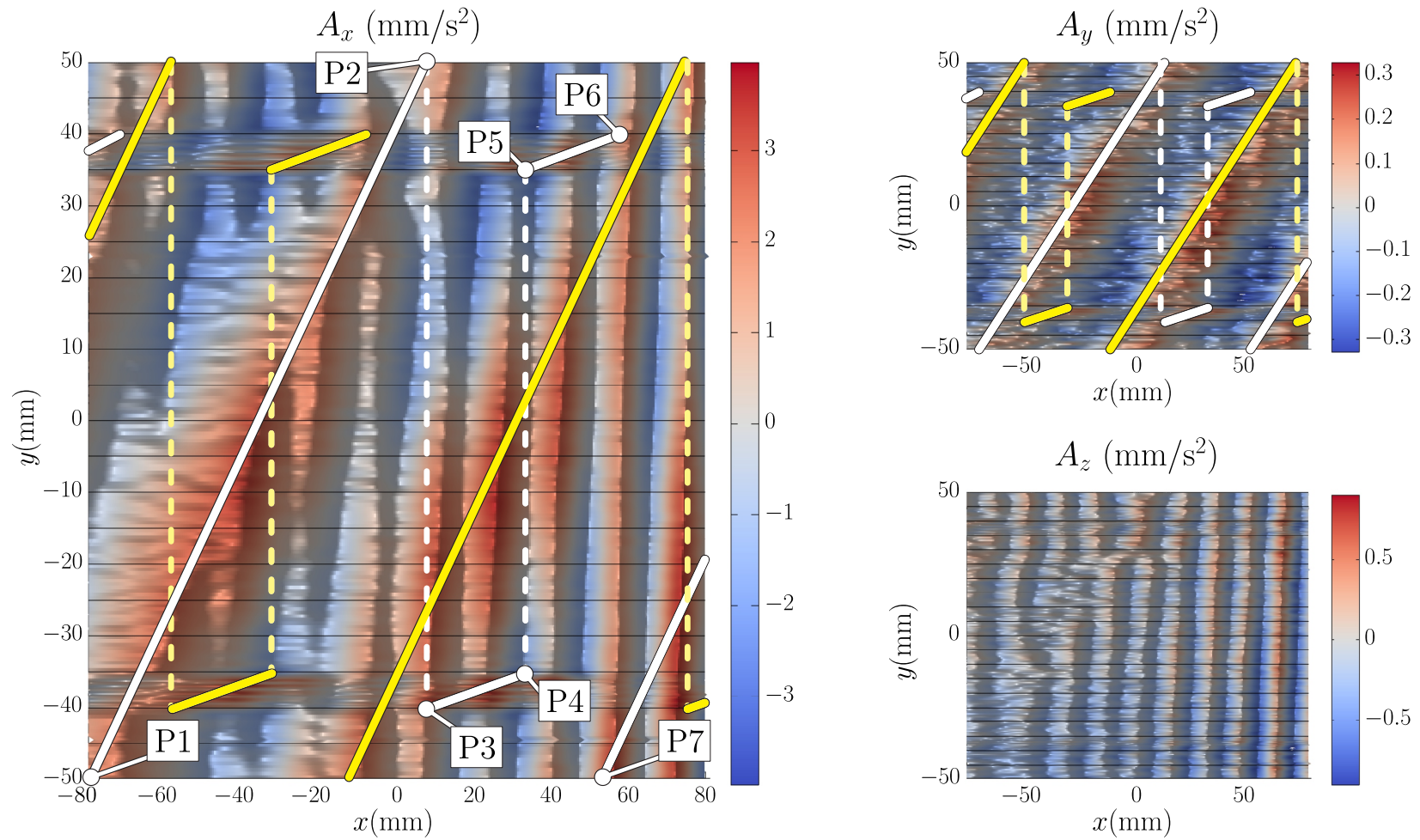**Result of the acceleration measurement $\mathbf{A}(t)$**

Figure 4.26 shows the result of the acceleration measurements $\mathbf{A}(t)$ from $x_{D,min} = -80.00\,\text{mm}$ to $x_{D,max} = 80.00\,\text{mm}$ for the UUT made of GLARE. In contrast to the examined force signals, which are primarily studied for the reason of defect detection, the analysis of recorded acceleration components serves to illustrate the systematic shift of the distortion pattern which was identified in the previous study on the stacked aluminum sheets. The depicted range of x-positions is slightly extended compared to the force DRS $\Delta\mathbf{F}(t)$ (Fig. 4.25) in order to obtain a complete overview of the repeating distortion pattern.

The results show dominating distortion patterns in $A_x(t)$ and $A_y(t)$ superimposed with oscillations with periodicity Δx_P of about $\approx 15\,\text{mm}$.

Following the distortion pattern (white path) in $A_x(t)$ according to the order of subsequent experiments (P1–P6), a continues shift of the distortion pattern is revealed. Starting at $y = -50\,\text{mm}$ (P1) the pattern shows a shift to positive x-direction for progressing experiments (P1⇒P2). Because the step size and number of repetitions stays the same until $y = 50\,\text{mm}$ (P2), the pattern also has a constant moderate shift. After the 404 observations the pattern is shifted by 86 mm. Subsequently, the first refined scan starts at $y = -40\,\text{mm}$ (P3) and ends at $y = -36\,\text{mm}$ (P4) using reduced step size ($\Delta y_D = 0.2\,\text{mm}$) and increased number of repetitions ($K_D = 5$). The observed x-shift after 130 observations is about 26 mm. In the second refined scan, starting at $y = 35\,\text{mm}$ (P5), the distortion starts at the same x-position where the first refined scan had ended (P4) and continuous until $y = 40\,\text{mm}$ (P6). The x-shift after 130 observations is about 25 mm.

Comparing the x-shift per observation for the three subsequent scans

$$\frac{\Delta x}{\text{rep}} \approx \frac{86\,\text{mm}}{404}\bigg|_{\text{P1⇒P2}} \approx \frac{26\,\text{mm}}{130}\bigg|_{\text{P3⇒P4}} \approx \frac{25\,\text{mm}}{130}\bigg|_{\text{P5⇒P6}} \tag{4.25}$$

an average x-shift of $\approx 0.2\,\text{mm/rep}$ is identified.

A detailed examination of the experimental setup revealed that the only component, which is able to cause such a wide variation of spatial distortion, without any noticeable changes of the arrangement of the elements of the experimental setup, is the belt gear of the linear drive. This *belt slip* must be anisotropic since the return run after each observation does not compensate this effect. This theory does also explain the occurrence of diagonal patterns in previous investigations based on the same linear drive (cf. Chapter 2). It should be noted that the diagonal patterns shown in Chapter 2 are characterized by a negative slope, which additionally supports this explanation since the linear drive in the previous experimental setup was mounted the other way around.

A second distortion pattern (yellow path) can be observed which is very similar to the first pattern (white path). This second pattern is shifted by $\approx 65\,\text{mm}$ with respect to the first pattern which corresponds to $65\,\text{mm}/(62\,\text{mm}\pi) \approx 1/3$ turn periodicity. At point P7, the third distortion pattern starts with the same shift of $\approx 65\,\text{mm}$. Considering the planetary gear with gear ratio $i = 3$, the periodicity of the distortion along the x-direction corresponds to one turn of the

servomotor of the linear drive which might be the cause of the repeating distortion. Another possible cause is a non-constant gear ratio which can likely be caused by the geometrical tolerance of the belt gear components, i.e. the set of two pulleys of the belt drive.

The non-constant gear ratio results in a small variation of the velocity, which directly affects all measurands.

Result of the DiLET voltage measurement $V_z(t)$

Figure 4.27 shows the measurement result of the 1-axis DiLET sensor $V_z(t)$ (a) and the corresponding DRS $\Delta V_z(t)$ (b) for gain $g_{DF} = 10$.
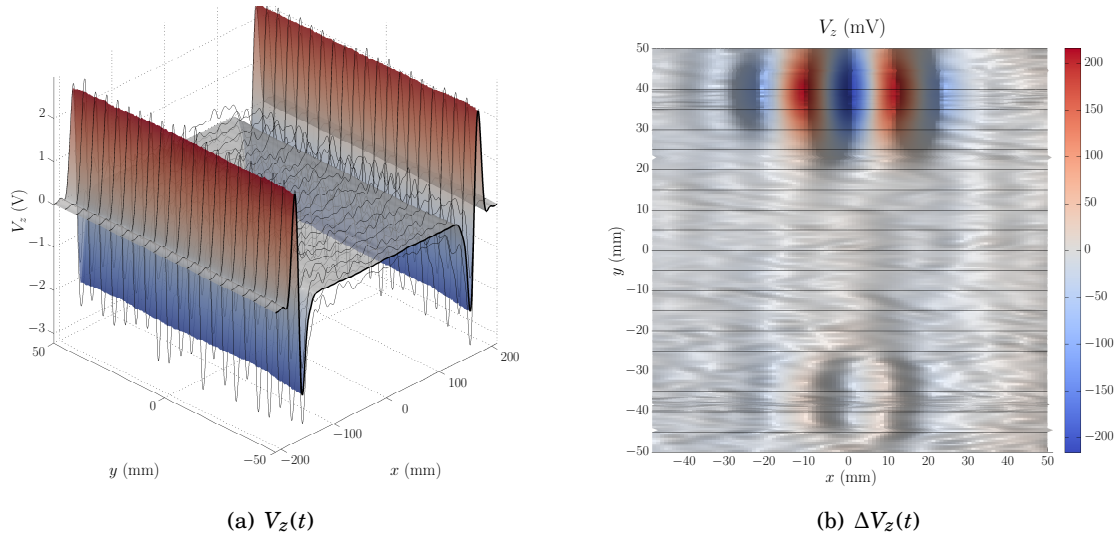

(a) $V_z(t)$ (b) $\Delta V_z(t)$

Figure 4.27: Measurement result of the 1-axis DiLET sensor $V_z(t)$ and its DRS $\Delta V_z(t)$ from $x_{D,min} = -50.00\,\text{mm}$ to $x_{D,max} = 50.00\,\text{mm}$ for the stacked aluminum sheets including a $5\,\text{mm} \times 5\,\text{mm} \times 4\,\text{mm}$ defect at depth $d = 2\,\text{mm}$.

The measurement result of the induced voltage $V_z(t)$ shows significant responses at the leading and trailing edge of the UUT in the range of $V_z(t) \approx -2.2\,\text{V}$ to $2.6\,\text{V}$, which is only a slight decrease in comparison to the extrema in the case of the stacked aluminum sheets. This result is surprising because the UUT is much thinner than the stacked aluminum sheets and the composite material is expected to have a lower effective electrical conductivity due to its metal volume fraction of 66%.

Figure 4.27(b) shows the estimated DRS $\Delta V_z(t)$, which has a local maximum of the absolute value of the voltage $\max(|\Delta V_z(t)|) \approx 0.218\,\text{V}$ at $y = 38.50\,\text{mm}$ and another local maximum $\max(|\Delta V_z(t)|) \approx 0.028\,\text{V}$ at $y = -37.00\,\text{mm}$.

The slot defect at $y_{D1} = 37.50\,\text{mm}$ is undeniably detected by a very significant defect response more than $\pm 20\,\text{mm}$ lateral to the actual position of the defect. The response signal shows a similar signal shape as in the previous study with a quadratic defect shape.

The second defect, a drilled hole with diameter $\varnothing 2.0\,\text{mm}$ at $y_{\text{D2}} = -37.5\,\text{mm}$, is also detected by a significant defect response $\pm 10\,\text{mm}$ lateral to the position of the defect. The signal shape is very similar to that of the slot defect, but of much lower amplitude.

In this detection problem, the benefits of the hill shading technique become pretty obvious. While the slot defect dominates the DRS with a ten times higher response, the second defect is only perceptible by the change in brightness proportional to the sign of the partial derivative in the x-direction.

As in the previous study, it can be observed that the signal is superimposed with minor oscillations with amplitudes of these distortion approximately $< 10\,\text{mV}$. This results in an estimated signal to distortion ratio of about

$$\text{SDR}_{\text{D1}} = 10\log_{10}\left(\frac{0.218}{0.01}\right) \approx 13.4\,\text{dB} \, , \tag{4.26}$$

for the slot defect and

$$\text{SDR}_{\text{D2}} = 10\log_{10}\left(\frac{0.028}{0.01}\right) \approx 4.5\,\text{dB} \, , \tag{4.27}$$

for the drill hole of $\varnothing 2.0\,\text{mm}$.

Concluding remarks

The study of a UUT made of GLARE with two artificial subsurface defects included, illustrates the detection capabilities of the experimental setup in modern industrial applications. The combination of force sensor, acceleration sensor, and 1-axis DiLET sensor is utilized to successfully detect both defects. Furthermore, the result is used to confirm the hypothesis on the cause of one of two repeating distortion patterns, which are present in all signal components.

The study serves as an extended test of the alignment procedure in cases of insufficient reference signals. The observed narrow confidence interval, even for a very low number of repetitions, supports the high repeatability of the experiments. Under these conditions it can be assumed that the violation of the assumption on statistically independence does not influence the alignment procedure. However, the distortion pattern can have a significant influence on the probability of detection, especially in the case of small defects with no dominant expansion in moving direction.

In order to complete this investigation, the key values of the experimental study are summarized in Table 4.7. The table includes also the key values of the measured acceleration, even if they were not discussed explicitly.

Table 4.7: Results of the experimental study of the UUT made of GLARE*.

Parameter		Value	Unit	y-position	
Force	$\max\!\big(F_x(t)\big)$	0.47	N	-37.40	mm
	$\max\!\big(F_z(t)\big)$	0.15	N	-50.00	mm
	$\min\!\big(F_z(t)\big)$	-0.15	N	-50.00	mm
Force DRS	$\max\!\big(|\Delta F_x(t)|\big)$	7	mN	-36.80	mm
with $y \le 0\,\mathrm{mm}$	$\max\!\big(|\Delta F_y(t)|\big)$	1	mN	-49.50	mm
	$\max\!\big(|\Delta F_z(t)|\big)$	1	mN	-35.50	mm
Force DRS	$\max\!\big(|\Delta F_x(t)|\big)$	23	mN	40.00	mm
with $y \ge 0\,\mathrm{mm}$	$\max\!\big(|\Delta F_y(t)|\big)$	3	mN	49.50	mm
	$\max\!\big(|\Delta F_z(t)|\big)$	11	mN	40.50	mm
Acceleration	$\max\!\big(|A_x(t)|\big)$	10.2	mm/s^2	-50.00	mm
	$\max\!\big(|A_y(t)|\big)$	1.2	mm/s^2	8.00	mm
	$\max\!\big(|A_z(t)|\big)$	2.2	mm/s^2	-36.80	mm
DiLET	$\max\!\big(V_z(t)\big)$	2.59	V	8.00	mm
	$\min\!\big(V_z(t)\big)$	-2.22	V	-50.00	mm
DiLET DRS with $y \le 0\,\mathrm{mm}$	$\max\!\big(|\Delta V_z(t)|\big)$	0.218	V	38.50	mm
DiLET DRS with $y \ge 0\,\mathrm{mm}$	$\max\!\big(|\Delta V_z(t)|\big)$	0.028	V	-37.00	mm

*Values rounded to significant figures with respect to the standard deviation.

4.6 Intermediate Summary

The chapter on experimental studies dealt with the systematic examination of the measurement procedure of LET. The main focus of this chapter is on comprehensibility and repeatability of the presented studies. Furthermore, the experimental results serve as objective data for the validation of numerical approaches as they are used for the theoretical determination of the Lorentz force.

At first, the measurement procedure of LET is described in terms of a measurement principle and a measurement method. The measurement principle in LET is decomposed into a causal sequence, in terms of cause and effect, resulting in two basic cause-effect-relationships and one or more force measurement principles. Afterwards, the logical organization of all operations used to perform an LET measurement are explained in the measurement method. The following description covers the realization of the rectilinear motion of the UUT relative to the stationary PM and the attached sensor system. The analysis of this particular realization separates six individual components and describes their respective function.

After the description of the measurement procedure the main components of the experimental setup and their functional relationship are explained and selected elements are described in detail. The specifications of the linear drive and the straightness measurements for the qualification of the linear guide are discussed, as well as the relevance of velocity deviations. After a brief description of the used 2D-positioning stage, a detailed characterization of the sensor system is given. All four components of the sensor system are analysed and the necessary sensor sensitivities are derived and listed. The description of the experimental setup is closed with the characterization of the data acquisition devise and the developed MCS for the main devices.

The next section is about DSP in LET and the extension of the deterministic (ideal) measurement process to a real measurement process, which considers physical quantities as random variables. Based on this generalization of the problem two different concepts of signal ensembles are introduced, namely the ideal and the artificial signal ensemble. It has been highlighted that the statistical properties of the LET signals are not independent of time. Thus, a single signal $x_h(t)$ of the non-stationary process can not provide a complete measurement result, i.e. expected value of the measurand $\mathbf{F}(t)$ and corresponding experimental standard deviation $\sigma_{\mathbf{F}}(t)$. Afterwards, different methods for signal alignment are discussed, wherein the cross-correlation of the x-component of the force turned out to be the most appropriate solution for the creation of artificial signal ensembles.

In order to complete the section on DSP in LET, the flowchart of the developed DSP procedure has been explained in all its components. This also includes the calculation of the expected value of the measurand and the experimental standard deviation of the mean, which in combination build a complete measurement result of the non-stationary signals.

The next two sections give a representative overview of the measurement performance of the experimental setup for applications with and without defects.

The discussed results of the first two studies illustrate the principal features of the recorded signals and verify the performance of the developed alignment procedure, as well as its robustness for distinctly different signal shapes. Especially the study of the monolithic aluminum bar serves as a reference experiment for non-ferromagnetic UUTs with high isotropic electrical conductivity.

The last two studies focus on the examination of the DRS from artificial subsurface defects in non-ferromagnetic materials. The study of stacked aluminum sheets, including a large subsurface defect, has shown the DRS of the applied transducers for a complete scan of the UUT with multiple repetitions (observations). Thus, an expectation was created for the shape and relative magnitudes of DRSs for UUTs with high anisotropic electrical conductivity. The study of the UUT made of GLARE illustrated the detection capabilities of the enhanced experimental setup and serves as a reference for the evaluation of LET in recent industrial applications.

From these four employed studies, three *key points* can be deduced for the further development of the measurement method of LET.

First, in all measurements a systematic harmonic distortion is observable in the seven presented sensor outputs, which potentially obscures the DRS of a present defect. A possible cause of this distortion is the dynamic behavior of the components of the experimental setup, e.g. 3-axes force sensor K3D40.

Second, the occurrence of diagonal patterns is observed which are proportional to the number of previous observations. The phenomenon is traced back to a non-constant gear ratio, which can likely be caused by the geometrical tolerance of the belt gear components, i.e. the set of two pulleys of the belt drive. The non-constant gear ratio results in a small variation of the velocity, which directly affects all measurands. The variation is slightly shifted with every measurement due to an anisotropic belt slip, which causes the diagonal pattern in successive measurements. This phenomenon also helps to explain not understood disturbance signals in previous works.

Third, it was observed that the z-component of the force is less influenced by both types of distortions than $F_x(t)$ and $F_y(t)$. This robustness against disturbances is even more pronounced for the voltage signal of the 1-axis DiLET sensor.

MECHANICAL MODELING

This chapter deals with the mechanical modeling of the dynamics of the experimental setup for LET. It has been shown that in all measurements a systematic harmonic distortion can be observed (Section 4.4 & 4.5). This distortion is identified to be one of the major limitations for the detection capability of the LET method. In order to overcome these limitations, it is necessary to understand the mechanics of the experimental setup and to formulate a mathematical model, which can describe the response of the measurement apparatus to the time-varying Lorentz force.

Such a mathematical model can be used to improve the prediction of the measured force components for a specific experimental setup and does serve as an extension of the electromagnetic field computations for the modeling of LET. Furthermore, the mathematical model can support the design process for the improvement and development of new experimental setups for LET. Another important aspect of the mathematical description is the design of digital filters in order to calculate an estimate of the corrected measurement result of the Lorentz force. The method to obtain a mathematical description of the dynamic behavior of the measurement process is called *system identification* [6, 90].

The main contribution of this chapter is the presentation of a system identification procedure for LET to obtain a *minimal model* for two concrete measurement results, in order to describe the dominant dynamic characteristics of the experimental setup sufficiently. In the first case, two independent single-input/single-output models are defined to describe the dominant dynamical behavior of a former prototype of the experimental setup at high velocities. In the second case, a multi-input/multi-output model with three degrees of freedom is used to model the dynamics of the actual experimental setup, as it is described in Sec. 4.2.

The presented procedure consists of four steps: (i) signal analysis, (ii) signal pre-processing, (iii) selection of the model structure, and (iv) parameter estimation.

The *analysis* of the measurement result is supported by the comparison with results of numerical simulations and is used to reveal the dynamic aspects of the systematic measurement errors (bias). The *signal pre-processing* is a necessary step for the successful estimation of the model parameters. It is based on the knowledge about the physical phenomenon studied in Chapter 3 and the examination of the measurement apparatus in Sec. 4.2. The *selection of the model structure* aims at finding a minimal model, which can describe the dominant dynamical behavior of the experimental setup. It determines the degree of freedom (DOF) and the number of parameters to be identified. The *parameter estimation* is the process of estimating the model parameters in order to minimize a cost function, which describes the difference between predicted and observed sensor output.

5.1 Mechanical Modeling without Sensor Crosstalk

The first example for mechanical modeling of the experimental setup is applied to a measurement result obtained from an experiment performed on a former prototype of the setup.

The UUT is a monolithic aluminum bar with size $250\,\text{mm} \times 50\,\text{mm} \times 50\,\text{mm}$. It has an isotropic electrical conductivity $\bar{\sigma} \pm 2u(\bar{\sigma}) = (19.8 \pm 0.16)\,\text{MS/m}$ at $20\,°\text{C}$, determined using the ECT device Elotest N300. The used PM is of cylindrical shape with diameter $D = 15.0\,\text{mm}$ and height $H = 25.0\,\text{mm}$. It is axially magnetized and characterized by a material grade of N38, which corresponds to a nominal magnetic remanences of $B_{\text{r,N}} = 1.17\,\text{T}$. The measurement result is part of an experimental study, which consists of repeated observations ($K = 20$) at $y = 0.00\,\text{mm}$ and $h = 1.00\,\text{mm}$ for different velocities. The discussed measurement result is obtained at $v_{\text{N}} = 2.00\,\text{m/s}$.

The numerical calculations are performed in 3D using a scalar magnetic potential formulation outside the conductor, and a modified magnetic vector potential formulation inside the conductor [21].

5.1.1 Signal Analysis

Figure 5.1 shows the complete measurement result (solid line) of the force $\mathbf{F}_{\text{Exp}}(t)$ for the monolithic aluminum bar in comparison with the predicted (dashed line) Lorentz force from numerical field computations. The solid lines show the expected value of the respective force component $\bar{F}_{\text{Exp},i}(t)$ of the $K = 20$ observations, with $i \in \{x, y, z\}$. The estimate of the 95 %-confidence interval is not recognizable, because even the maximum of the experimental standard deviation of the mean (eSDM) $\max\left(u\left[\bar{\mathbf{F}}(t)\right]\right) = \left[3.25\,\text{mN}, 1.65\,\text{mN}, 8.15\,\text{mN}\right]^{\text{T}}$ is too small in comparison to the shown force range. The data are plotted against the joint time t of the artificial signal ensemble $\{x_k(t)\}$. The predicted Lorentz force $F_{\text{Sim},i}(x)$, with $\Delta x = 1\,\text{mm}$, is transformed to the time domain $F_{\text{Sim},i}(t)$ using spline interpolation provided by the MATLAB™ function `interp1` [81], with 'spline'-option, constant velocity $v_{\text{Sim}} = 2\,\text{m/s}$, and virtual sampling frequency $f_{\text{Sim,s}} = 10\,\text{kHz}$.
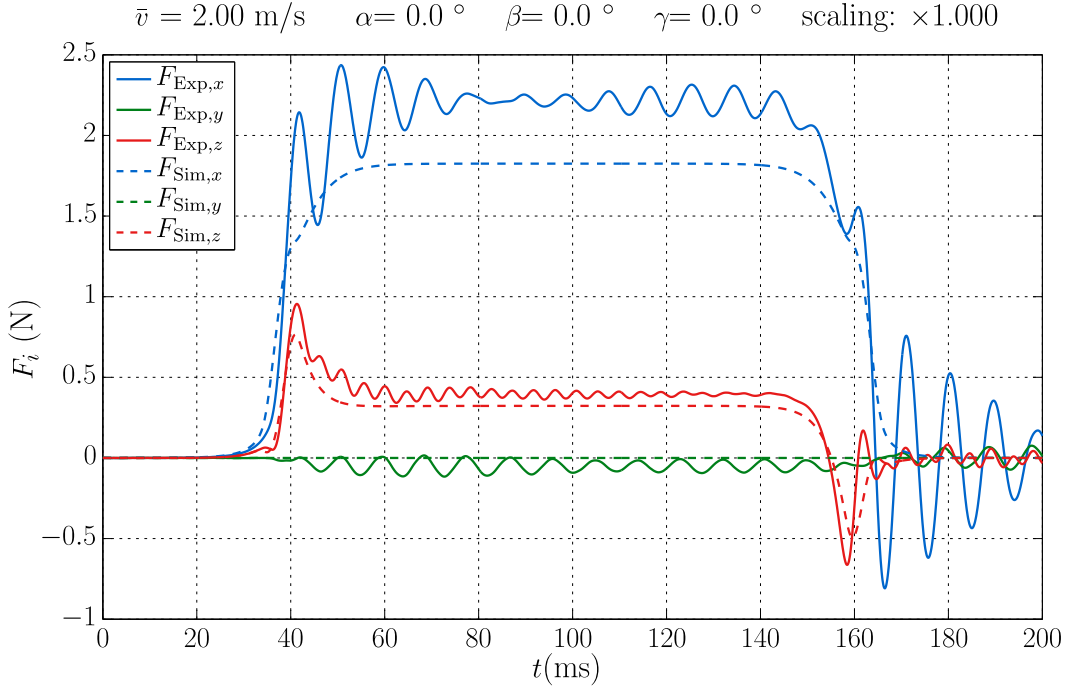
Figure 5.1: Comparison of the complete measurement result (solid line) of the force $\mathbf{F}_{\text{Exp}}(t)$ for the monolithic aluminum bar and the predicted (dashed line) Lorentz force from numerical field computations.

The direct comparison of measured and predicted force components reveals multiple differences in the signals. Most notably are the oscillatory disturbances, which are superimposed to the three measured force components $F_{\text{Exp},i}(t)$. Each disturbance occurs at the leading and trailing edge of the UUT and shows one respective dominant oscillation frequency and an immediate decay after each excitation. Experimental investigations have shown that depending on the relative velocity and the PM shape, these excitations can lead to significant vibrations of the experimental setup. The mechanical modeling in this study will be focused on these harmonic distortions.

The second notable difference can be seen for the mean value of the respective force components between the leading and trailing edge of the UUT. The measured x- and z-component of the force are significantly larger, while the mean of the y-component is not zero as it is expected at the centerline ($y = 0\,\text{mm}$). This inconsistency can be explained with the unintended rotatory misalignment of the force sensor relative to the defined coordinate system S'.

A less obvious distinction is revealed by the time difference between the peaks in the z-component of the respective signals. It can be observed that this time gap is slightly shorter in the measured force than in the simulation results. A subsequent examination of the slide positioning, using laser interferometer XL-80 by *Renishaw plc*, revealed an increased travel in comparison to the set value caused by an insufficient configuration of the controller of the linear drive. The resulting gear ratio deviation caused the slightly increased mean velocity $\bar{v}$.

5.1.2 Signal Pre-Processing

Before the simulation can be used for the parameter estimation of a mechanical model, several inconsistencies between the numerical field computation and real measurement results have to be adjusted.

5.1.2.1 Pre-Processing Methods

First, the velocity difference is corrected by estimating the mean velocity during the experiment $\bar{v}_{\text{Exp}}$, assuming a constant sampling rate f_s of the ADC. The velocity v_{Sim} in the interpolation procedure is varied until the mean squared error $\text{MSE} = \sqrt{\sum_i \left(\text{MSE}_i \right)^2}$ is minimal with

$$\text{MSE}_i = \frac{1}{N} \sum_{n=1}^{N} \left(F_{\text{Exp},i}[n] - F_{\text{Sim},i}[n] \right)^2 , \tag{5.1}$$

where $F_i[n] = F_i(nT_s)$, where $T_s = 1/f_s$ and $i \in \{x, y, z\}$. The optimization is performed using the modified simplex search method of [72] implemented in MATLAB™ function fminsearch.

The second step is the estimation of the assumed rotatory misalignment of the force sensor. For simplicity it is assumed that the misalignment only affects the measurement of the force components but not the orientation of the PM. Thus, the influence of a rotated primary magnetic field $\mathbf{B}^{(p)}$ on the electromagnetic interaction with the UUT is neglected.

To estimate the sensor rotation, it is preferable to calculate a rotation matrix which transforms the simulated force signals according to the rotated sensor coordinate system. The rotation of the measured force signals, according to the ideal coordinate system of the simulation results, would lead to a superposition of the harmonic distortion which is contradicting to the observations made.

The third step is the estimation of unconsidered process uncertainties by the calculation of a linear scaling factor $s_l \in \mathbb{R}$, which minimizes the MSE between simulated and the measured signals. Using a linear scaling factor implies the assumption that the magnetic remanence B_r, which has a quadratic influence on all components of the Lorentz force, has the main contribution to the unconsidered process uncertainties. This assumption is supported by the results of the uncertainty analysis of the electromagnetic field problem [147] using actual uncertainties of the developed experimental setup.

The result of the second and third pre-processing step are highly dependent from each other and only lead to a sufficient estimate if executed together. A robust implementation is obtained when using a *closed-form quaternion based solution* [49, 144, 155] for the parameters of the Helmert transformation. This transformation is frequently used in geodesy and describes a seven-parameter transformation of one datum to another as

$$\mathbf{x}_{\text{HT}} = \mathbf{t} + s_l \big[\mathbf{R} \big] \mathbf{x} \tag{5.2}$$

where $\mathbf{x}_{\text{HT}}$ is the transformed vector, $\mathbf{t}$ is the translation vector, s_l is the mentioned linear scaling factor, $\big[\mathbf{R} \big]$ is the rotation matrix, and $\mathbf{x}$ is the initial vector. The result of the closed-form
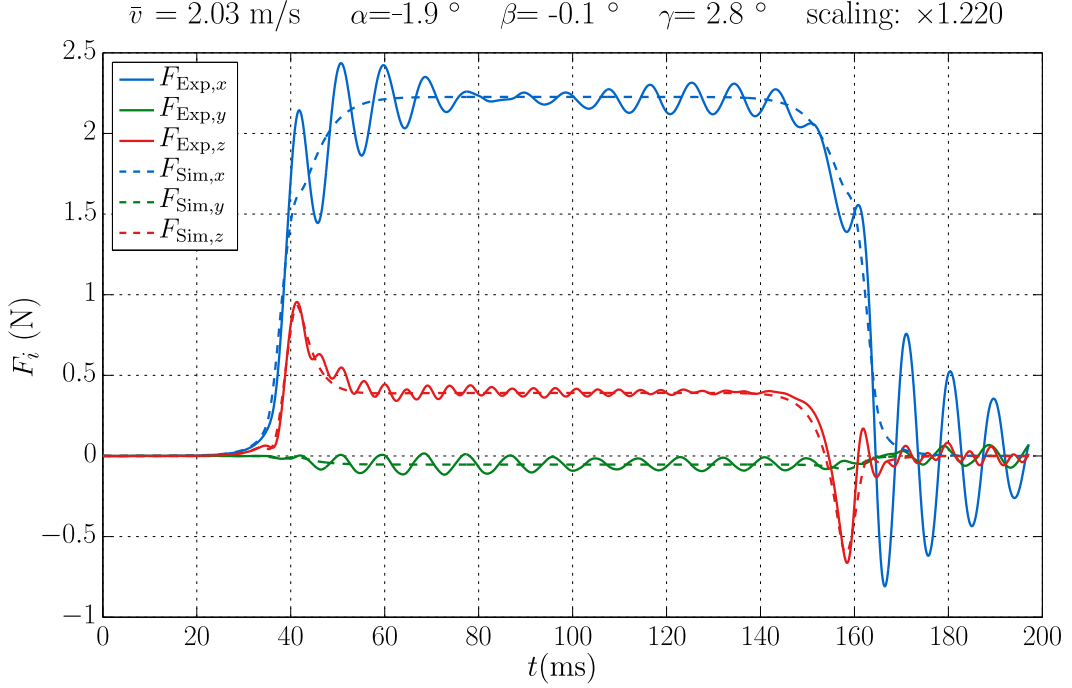
Figure 5.2: Result of the pre-processing procedure with estimated mean velocity v_est, rotation of simulated Lorentz force, and linear upscaling of $s_1 = 1.220$. The effective value of the magnetic remanence $B_\text{r,eff}$ is estimated as $B_\text{r,eff} = \sqrt{s_1}B_\text{r,N} = \sqrt{1.22}\,1.17\,\text{T} = 1.29\,\text{T}$.

solution for the Helmert transformation provides in addition to s_1 and $[\mathbf{R}]$ also $\mathbf{t}$ which is negligible small since the measured force signals are already offset-corrected.

The yaw, pitch, and roll angles α, β, and γ can be calculated from the estimated rotation matrix $[\mathbf{R}]$ according to the z, y', x''-convention using [26] as

$$\alpha = \text{atan2}(r_{21}, r_{11}) \tag{5.3a}$$

$$\beta = \text{atan2}\left(-r_{31}, \sqrt{r_{11}^2 + r_{21}^2}\right) \tag{5.3b}$$

$$\gamma = \text{atan2}(r_{32}, r_{33}) \tag{5.3c}$$

where r_{ij} are the matrix elements of $[\mathbf{R}]$.

5.1.2.2 Pre-Processing Results

Figure 5.2 shows the result of the described pre-processing methods. The mean velocity during all measurements is estimated to $\bar{v} = 2.03\,\text{m/s}$, which is a deviation of 1.5% compared to the nominal value of $v = 2.00\,\text{m/s}$ m/s. Additional investigations of the experimental setup have shown that the effective radius of the belt-pulley combination of the linear drive is greater than previously defined in the controller settings which caused the discrepancy in velocity. The sensor misalignment with yaw, roll, and pitch angle are estimated as $\alpha = 1.9°$, $\beta = -0.1°$, and

$\gamma = 2.8°$, respectively. This deviation is reasonable taking into consideration the expectable uncertainties of position and relative orientation of linear drive and 3-axes force sensor.

However, the scaling factor of $s_l = 1.220$ does not confirm the parameters used for the simulation. Assuming a dominant influence of the magnetic remanence B_r on the remaining deviation, then the effective value of the magnetic remanence $B_{r,\text{eff}}$ could be estimated as $B_{r,\text{eff}} = \sqrt{s_l} B_{r,N}$. A later examination revealed that the used PM was mislabeled and the PM actual material was N42 ($B_r = 1.29\,\text{T}$) instead of N35 ($B_r = 1.17\,\text{T}$).

The pre-processing was therefore repeated with a numerical simulation with the correct magnetic remanence and velocity, resulting in a new scaling factor of $s_l = 1.003$. This result also confirms that a linear scaling factor in the pre-processing is suitable for the estimation of the effective value of the magnetic remanence $B_{r,\text{eff}}$, if the remaining input parameters (e.g. h, σ) are well known.

5.1.3 Model Selection

The model selection for the minimal model is the definition of a *ordinary differential equation* (ODE) model which describes the dominant oscillatory distortion that is observed in the measured forces. The underlying conjecture for the selection is that the square-wave-like absolute value of the Lorentz force is creating an *impact load* on the deflection body of the force sensor which leads to an impulse response of all three components. The force sensor is considered to behave as a series connection of independent compliant structures each with a *single degree of freedom* (SDOF).

Under these assumptions it is possible to model each axis of the force sensor as a *damped* SDOF system with a single *eigenfrequency* in order to describe the dynamic behavior of the sensor due to an acting Lorentz force at high velocities. Each model is characterized by discrete parameters which are constant, i.e. independent of time and the system state.

The *linear* ODE which describes the dynamics of a SDOF system is deduced in classical mechanics according to Newton's 2nd law as

$$m_i \frac{d^2 x_i}{dt^2} + c_i \frac{dx_i}{dt} + k_i x_i = F_{L,i}(t) \,, \tag{5.4}$$

with $i \in \{x, y, z\} = 1, 2, 3$, where m_i is the inertial mass of the body, c_i the damping coefficient (viscous damper), k_i the stiffness of the system, and $F_{L,i}(t)$ the excitation of the system (Lorentz force). The dependent variable $x_i(t)$ is the *generalized coordinate* of the system which is measured from *static equilibrium*. Thus the gravitational force does not appear in the equations which simplifies the subsequent parameter estimation with the nulled measured force signals. In the context of a *state-space representation*, which is commonly used in control engineering, the generalized coordinate $x_i(t)$ is the single *internal state variable* that can represent the entire state of the respective SDOF system [95].

By dividing (5.4) with the mass m_i gives the *equation of motion* written as

$$\frac{d^2 x_i}{dt^2} + 2\zeta \omega_{0i} \frac{dx_i}{dt} + \omega_{0i}^2 x_i = \frac{F_{\text{L},i}(t)}{m_i} \, ,$$

(5.5)

where ζ_i is the (dimensionless) damping ratio and ω_{0i} the undamped angular frequency which together describe the *linear time-invariant* (LTI) system in the time domain. The coefficients ζ_i and ω_{0i} are given by

$$\zeta_i = \frac{c_i}{2\sqrt{k_i m_i}} \quad \text{and} \quad \omega_{0i}^2 = 4\pi^2 f_{0i}^2 = \frac{k_i}{m_i} \, ,$$

(5.6)

where $f_{0i} = \omega_{0i}/2\pi$ is the (undamped) eigenfrequency of the oscillator.

In the following only force profiles examined along the centerline are considered ($y = x_2 = 0$). In this case the y-component of the Lorentz force $F_{\text{L}y}$ has been found to be equal to zero and does not have to be considered in the model. Each of the remaining two force components $F_{\text{L}1}(t) = F_{\text{L}x}(t)$ and $F_{\text{L}3} = F_{\text{L}z}(t)$, serves as an input for the corresponding SDOF systems.

5.1.4 Parameter Estimation

The parameter estimation of the SDOF systems described in (5.5) is performed individually for each component of the two considered force components ($i \in \{x, z\} = 1, 3$). The estimation procedure is based on the direct comparison of observed and predicted system state and serves to minimize the error between both signals.

The first step of the estimation procedure is the *Laplace transformation* of the ODE from time domain to an algebraic equation in the frequency domain given by

$$s^2 \widehat{x}_i + 2\zeta_i \omega_{0i} \widehat{x}_i s + \omega_{0i}^2 \widehat{x}_i = \frac{\widehat{F}_{\text{L},i}(s)}{m_i} \, ,$$

(5.7)

where $\widehat{F}_{\text{L},i}(s) = \mathscr{L}\{F_{\text{L},i}(t)\}(s)$ with $s \in \mathbb{C}$, is the Laplace transform of the input load and $\widehat{x}_i(s) = \mathscr{L}\{x_i(t)\}(s)$ is the Laplace transform of the generalized coordinate of the system (output).

Using (5.7) the output $\widehat{x}_i$ is related to the input $\widehat{F}_{\text{L},i}(s)$ by the transfer function $H_i^*(s)$ which is determined by

$$H_i^*(s) = \frac{\widehat{x}_i}{\widehat{F}_{\text{L},i}(s)} = \frac{1/m_i}{s^2 + 2\zeta_i \omega_{0i} s + \omega_{0i}^2} \, ,$$

(5.8)

describing the linear mapping of $\widehat{F}_{\text{L},i}$ on $\widehat{x}_i$.

With this representation of the dynamic system two difficulties arise. First, the displacement $x_{\text{Exp},i}(t)$ of the PM is not measured during the experiment. This requires an additional calibration of the force sensor to determine the deformation of the deflection body for a given load in order to estimate the deflection from the measurement result of the force $\mathbf{F}(t)$. Thus, the displacement $x_{\text{Exp},i}(t)$ can not be compared to the predicted output $x_i(t)$ of the minimal model. Second, the transfer function $H_i^*(s)$ includes the actual mass m_i of the oscillating body which

would have to be estimated by the summation of the PM mass m_{PM} and a part of the overall mass of the force sensor $m_{FS,i}$.

A simple way to overcome these difficulties is to use the *spring force* $F_{S,i}(t) = k_i x_i(t)$ of the model as a *derived state variable* for the observation (output) of the system state. The spring force $F_{S,i}(t)$ is invariant on the mass m_i if the generalized coordinate is defined in static equilibrium. Therefore, the mass m_i can be set to an arbitrary number, as long as there is no requirement for determining the displacement $x_i(t)$ of the mass. The number of parameters that need to be estimated for each model is reduced to two parameters.

With this in mind, an alternative transfer function $H_i(s)$ is defined as

$$H_i(s) = \frac{\widehat{F}_{S,i}(s)}{\widehat{F}_{L,i}(s)} = \frac{\omega_{0i}^2}{s^2 + 2\zeta_i \omega_{0i} s + \omega_{0i}^2} \,, \tag{5.9}$$

with the Laplace transform of the spring force $\widehat{F}_{S,i}(s)$. The spring force in the SDOF model $F_{S,i}(t)$ can directly be compared to the measured force component $F_{Exp,i}(t)$.

The next step of the estimation procedure is the simulation of the time response $F_{S,i}(t)$ of the dynamic system on the excitation $F_{L,i}(t)$ obtained from numerical computations of the electromagnetic field problem. For this purpose, a simulation environment is implemented in MATLAB™. It includes the creation of the *single-input/single-output* (SISO) transfer function model using the function `tf` and the simulation of the system response using function `lsim` with discretized sampling period of $\Delta t = 0.1\,\mathrm{ms}$.

The objective function of this optimization problem is defined as the mean squared error

$$\mathrm{MSE}_{S,i} = \frac{1}{N} \sum_{n=1}^{N} \left(F_{Exp,i}[n] - F_{S,i}[n] \right)^2 \,, \tag{5.10}$$

of the derived system output $F_{S,i}(t)$ and the measured force component $F_{Exp,i}(t)$ which is a common measure of estimation quality. In this simulation environment the parameters ζ_i and ω_{0i} are estimated using the MATLAB™ function `fminsearch`.

5.1.5 Results

Figures 5.3(a) and 5.3(b) show the simulated spring forces $F_{S,i}(t)$ for the mechanical model with estimated parameters ζ_i and ω_{0i} in comparison to the measured force components $F_{Exp,i}(t)$ and the model input loads $F_{Sim,i}(t)$. The estimated mean velocity $\bar{v}$ and optimal parameters are depicted on top of each graph together with the value of the *normalized root mean squared error*

$$\mathrm{NRMSE}_{S,i} = \frac{\sqrt{\mathrm{MSE}_{S,i}}}{\Delta F_{Exp,i}} = \frac{\sqrt{\frac{1}{N} \sum_{n=1}^{N} \left(F_{Exp,i}[n] - F_{S,i}[n] \right)^2}}{\max\left(F_{Exp,i}[n] \right) - \min\left(F_{Exp[n],i} \right)} \,, \tag{5.11}$$

which is an estimator of the relative error of the predicted system response.

As a result, a very good agreement can be observed with $\mathrm{NRMSE}_{S,x} = 2.66\%$ and $\mathrm{NRMSE}_{S,z} = 2.00\%$. The estimated undamped angular frequencies ω_{0i} correspond to the experimentally acquired parameters from dynamic sensor calibration procedure of the force sensor without PM [128].
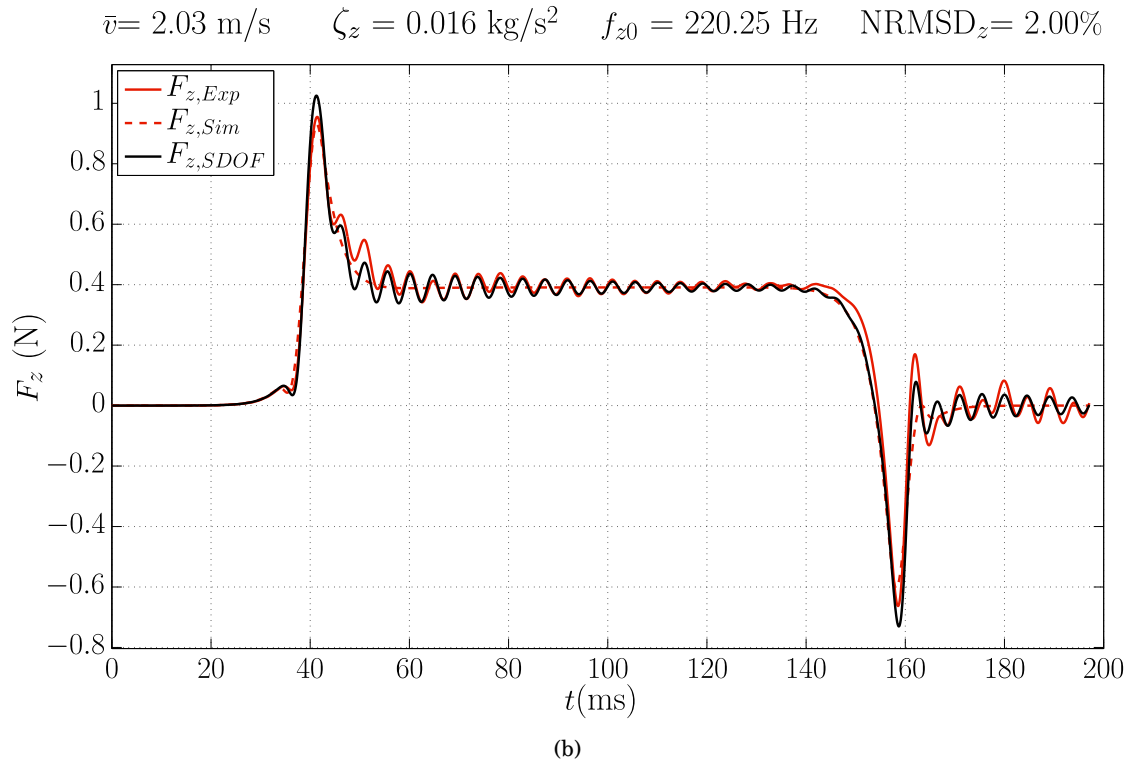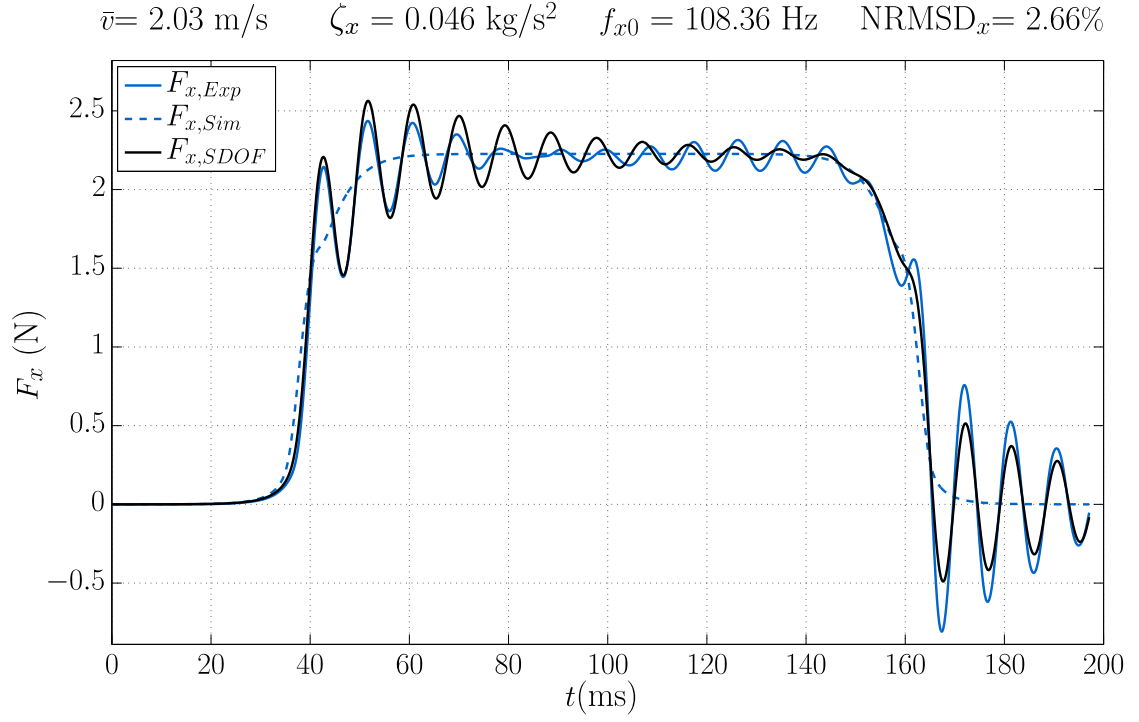
(a)

(b)

Figure 5.3: Comparison of the simulated spring forces $F_{\mathrm{S},i}(t)$, the measured force components $F_{\mathrm{Exp},i}(t)$ and the model inputs $F_{\mathrm{Sim},i}(t)$ (Lorentz force components) for $i \in \{x, z\} = 1, 3$.

A disagreement in oscillation characteristics in the x-component of the force can be observed. After the leading edge, the estimated model output is larger (overshoot) than the measured sensor output, while at the trailing edge the estimated model output is smaller. This deviance can be caused by a force depending (implicit time depending) damping ratio $k_i = k_i(F_i(t))$ due to additional eddy current damping or an unconsidered crosstalk between the different sensor axes.

5.2   Mechanical Model with Sensor Crosstalk

The second presented case for the system identification procedure is applied to a measurement result comparable to the experimental studies in Section 4.5. It is an example for the need to consider form deviation of the UUT leading to an extended pre-processing procedure. Furthermore, this example demonstrates how a minimal model can describe correlating oscillations and sensor crosstalk by a multi-input/multi-output (MIMO) model with only three degrees of freedom.

The study examines the measurement result of a stack of 24 aluminum sheets, each with size of $250\,\text{mm} \times 50\,\text{mm} \times 2\,\text{mm}$, similar to Section 4.5.1 but without an included artificial defect. The sheets are naturally coated with an aluminum oxide layer and are separated additionally with electrical insulation paper ($40\,\mu\text{m}$). Thus, the sheets are regarded as electrically insulated from each other which is considered in the numerically computed Lorentz force components (inputs) with $\sigma_{zz} = 0\,\text{S/m}$. The testing velocity is $v = 0.50\,\text{m/s}$ and the lift-off distance is $h = 1.00\,\text{mm}$. The used PM is a custom-built cylindrical Halbach structure already tested in Section 4.4.2. It is characterized by a highly focused magnetic field at the bottom of the PM which results in a shorter rise time of the square-wave-like Lorentz force leading to a significant dynamic response of the experimental setup. The mass of the Halbach structure is approximately $60\,\%$ higher than the mass of the PM in the first case and the expected Lorentz force is larger despite the fact that the testing velocity is only a quarter of the previous case.

The incremental position encoder was used to adjust the parameters of the control loop of the linear drive to ensure a correct mean velocity $\bar{v}$ and reduced experimental standard deviation σ_v during operation. Furthermore, the 3-axes accelerometer was used to obtain additional information of the system state. The measured acceleration $\mathbf{A}_{\text{Exp}}(t)$ near the force sensor enables the partial observation of the oscillation of the measurement frame caused by the Lorentz force excitation. Due to various changes in the experimental setup, the system is expected to have a different dynamic behavior compared to the first case.

5.2.1   Signal Analysis

Figure 5.4 shows the expected value $\mathbf{F}_{\text{Exp}}(t)$ (solid line) of the measured force in comparison with the predicted Lorentz force $\mathbf{F}_{\text{Sim}}(t)$ (dashed line) from numerical field computations. A significant difference of the mean value of the measured and simulated results between leading
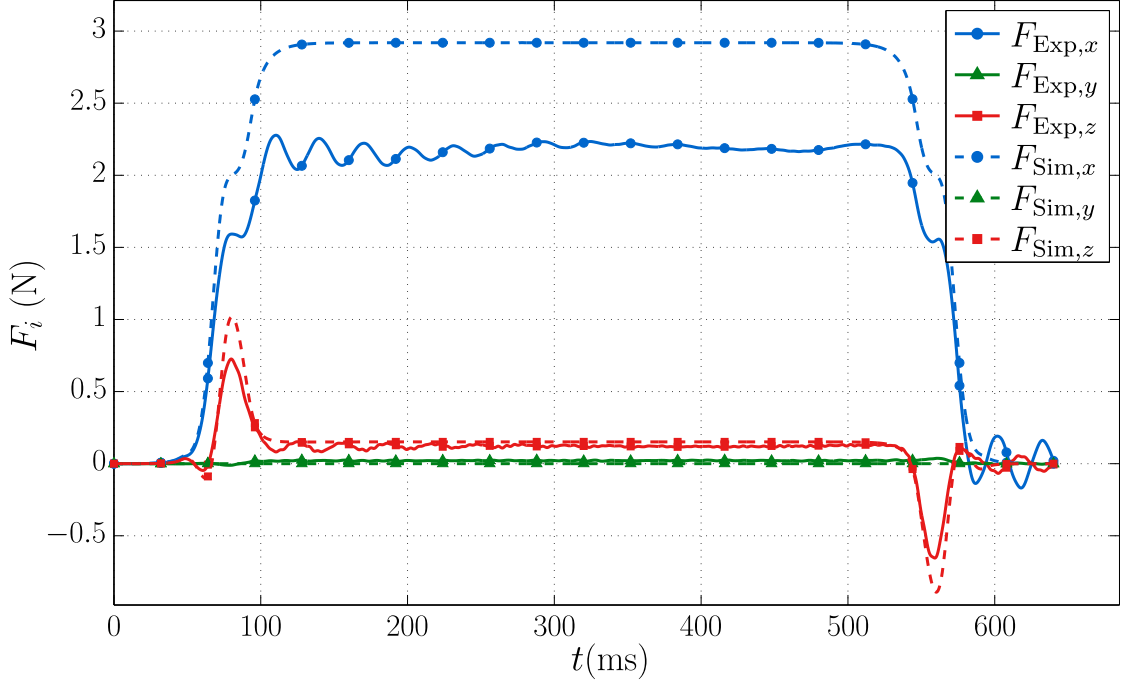
Figure 5.4: Comparison of measured force $\mathbf{F}_{\text{Exp}}(t)$ (solid line) and simulated Lorentz force $\mathbf{F}_{\text{Sim}}(t)$ (dashed line) of the stacked aluminum sheets.

and trailing edge can be observed in the direct comparison. The x-component of the simulated force overestimates the Lorentz force quite clearly by more than 30 %. A similar deviation can be seen in the result of the z-component, with an overestimate of approximately 23 %. In $F_{\text{Exp},x}(t)$ and $F_{\text{Exp},z}(t)$ similar oscillation patterns are observed. The y-component of the measured force is negligibly small and shows no notable oscillations compared to the other two components.

The enlarged view of the complete measurement result of the measured force components $F_{\text{Exp},i}(t)$ is given in Fig. 5.5. It shows the estimate of the 95 %-confidence interval of $K = 20$ observations. The *average* eSDM of the range shown in Fig. 5.4 is about $\bar{u}\big(\bar{\mathbf{F}}[n]\big) = \big[12.6\,\text{mN}, 1.9\,\text{mN}, 2.8\,\text{mN}\big]^{\text{T}}$ which indicates a low influence of random disturbances below the digital filter frequency of $f_{\text{c}} = 500$ Hz from DSP. The *median* of the *relative* uncertainty (relative eSDM)

$$\tilde{u}_{\text{rel},i}[n] = \frac{u_i\big(\bar{F}_i[n]\big)}{\bar{F}_i[n]} \; , \tag{5.12}$$

is particularly useful to estimate the amount of noise relative to the measured signal. The relative eSDM is $\tilde{u}_{\text{rel},x} = 0.8\,\%$, $\tilde{u}_{\text{rel},y} = 10.6\,\%$, and $\tilde{u}_{\text{rel},z} = 2.4\,\%$.

All three measured force components show three characteristic oscillation patterns in the low, meso, and high frequency range.

The x- and z-component are distorted by a *low-frequency* oscillation (≤ 6 Hz). The frequency of this oscillation is identified to be proportional to the mean testing velocity $\bar{v}$, but the oscillation pattern is not correlated with velocity deviations $\Delta v(t) = v(t) - \bar{v}$ during the experiments. This
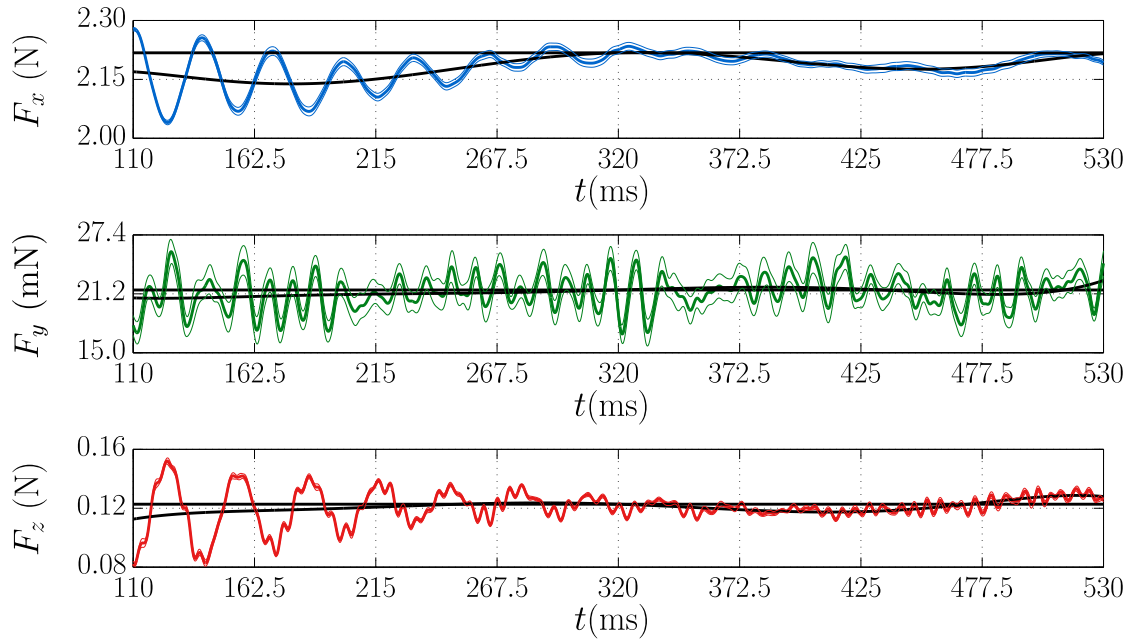
Figure 5.5: Enlarged view of the complete measurement result of the force components $F_{\text{Exp},i}(t)$ and polynomial curve fit (black curve) of low-frequency oscillations.

spatial variations are most likely caused by surface undulations of the UUT due to an uneven clamping force on the aluminum sheets for fixation. These surface undulations result in a spatial variation of the lift-off distance $\Delta h(x,y)$ which directly affects the Lorentz force. A polynomial curve fit (black curve) of this effect is depicted for all three components.

The y- and z-component show similar *high-frequency* oscillations which are in the range of identified eigenfrequencies of the 3-axes force sensor. The oscillations show more complex patters like *beating* and no substantial decay.

The x- and z-component of the measured force are additionally distorted by *meso-frequency* oscillations which dominate the overall dynamics of the measurement result. The oscillations are characterized by a frequency of about $30\,\text{Hz}$ for $F_{\text{Exp},x}(t)$ and $F_{\text{Exp},z}(t)$ which indicates a sensor crosstalk or the presence of an additional vibrating object.

Figure 5.6 shows the comparison of the measured accelerations $\mathbf{A}_{\text{Exp}}(t)$ and the estimated force deviations $\Delta\mathbf{F}_{\text{Exp}}(t)$ along the x-, y-, and z-direction. Each measured force component is coupled to the corresponding acceleration and shows a distinctive anti-correlation. This observation further supports the idea of an additional oscillating object which is connected to the force sensor and is indirectly excited by the Lorentz force.
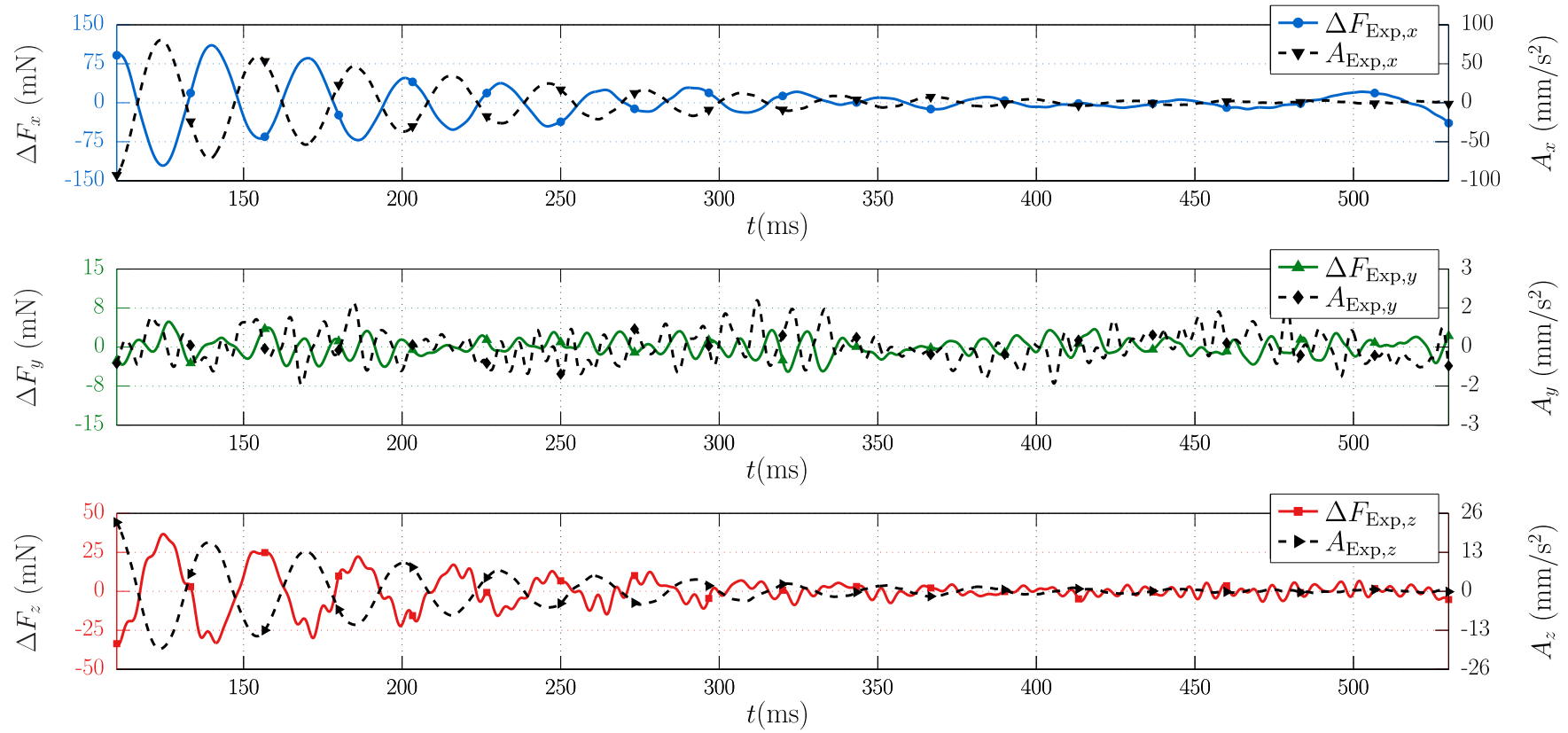
Figure 5.6: Comparison of the measured acceleration $\mathbf{A}_{\mathrm{Exp}}(t)$ and drift-corrected force components $\Delta F_{\mathrm{Exp},i}(t)$ shows strong (anti-) correlation along x- and z-direction of *meso-frequency* oscillations.

A frequency analysis of the velocity, force and acceleration signals shown in Fig. 5.7 confirmed this observation. For the comparison the actual value of the Fourier-transformed signals is of no particular interest, since different physical quantities are compared. Therefore, the depicted components are normalized to the maximum component of the corresponding physical quantity, i.e. $|v(f)|$ is normalized to $\max|v(f)|$, $|F_{\mathrm{Exp},i}(f)|$ is normalized to $\max|F_{\mathrm{Exp},x}(f)|$, and $|A_{\mathrm{Exp},i}(f)|$ is normalized to $\max|A_{\mathrm{Exp},x}(f)|$.
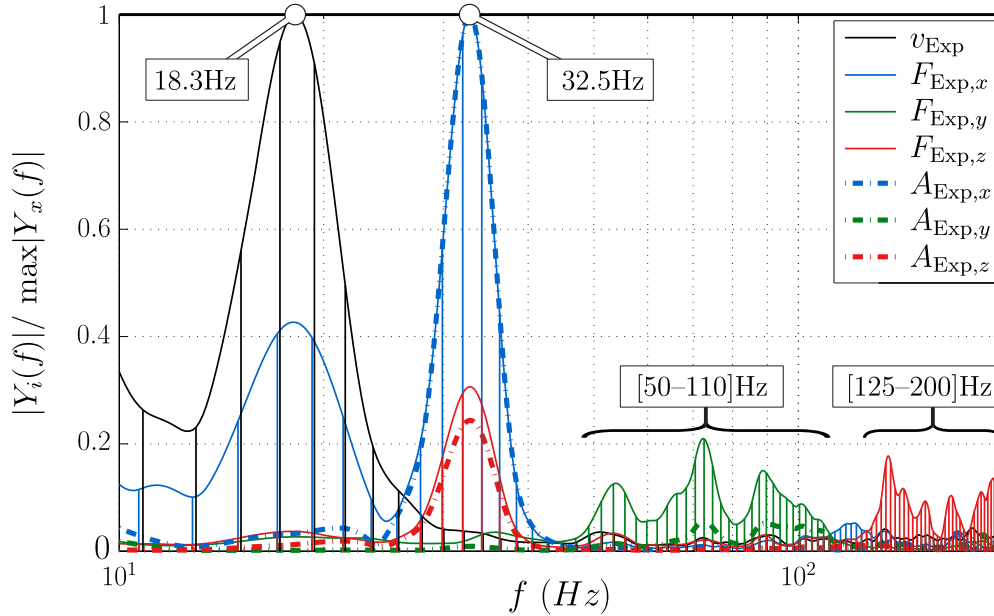

Figure 5.7: Frequency analysis of the velocity $v_{\mathrm{Exp}}(f)$, force component signals $F_{\mathrm{Exp},i}(f)$ and acceleration signals $A_{\mathrm{Exp},i}(f)$.

The most important result is the perfect match of the x- and z-components of the measured force and acceleration at $f_{\mathrm{m}} = 32.5\,\mathrm{Hz}$. The proportion of $|F_{\mathrm{Exp},z}(f_{\mathrm{m}})|/|F_{\mathrm{Exp},x}(f)|$ is almost equal to $|A_{\mathrm{Exp},z}(f_{\mathrm{m}})|/|A_{\mathrm{Exp},x}(f_{\mathrm{m}})|$ and confirms the observation of meso-frequency oscillations in the time domain.

Another interesting result is the correlation between the vibration of the slide ($|v_{\mathrm{Exp}}(f)|$) of the linear drive and the x-component of the measured force $|F_{\mathrm{Exp},x}(f_{\mathrm{m}})|$ at $18.3\,\mathrm{Hz}$, wherein at $32.5\,\mathrm{Hz}$ no correlation is observed. This suggests that the oscillatory motion of the slide results in a time-dependent Lorentz force which is observable in the measured force, while the oscilatory motion of the PM does not influence the motion of the slide. A contribution to the mathematical formulation of the former phenomenon is given in [149].

The high-frequency oscillations of the y- and z-components of the measured force (cf. Fig.5.5 and Fig.5.6) are not characterized by a single discrete frequency, but are composed of an aggregation of multiple frequencies. In the range of [50–110]Hz, $|F_{\mathrm{Exp},y}(f)|$ has its characteristic response with local maxima at [54, 73, and 89]Hz. A similar response can be found for $|A_{\mathrm{Exp},x}(f)|$. In the range of [125–200]Hz $|F_{\mathrm{Exp},z}(f)|$ has its characteristic response with local maxima

at [135, 168, and 193]Hz. A fact worth mentioning is that the measured acceleration only matches with the last two oscillations, but at 135Hz no significant correlation can be observed. Considering the discussed eigenfrequencies of the first example, this suggests that at 135Hz the z-components responds with its eigenfrequency. The eigenfrequency contributes to the high-frequency oscillation, but does not affect the vibration of the measurement frame.

These observations suggest a complex crosstalk between different components of the experimental setup. However, the energy contribution of these low-amplitude oscillations is negligible compared to the dominating oscillation pattern at 32.5 Hz.

In order to further examine the proportion of accelerations at 32.5 Hz a *correlation analysis* in the time domain between acceleration components $A_{\mathrm{Exp},i}(t)$ is performed. Figure 5.8 shows a linear correlation between the x- and z-component with the observed *meso-frequency* oscillation. The correlation is described by the slope κ_A of the measured accelerations in the A_z-A_x-plane and will be used for the reduction of the model structure. A significant correlation with the y-component is not confirmed.
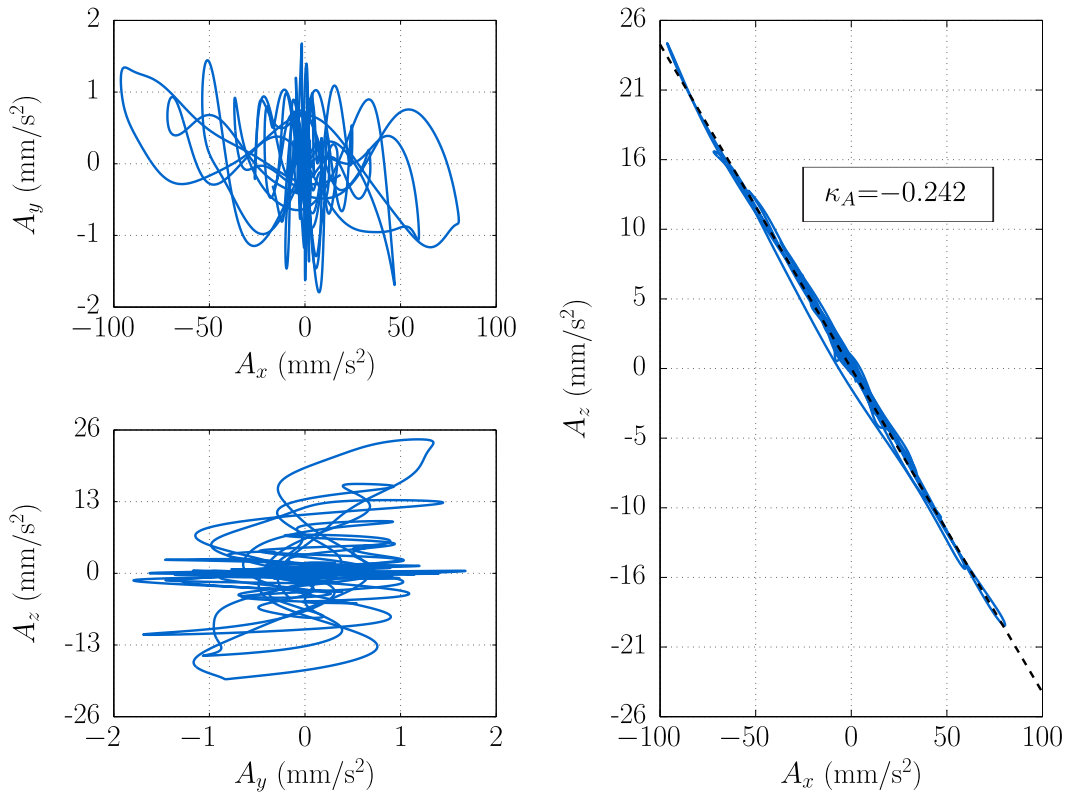

Figure 5.8: Correlation analysis of acceleration components $A_{\mathrm{Exp},i}(t)$. A linear correlation expressed by the coupling factor κ_A can be observed for the measured accelerations in the x-z-plane.

5.2.2 Signal Pre-Processing

The signal pre-processing for the discussed measurements is based on the results of the signal analysis and the findings in the previous case. The process is fully automated and requires no human intervention. The goal of signal pre-processing is to modify the simulated Lorentz force $\mathbf{F}_{\mathrm{Sim}}(t)$ to significantly improve the parameter estimation of a mechanical model.

5.2.2.1 Pre-Processing Methods

The first step in pre-processing is the resampling of the simulated results assuming a constant sampling rate f_{s} and velocity v_{Sim}. Using the result of the incremental position encoder, it has been proved that the adjusted control parameters are more sufficient to obtain correct mean velocity than in the previous case.

The second step is to take into account the effect of surface undulations which are leading to low-frequency oscillations depicted in Fig. 5.4(b). The straight black lines in each plot indicate the estimated force at the center of the specimen where the contact forces between UUT and PM was measured during the preparation step (cf. Sec.4.1.2). The black curves are determined by a higher order polynomial fit, which is formulated as an ordinary least squares problem, using a polynomial ansatz function of order six. The simulated force components of the x- and z-component are multiplied by the corresponding polynomial function normalized by the constant value at the center of the specimen. The y-component of the force is remained unchanged due to the observed lack of significance to the final result.

The second step is the estimation of the rotatory misalignment of the force sensor relative to the defined coordinate system in combination with the estimation of a linear scale factor. The estimation is again implemented as the beforehand described closed-form solution. The linear transformation (scaling and rotation) is necessarily applied to the simulated signals. Otherwise, the rotation of the measured data would lead to an unwanted superposition of the oscillations, disguising the existing crosstalk and finally, resulting in an unsuited model structure.

5.2.2.2 Pre-Processing Results

The result of the pre-processing procedure is shown in Fig. 5.9 together with the parameters of the estimated rotation and downscaling of the simulated Lorentz force $\mathbf{F}_{\mathrm{Sim}}(t)$.

The misalignment of the force sensor is estimated as α = -0.7°, β = 0.0°, and γ = -1.8° yaw, roll, and pitch angle, respectively. This is a reduction in comparison to the former experimental setup used in the first discussed case. The improved sensor alignment is made possible by the redesign of the sensor system mounting, including a spherical joint for increased sensitivity for angular adjustment.

The estimated scaling factor of s_{l} = 0.761 does not confirm the parameters used for the simulation of the complex Halbach structure. Assuming a dominant influence of the uncertainty
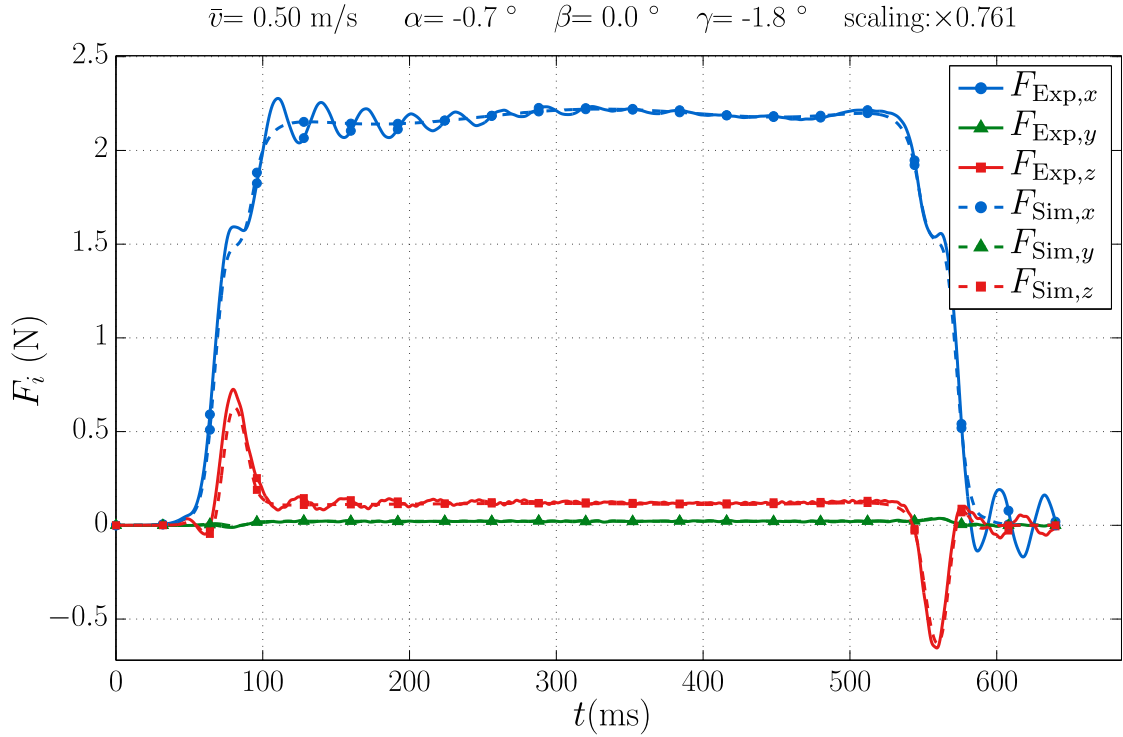
Figure 5.9: Result of the pre-processing procedure with estimated rotation of simulated Lorentz force and linear downscaling of $s_l = 0.761$. The effective value of the magnetic remanence $B_{r,eff}$ is estimated as $B_{r,eff} = \sqrt{s_l} B_{r,N} = \sqrt{0.761}\, 1.44\,\mathrm{T} = 1.26\,\mathrm{T}$.

of the magnetic remanence B_r, the effective value $B_{r,eff}$ is estimated as $B_{r,eff} = \sqrt{s_l} B_{r,N} = \sqrt{0.761}\, 1.44\,\mathrm{T} = 1.26\,\mathrm{T}$.

5.2.3 Model Selection

The model selection for a minimal model that considers sensor crosstalk is defined by a *system* of ODEs, describing the analyzed oscillatory distortions and the interaction of the significant components of the measurement. Thus, the modeling is reduced to the interaction of the x- and z-component of force and acceleration. The extended model will also be characterized by discrete parameters which are independent of time and the system state.

The assumption holds that the square-wave-like absolute value of the Lorentz force is considered as an impact load to the deflection body of the force sensor which causes the dynamic response. However, the strong correlation observed for the four measurands contradicts the previously assumed independence of individual compliant structures. $F_{Exp,x}$ and $F_{Exp,z}$ show the same oscillatory distortion at about $33\,\mathrm{Hz}$ which contravenes the significantly different dynamic parameters of the sensor axes, previously identified. Furthermore, the measured force components are strongly correlated (anti-correlation) to the respective measured acceleration components. These correlations do not imply a specific causation. However, they indicate an

underlying relationship between the measurands, since a simple coincidence can be ruled out.

The acceleration components are measured at the base plate of the force sensor and do partially describe its motion. Considering that the PM and the deflection body of the force sensor are successfully described as a damped SDOF system, a *third* damped SDOF system can be introduced whose generalized coordinate is indirectly described by the measured acceleration components. This third body is assumed to have a significantly higher mass than the two others, since the plate is mounted on the series connection of 2D-positioning stage and measurement frame. Such a high mass could be (indirectly) excited by the Lorentz force, but would be unaffected by the system state of the two connected damped SDOF systems.

A mechanical model that describes the observed behavior is synthesized by means of a *system of spring-mass-damper elements* in a series and parallel circuit (Fig. 5.10). The forces $F_{L,1}(t)$ and
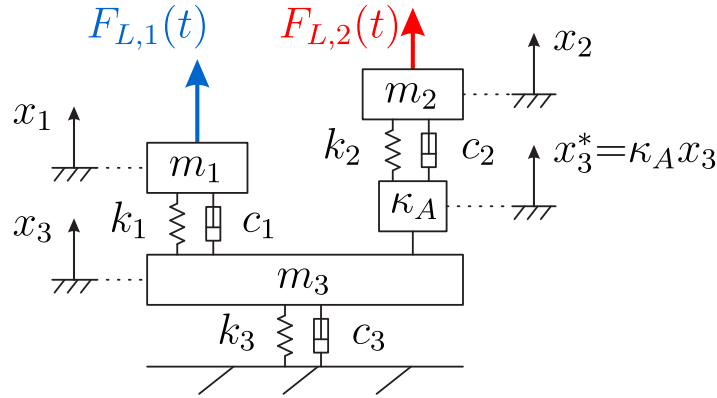

Figure 5.10: Mechanical model of a series and parallel circuit of three SDOF systems. The mass m_3 (measurement frame) is coupled directly with the mass m_1 (x-component of the force sensor) and indirectly coupled with mass m_2 (z-component). The coupling coefficient κ_A implements the linear correlated oscillations of the measured acceleration.

$F_{L,2}(t)$ are intended to represent the x- and z-components of the measured force, respectively. They describe the excitation of the MIMO system due to the Lorentz force (system input). The masses m_1 and m_2, as well as the corresponding spring and damping parameters, represent the dynamic properties of the corresponding force sensor axes. The mass m_3 represents the measurement frame coupled to the ground by spring and damper to model the *anti-vibration pads* shown in the description of the experimental setup (Sec. 4.2). The variables x_i describe the generalized coordinates (displacements) of the corresponding masses m_i and define the system state (system output).

The system of coupled ODEs is obtained by analyzing the free-body diagram (not shown) of each body. The resulting set of equations in the time domain is

$$m_1\ddot{x}_1 + c_1\dot{x}_1 + k_1x_1 - c_1\dot{x}_3 - k_1x_3 = F_{L,1}(t) \qquad (5.13a)$$

$$m_2\ddot{x}_2 + c_2\dot{x}_2 + k_2x_2 - \kappa_A c_2\dot{x}_3 - \kappa_A k_2x_3 = F_{L,2}(t) \qquad (5.13b)$$

$$m_3\ddot{x}_3 + \left(c_1 + \kappa_A c_2 + c_3\right)\dot{x}_3 + \left(k_1 + \kappa_A k_2 + k_3\right)x_3 - c_1\dot{x}_1 - k_1x_1 - c_2\dot{x}_2 - k_2x_2 = 0 \qquad (5.13c)$$

with the coupling coefficient κ_A and the constant parameters m_i, c_i, and k_i.

5.2.4 Parameter Estimation

The parameter estimation of the 3-degree-of-freedom system described in (5.13) is performed simultaneously for all components. The first step of the estimation process is the Laplace transformation of the system of ODEs from the time domain to the frequency domain:

$$m_1 s^2 \widehat{x}_1 + c_1 s \widehat{x}_1 + k_1 \widehat{x}_1 - (c_1 s + k_1)\widehat{x}_3 = \widehat{F}_{L,1}(s) \quad (5.14a)$$

$$m_2 s^2 \widehat{x}_2 + c_2 s \widehat{x}_2 + k_2 \widehat{x}_2 - (\kappa_A c_2 s + \kappa_A k_2)\widehat{x}_3 = \widehat{F}_{L,2}(s) \quad (5.14b)$$

$$m_3 s^2 \widehat{x}_3 + (c_1 + \kappa_A c_2 + c_3)s\widehat{x}_3 + (k_1 + \kappa_A k_2 + k_3)\widehat{x}_3 - (c_1 s + k_1)\widehat{x}_1 - (c_2 s + k_2)\widehat{x}_2 = 0 \quad (5.14c)$$

This system of ODEs can be rearranged and written into matrix form $[\mathbf{A}(s)]\widehat{\mathbf{x}}(s) = \widehat{\mathbf{F}}(s)$ as

$$\begin{bmatrix} m_1 s^2 + c_1 s + k_1 & 0 & -c_1 s - k_1 \\ 0 & m_2 s^2 + c_2 s + k_2 & -\kappa_A c_2 s - \kappa_A k_2 \\ -c_1 s - k_1 & -c_2 s - k_2 & m_3 s^2 + (c_1 + \kappa_A c_2 + c_3)s + (k_1 + \kappa_A k_2 + k_3) \end{bmatrix} \begin{bmatrix} \widehat{x}_1 \\ \widehat{x}_2 \\ \widehat{x}_3 \end{bmatrix} = \begin{bmatrix} \widehat{F}_{L,1}(s) \\ \widehat{F}_{L,2}(s) \\ 0 \end{bmatrix}$$

$$(5.15)$$

The non-symmetric matrix $[\mathbf{A}(s)]^{3\times3}$ represents the inverse of the *transfer function matrix* $[\mathbf{H}(s)]^{3\times3}(s)$. This MIMO transfer function describes the linear mapping of the system input $[\widehat{\mathbf{F}}(s)]^{3\times1}$ on the system output $[\widehat{\mathbf{x}}(s)]^{3\times1}$ in the frequency domain. Due to the complex structure of the mechanical system, the inverse of $[\mathbf{A}(s)]^{3\times3}$ is calculated symbolically using MATLAB™ Symbolic Math Toolbox [81]. As a result, the transfer function matrix $[\mathbf{H}(s)]^{3\times3}$ is obtained consisting of polynomials in s of order six.

Since there is no direct excitation acting on mass m_3, the transfer function matrix $[\mathbf{H}(s)]^{3\times3}$ can be reduced to the matrix $[\mathbf{H}_{\mathrm{red}}(s)]^{3\times2}$. This *reduced* transfer function matrix describes the mapping of the reduced input $[\widehat{\mathbf{F}}_{\mathrm{red}}(s)] = [\widehat{F}_{L,1}(s), \widehat{F}_{L,2}(s)]^{\mathrm{T}}$ on the output $[\widehat{\mathbf{x}}(s)]^{3\times1}$. In order to compute simultaneously the acceleration of mass m_3 during the parameter estimation, the matrix $[\mathbf{H}_{\mathrm{red}}(s)]^{3\times2}$ is augmented by an additional raw. This additional raw is simply a copy of the third raw of the matrix $[\mathbf{H}_{\mathrm{red}}(s)]^{3\times2}$ which defines the influence of the input $[\widehat{\mathbf{F}}_{\mathrm{red}}(s)]^{2\times1}$ on the displacement $\widehat{x}_3$ resulting in the matrix $[\mathbf{H}^*_{\mathrm{red}}(s)]^{4\times2}$. By multiplying the diagonal matrix $\mathrm{diag}(1,1,1,s^2)$ with $[\mathbf{H}^*_{\mathrm{red}}(s)]^{4\times2}$, the *augmented* transfer function matrix $[\mathbf{H}_{\mathrm{aug}}(s)]^{4\times2}$ is derived. It describes the linear mapping of the reduced system input $[\widehat{\mathbf{F}}_{\mathrm{red}}(s)]^{2\times1}$ on the augmented system output $[\widehat{\mathbf{x}}_{\mathrm{aug}}(s)] = [\widehat{x}_1, \widehat{x}_2, \widehat{x}_3, s^2\widehat{x}_3]^{\mathrm{T}}$ in the frequency domain.

The second step of the estimation procedure is to simulate the time response $[\mathbf{x}_{\mathrm{aug}}(t)] = [x_1, x_2, x_3, \ddot{x}_3]^{\mathrm{T}}$ of the dynamic MIMO model to the excitation $\mathscr{L}^{-1}\{\widehat{\mathbf{F}}_{\mathrm{red}}(s)\}$ given by the pre-processed result of the simulated Lorentz force $\mathbf{F}_{\mathrm{Sim}}(t)$. For this purpose, a simulation environment is implemented in MATLAB™ analogously to the environment described in the first case.

123

The *nine* parameters m_i, c_i, and k_i are estimated using a *global search* strategy with local solvers, e.g. fminsearch and fminunc, to find local minima from *multiple start points*. The uniformly distributed start points are restricted to physically meaningful bounds, considering the mass of the experimental setup and observed eigenfrequencies up to 300 Hz. Furthermore, the *simulated annealing* technique [68] is used for generating additional start points to sample multiple basins of attraction.

The *objective function* of this optimization problem is the *combined error* defined as

$$\mathrm{NRMSE}_C = \sqrt{\sum_j \sum_i \left(\mathrm{NRMSE}_{j,i} \right)^2} \, , \tag{5.16}$$

where $j \in \{S, A\}$ and $i \in \{1, 2\}$, while $\mathrm{NRMSE}_{j,i}$ is defined analogously to (5.11). For the calculation of $\mathrm{NRMSE}_{S,i}$ the needed spring forces are defined as $F_{S,1}(t) = k_1(x_1 - x_3)$ and $F_{S,2}(t) = k_2(x_2 - \kappa_A x_3)$. The acceleration component of mass m_3 in the x_1- and x_2-axis are defined as $A_1(t) = \ddot{x}_3(t)$ and $A_2(t) = \kappa_A \ddot{x}_3(t)$.

5.2.5 Results

The comparison of measured force and acceleration components with simulated system outputs is shown in Fig. 5.11 for a set of estimated system parameters. Figure 5.11(a) shows the simulated spring forces $F_{S,i}(t)$ in comparison with the measured force components $F_{\mathrm{Exp},i}(t)$. The calculated NRMSE for the simulated spring forces and the x- and z-component of the measured force are 1.3 % and 2.3 %, respectively. The result shows how the system responds to the rapidly rising Lorentz force near the leading edge of the UUT. The dominant oscillation has the same dynamic characteristics (frequency and decay) for both force components. At approximately $x = 0$ mm ($t = 320$ ms), the vibration with $f \approx 33$ Hz is decayed so that it is barely visible.

Figure 5.11(b) shows the comparison of the simulated generalized accelerations $A_i(t)$ of the same simulation and the measured acceleration components $A_{\mathrm{Exp},i}(t)$. The calculated NRMSE for $A_i(t)$ and $A_{\mathrm{Exp},i}(t)$ is 5.7 % and 6.3 % for the x- and z-component.

This very good result confirms that the presented system identification procedure enables to obtain a minimal model which describes the dominant dynamic characteristics for a concrete measurement result. The selected model structure is capable of describing the complex dynamics of the measured components.

The dominant oscillations agree well, however a slight phase deviation is ascertainable especially after the leading and trailing edge of the UUT. A likely cause of this could be a time variant damping ratio $\zeta_i(t) = c_i(t)/(2\sqrt{m_i k_i})$ due to Lorentz force damping. The result of the accelerations supports the assumption that a third mass m_3 causes the correlating oscillations of all sensor axes. However, the relative deviations, especially at the first peaks, indicate that the chosen ansatz of a linear damping force $c_3 \dot{x}_3$ with constant damping ratio c_3 is only a first assumption to model the oscillation of the third mass.
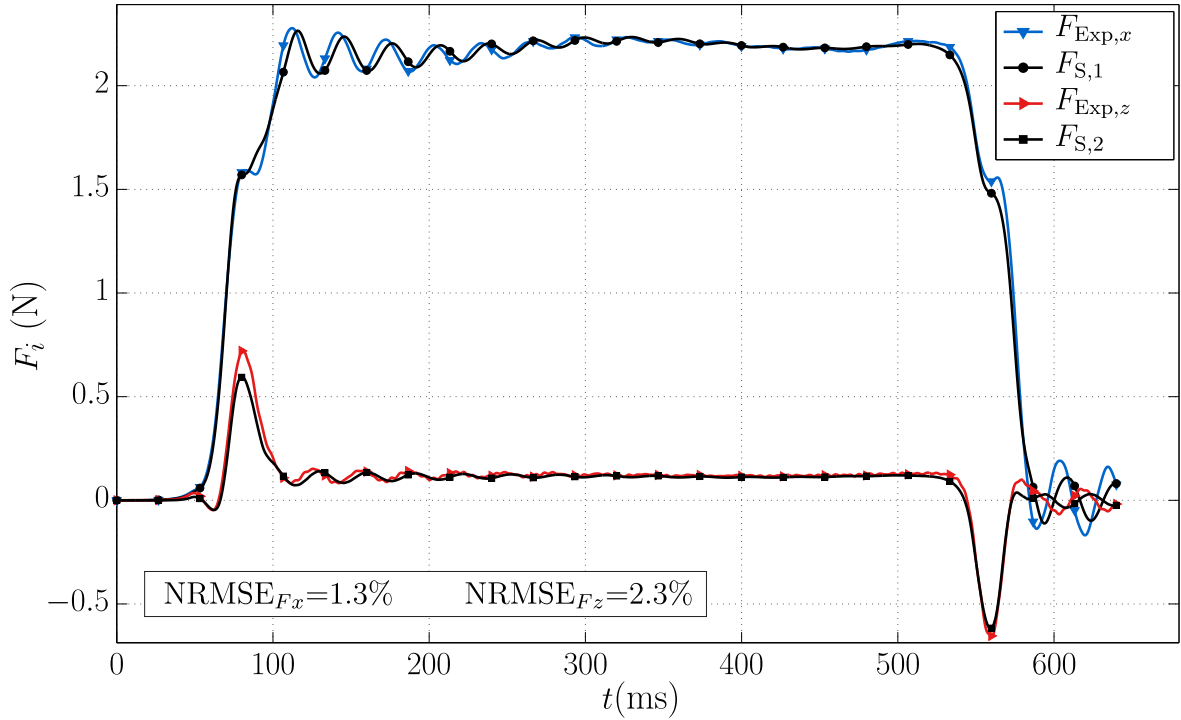
(a) Force components
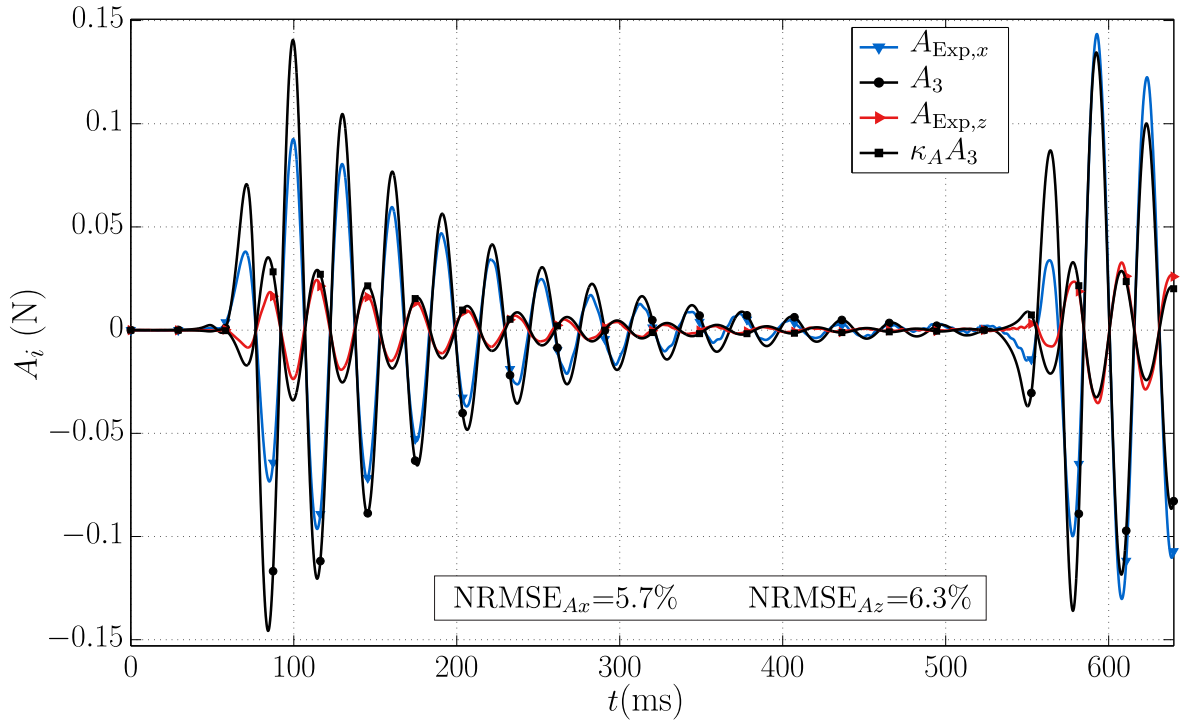
(b) Acceleration components

Figure 5.11: Comparison of simulated and measured system outputs for the identified MIMO system: (a) Comparison of simulated spring force components $F_{S,i}(t)$ (outputs), measured force components $F_{Exp,i}(t)$, and the predicted Lorentz force $F_{Sim,i}(t)$ (inputs). (b) Comparison of simulated generalized accelerations $A_i(t)$ and measured acceleration components $A_{Exp,i}(t)$

.

5.3 Filter Design

The two presented studies on mechanical modeling show how the dominant dynamics of the experimental setup can be described by simple LTI systems. Such mathematical models can serve as an extension of the electromagnetic field computations for LET to predict the measurement result on a particular experimental setup.

Another possibility is to consider the dynamic behavior of the experimental setup as a *frequency-dependent sensitivity* of the sensor which results in systematic measurement error for dynamic measurements [35, 126]. Depending on the selected model structure and the estimated system parameters, it is possible to design a compensation filter which reduces the *dynamic errors* resulting in an estimate of the measurement result of the Lorentz force (corrected measurement result).

For this purpose, in general analogue and digital filters can be used to reduce the dynamic errors. However, depending on the application one of the two techniques is better suited to deal with the filtering task. For the described sensor system the dynamic parameters vary with changing PM, UUT, and experimental parameters, e.g. velocity and lift-off distance. Therefore, an analogue filter would have to be readjusted for each experiment which comes with additional effort and measurement complexity in the case of frequently changing measuring conditions [57]. Digital filters on the other hand, can be designed in the post-processing step to change their characteristics based on the actual measurement result (input). In the following, the design and application of a digital compensation filter is shown for the first described case.

5.3.1 Compensation Filter Design for SDOF-Systems

For a SDOF system the design of a digital filter is possible with little effort. In the first step of filter design, the transfer function $H_i(s)$ from (5.9) has to be discretized in time to $H_i(z)$ using a bilinear transformation [98] or the impulse-invariance method [3, 100]. Both methods to perform the analogue-to-digital transfer function conversion are included in MATLAB™ functions `bilinear` and `impinvar` [81] and have shown to be equally suited in this particular application. For the bilinear transformation, an additional step is necessary where the denominator of the calculated discrete transfer function has to be set to the sum of all denominator coefficients in order to obtain an stable filter.

In the second step of filter design, the inverse of the discrete transfer function $H_i^{-1}(z)$ is calculated. Afterwards, the filter coefficients are determined by comparing the coefficients of the discrete transfer function with the digital filter in normal form [34]. The resulting compensation filter is a finite impulse response (FIR) filter.

In Fig. 5.12 the *frequency response* of the SDOF transfer function $H_i(z)$ (solid line) for $i \in \{x, z\}$ is shown together with the corresponding compensation filter $H_i^{-1}(z)$ (dashed line).

By filtering the measurement signal with the corresponding inverse filter, theoretically a constant amplitude and phase response can be achieved. In practice, the identified transfer
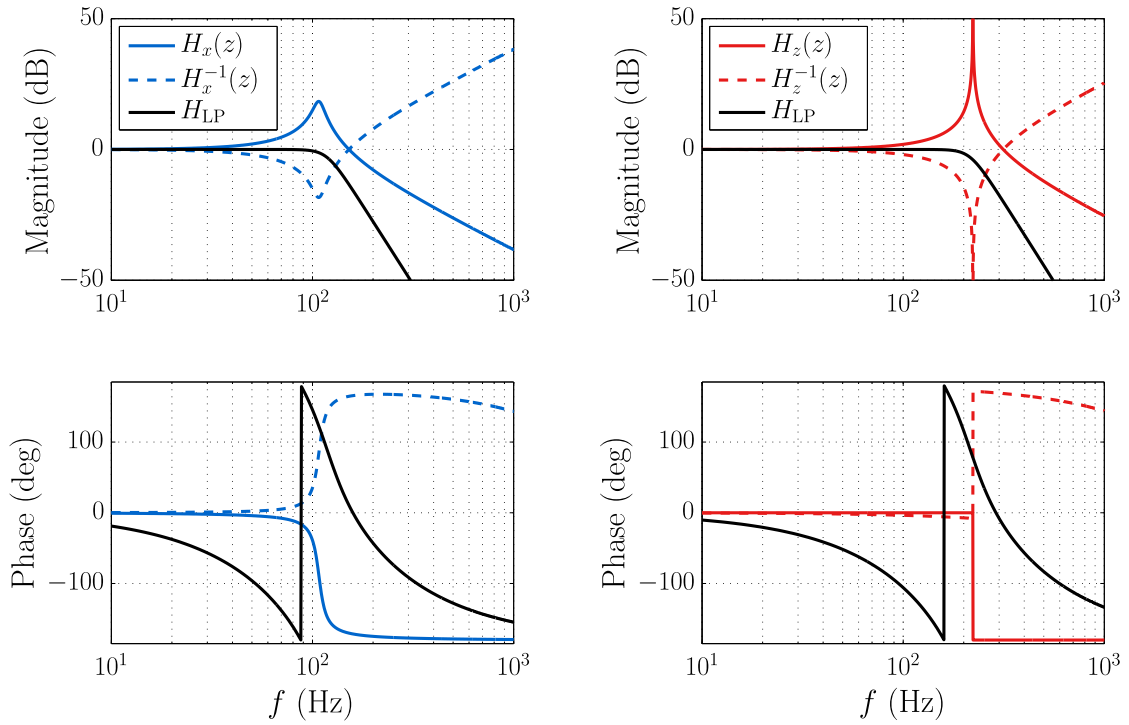
Figure 5.12: Frequency response of the SDOF transfer functions $H_i(z)$ (solid line) for $i \in \{x, z\}$ and the corresponding compensation filters $H_i^{-1}(z)$ (dashed line). The black curves show the frequency response of the cascaded Butterworth low-pass filter of 6th order with a cutoff frequency $f_{c,x} = 120$ Hz and $f_{c,z} = 215$ Hz.

functions are only estimates of the dynamic behavior of the experimental setup up to the first eigenfrequency, while higher modes are not considered. Furthermore, the measured signals are superimposed with high-frequency noise from various sources, e.g. measurement amplifier. These higher frequency components are strongly amplified by the inverse filter and do corrupt the estimated sensor input. Depending on the desired measurement bandwidth and the properties of additional noise, an additional low-pass filter has to be used to reduce the influence of the high frequency components. In this example, one individual Butterworth low-pass filter H_{LP} (black curves) of 6th order is designed for each sensor component with cutoff frequencies $f_{c,x} = 120$ Hz, $f_{c,y} = 275$ Hz, and $f_{c,z} = 215$ Hz, respectively. The filter parameters were optimized in order to minimize the NRMSD of the filtered force component $F_{Exp,Filt,i}$ and the pre-processed simulation results for the Lorentz force $F_{Sim,i}$ shown in Fig. 5.2.

5.3.2 Corrected Measurement Result using Compensation Filter

Figure 5.13 shows the component-wise comparison of the measured force $F_{Exp,i}$ (solid line), the pre-processed simulation results for the Lorentz force $F_{Sim,i}$ (dashed line), and the filtered measurement result $F_{Exp,Filt,i}$ (black line).
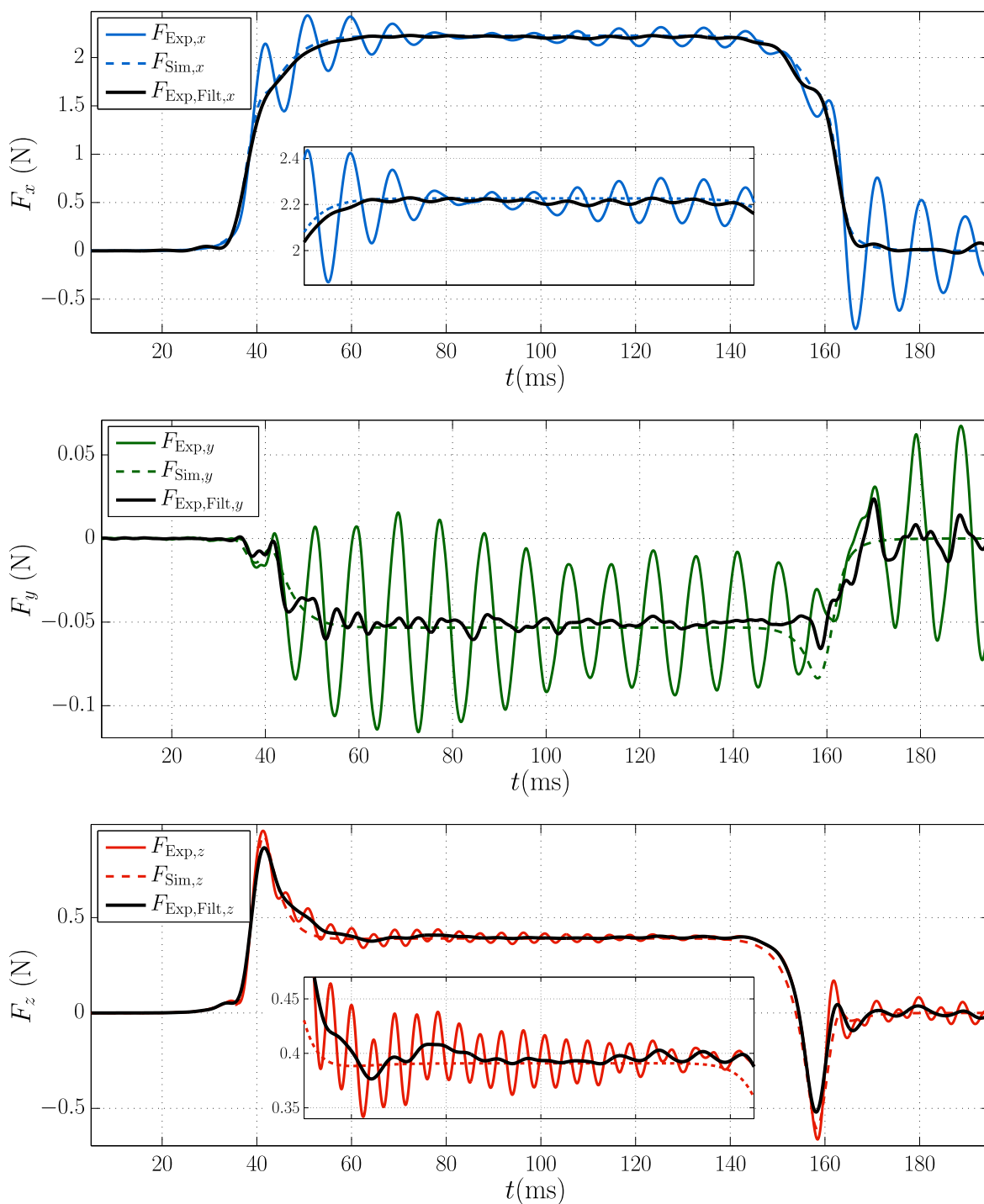
Figure 5.13: Comparison of the measured force $F_{\mathrm{Exp},i}$ (solid line), the pre-processed simulation results for the Lorentz force $F_{\mathrm{Sim},i}$ (dashed line), and the filtered measurement result $F_{\mathrm{Exp,Filt},i}$ (black line)

The comparison shows a very good agreement between the simulated Lorentz force and the filtered measurement result. The NRMSD between the corresponding components is 1.425 %, 8.554 %, and 1.914 % for the x-, y-, and z-component, respectively. The compensation filter reduces dynamic measurement errors caused by the characteristics of the force sensor and allows the estimation of the Lorentz force at high velocities. The formerly dominant eigenfrequencies no longer distort the observation of the Lorentz force which significantly improves the quality of the measurement results.

5.4 Intermediate Summary

The presented studies contribute to the mechanical modeling of the dynamics of the experimental setup in the framework of LET. The process of system identification is discussed exemplarily for two different scenarios, using force profiles computed in numerical field simulations as known input signals.

In the first case, two independent SISO models are used to describe the dominant dynamical behavior of the experimental setup at high velocities ($\bar{v}$ = 2 m/s) for a cylindrical PM. The necessary steps of signal analysis and pre-processing methods are explained in detail and the calculated results are discussed. As a consequence, an unwanted deviation of the mean velocity $\bar{v}$ is identified, as well as a misalignment of the used force sensor. These observations were used to improve the experimental setup for better velocity constancy and a more accurate sensor alignment. Furthermore, a linear scaling factor is introduced to compensate the linear influence of unconsidered process uncertainties. In conjunction with knowledge from an uncertainty analysis it is possible to define an effective magnetic remanence $B_{r,eff}$ of the PM in order to validate the assumed parameters of numerical field computation of the Lorentz force.

The pre-processed Lorentz force signals are used as the input for the simulation of the time response of the system. Therefore, two independent SISO models are selected to describe the dominant behavior of the corresponding sensor component. As a result, a very good agreement between predicted system behavior and measurements is observed, with a relative normalized error less than four percent. The identified models allow to describe the harmonic distortions in LET measurements occurring at high velocities and provides additional knowledge of the experiment setup.

In the second case, a MIMO model with a degree of freedom equal to three is used to model the dynamics of the experimental setup at the typical testing velocity of $\bar{v} = 0.50$ m/s with the Halbach structure used in the experimental studies (Sec.4.4.2). The signal analysis and pre-processing methods from the previous case are extended in order to consider surface undulations of the UUT. Furthermore, an analysis of the complex frequency spectrum was performed to identify important correlations between the different components of the experimental setup. This analysis revealed a causal connection between the motion of the measurement frame, observed by acceleration measurements, and the measured force components. This observation

supported the theory of an additional third mass which describes unconsidered crosstalk between the sensor axes. The identification process is described analogously to the first case, but has been shown to be significantly more time consuming. Finally, the results of the predicted forces and accelerations are compared to the measured time signals, showing a very good agreement.

The modeling process shows that the careful signal analysis is the most important step for a successful system identification. Based on the acquired knowledge about the characteristics of the measurement signals, an individually designed process of signal pre-processing and model selection can take place.

The third section of this chapter describes the design of digital FIR filters to consider the frequency-dependent sensor sensitivity. The filter design is described and the frequency response of the obtained compensation filters are discussed. Finally, the optimized compensation filters are applied to the first discussed scenario of this chapter, showing a significantly improved prediction of the Lorentz force for high-velocity measurements with force sensors of limited bandwidth.

6

SUMMARY AND OUTLOOK

6.1 Summary & Discussion

Chapter 2 presents the state-of-the-art in nondestructive testing with special focus on the preparatory work regarded to LET and the measurement capabilities achieved with former experimental studies are given.

The chapter on dimensional analysis (Chapter 3) contributes to the process of modeling of electromagnetic levitation and breaking problems and provides qualitative insights into the measurement principle of LET. The derived dimensionless representation of the investigated problem fully describes the phenomenon with six dimensionless parameters instead of ten dimensional parameters and is completely independent of the used dimensional system. The performed parametric study illustrates the advantages of the dimensionless representation and shows the dependency of the dimensionless force components $\tilde{F}_{x,z}$ on the magnetic Reynolds number R_{m} and the dimensionless plate thickness τ. The main result of the parametric study is the observation of four distinguishable regions of dependence which are described by simple power laws. It was observed that the location of the transition zones between the separated regions is highly dependent on the dimensionless geometric parameters δ and ξ, which describe the dimensionless diameter and the aspect ratio of the PM, respectively. The evaluation of the numerical investigations resulted in a generalized representation of the two dimensionless force components, which is completely invariant to the four dimensionless input parameters. Based on these findings, three scaling laws were derived, which are of practical value for questions in prototype construction and the evaluation of measurement results. Especially the scaling law of electrodynamic (complete) similarity supports the design of prototypes independent of the chosen geometric scale.

The downside of the presented scaling laws is the high level of abstraction included in the

dimensionless representations, especially when dealing with the generalized representation. Furthermore, the study is focused on non-ferromagnetic materials i.e. it has to be expanded significantly, especially when dealing with materials whose magnetization M depends on the magnetizing field H ($\partial M/\partial H \neq 0$).

In the chapter about experimental studies (Chapter 4) a systematic examination of the measurement procedure of LET is presented, providing a representative overview of the measurement performance of the developed experimental setup. Specifically, the measurement procedure of LET is categorized in terms of the applied measurement principle and the defined measurement method. The physical phenomena described in Chapter 3 are reduced to a verbal sequence of two cause-effect-relationships, which allows the separation of the electromagnetic phenomena from the measurement principles necessary to measure the acting force components. Subsequently, the particular realization applied in this thesis is decomposed into six individual components and analyzed in terms of their functional relationships. Special focus is put on the characterization of a novel sensor system including the derivation of the sensor sensitivities.

A further important aspect of this chapter is the extension of the deterministic (ideal) measurement process to a real measurement process, which considers dependent physical quantities as random variables. It has been analyzed that the statistical properties, e.g. mean and variance of a physical quantity, are not independent of time. It follows that a single measured signal $x_h(t)$ of the non-stationary process can not provide a complete measurement result in terms of expected value and the corresponding variance. Therefore, the assembling of an artificial signal ensemble of sequential measurements is suggested, which for the first time enables the calculation of complete measurement results in LET.

The 4th chapter closes with a comprehensive experimental study on UUTs with and without artificial defects. In the four presented applications, all three components of the force are analysed, for the first time in combination with acceleration recordings of the measurement frame and measurements of the variation of the secondary magnetic field. Furthermore, the studies show complete scans of UUTs made of stainless steel and industrially relevant fibre metal laminates. The four investigations provide, for the first time, complete measurement results of all measurands, and allow the evaluation of measurement uncertainty in LET and DiLET. Three key points are deduced from these studies: (a) all measurements are superimposed with systematic harmonic distortions, (b) diagonal patterns, already observed in the results published by Uhlig in [141], can be traced back to variations of the velocity caused by a non-constant gear ratio of the linear drive, and (c) the z-component of the force, as well as the voltage signal of the 1-axis DiLET sensor are less influenced by both types of distortions.

In conclusion, it can be stated that the studies do not show a clear increase in the detection performance of the method, but rather provide, for the first time, a complete measurement result with a clear distinction of random and systematic deviations.

The chapter on mechanical modeling of the dynamics of the experimental setup (Chapter 5) presents the process of system identification exemplarily for two scenarios of practical

importance. By utilizing force profiles from numerical field simulations, the first discussed case illustrates the necessary steps for developing independent SISO models to describe the dominant dynamical behavior of the experimental system at high velocities. The main findings of the step of pre-processing are the identification of an unwanted deviation of the mean velocity $\bar{v}$ and the misalignment of the used force sensor. The pre-processed simulations are used to calculate the time response of the systems. The estimated model parameters result in independent models which allow the prediction of the harmonic distortions occurring in LET measurements at high velocities. The second discussed case illustrates the rise in complexity when modeling the dynamics of the experimental setup at typical velocities of about $v = 0.5\,\mathrm{m/s}$ with a Halbach structure as PM system. The signal analysis and pre-processing steps are extended in order to consider the relevant surface undulations of the UUT. One of the main findings is the revealed causal connection between the motion of the measurement frame and the measured force components by analyzing the frequency spectra of all recorded signals for correlation. In consequence, the identification process supports a model with an additional mass which can be used to consider the observed crosstalk of the sensor axes, resulting in a very good agreement between observed and predicted measurement results.

Finally, the 5th chapter describes the design process of digital FIR filters in order to consider the frequency dependent sensitivity of the force sensor. In the result, the optimized compensation filter shows significantly improved prediction of the Lorentz force for high velocities with force sensors of limited bandwidth. However, the presented method lacks robustness in describing more complex interactions of the sensor axes.

6.2 Outlook

The present work includes both theoretical and practical investigations and contributes to the development of Lorentz force eddy current testing. The presented results raised further questions and showed new development possibilities, which should be torn as follows.

One of the promising future tasks is based on the dimensional analysis performed on the presented electromagnetic levitation and braking problem in Chapter 3. By using the findings of the numerical studies on well-defined dependencies at specific working points, the identified regions and accompanied scaling laws can be used to determine the partial derivatives and thus calculate the different sensitivities necessary to determine the combined standard uncertainty of correlated and uncorrelated input quantities according to the *Guide to the Expression of Uncertainty in Measurement* (GUM) [59].

A further prospective task lies in the extension and partial modification of the measuring method. Two approaches could be used: (a) the measurement of the secondary magnetic field in all three components, e.g. by means of differential coils, and (b) using so-called 6-axes force-/torque sensors like presented by Schleichert [129] for the additional measurement of the torque acting on the system of permanent magnets.

Another approach is the improvement of the existing measurement procedure by minimizing the influence of the undesirable interaction of the force to be measured and the experimental setup. A promising measurement apparatus has been presented by Gorges *et al.* [41] where measurement frame and linear drive are rigidly connected and the stiffness and mass of these components is drastically increased. In addition, it is shown that the choice of the suitable point of operation, e.g. reduced testing velocity v, can significantly reduce the impact of the observed natural oscillation of the mechanical components discussed in Chapter 5. Therefore, it has a positive influence on the signal to distortion ratio (cf. Chapter 4) of the measured Lorentz force.

It is particularly important for future studies that these technical improvements are aligned with real industrial requirements and adapted to specific applications. Furthermore, it should be noted that in all experiments the z-component of force and the induced secondary magnetic field have shown to be particularly robust against the identified disturbing influences. Hence, the use of these quantities should be preferred.

In addition to the approach of intensifying the efforts to improve the measurement method discussed, a variation of the method with respect to the required relative movement of the magnet system and the UUT can bring significant advantages. A promising approach is the movement of the magnet system on a closed trajectory, such as a linear oscillatory motion or a closed circular motion. This could allow a portable use of the measuring principle, which opens up new fields of industrial applications. For example, using large magnet systems moving at high speed on a circular path can lead to a drastic increase in the temporal variation of the primary magnetic field. Such a method opens the possibility of making electromagnetic measuring methods competitive for low conductive materials like carbon fibre reinforced plastics or filled, electrically conductive plastics.

BIBLIOGRAPHY

[1] P. S. Addison, *The illustrated wavelet transform handbook: Introductory theory and applications in science, engineering, medicine, and finance*. Bristol, UK and Philadelphia: Institute of Physics Pub, 2002.

[2] Analog Devices Inc., "Data Sheet - AD624."
[URL]: www.analog.com/media/en/technical-documentation/data-sheets/AD624.pdf, (2016-12-01)

[3] A. Antoniou, *Digital filters: Analysis, design, and applications*, 2nd ed. Dubuque, Iowa: McGraw-Hill, 2000.

[4] Applied Inspection Ltd, "Visual Testing."
[URL]: www.appliedinspection.co.uk/ndt/visual-testing/, (2016-12-01)

[5] ASC GmbH, "Data Sheet - ASC 5511LN-002."
[URL]: www.asc-sensors.de/uploads/tx_ascproducts/ASC_5511LN_5515LN_Dez15.pdf, (2016-12-01)

[6] K. J. Åström and P. Eykhoff, "System identification—A survey," *Automatica*, vol. 7, no. 2, pp. 123–162, 1971.

[7] ASNT, "Introduction to Nondestructive Testing," 2016.
[URL]: www.asnt.org/MinorSiteSections/AboutASNT/Intro-to-NDT, (2016-12-01)

[8] E. Bachelet, "Foucault and Eddy Currents put to Service," *The Engineer*, vol. 114, pp. 420–421, Oct. 1912.

[9] W. E. Baker, P. S. Westine, and F. T. Dodge, *Similarity methods in engineering dynamics: Theory and practice of scale modeling*, rev. ed ed., ser. Fundamental studies in engineering. Amsterdam and New York: Elsevier, 1991, vol. 12.

[10] H. Bangcheng, Z. Shiqiang, W. Xi, and Y. Qian, "Integral Design and Analysis of Passive Magnetic Bearing and Active Radial Magnetic Bearing for Agile Satellite Application," *IEEE Transactions on Magnetics*, vol. 48, no. 6, pp. 1959–1966, 2012.

[11] G. I. Barenblatt, *Dimensional analysis*. [S.l.]: Taylor & Francis, Inc., 1987.

[12] Benor AS, "Radiographic Testing."
[URL]: www.benor.no/images/services/ndt/vt-pt-mt-et-ut-rt/RTFI20II20-Slag.jpg, (2016-12-01)

[13] S. R. Bistafa, "On the derivation of the terminal velocity for the falling magnet from dimensional analysis," *Revista Brasileira de Ensino de Física*, vol. 34, no. 2, pp. 1–4, 2012.

[14] H. Bleuler, "A Survey of Magnetic Levitation and Magnetic Bearing Types," *JSME international journal. Ser. 3, Vibration, control engineering, engineering for industry*, vol. 35, no. 3, pp. 335–342, 1992.

[15] R. H. Borcherts, L. C. Davis, J. R. Reitz, and D. F. Wilkie, "Baseline specifications for a magnetically suspended high-speed vehicle," *Proceedings of the IEEE*, vol. 61, no. 5, pp. 569–578, 1973.

[16] R. N. Bracewell, *The Fourier transform and its applications*, 3rd ed., ser. McGraw-Hill series in electrical and computer engineering. Circuits and systems. Boston: McGraw Hill, 2000.

[17] H. Brauer and M. Ziolkowski, "Eddy Current Testing of Metallic Sheets with Defects Using Force Measurements," *Serbian Journal of Electrical Engineering*, vol. 5, no. 1, pp. 11–20, 2008.

[18] P. W. Bridgman, *Dimensional analysis*. New Haven: Yale University Press, 1963.

[19] E. Buckingham, "On Physically Similar Systems; Illustrations of the Use of Dimensional Equations," *Physical Review*, vol. 4, no. 4, pp. 345–376, 1914.

[20] A. Canova and B. Vusini, "Analytical Modeling of Rotating Eddy-Current Couplers," *IEEE Transactions on Magnetics*, vol. 41, no. 1, pp. 24–35, 2005.

[21] M. Carlstedt, K. Porzig, R. P. Uhlig, M. Zec, M. Ziolkowski, and H. Brauer, "Application of Lorentz force eddy current testing and eddy current testing on moving nonmagnetic conductors," *International Journal of Applied Electromagnetics and Mechanics*, vol. 45, no. 1, pp. 519–526, 2014.

[22] M. Carlstedt, K. Weise, M. Ziolkowski, R. Schmidt, and H. Brauer, "Estimation of Lorentz force from dimensional analysis Similarity solutions and scaling laws," *IEEE Transactions on Magnetics*, vol. 52, no. 8, p. 7004813, 2016.

[23] C. Chatfield, *The analysis of time series: An introduction*, 4th ed. London and New York: Chapman and Hall, 1989.

[24] Comptes Rendus de la 3e CGPM, "Declaration on the unit of mass and on the definition of weight; conventional value of g_n^*," p. 70, 1901.

[25] COMSOL Multiphysics, 2014. Version 4.4. COMSOL, Inc., Burlington, MA, USA.

[26] J. J. Craig, *Introduction to robotics: Mechanics and control*, 3rd ed. Upper Saddle River, N.J.: Pearson/Prentice Hall, 2005.

[27] I. Daubechies, "The wavelet transform, time-frequency localization and signal analysis," *IEEE Transactions on Information Theory*, vol. 36, no. 5, pp. 961–1005, 1990.

[28] P. A. Davidson, *An introduction to magnetohydrodynamics*, ser. Cambridge texts in applied mathematics. Cambridge and New York: Cambridge University Press, 2001.

[29] D. de Zutter, "Levitation force acting on a three-dimensional static current source moving over a stratified medium," *Journal of Applied Physics*, vol. 58, no. 7, pp. 2751–2758, 1985.

[30] N. Derby and S. Olbert, "Cylindrical magnets and ideal solenoids," *American Journal of Physics*, vol. 78, no. 3, pp. 229–235, 2010.

[31] G. Donoso, C. L. Ladera, and P. Martín, "Damped fall of magnets inside a conducting pipe," *American Journal of Physics*, vol. 79, no. 2, pp. 193–200, 2011.

[32] E. R. Dougherty, *Random processes for image and signal processing*, ser. SPIE/IEEE series on imaging science & engineering. Bellingham, Wash. and New York: SPIE Optical Engineering Press and Institute of Electrical and Electronics Engineers, 1999.

[33] B. Ebrahimi, M. B. Khamesee, and F. Golnaraghi, "Permanent magnet configuration in design of an eddy current damper," *Microsystem Technologies*, vol. 16, no. 1, pp. 19–24, 2010.

[34] S. Eichstädt, C. Elster, T. J. Esward, and J. P. Hessling, "Deconvolution filters for the analysis of dynamic measurement processes: a tutorial," *Metrologia*, vol. 47, no. 5, pp. 522–533, 2010.

[35] S. Eichstädt, A. Link, and C. Elster, "Dynamic uncertainty for compensated second-order systems," *Sensors (Basel, Switzerland)*, vol. 10, no. 8, pp. 7621–7631, 2010.

[36] C. Elbuken, M. B. Khamesee, and M. Yavuz, "Eddy current damping for magnetic levitation: downscaling from macro- to micro-levitation," *Journal of Physics D: Applied Physics*, vol. 39, no. 18, pp. 3932–3938, 2006.

[37] W. Feller, *An introduction to probability theory and its applications*, 3rd ed., ser. Wiley series in probability and mathematical statistics. New York: Wiley, 1968-.

[38] C. Friedman, "The Frequency Interpretation in Probability," *Advances in Applied Mathematics*, vol. 23, no. 3, pp. 234–254, 1999.

[39]   E. P. Furlani, *Permanent magnet and electromechanical devices: Materials, analysis, and applications*. San Diego and London: Academic Press, 2001.

[40]   S. Gholizadeh, "A review of non-destructive testing methods of composite materials," *Procedia Structural Integrity*, vol. 1, pp. 50–57, 2016.

[41]   S. Gorges, H. Brauer, M. Ziolkowski, M. Carlstedt, K. Weise, R. Schmidt, and J. Mengelkamp, "Motion-induced Eddy Current Testing of Composite Materials," *19th World Conference on Non-Destructive Testing 2016*, 2016.
[URL]: www.ndt.net/article/wcndt2016/papers/p80.pdf, (2016-12-01)

[42]   C. A. Guderjahn, "Magnetic Suspension and Guidance for High Speed Rockets by Superconducting Magnets," *Journal of Applied Physics*, vol. 40, no. 5, p. 2133, 1969.

[43]   S. V. Gupta, *Units of measurement: Past, present and future : international system of units*, ser. Springer series in materials science. Heidelberg: Springer, 2010, vol. 122.

[44]   K. D. Hahn, "Eddy current damping of a magnet moving through a pipe," *American Journal of Physics*, vol. 66, no. 12, p. 1066, 1998.

[45]   B. Halbedel, C. Resagk, A. Wegfrass, C. Diethold, M. Werner, F. Hilbrunner, and A. Thess, "A Novel Contactless Flow Rate Measurement Device for Weakly Conducting Fluids Based on Lorentz Force Velocimetry," *Flow, Turbulence and Combustion*, vol. 92, no. 1-2, pp. 361–369, 2014.

[46]   M. G. Hebsur, R. D. Noebe, and D. M. Revilock, "Impact Resistance of Lightweight Hybrid Structures for Gas Turbine Engine Fan Containment Applications," Cleveland, OH, United States.
[URL]: www.ntrs.nasa.gov/search.jsp?R=20030032275, (2016-12-01)

[47]   C. Hellier, *Handbook of nondestructive evaluation*. New York: McGraw-Hill, 2003.

[48]   B. Horn, "Hill shading and the reflectance map," *Proceedings of the IEEE*, vol. 69, no. 1, pp. 14–47, 1981.

[49]   B. Horn, "Closed-form solution of absolute orientation using unit quaternions," *Journal of the Optical Society of America A*, vol. 4, no. 4, p. 629, 1987.

[50]   K. Hutter and K. Jöhnk, *Continuum Methods of Physical Modeling*. Berlin, Heidelberg: Springer Berlin Heidelberg, 2004.

[51]   Hyung-Woo Lee, Ki-Chan Kim, and Ju Lee, "Review of maglev train technologies," *IEEE Transactions on Magnetics*, vol. 42, no. 7, pp. 1917–1925, 2006.

[52]   H. Inoue, "Force feedback in precise assembly tasks," *Bulletin of the Electrotechnical Laboratory*, vol. 38, no. 12, pp. 775–789, 1974.

[53]   G. Ireson and J. Twidle, "Magnetic braking revisited: activities for the undergraduate laboratory," *European Journal of Physics*, vol. 29, no. 4, pp. 745–751, 2008.

[54]   B. Irvine, M. Kemnetz, A. Gangopadhyaya, and T. Ruubel, "Magnet traveling through a conducting pipe: A variation on the analytical approach," *American Journal of Physics*, vol. 82, no. 4, pp. 273–279, 2014.

[55]   ISO 3059:2012, "Non-destructive testing - Penetrant testing and magnetic particle testing - Viewing conditions," 31.12.2012.

[56]   ISO 3452-2:2013, "Non-destructive testing - Penetrant testing - Part 2: Testing of penetrant materials," 31.09.2014.

[57]   M. Jafaripanah, B. M. Al-Hashimi, and N. M. White, "Application of Analog Adaptive Filters for Dynamic Sensor Compensation," *IEEE Transactions on Instrumentation and Measurement*, vol. 54, no. 1, pp. 245–251, 2005.

[58] N. Jain, "Analysis of the Global Nondestructive Test Equipment Market: Understanding Industry Dynamics Key to Growth."
[URL]: www.frost.com/c/10057/sublib/display-report.do?id=NAEE-01-00-00-00, (2016-12-01)

[59] JCGM , "Evaluation of measurement data - Guide to the Expression of Uncertainty in Measurement (GUM): GUM 1995 with minor corrections," 1st ed. Genève, Switzerland: International Organization for Standardization, 2008, vol. JCGM 100:2008.

[60] J. H. Lever, "Technical assessment of Maglev system concepts: Final report by the government Maglev system assessment team," New York.

[61] J. W. Jansen, E. A. Lomonova, and J. M. M. Rovers, "Effects of eddy currents due to a vacuum chamber wall in the airgap of a moving-magnet linear actuator," *Journal of Applied Physics*, vol. 105, no. 7, pp. 07F111–1–3, 2009.

[62] D. C. Jiles, "Review of magnetic methods for nondestructive evaluation," *NDT International*, vol. 21, no. 5, pp. 311–319, 1988.

[63] D. C. Jiles, "Review of magnetic methods for nondestructive evaluation (Part 2)," *NDT International*, vol. 23, no. 2, pp. 83–92, 1990.

[64] Joint Committee for Guides in Metrology, "International vocabulary of metrology – Basic and general concepts and associated terms (VIM)," 15.12.2007.
[URL]: www.iso.org/iso/catalogue_detail.htm?csnumber=45324, (2016-12-01)

[65] R. Kacker and A. Jones, "On use of Bayesian statistics to make the Guide to the Expression of Uncertainty in Measurement consistent," *Metrologia*, vol. 40, no. 5, pp. 235–248, 2003.

[66] M. Kanamori and Y. Ishihara, "Finite-Element Analysis of an Electromagnetic Damper Taking into Account the Reaction of the Magnetic Field," *JSME International Journal Series III - Vibration Control Engineering, Engineering for Industry*, vol. 32, no. 1, pp. 36–43, 1989.

[67] KBFI-UNIO Ltd, "Radiographic Testing."
[URL]: www.kbfiunio.hu/sites/default/files/radiografia_0.jpg, (2016-12-01)

[68] S. Kirkpatrick, C. D. Gelatt, and M. P. Vecchi, "Optimization by simulated annealing," *Science (New York, N.Y.)*, vol. 220, no. 4598, pp. 671–680, 1983.

[69] KLAUS GROSS KG, "Visual Testing."
[URL]: www.klaus-gross.com/en/vt.html, (2016-12-01)

[70] A. L. Kohan, *Boiler operator's guide*, 4th ed. New York: McGraw Hill, 1998.

[71] S. Kumar and D. G. Mahto, "Recent Trends in Industrial and Other Engineering Applications of Non Destructive Testing: A Review," *International Journal of Scientific & Engineering Research*, no. Volume 4, Issue 9, 2013.
[URL]: www.ssrn.com/abstract=2770922, (2016-12-01)

[72] J. C. Lagarias, J. A. Reeds, M. H. Wright, and P. E. Wright, "Convergence Properties of the Nelder–Mead Simplex Method in Low Dimensions," *SIAM Journal on Optimization*, vol. 9, no. 1, pp. 112–147, 1998.

[73] S.-W. Lee and R. C. Menendez, "Force on current coils moving over a conducting sheet with application to magnetic levitation," *Proceedings of the IEEE*, vol. 62, no. 5, pp. 567–577, 1974.

[74] Y. Levin, da Silveira, Fernando L., and F. B. Rizzato, "Electromagnetic braking: A simple quantitative model," *American Journal of Physics*, vol. 74, no. 9, pp. 815–817, 2006.

[75] C. S. MacLatchy, "A Quantitative Magnetic Braking Experiment," *American Journal of Physics*, vol. 61, no. 12, pp. 1096–1101, 1993.

[76] MarketsandMarkets, "Global Non-Destructive Testing (NDT) Equipment Market - By Technology, Verticals & Geography (2013 - 2018)."

[77] MarketsandMarkets, "Non Destructive Testing (NDT) Market by Method (UT, RT, LPT, MPT, ECT, VI), End-User (Aerospace & Defense, Power Generation, Infrastructure, Oil & Gas, Automotive), Technique, Application & Region (G7, BRICS, RoW): Global Forecast to 2020."
      [URL]:   www.marketsandmarkets.com/Market-Reports/nondestructive-testing-market-257342201.html, (2016-12-01)

[78] G. Marsh, "Composites lift off in primary aerostructures," *Reinforced Plastics*, vol. 48, no. 4, pp. 22–27, 2004.

[79] Marshall Space Flight Center, "Ultrasonic Testing of Aerospace Materials: Lesson 765: UT pulse-echo method."
      [URL]: www.llis.nasa.gov/lesson/765, (2016-12-01)

[80] Materials KTN, "NDT in the UK: Why it's Important to the Economy," 23.4.2015.
      [URL]: www.bindt.org/downloads/Materials-KTN-Future-of-NDT-in-UK-economy.pdf, (2016-12-01)

[81] MATLAB, 2013. R2013a. The MathWorks, Inc., Natick, MA, USA.

[82] J. McCurry, "Japan's maglev train breaks world speed record with 600km/h test run," *The Guardian*, 21.04.2015.
      [URL]: www.gu.com/p/47y3y/fb, (2016-12-01)

[83] R. C. McMaster, P. McIntire, and M. L. Mester, *Electromagnetic testing: Eddy current, flux leakage, and microwave nondestructive testing*, 2nd ed., ser. Nondestructive testing handbook. Columbus, OH: American Society for Nondestructive Testing, 1986, vol. v. 4.

[84] ME-Meßsysteme GmbH, "Data Sheet - GSV-1A4."
      [URL]: www.me-systeme.de/docs/de/datasheets/gsv-1a4.pdf, (2016-12-01)

[85] ME-Meßsysteme GmbH, "Data Sheet - GSV-1M."
      [URL]: www.me-systeme.de/de/datasheets/gsv1l-gsv1m.pdf, (2016-12-01)

[86] ME-Meßsysteme GmbH, "Data Sheet - K3D40."
      [URL]: www.me-systeme.de/de/datasheets/k3d40.pdf, (2016-12-01)

[87] J. Meins, L. Miller, and W. J. Mayer, "The high speed Maglev transport system TRANSRAPID," *IEEE Transactions on Magnetics*, vol. 24, no. 2, pp. 808–811, 1988.

[88] P. E. Mix, *Introduction to nondestructive testing: A training guide*, 2nd ed. Hoboken, N.J.: Wiley, 2005.

[89] F. Morinière, R. Alderliesten, M. Tooski, and R. Benedictus, "Damage evolution in GLARE fibre-metal laminate under repeated low-velocity impact tests," *Open Engineering*, vol. 2, no. 4, 2012.

[90] J. A. Mulder, J. H. Breeman, K. W. Iliff, R. E. Maine, and J. K. Sridhar, *Identification of dynamic systems - Applications to Aircraft: L'identification des systèmes dynamiques : applications aux aéronefs*, ser. AGARDograph. Neuilly-sur-Seine, France: AGARD, 1986-1994, vol. no. 300, v. 3.

[91] National Instruments Corporation, "Data Sheet - NI 4472 Series."
      [URL]: www.ni.com/pdf/products/us/3sv414-416.pdf, (2016-12-01)

[92] National Instruments Corporation, "Data Sheet - NI PXI-1036."
      [URL]: www.ni.com/datasheet/pdf/en/ds-447, (2016-12-01)

[93] Newmark Systems Inc., "Data Sheet - NLS4 Series."
      [URL]: www.newmarksystems.com/linear-positioners/nls4-series, (2016-12-01)

[94] Newmark Systems Inc., "Data Sheet - NSC-G Series."
      [URL]: www.newmarksystems.com/motion-controllers/nsc-g-series, (2016-12-01)

[95] N. S. Nise, *Control systems engineering*, 6th ed. Hoboken, NJ: Wiley, 2011.

[96] NMI Staff, "Final Report on The National Maglev Initiative (NMI)," Washington, DC.

[97] Olympus Corporation, "NDT Instruments EPOCH 600: Software Features."
[URL]: www.static5.olympus-ims.com/data/Image/Epoch600/BEA1.jpg?rev=43D9, (2016-12-01)

[98] A. V. Oppenheim and R. W. Schafer, *Discrete-time signal processing*, 3rd ed., ser. Prentice Hall signal processing series. Upper Saddle River: Pearson, 2010.

[99] A. V. Oppenheim, R. W. Schafer, and J. R. Buck, *Discrete-time signal processing*, 2nd ed., ser. Prentice Hall signal processing series. Upper Saddle River, N.J.: Prentice Hall, 1999.

[100] T. W. Parks and C. S. Burrus, *Digital filter design*, ser. Topics in digital signal processing. New York: Wiley, 1987.

[101] M. H. Partovi and E. J. Morris, "Electrodynamics of a magnet moving through a conducting pipe," *Canadian Journal of Physics*, vol. 84, no. 4, pp. 253–271, 2006.

[102] J. A. Pelesko, M. Cesky, and S. Huertas, "Lenz's law and dimensional analysis," *American Journal of Physics*, vol. 73, no. 1, pp. 37–39, 2005.

[103] B. Pesch, *Bestimmung der Messunsicherheit nach GUM*, ser. Grundlagen der Metrologie. Norderstedt: Books on Demand, 2003.

[104] R. F. Post and D. D. Ryutov, "The Inductrack: a simpler approach to magnetic levitation," *IEEE Transactions on Appiled Superconductivity*, vol. 10, no. 1, pp. 901–904, 2000.

[105] R. F. Post, "Maglev: A New Approach," *Scientific American*, vol. 282, no. 1, pp. 82–87, 2000.

[106] Premier NDT Services Inc., "Liquid Penetrant Testing."
[URL]: www.premierndtservices.com/pages/liquidpenetrant.html, (2016-12-01)

[107] J. F. Price, "Dimensional analysis of models and data sets," *American Journal of Physics*, vol. 71, no. 5, p. 437, 2003.

[108] G. Pulugundla, C. Heinicke, C. Karcher, and A. Thess, "Lorentz force velocimetry with a small permanent magnet," *European Journal of Mechanics - B/Fluids*, vol. 41, pp. 23–28, 2013.

[109] I. Rahneberg, D. Dontsov, W. Pöschel, W. Schott, and E. Manske, "Charakterisierung von Linearführungen mit Mehrstrahlinterferometern," *Beiträge der 17. ITG/GMA-Fachtagung vom 3. bis 4. Juni 2014*, 2014.
[URL]: www.vde-verlag.de/proceedings-de/453622027.html, (2016-12-01)

[110] O. Reynolds, "Opening Address to the Mechanical Science Section," *Nature*, vol. 36, no. 933, pp. 462–475, 1887.

[111] R. Schwab, "Magnetic Particle Inspection," Karlsruhe, 26.02.2014.
[URL]: www.youtube.com/watch?v=qpgcD5k1494, (2016-12-01)

[112] H. G. Ramos, T. Rocha, D. Pasadas, and A. L. Ribeiro, "Faraday induction effect applied to the detection of defects in a moving plate," *Review of Progress in Quantitative Nondestructive Evaluation*, vol. 32, no. 1, pp. 1490–1497, 2013.

[113] H. M. G. Ramos, T. Rocha, D. Pasadas, and A. Ribeiro, "Velocity induced eddy currents technique to inspect cracks in moving conducting media," *Proceedings of the International Instrumentation and Measurement Technology Conference (I2MTC)*, pp. 931–934, 2013.

[114] H. G. Ramos, T. Rocha, A. L. Ribeiro, and D. Pasadas, "GMR versus differential coils in velocity induced eddy current testing," *Proceedings of the International Instrumentation and Measurement Technology Conference (I2MTC)*, pp. 915–918, 2014.

[115] J. R. Reitz, "Forces on Moving Magnets due to Eddy Currents," *Journal of Applied Physics*, vol. 41, no. 5, pp. 2067–2071, 1970.

[116] J. R. Reitz, "Force on a Rectangular Coil Moving above a Conducting Slab," *Journal of Applied Physics*, vol. 43, no. 4, pp. 1547–1553, 1972.

[117] Renishaw plc., "Data Sheet - RGSZ20 scale."
[URL]: www.renishaw.com/media/pdf/en/ccc958b233d1407ca03dab2bec32139a.pdf, (2016-12-01)

[118] Renishaw plc., "Data Sheet - T0100 A 40 A."
[URL]: www.renishaw.com/media/pdf/en/dcc4b48f350d487981abc7d1ce6b4806.pdf, (2016-12-01)

[119] Renishaw plc., "Data Sheet - T1000-50A."
[URL]: www.renishaw.com/media/pdf/en/ffda12c3199d44ea8d74f7c625fee290.pdf, (2016-12-01)

[120] P. L. Richards, "Magnetic Suspension and Propulsion Systems for High-Speed Transportation," *Journal of Applied Physics*, vol. 43, no. 6, pp. 2680–2691, 1972.

[121] T. Rocha, H. Ramos, A. L. Ribeiro, and D. Pasadas, "Sub-Surface Defect Detection with Motion Induced Eddy Currents in Aluminium," *Proceedings of the International Instrumentation and Measurement Technology Conference (I2MTC)*, pp. 930–934, 2015.

[122] T. J. Rocha, H. G. Ramos, A. Lopes Ribeiro, D. J. Pasadas, and C. S. Angani, "Studies to optimize the probe response for velocity induced eddy current testing in aluminium," *Measurement*, vol. 67, no. 1, pp. 108–115, 2015.

[123] T. J. Rocha, H. G. Ramos, A. Lopes Ribeiro, and D. J. Pasadas, "Magnetic sensors assessment in velocity induced eddy current testing," *Sensors and Actuators A: Physical*, vol. 228, no. 1, pp. 55–61, 2015.

[124] Rohmann GmbH, "Data Sheet - Elotest N300."
[URL]: www.rohmann.de/datasheets/instruments/N300_eng_04.pdf, (2016-12-01)

[125] M. K. Roy, M. K. Harbola, and H. C. Verma, "Demonstration of Lenz's law: Analysis of a magnet falling through a conducting tube," *American Journal of Physics*, vol. 75, no. 8, p. 728, 2007.

[126] B. Saggin, S. Debei, and M. Zaccariotto, "Dynamic error correction of a thermometer for atmospheric measurements," *Measurement*, vol. 30, no. 3, pp. 223–230, 2001.

[127] W. M. Saslow, "Maxwell's theory of eddy currents in thin conducting sheets, and applications to electromagnetic shielding and MAGLEV," *American Journal of Physics*, vol. 60, no. 8, pp. 693–711, 1992.

[128] J. Schleichert, M. Carlstedt, R. Marangoni, I. Rahneberg, and T. Fröhlich, "Dynamic characterization of a multi-component force transducer using a Lorentz force load changer," in *2014 Shaping the Future by Engineering : Proceedings*.

[129] J. Schleichert and T. Fröhlich, Eds., *Dynamic Calibration of a Multi-Component Force-/Torque Transducer: AMA Service GmbH, P.O. Box 2352, 31506 Wunstorf, Germany*, 2015.

[130] A. Seyed Yaghoubi, Y. Liu, and B. Liaw, "Low-Velocity Impact on GLARE 5 Fiber-Metal Laminates: Influences of Specimen Thickness and Impactor Mass," *Journal of Aerospace Engineering*, vol. 25, no. 3, pp. 409–420, 2012.

[131] J. A. Shercliff, *The theory of electromagnetic flow-measurement*, ser. Cambridge science classics. Cambridge [Cambridgeshire] and New York, NY, USA: Cambridge University Press, 1987, ©1962.

[132] H. A. Sodano, "Eddy Current Damping in Structures," *The Shock and Vibration Digest*, vol. 36, no. 6, pp. 469–478, 2004.

[133] H. A. Sodano, D. J. Inman, and W. K. Belvin, "Development of a New Passive-Active Magnetic Damper for Vibration Suppression," *Journal of Vibration and Acoustics*, vol. 128, no. 3, p. 318, 2006.

[134] C. Soutis, "Fibre reinforced composites in aircraft construction," *Progress in Aerospace Sciences*, vol. 41, no. 2, pp. 143–151, 2005.

[135] Statista GmbH, "Global stainless steel production from 2005 to 2014: Stainless Steel in Figures 2015," 2015. [URL]: www.statista.com/statistics/223028/world-stainless-steel-production/, (2016-12-01)

[136] C. Stelian, Y. Yu, B.-w. Li, and A. Thess, "Influence of velocity profile on calibration function of Lorentz force flowmeter," *Applied Mathematics and Mechanics*, vol. 35, no. 8, pp. 993–1004, 2014.

[137] J. Sun, D. Chen, and Y. Ren, "Stiffness Measurement Method of Repulsive Passive Magnetic Bearing in SGMSCMG," *IEEE Transactions on Instrumentation and Measurement*, vol. 62, no. 11, pp. 2960–2965, 2013.

[138] T. Szirtes and P. Rózsa, *Applied dimensional analysis and modeling*, 2nd ed. Amsterdam and New York: Elsevier/Butterworth-Heinemann, 2007.

[139] A. Thess, E. Votyakov, and Y. Kolesnikov, "Lorentz Force Velocimetry," *Physical Review Letters*, vol. 96, no. 16, pp. 164 501(1–1 645 014), 2006.

[140] A. Thess, E. Votyakov, B. Knaepen, and O. Zikanov, "Theory of the Lorentz force flowmeter," *New Journal of Physics*, vol. 9, no. 8, pp. 299(1–2927), 2007.

[141] R. P. Uhlig, "Identification of Material Defects in Metallic Materials Using Lorentz Force Eddy Current Testing," Ph.D. dissertation, Technische Universität Ilmenau, Ilmenau, Germany, 2013.

[142] R. P. Uhlig, M. Zec, H. Brauer, and A. Thess, "Lorentz Force Eddy Current Testing: a Prototype Model," *Journal of Nondestructive Evaluation*, vol. 31, no. 4, pp. 357–372, 2012.

[143] R. P. Uhlig, M. Zec, M. Ziolkowski, and H. Brauer, "Lorentz Force Eddy Current Testing: Validation of Numerical Results," *Proceedings of the Electrotechnical Institute*, no. 251, pp. 135–145, 2011.

[144] G. A. Watson, "Computing Helmert transformations," *Journal of Computational and Applied Mathematics*, vol. 197, no. 2, pp. 387–394, 2006.

[145] K. Weise, "Advanced Modeling in Lorentz Force Eddy Current Testing," Ph.D. dissertation, Technische Universität Ilmenau, Ilmenau, Germany, 2016.

[146] K. Weise, M. Carlstedt, M. Ziolkowski, and H. Brauer, "Uncertainty Analysis in Lorentz Force Eddy Current Testing," *IEEE Transactions on Magnetics*, vol. 52, no. 3, p. 6200104, 2016.

[147] K. Weise, L. Di Rienzo, H. Brauer, J. Haueisen, and H. Toepfer, "Uncertainty Analysis in Transcranial Magnetic Stimulation Using Non-intrusive Polynomial Chaos Expansion," *IEEE Transactions on Magnetics*, vol. 51, no. 7, p. 5000408, 2015.

[148] K. Weise, R. Schmidt, M. Carlstedt, M. Ziolkowski, H. Brauer, and H. Toepfer, "Optimal Magnet Design for Lorentz Force Eddy Current Testing," *IEEE Transactions on Magnetics*, vol. 51, no. 9, p. 6201415, 2015.

[149] K. Weise, M. Ziolkowski, M. Carlstedt, H. Brauer, and H. Toepfer, "Oscillatory Motion of Permanent Magnets Above a Conducting Slab," *IEEE Transactions on Magnetics*, vol. 51, no. 10, p. 7209113, 2015.

[150] WNDTI – Welding and NDT Institute, "Eddy Current Testing." [URL]: www.wndti.gr/en/training-of-ndt/eddy-current-testing/, (2016-12-01)

[151] Won-Jong Kim, D. L. Trumper, and J. H. Lang, "Modeling and vector control of planar magnetic levitator," *IEEE Transactions on Industry Applications*, vol. 34, no. 6, pp. 1254–1262, 1998.

[152] O. Zahran, , S. Shihab, and W. Al-Nuaimy, "Recent Developments in Ultrasonic Techniques for Rail-track Inspection," Northampton, 2002.

[153] M. Zec, "Theory and Numerical Modelling of Lorentz Force Eddy Current Testing," Ph.D. dissertation, Technische Universität Ilmenau, Ilmenau, Germany, 2013.

[154] M. Zec, R. P. Uhlig, M. Ziolkowski, and H. Brauer, "Differentieller Sensor, Prüfsystem und Verfahren zur Detektion von Anomalien in elektrisch leitfähigen Materialien," Patent EP2 893 336 A1.

[155] H. Zeng and Q. Yi, "Quaternion-Based Iterative Solution of Three-Dimensional Coordinate Transformation Problem," *Journal of Computers*, vol. 6, no. 7, 2011.

[156] O. C. Zienkiewicz, R. L. Taylor, and J. Z. Zhu, *The Finite Element Method: Its Basis and Fundamentals*, 6th ed. Amsterdam: Elsevier Butterworth-Heinemann, 2005.

[157] M. Ziółkowski, *Modern methods for selected electromagnetic field problems*. Szczecin: Wydawnictwo Uczelniane Zachodniopomorskiego Uniwersytetu Technologicznego, 2015.

[158] L. Zuo and X. Tang, "Large-scale vibration energy harvesting," *Journal of Intelligent Material Systems and Structures*, vol. 24, no. 11, pp. 1405–1430, 2013.

[159] L. Zuo, B. Scully, J. Shestani, and Y. Zhou, "Design and characterization of an electromagnetic energy harvester for vehicle suspensions," *Smart Materials and Structures*, vol. 19, no. 4, pp. 045 003(1–10), 2010.

Ich versichere, dass ich die vorliegende Arbeit ohne unzulässige Hilfe Dritter und ohne Benutzung anderer als der angegebenen Hilfsmittel angefertigt habe. Die aus anderen Quellen direkt oder indirekt übernommenen Daten und Konzepte sind unter Angabe der Quelle gekennzeichnet.

Bei der Auswahl und Auswertung folgenden Materials haben mir die nachstehend aufgeführten Personen in der jeweils beschriebenen Weise unentgeltlich geholfen. Die fachliche Betreuung der Arbeit erfolgte durch Dr.-Ing. Hartmut Brauer, Dr.-Ing. habil. Marek Ziolkowski, Univ.–Prof. Dr.–Ing. habil. Klaus Zimmermann und Univ.–Prof. Dr.–Ing. habil. Hannes Töpfer. Ein Teil der Arbeit im DFG-Graduiertenkolleg ist in Kooperation mit Dr.-Ing. Konstantin Weise (geb. Porzig) entstanden. Die daraus entstandenen Ergebnisse sind entsprechend im Text gekennzeichnet und die gemeinsame Autorenschaft wurde bei den Quellen benannt.

Weitere Personen waren an der inhaltlich-materiellen Erstellung der vorliegenden Arbeit nicht beteiligt. Insbesondere habe ich hierfür nicht die entgeltliche Hilfe von Vermittlungs- bzw. Beratungsdiensten (Promotionsberater oder anderer Personen) in Anspruch genommen. Niemand hat von mir unmittelbar oder mittelbar geldwerte Leistungen für Arbeiten erhalten, die im Zusammenhang mit dem Inhalt der vorgelegten Dissertation stehen.

Die Arbeit wurde bisher weder im In- noch im Ausland in gleicher oder ähnlicher Form einer Prüfungsbehörde vorgelegt.

Ich bin darauf hingewiesen worden, dass die Unrichtigkeit der vorstehenden Erklärung als Täuschungsversuch bewertet wird und gemäß §7 Abs. 10 der Promotionsordnung den Abbruch des Promotionsverfahrens zur Folge hat.

_____   _____
(Ort, Datum)   *(Unterschrift)*